Actuation and motion detection of different micro- and nano-structures

Dmitrii Tumanov

Communauté
UNIVERSITÉ Grenoble Alpes

THÈSE

Pour obtenir le grade de

DOCTEUR DE LA COMMUNAUTE UNIVERSITE GRENOBLE ALPES

Spécialité : **Nanophysique**

Arrêté ministériel : 25 mai 2016

Présentée par

Dmitrii TUMANOV

Thèse dirigée par **Jean-Philippe POIZAT**

préparée au sein du **Institut NÉEL – CNRS Grenoble**
dans **l'École Doctorale de Physique de Grenoble**

Actuation and motion detection of different micro- and nano-structures

Thèse soutenue publiquement le **23 juin 2017**,
devant le jury composé de :

Monsieur Christophe COUTEAU
Enseignant-Chercheur, Université Technologique de Troyes, Rapporteur
Monsieur Taha BENYATTOU
Directeur de recherche, CNRS delegation Rhône-Auvergne, Rapporteur
Monsieur Serge HUANT
Directeur de recherche, CNRS delegation Alpes, Président
Monsieur Julien CLAUDON
Ingénieur-Chercheur, CEA Grenoble, Examinateur

Acknowledgments

I would like to express my gratitude to the whole NPSC team as well as to all employees of the Néel Institute and CEA, with whom I worked. Each of you has shown a great enthusiasm and desire to help allowed me to overcome the many difficulties that have risen in my way during these years. I would like to thank personally all those who helped me to gain valuable experiences and thereby made a contribution to my individual development as a scientist.

First of all, I thank Dr. Julien Claudon and Dr. Jean-Michel Gérard for the experimental structures (so-called photonic trumpets), whose physical properties are outstanding.

I express my gratitude to Dr. Pierre-Louis de Assis for both his attentive guidance during my first days in the Institute that helped me to adapt quickly to the laboratory and his numerical simulations, which perfectly supplement my experimental results.

I would also like to express my appreciation to Dr. Pierre Verlot. His deepest knowledge in nano-mechanics together with his cheerful and optimistic mind energized me and inspired to self improvement.

I would like to acknowledge Dr. Taha Benyattou, whose theoretical calculations refuted our initial assumptions about the origin of observed physical effects.

I thank my closest colleague Dr. Hoai Anh Nguyen for the tips in the laboratory and useful advices about PhD's life. Besides, I express my sincere gratitude to Nitika Vaish, who was a Master student and currently is a PhD student in our team. Her assistance in the lab helped me to advance in this research.

I thank Edward Wagner and Dr. Arnauld Gloppe for the technical support of LabView and Python software, which are used to manage our experimental setup. I also thank Fabrice Donatini and Sebastien Pairis for the time spent together at SEM. Your help is a valuable contribution to the results presented in this thesis.

Last but not least, I would like to acknowledge my scientific adviser, Dr. Jean-Philippe Poizat. His critical comments and constructive suggestions helped me to stay focused and do not get lost among the unexpected phenomena occurring in my experiments. His wise mentoring encouraged me to do my best at every step of the research and achieve desired goals, successfully following through seemingly impossible tasks.

My PhD scholarship was supported by the Auvergne-Rhone-Alpes region.

Abstract

This thesis is related to the field of opto-mechanics and the use of different techniques for the measurement and manipulation of mechanical properties of nano-structures.

First part of the work is dedicated to the photonic wires. These objects are GaAs structures with an inverted conical shape of length of the order of 10 µm and diameter of less than 1 µm, containing a layer of InAs quantum dots inside. Wide-range static stress-tuning of quantum dots photoluminescence spectrum was demonstrated using nano-manipulators to bend the wires. Additionally, owing to the spatial dependence of the spectral shift, this technique offers the possibility of QD positions mapping.

The second part of this work concerns the optical actuation of these photonic wires. A laser beam focused on the wire and modulated at the mechanical resonance frequency can set the wire in motion. The physical mechanisms responsible for these effects are presented and discussed.

In the third part is presented a method enabling the detection of mechanical oscillations of small (less than 50 nm in diameter) nanowires with the use of a Scanning Electron Microscope. This original method offers a possibility to detect the motion of many types of micro- and nano-electromechanical devices which are too small to be detected optically owing to light diffraction limit. Moreover, this method also affects the mechanical properties of the structures via a back-action force that becomes non-negligible for such small devices. It opens up the possibility for further fundamental studies related to cooling of the mechanical motion.

Résumé

Cette thèse s'inscrit dans le domaine de l'opto-mécanique et propose l'utilisation de différentes techniques de mesure et de manipulation des propriétés mécaniques de nano-structures.

La première partie de ce travail est dédiée aux fils photoniques. Ces objets sont des structures en GaAs en forme de cône inversé, avec une longueur d'une dizaine de µm et un diamètre inférieur au µm, contenant une couche de boîtes quantiques à l'intérieur. Nous avons démontré une méthode de réglage statique du spectre de photoluminescence de ces boîtes quantiques sensibles à la contrainte, en utilisant des nano-manipulateurs pour contraindre mécaniquement les fils. De plus, grâce à la dépendance spatiale du décalage spectral, il est possible d'établir une carte de la position des boîtes quantiques.

La deuxième partie de ce travail concerne la mise en mouvement de ces fils photoniques à l'aide d'un faisceau laser modulé à la fréquence de résonance mécanique. Les mécanismes physiques à l'origine de ces effets sont présentés et discutés.

Dans la troisième partie, nous présentons une méthode permettant l'observation d'oscillations mécaniques de nano-fils fins (moins de 50 nm de diamètre) en utilisant un microscope électronique à balayage. Cette méthode originale offre la possibilité de contrôler de nombreux types de structures micro et nano-électromécaniques, dont la détection du mouvement n'est pas possible optiquement en raison de la limite de diffraction de la lumière. De plus, cette méthode permet également d'agir sur les propriétés mécaniques des structures via une force de contre-réaction qui devient non négligeable pour ces structures très légères. Cela ouvre la possibilité d'études fondamentales complémentaires liées au refroidissement du mouvement mécanique.

Contents

Chapter 1

Introduction

1.1 Context

Outstanding achievements of modern physics in fabrication of different kinds of micro- and nanostructures lead to a high demand on development of new experimental techniques allowing different types of investigations and manipulations of such structures. In my thesis I concentrated on opto-mechanical interactions becoming significant in such structures due to their small sizes. It includes both: influence of a mechanical change on optical properties of a quantum dots (QDs) based structure and possibility to impact on nanostructure's mechanical properties via interaction with the light. Investigation of such dependencies opens up a possibilities of QDs tuning and mapping for the QD-based nanostructures as well as possibilities to manipulate the motion of nanooscillators. Moreover, a trend to structures' miniaturization enforces us to investigate the utilization of electron-beams instead of the light, which demonstrates interesting possibilities of structures' manipulations.

1.1.1 QD-based structures

Structures based of quantum dots find nowadays a wide range of applications. There are two big families of QDs depending on their fabrication technique. These are colloidal QDs, which are synthesized from solutions (much like traditional chemical processes), and epitaxial QDs, which are grown on the basis of a crystalline substrate via a crystalline overlayer deposition process.

Colloidal quantum dots are widely used in medical and biological research. Besides, they demonstrate outstanding photostability and fluorescence brightness, that makes them a good substitute for traditional luminophores, both organic and inorganic. Nowadays, it is already possible to buy a TV with a quantum dot-powered screen. QD-based LEDs are characterized by small possible size, pure and saturated emission colors with narrow bandwidth as well as low power consumption.

Epitaxial QDs also found the greatest application in optics due to theirs unique optical properties. They allowed to improve the efficiency of solar elements. Miniature QD-based lasers are used in communications devices and demonstrates both high speed data transfer and low power consumption, etc. Apart from various types of classical applications its quantum origin is also in demand. The most known is a possibility for the realization of single-photon source and optical transistor, which are the basis for quantum optical cryptographic communications and

computations [1]. An ideal device in this case requires that a single photon sent into the system always interact with the quantum dot as well as every photon emitted by the quantum dot will be collected at the output of the device. Nevertheless, a QD emits light in all directions that makes a light collection to be difficult. Besides, the large refractive index of shell semiconductor allows only a small part of the emitted light to leave the structure. Most part of light suffers from an internal reflections at the interface. One-dimensional structures (in which propagation of the electromagnetic field is possible in a single direction) has a potential for such device realization [2]. Such systems have high both coupling of a light source with a quantum emitter and collection of the light emitted from the embedded emitter. Various types of system have been already proposed, such as optical micro-cavities [3], pillar micro-cavities [4, 5], photonic crystals [6], etc. Photonic wires considered in this thesis were also developed for that applications [7] and good results were already reached [8, 9, 10].

1.1.2 Nano-mechanical resonators

Nowadays, small mechanical devices are used in many fields of science and find applications in technology. For example, micron-scale cantilevers are used in atomic-force microscopy (AFM) for surfaces mapping. Due to their small sizes they are very sensitive to environmental influences. Thus, possibility to detect small changes in their behavior allows us to produce sensors based on these devices. Micro- and nano-electromechanical systems (MEMS and NEMS) are commonly used today as accelerometers, angular velocity sensors, gyroscopes, magnetometric and barometric sensors. Nano-mechanical resonators are used as electromagnetic oscillations generators providing on-chip frequency reference. Possibility to detect changes in oscillation frequency caused by adsorption of small particles makes them perfect for mass sensing [11]. There are developments in the field of charge sensing [12], and even spin detection [13]. Devices coupled to electrodynamic, electrostatic, thermoelastic and many others physical effects find their technological implementations. At the level of fundamental science, nano-mechanical resonators allows to observe quantum phenomena such as zero-point fluctuations [14, 15, 16], quantum back-action noise [17], creation of non-classical optomechanical states [18].

Further developments tends to successive decreasing of resonator's size in order to obtain lower mass and therefore higher sensitivity, lower power consumption, etc. It also requires the development of new detection techniques, because application of currently used all optical detection methods is limited by the diffraction limit of light, that makes it difficult to detect the motion of the structures, whose size is less than 100 nm. Experiments conducted in the Chapter 5 demonstrate the possibility to detect the motion of such structures detecting secondary electrons appearing under electronic beam illumination of the oscillator.

1.1.3 Opto-mechanical coupling

Light emission of a QD embedded into one-dimensional micro- and nano-structures is coupled to the strain field, which can be adjusted in a relatively wire range due to structure's small sizes. Such coupling appearing for photonic wires was demonstrated in [19, 20].

Experiments conducted in the Chapter 3 demonstrate the possibility of the QDs mapping (identification of the exact QD's position inside the structure) based on such coupling. The other method of QDs mapping based also on this idea was recently presented by our team in [21]. Such information is important because position of the QD defines its coupling with a light source.

The other important result of that chapter is a demonstration of a relative static strain-tuning of light emission of several QDs embedded in the same structure. It opens up the possibility of realization of collective effects based on these structures, in which several (at least 2) QDs have to be brought in resonance.

Experiments conducted in the Chapter 4 are dedicated to development of optical motion actuation technique, which lacks the drawbacks and limitations inherent in piezoelectric method used in [19, 20]. Such method is presented and effects appearing in light-matter interaction are discussed. Further development of this technique will allow to implement a feedback cooling (i.e. the possibility to damp the motion of the nanostructures) as well as to provide a fine static strain-tuning resembling the one from the Chapter 3.

1.2 Thesis outline

Thesis is organized in 5 upcoming chapters, presenting 3 different scientific research, which was briefly introduced above. The most part of the thesis is dedicated to so called photonic wires, presentation of which one of the chapters is devoted..

Chapter 2 describes the experimental structures used for the studies in chapters 3 and 4: conical-shaped GaAs photonic wires with embedded InAs quantum dots. This chapter gives the general information about the properties of self-assembled InAs QDs embedded in a GaAs medium. The manufacturing process of different types of such structures is described. Besides, main features of resulting structures are highlighted. This chapter also contains the analysis of mechanical properties of photonic wires.

Chapter 3 presents the original method of static stress-tuning of a QD embedded in a photonic wire. An original experimental setup based on a Scanning Electron Microscope and allowing utilization of photo-luminescence spectroscopy together with high-precision control and tuning of QD's stress using nanomanipulators will be presented. A QD mapping method will be proposed based on the capabilities of this experiment. Comparison of experimentally obtained data with theoretical expectations will be provided.

Chapter 4 observes the possibility of optical actuation of photonic wire's motion. Experimental demonstration of such possibility will be provided. Different physical effects and their contributions will be considered based on both theoretical calculations and experimental results. Advantages and possible future perspectives will be discussed.

Chapter 5 presents the original method of motion observation of different types of nanostructures using Scanning Electron Microscope. This method enlarges in the lower side the range of possible nanostructures' sizes, the motion of which can be detected. The back-action effect (i.e. the impact of a measurement technique on a measured results) will be demonstrated.

Thesis ends by a Chapter 6, which summarizes all the main results obtained during this work and gives the basis for further investigations.

Chapter 2

Photonic wires with embedded quantum dots

Contents

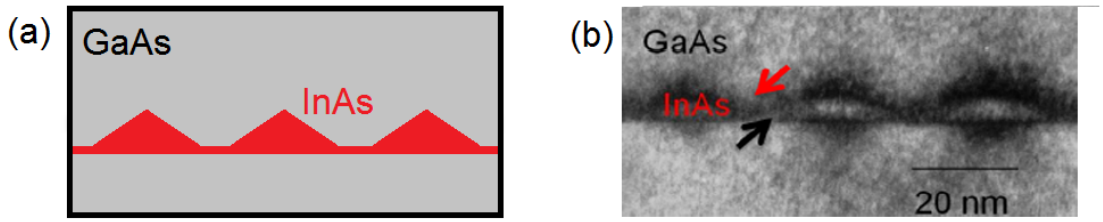

Figure 2.1: (a) Sketch of self-assembled InAs QD embedded in a GaAs matrix. Red triangle is a QD and a red line connecting all triangles is a wetting layer. (b) Transmission electron microscopy (TEM) image of a self-assembled InAs QD embedded in a GaAs matrix. [7]

2.1 Self-assembled quantum dots

Quantum dot (QD) is a semiconductor structure, consisting from a very small droplet of one semiconductor material surrounded by the other semiconductor material with a larger bandgap. The typical size of inclusion is about a few tens of nanometers. Thus, electron and holes in the QD are confined in all three dimensions. As a result, spectrum of charge carrier energy states becomes discrete. That's why QDs are usually considered as zero-dimensional structures or artificial atoms. Despite that QD is relatively big with respect to one atom and consists of thousands of them, it demonstrates similar optical properties caused by quantized energy spectrum and localized charge carriers.

Self-assembled semiconductor QDs appear in the process of layer-by-layer growth due to the relief of elastic energy between two materials with a large lattice mismatch ("Stranski-Krastanov" growth mode [22]). Initially, deposition of one material on the substrate of the other material lead to formation of strained layer which is referred to as 'wetting layer'. Further during a growing process when layer thickness reaches critical value (that depends on strain and the chemical potential of the deposited film), growth continues through the nucleation and creation of 'islands'. Growth conditions (such as deposition rate, temperature, etc.) define size and shape of the 'island' as well as the wetting layer structure. Organized in a such way QDs are then covered, usually, by the same material, which is used for the substrate. It protects QDs from oxidation and prevents interactions with surface states.

In our case all self-assembled InAs QDs are grown by molecular beam epitaxy (MBE). Lattice mismatch between GaAs and InAs is about 7%. Resulting QDs have diameters of about 20-30 nm and heights of about 2-3 nm. A sketch and a real image of the GaAs structure with embedded InAs self-assembled QDs are presented on the Figure 2.1.

The confinement potential of a QD can be simply described by a square-well potential (see Figure 2.2,a). Quantized energy spectrum of a QD can be found by solving the Schrodinger equation

$$\left[-\frac{\hbar^2}{2m^*}\nabla^2 + V(\overrightarrow{r})\right]\Psi(\overrightarrow{r}) = E\Psi(\overrightarrow{r})$$

where m^* is the effective mass, $V(\overrightarrow{r})$ is the effective potential, E is the energy sate, and $\Psi(\overrightarrow{r})$ is the wave-function of an electron or a hole.

Exciton is a quasi-particle made of an electron and a hole, which interact due to attractive Coulomb force. Such exciton can be spatially localized inside the QD during its life-time (in

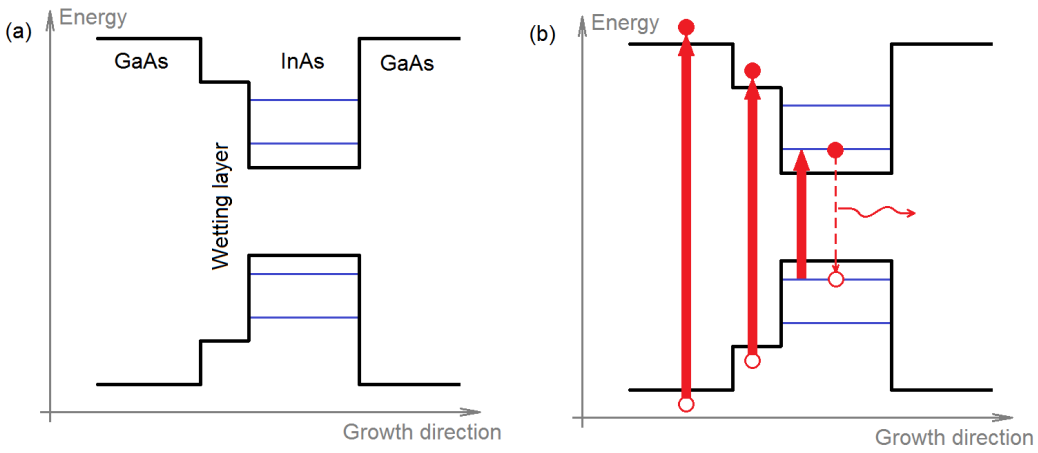

Figure 2.2: (a) A sketch demonstrating simplified square-well potential well of a QD in a growing direction. A band-gap of a wetting layer has a value in between values for the GaAs and InAs. Blue lines are the discrete energy levels of electron and holes in conductive and valence band respectively. (b) A sketch demonstrating 3 ways of optical excitation. From left to right: excitation above bandgap of GaAs, excitation in a wetting layer, resonant excitation. An electron is shown as a filled circle, a hole - a hollow circle.

order of ns) and can recombine either radiatively or non-radiatively. When an electron and a hole are trapped in the ground states of respectively the conduction and the valence band of the QD, the decay mode is mainly a radiative recombination. This is the basis of a photo-luminescence experiment, in which charge carriers can be optically excited via one of 3 possible mechanisms (see Figure 2.2,b): excitation above band-gap of GaAs, excitation in a wetting layer, resonant excitation (it means that energy is exactly equal to energy difference between two QD levels in valence and conductive bands).

Excitation above the bandgap of GaAs (which is at low temperature equal to 1.52 eV that corresponds to a wavelength of 817 nm) creates charge carries in GaAs and only a fraction of them can be captured by the wetting layer. The excitation in a wetting layer is the most effective way to create charge carriers near the QD, which further relax within the conduction and valence band of the QD during a few tens of picoseconds time scale. Resonant excitation allows to create charge carriers directly inside the QD, but it strictly limited by the wavelength. In case of resonant excitation in between of non-ground QD levels charge carriers quickly (in order of ps) decay non-radiatively to the corresponding ground states [10].

2.2 Manufacturing of photonic wires

The photonic wire's family consists of various different types of structures, each of which intended to be optimal for different kinds of application. All of them were developed and grown in the group of J. Claudon and J-M. Gérard, which is a part of our joint Nanophysics and Semiconductors (NPSC) team. Each type of structure requires its own growing parameters. Here we briefly discuss common features of the process. A whole technological process is shown on the Figure 2.3 and typical final devices are shown on the Figure 2.4.

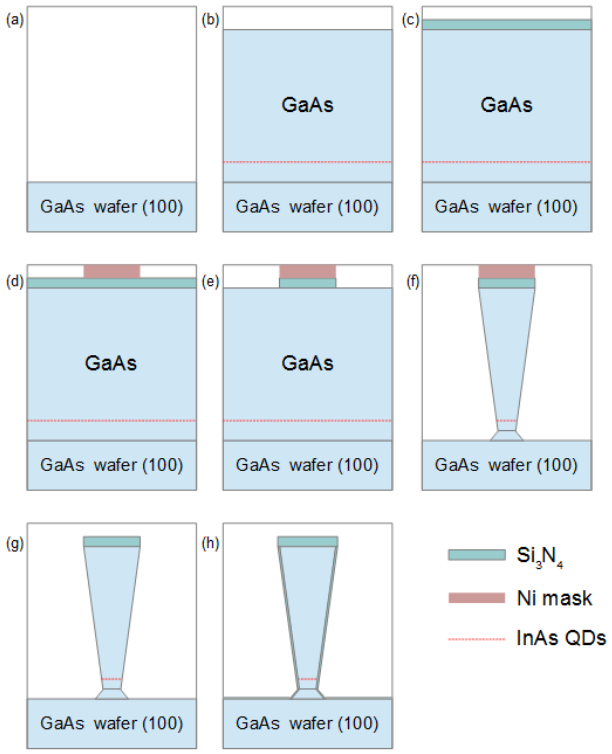

Figure 2.3: Technological process of photonic wire's growth. (a) Growing starts from a GaAs (100) wafer. (b) Using Molecular Beam Epitaxy (MBE) one grows a GaAs layer of the thickness equal to the desirable height of photonic wires. A thin layer of self-assembled QDs can be also grown at any place inside the GaAs layer. For the structures, where it is important to provide a QD's laser excitation with maximum efficiency, a Si_3N_4 anti-reflection coating can be grown on the top using Plasma-Enhanced Chemical Vapor Deposition (PECVD). (c) To define a position of the certain structure Ni mask is used. This mask represents a disk made by electron-beam lithography with the diameter equal to the top diameter of the structure. (d,e) The conical shape of the photonic wire is obtained using Reactive Ion Etching (RIE) with accurate control of etching parameters from top to down that allows to produce a cone with desirable angle. (f) To remove a mask a diluted nitric acid solution is used. (g) If it is required the final structure can be covered by thin Si_3N_4 shell to passivate the surface and suppress surface effects [23].

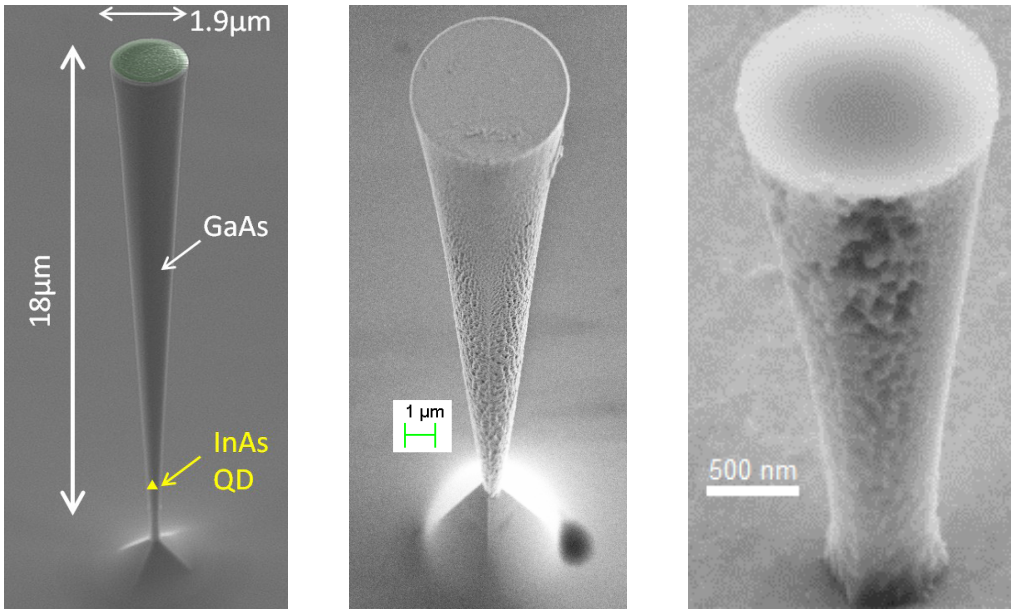

(a) (b) (c)

Figure 2.4: (a) GaAs photonic wire with height of about 18 µm, nominal top of 1.9 µm and a half-angle of 2.3 degree. The InAs QD's layer is located about 1 µm above the substrate. Anti-reflection Si_3N_4 coating (is showed by green) has a thickness of 115 nm. Such kind of structures are used in Chapter 3. (b) GaAs photonic wire with height of about 26 µm, nominal top of 5.5 µm and a half-angle of 5.3 degree. There is no anti-reflection coating on top. Such kind of structures are used in Chapter 4. (c) GaAs photonic wire with height of about 3 µm, nominal top diameter of 1.4 µm and a half-angle of 7.8 degree. Such kind of structures are used in Chapter 4. All images are obtained using Scanning Electron Microscopy. Images (a) and (c) are provided by J. Claudon.

During the growing process not only one structure but many of them are grown on the same substrate. The height and the angle are equal for all of them but top diameter can be controlled independently varying the diameter of Ni mask disk. Positions of the structure is defined by position of mask disk, which is easily controlled. So usually on the experimental sample the structures are organized in matrices, where all trumpets have different diameters. Every matrix has one letter and one number in its name which relate to the order of this matrix on the sample in horizontal and vertical direction respectively. Each matrix is separated to several blocks, each of which typically contains 50 trumpets organized in 5 by 10 array. The value of maximal structure's top diameter (that corresponds to the upper left trumpet) is shown at the left side of the block. On the Figure 2.5 one block of the F1 matrix from the one of our experimental samples is shown.

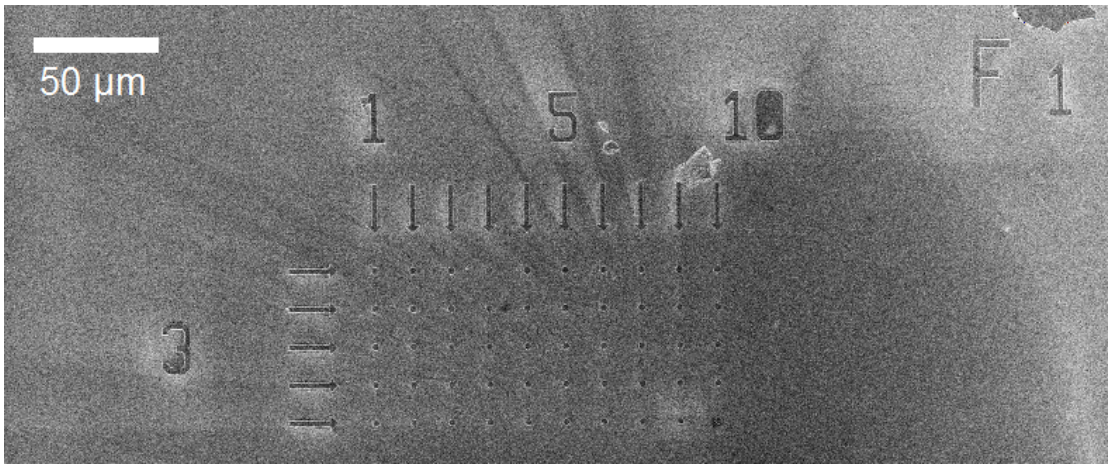

Figure 2.5: Top view image of the sample obtained with Scanning Electron Microscope. One block of F1 matrix is presented, where the structures with top diameters from 3 to 2.51 µm are located. Upper left trumpet has a maximal top diameter of 3 µm (the value is shown on the left side of the block). The next right trumpet has always 10 nm less nominal diameter, and the next down – 100 nm. Distance between neighbors structures is 15 µm. A white line in top left corner is given for the scale of 50 µm.

To collect all photons emitted by QD at the top of the structure trumpets with a mirror from the bottom are required. A mirror can be introduced either growing Dielectric Bragg Mirrors (DBR) or sticking trumpets on a metallic mirror [7, 24]. One of the investigated samples in Chapter 3 is of this type. In this case required GaAs layer is growing in reversed way. It means that the earlier grown layer will be closer to the top of the final trumpet. Technological process is shown on the Figure 2.6. Resulting structures are presented on the Figure 2.7. It has a height of 12 µm length and 6.5 degree opening angle. Nominal top diameter is changing from 1 to 3 µm. QD layer is located 110 nm above the golden mirror.

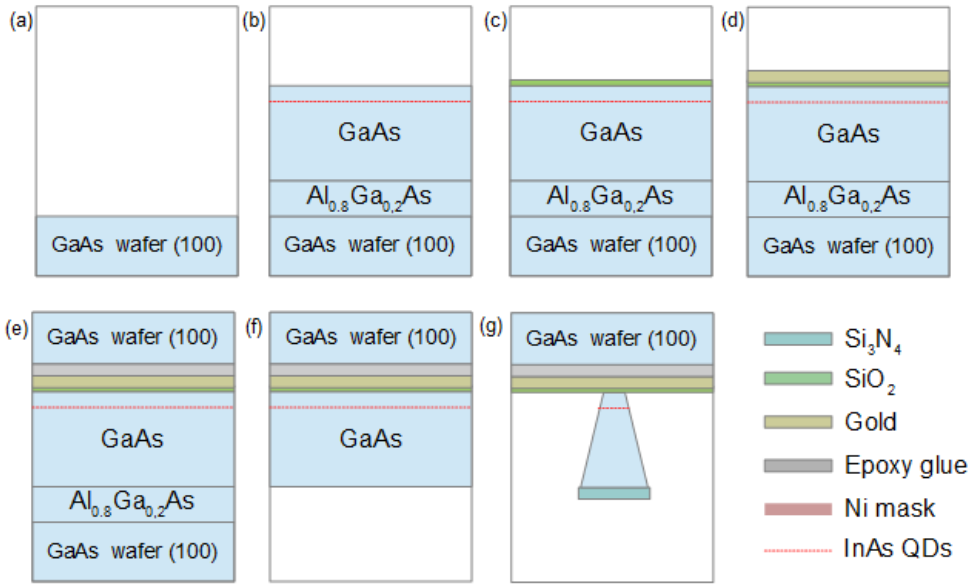

Figure 2.6: Technological process of creation a photonic wire with a mirror from its bottom. (a) Growing starts from a GaAs (100) wafer. (b) In this particular case a 500 nm-thick AlGaAs buffer is grown before a 12 µm-thick layer of GaAs to separate the wafer and GaAs layer. (c,d) After depositing 10 nm of SiO_2 layer a golden 250 nm mirror covers a whole structure. (e) Then structure is glued to the other GaAs wafer and turned upside down. (f) After polymer curing, the growth wafer and the buffer are removed using a combination of physical and selective wet etching. (g) Now, all steps that are used for the presented above photonic wire's growth should be repeated.

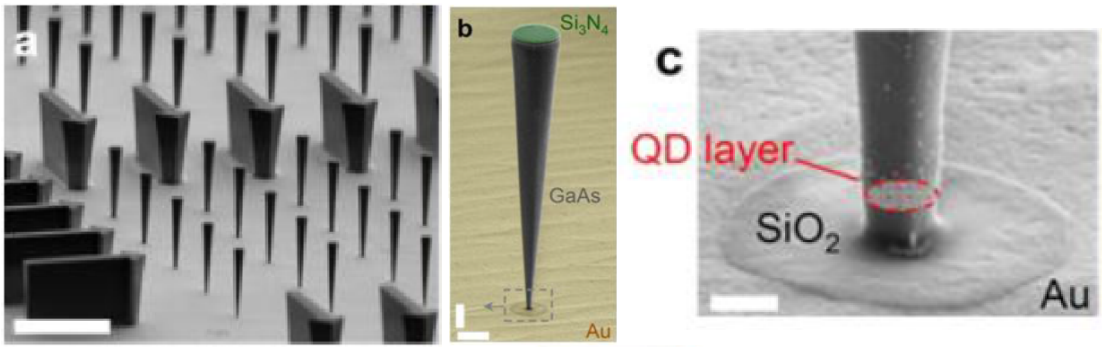

Figure 2.7: (a) Tilted view image of the sample obtained with Scanning Electron Microscope and published in [24]. A white line at down left corner is a scale bar of 15 µm. (b) Zoomed colored image of one structure. It has a height of 12 µm length, 3.25 degree half-angle and nominal top diameter of 1.55 µm. A white scale bar is equal to 1 µm. (c) Zoomed (scale bar is equal to 200 nm) image of the basis of the same structure. QD layer is located 110 nm above the golden mirror.

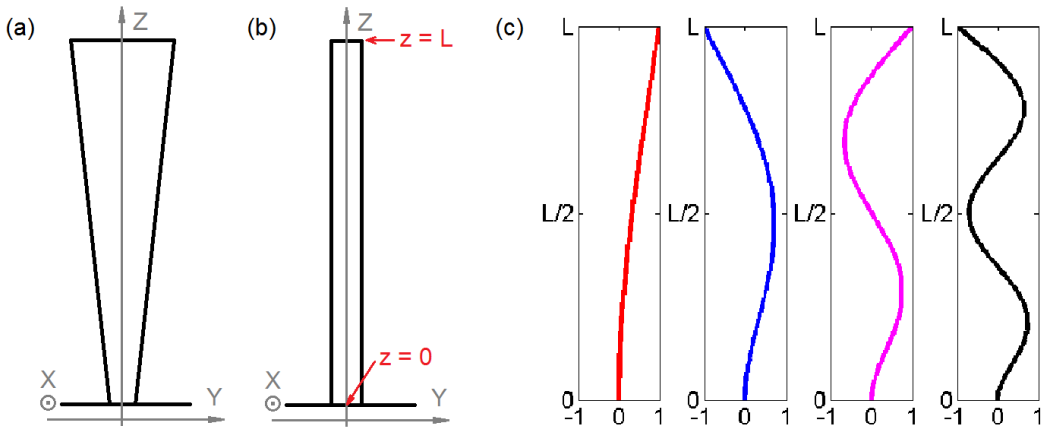

Figure 2.8: Coordinate system for the (a) photonic wire (b) beam. (c) Shape of the first four flexural modes are shown from left to right by different colors. Maximum displacement at the top of the structure (z = L) is equal 1 arbitrary unit for all modes.

2.3 Mechanics of photonic wires

The photonic wire can be considered as a single-clamped mechanical oscillator. Each flexural mode is split into 2 orthogonally polarized eigenmodes. Thus, we need to consider only 1D oscillations of the structure. Transverse oscillations of a one-dimensional Bernoulli-Euler beam can be described by [25]

$$\mu(z) \cdot \frac{\partial^2 u_y(z,t)}{\partial t^2} + \frac{\partial^2}{\partial z^2}\left(E \cdot I_x \cdot \frac{\partial^2 u_y(z,t)}{\partial z^2}\right) = q_y \tag{2.1}$$

where E is the Young modulus, I_x is the second moment of area with respect to x-axis, μ is a mass per unit length, $u_y(z,t)$ is the deflection along y-axis of the structure from the z-axis, which is the axis of the structure's symmetry at the equilibrium. See coordinate system on the Figure 2.8a.

For homogeneous beam with constant cross-section (it assumes not a conical but cylindrical cross-section of the structure, as it is shown on the Figure 2.8,b) in the absence of perturbing forces $q_y = 0$ we can simplify it as

$$\mu \frac{\partial^2 u_y(z,t)}{\partial t^2} + E \cdot I_x \cdot \frac{\partial^4 u_y(z,t)}{\partial z^4} = 0 \tag{2.2}$$

Taking into account that natural oscillations have a harmonic behavior solution can be found as

$$u_{y_i}(z,t) = v_i(z) \cdot \sin(\omega_i t + \varphi_i) \tag{2.3}$$

where ω_i and φ_i is respectively frequency and a phase of the mode, $v_i(z)$ is a stationary solution of the equation and i is a positive integer number of the solution (mode). It gives us a simple fourth-order differential equation equation

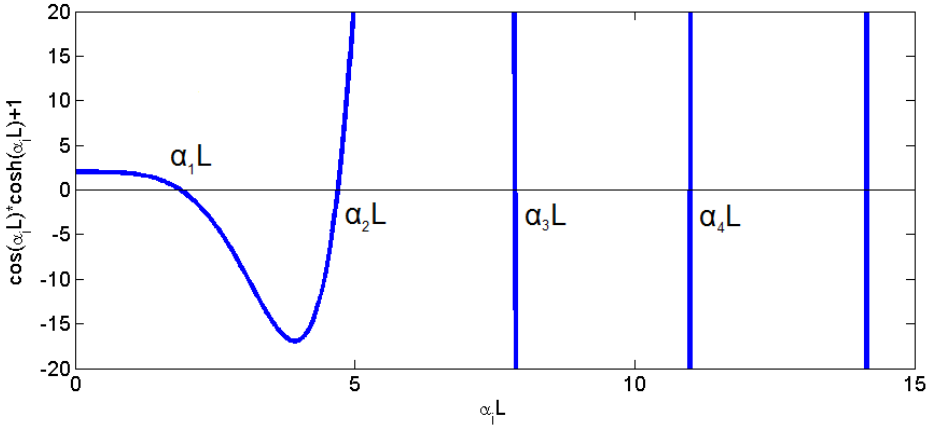

Figure 2.9: Graphic representation of several first roots of the equation (2.7). The values are $\alpha_1 L = 1.88$, $\alpha_2 L = 4.69$, $\alpha_3 L = 7.85$, $\alpha_4 L = 11$.

$$v_i^{IIII}(z) - \alpha_i^4 \cdot v_i(z) = 0, \tag{2.4}$$

where $\alpha_i = \sqrt[4]{m_0 \cdot \omega_i^2/(E \cdot I_x)}$ is a wavenumber. There is infinite (but countable) number of the solutions that have a common expression

$$v_i(z) = A_i \cdot \sinh(\alpha_i z) + B_i \cdot \cosh(\alpha_i z) + C_i \cdot \sin(\alpha_i z) + D_i \cdot \cos(\alpha_i z) \tag{2.5}$$

For the cantilever beam, which is fixed from one side ($z = 0$) and has no no bending moment and shearing force at the free end ($z = L$), the following boundary conditions should be fulfilled:

$$v_i(0) = v_i^{'}(0) = v_i^{''}(L) = v_i^{'''}(L) = 0 \tag{2.6}$$

Thus, the spectrum of all possible wavenumbers is defined by the equality

$$\cos(\alpha_i L) \cdot \cosh(\alpha_i L) = -1 \tag{2.7}$$

Solving this transcendent equation relative to $\alpha_i L$ we can find an oscillation frequency as

$$\omega_i = \alpha_i^2 \sqrt{\frac{E \cdot I_x}{\mu}} = (\alpha_i L)^2 \cdot \frac{R}{L^2} \cdot \sqrt{\frac{E}{4\rho}} \equiv 2\pi f_i \tag{2.8}$$

where R is a radius of the cylindrical rod and L is its length, ρ is a density of GaAs. Here, we used $\mu = \rho\pi R^2$ and $I_x = \pi R^4/4$.

Roots of the equation (2.7) can be presented graphically (see Figure 2.9). These are the values at which a blue curve intersects X-axis (i.e. line y = 0).

The Young modulus of GaAs is equal to 85.5 GPa, whereas its density is 5320 kg/m^3. Thus, for the structure with length of 17 μm and diameter of 1 μm, first four eigenfrequencies are equal to 1.94 MHz, 12.2 MHz, 24 MHz and 66.7 MHz.

We see that flexural modes' frequencies scale as a ratio of the structures radius to its square length. The shape of the mode is then defined as

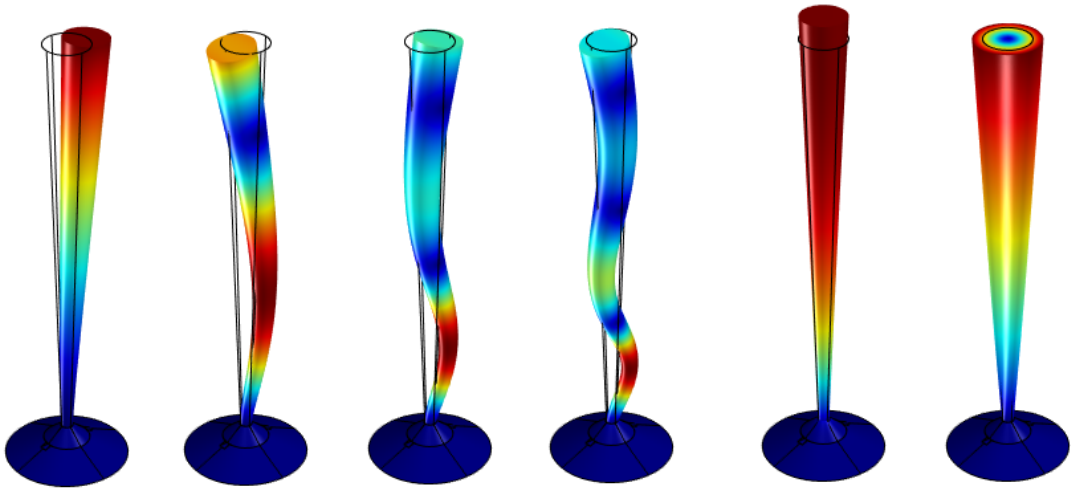

Figure 2.10: Shape of the photonic wire's oscillations for the first four flexural modes and two first order breathing modes. Flexural modes are doubly degenerate, because of the symmetry of the structure. Displacement of the structures is relative. Color shows the displacement and is distributed from blue (zero displacement from initial position) to red (maximum relative displacement). Equilibrium position is shown by black contour.

$$v_i(z) = A_i \left[(\cosh(\alpha_i z) - \cos(\alpha_i z)) + \frac{\cosh(\alpha_i L) + \cos(\alpha_i L)}{\sin(\alpha_i L) + \sinh(\alpha_i L)} (\sin(\alpha_i z) - \sinh(\alpha_i z)) \right] \tag{2.9}$$

where A_i is the motion amplitude of the free end at this frequency. We set it to one arbitrary unit for all modes on the Figure 2.8c to demonstrate the shape of the first four modes.

We used a finite-element commercial software COMSOL to calculate frequencies of flexural modes for the conical structures. On the Figure 2.10 are shown shapes of first four flexural modes as well as two non-flexural modes. It is so-called vertical breathing mode (structure becomes longer: oscillation along the axis of symmetry) and radial breathing mode (structure becomes thicker: oscillation in radial direction symmetrically with respect to the axis of structure). These modes also have higher orders, which are not shown. Colors on the Figure shows the relative structure's displacement from equilibrium position, which is shown by black contour. We can mention that maximum displacement does not correspond to the free end of the structure as it was in case for the rod (see Figure 2.8c).

Values of the different order flexural eigenfrequencies of the structure with height of 26 μm, top facet diameter of 5.5 μm and half-angle of 5 degree are shown on the Figure 2.11a. Modes of different orders demonstrate the same behavior with the change of model's parameters, so the data only for the first order mode are presented on the Figures 2.11c,d,e for different radius, half-angle and length correspondingly. We can see that it is still in direct ratio with a radius as it is for the rod model (see Equation 2.8). However, dependence on the length of the structure is more complicated than inverse ratio with the square of length as it was for the rod. Nevertheless, eigenmode frequency still decreases when length increases.

It is also can be noted that reducing structure's top radius at fixed half-angle or increasing the half-angle at fixed top radius, we are thereby decreasing eigenfrequency and approaching to the situation, when structure's radius at its bottom is equal to 0. At this point, the structure falls and its frequency becomes equal to 0 (no oscillations).

Displacement of the photonic wire's top facet arises a strain at the level of QDs layer. It will be presented in the next chapter.

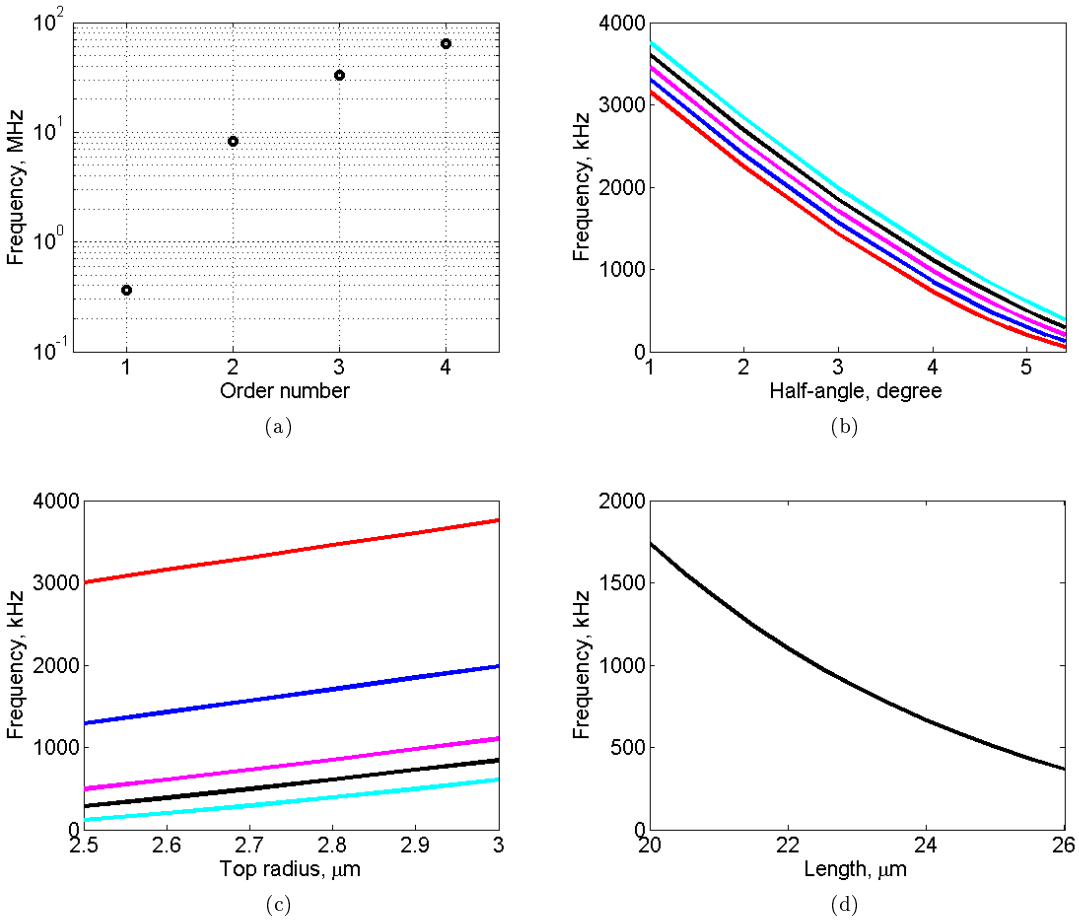

Figure 2.11: (a) Values of the frequency of different order flexural modes for the structure with height of 26 μm, top facet radius of 5.5 μm and half-angle of 5 degree. Data are presented in semi-log scale. (b) Frequency dependence on the half-angle of the structure with fixed top facet radius and height for values of top facet radius: 2.6 μm (red), 2.7 μm (blue), 2.8 μm (magenta), 2.9 μm (black), 3.0 μm (cyan) and height of 26 μm. (c) Frequency dependence on the top facet radius of the structure with fixed half-angle and height for values of half-angle: 1 degree (red), 3 degree (blue), 4.2 degree (magenta), 4.6 degree (black), 5 degree (cyan) and height of 26 μm. (d) Frequency dependence on the height of the structure with top facet radius of 5.5 μm and half-angle of 5 degree.

2.4 Conclusions

This chapter presents a family of the inverted conical shape micro-structures (so-called photonic trumpets), that will be investigated in the following two chapters. These structures have embedded QDs, that were also briefly presented in this chapter. Photonic wires have various configurations differing in their heights, top diameters and half-angles. Within the framework of this dissertation 4 experimental samples were investigated:

- Big Trumpet Sample. All structures are about 26 μm high. There are 5 matrices, which are insignificantly different by half-angle, whose value is about 5.3 degree. Each matrix contains 2 blocks of structures. Structures in the first block have top diameters from 6 μm to 5.51 μm (with 10 nm step between the nearest structures), in the second block - from 5.5 μm to approximately 5.2 μm. Structures with smaller top diameter have too small bottom diameter to remain stiff, so that they break down easily. Distance between two neighbor structures within one block is equal to 30 μm. On the Figure 2.4b one of these structures is shown.

- Medium Trumpet Sample. All structures are about 18 μm high and have a half-angle of about 2.3 degree. There are about 20 matrices. Each matrix contains structures with top diameters from 4 μm to approximately 1.7 μm (with 10 nm step between the nearest structures) organized in 5 blocks. Distance between two neighbor structures within one block is equal to 15 μm. The QD's layer is located about 1 μm above the substrate. Anti-reflection Si_3N_4 coating has a thickness of 115 nm. On the Figure 2.4a one of these structures is shown.

- Short Trumpet Sample. All structures are about 3 μm high and have a half-angle of about 7.8 degree. There are about 176 matrices. Each matrix contains structures with top diameters from 2 μm to approximately 1 μm (with 10 nm step between the nearest structures). On the Figure 2.4c one of these structures is shown.

- Mirrored Sample. All structures are about 12 μm high and have a half-angle of about 3.25 degree. Structures have top diameters from 3 μm to approximately 1.5 μm (with 10 nm step between the nearest structures). QD layer is located 110 nm above the golden mirror. Anti-reflection Si_3N_4 coating has a thickness of 115 nm. On the Figure 2.7b one of these structures is shown.

In Chapter 3 Medium Trumpet and Mirrored samples will be used to study a possibility of static stress-tuning of QDs embedded in such photonic wires. Chapter 4 dedicated to optical actuation of photonic wire's motion is mostly concentrated around Big Trumpet sample, however some experimental results for the Short Trumpet and Medium Trumpet samples are also presented.

Chapter 3

Static stress-tuning of a QD embedded in a photonic wire

Contents

3.1 Introduction

Quantum dot (QD) is a semiconductor structure that also referred to as an artificial atom: a single object with bound and discrete electronic states. Nevertheless QDs grown during one technical process are different (contrary to natural atoms), therefore absolute and relative tuning of QD is an important task in semiconductor physics.

Strain tuning of semiconductor QDs is widely used as a method of wide range (several meV) adjustment and precise control of emission wavelength over the time. It finds an application in fundamental quantum optical experiments aimed to development of quantum computers and quantum computations. Thus, in [26] it is shown that the possibility to bring QD emission wavelength to the D_2 absorption lines of rubidium 87 ($\lambda \sim 780$ nm) is a way to further realization of QD-based quantum memory.

Moreover, because of the fact that exciton and biexciton peaks related to the same QD react differently on the applied stress, it is possible to reduce and sometimes set to zero a binding energy [27] that allows to produce entangled photon pairs from QD using time reordering scheme [28]. The other way to produce entangled photons is to reduce a fine-structure splitting (FSS), which also depends on the applied stress, up to several μeV. The effect of FSS decreasing under uniaxial stress was demonstrated in [29] and realized in nanomembranes [30]. In comparison with annealing method of FSS control presented in [31, 32, 33] strain tuning is reversible and controllable.

It was also shown that emission of InAs/GaAs QD can be continuously adjusted in a range from 711 nm to 868 nm under a pressure from 0 to 4 GPa using diamond anvil cell (DAC) without critical losses of photo-luminescence (PL) intensity and without distraction of anti-bunching properties [34].

In our team it was already shown [20] that quantum dot embedded in a photonic wire is dynamically tuned via displacement of the structure's top (as a result of resonant mechanical excitation with a piezo-electrical transducer) that leads to a huge strain at the QD level. In continuation of this idea we decided to tune a QD in static mode. As it was shown in [19], when the photonic wire is bent there is a gradient of the stress in structure's cross-section. Changing of the structure's position changes the distribution of the stress. A transition energy of off-centered quantum dot (QD) embedded in the photonic wire depends on the applied stress and consequently depends on the photonic wire's position. Thus, it allows us to change the emission wavelength of the QD by changing the laser position on the top of the photonic wire. Due to the gradient of the stress in structure's cross-section two embedded QDs feels different stress for one fixed photonic wire's position. It means that tuning slope is also different for them, and it allows us to bring their transition energies in resonance, which opens the door to studying collective effects in light-matter interaction with two QDs. The collective spontaneous emission of an ensemble of N excited two-level systems predicted in [35] and firstly observed in [36] in optically pumped gas. Usually superradiance is transient: a system initially prepared in the excited state relaxes to the ground state rapidly and the collective emission terminates. But it was recently shown that steady-state superradiance can be achieved by coupling the emitters to a cavity mode [37, 38, 39, 40, 41]. But such investigations go beyond the scope of this thesis.

The general idea of the experiment presented in this chapter is to observe the impact of the externally applied static stress to the QD's transition energy. For that we want to affect the strain in the QD's layer by bending the structure and holding it in bent position. To do this we want to push the photonic wire from a side using a nanomanipulator that allows to control its position with precision of several nm. To observe the changing of energy we register

a photo-luminescence spectra of QDs at 4 K.

3.2 Experimental setup

To provide this experiment the experimental setup should meet the following requirements:

- Small mechanical devices with high precision of positioning should be used.
- The sample will be investigated at low temperature ~4 K to observe a photo-luminescence spectra of QDs. It means that experimental setup should have a vacuum chamber with possibility to bring a liquid helium to it to cool down the sample. Temperature of pushing device should be also as low as possible (equal to the temperature of the sample in ideal case) to prevent heating of the sample.
- This chamber should have a window to transmit the excitation laser as well as QD's luminescence, which is about 900 nm wavelength.
- This chamber should be big enough to place mechanical devices inside it. It should be possible to observe the sample with high spatial resolution.
- It is necessary to bring the tip of nanomanipulator in contact with chosen structure.
- Possibility to register the spectrum of QD's luminescence. It can be easily done having the high-resolving spectrometer.

It is necessary to track the position of the structure visually while pushing on it.

All this brings us to an idea to modify an existing Cathodoluminescence setup. This setup consists of a Scanning Electron Microscope (SEM) with a special chamber where sample's stage can be cooled down by liquid helium, parabolic mirror that collect the light from the sample and send it out of the SEM's chamber through the special window on its side and a spectrometer with achromatic focusing system and CCD camera (see Figure 3.1).

The SEM that we used is FEI Inspect F50. The electrons are generated by a Schottky field emission gun. The chamber is under high vacuum ($<10^{-5}$ Torr), that provides low-level of absorption on the sample surface. The resolution can be as small as 3 nm at 1 keV and goes down to 1 nm at maximum of 30 keV.

Parabolic mirror was specially developed to collect emission of the investigating structure. It has a hole on the upper plane to let electron beam reach the structure. Thus, we can see the sample due to detection of the secondary electrons and excite carriers (cathodoluminescence).

The high resolution IHR550 grating spectrometer is used to register luminescence spectra. We used first order mode of 600 grooves/mm IR grating and a silicon CCD camera with 2048 x 512 pixels and pixel's size equal to 13 x 13 μm. It allows us to observe a spectrum in 74.5 nm range around 900 nm with resolution of 36.4 pm. Working temperature of the camera is about –70 ^{o}C. In this spectrometer grating can be also used at zero order. Thus it acts as a mirror and allows to observe on a CCD chip a spot incoming through the entrance slit of the spectrometer. This mode is used to align the experimental setup.

We modify this setup by adding the laser that comes inside the SEM through the same window and illuminates the sample being focused with the same parabolic mirror. We have also placed nanomanipulator's stage inside the chamber of SEM. Resulting experimental setup is shown schematically on the Figure 3.1 and on the photo on the Figure 3.2.

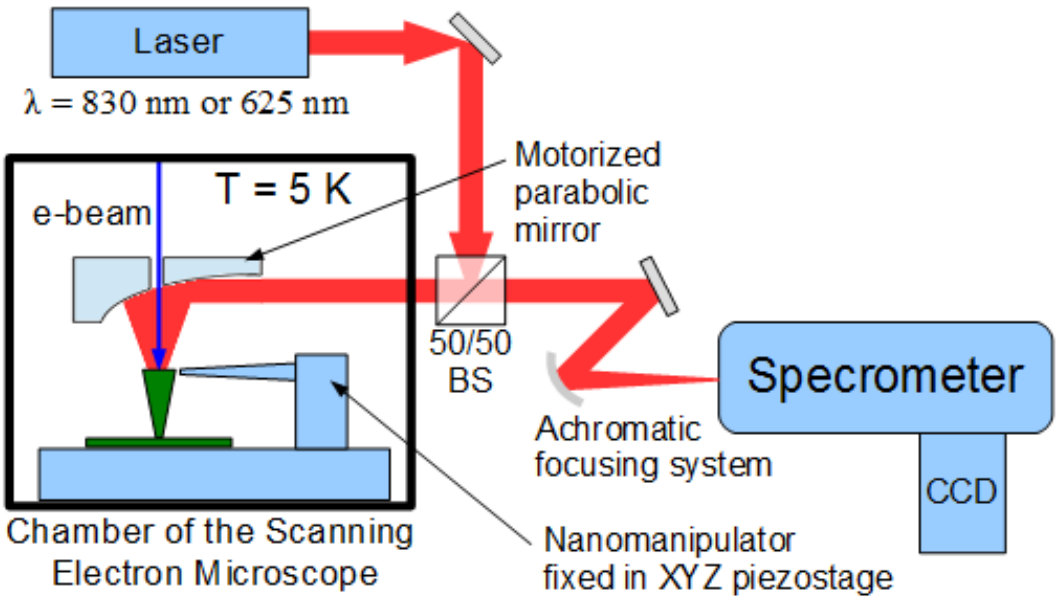

Figure 3.1: Schematic view of cathodoluminescence experimental setup modified for photoluminescence measurements by introduction of the laser beam into the SEM chamber using 50/50 beam splitter.

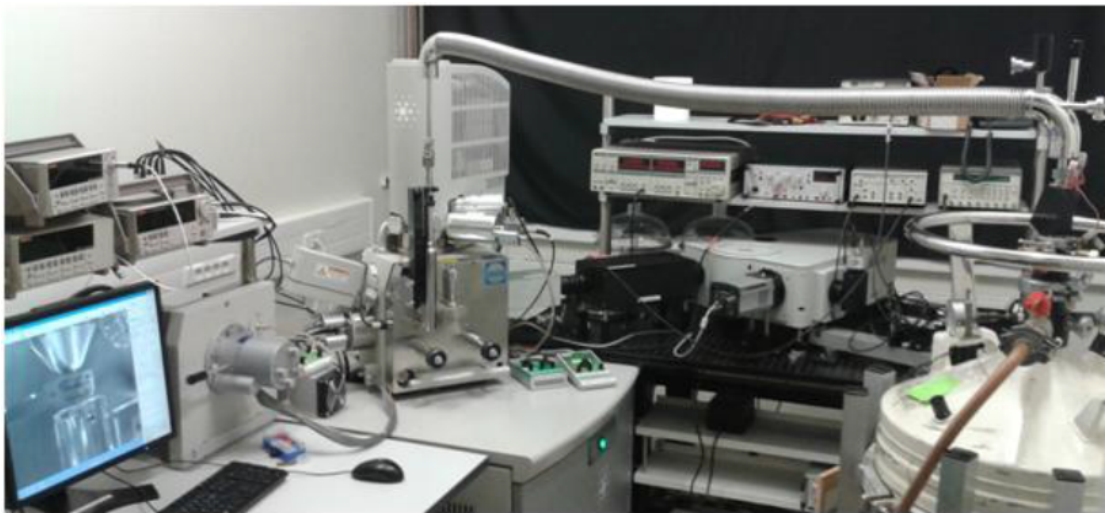

Figure 3.2: Photo of experimental setup.

To excite the luminescence of QDs we used two diode lasers with different wavelength: 830 nm – to create electron-hole pairs in wetting layer – and 625 nm to create carriers due to inter-band absorption. Both chips were mounted in laser diode mount with integrated temperature controller LDM9T/M and controlled by LDC 201 C laser diode controller. Lasers were used in continuous-wave mode. At the output they have a beam which is elliptical in cross-section. To compensate it we used anamorphic prism and a spatial filter.

A spatial filter consists of 2 lenses and a pinhole in between. Parallel laser beam is focused on the pinhole by first lens. Focal distance and a size of a pinhole are chosen to cut off all non-perfectness of the beam. We used 10 cm lens and 20 μm pinhole. After passing through the pinhole we recover a parallel laser beam mounting the second 10 cm lens at its focal distance.

To push on such small object a closed-loop piezo-stage with nanomanipulator is used. It allows us to measure and to control the position of the tip very precisely. We have a special stage where 4 tips can be mounted. Originally these tips are used to carry out spatially resolved I-V measurements. But we decided to use them for pushing our structures. Tips are connected to a cold finger with a wire to avoid the heating of the photonic wire while pushing.

Each tip can be moved along 3 directions: Z axis is coincident with e-beam and relates to the height of a tip with respect to the investigated structure, in the plane X axis is directed along a tip, Y – perpendicular to a tip (see Figure 3.3a). Each tip can be moved independently. They are are mounted at 45 degree with respect to the sample's sides. There is two modes to move a nanomanipulator. First one is a step mode driven by stick-slip motors, when tip is jumping from one position to the other. In this case range of adjustment can be very large about several mm whereas the step can be chosen by operator in a range from fractions of a millimeter to less than a micrometer. But in this mode tip exerts vibration because of a quick 'jump' and it can break the structure. We used it to bring the tip close to the photonic wire. The other mode is an analog mode, when position of the tip can be changed smoothly by applying a voltage to the piezo in a range of 1 μm with a step less then 1 nm theoretically. In such case knowledge about position are limited by precision of position's measurement, which is about 3 nm.

Tip's profile in XY and XZ planes is shown on the Figure 3.4a. Normal position of the tip on the SEM image is shown on the Figure 3.4b by green color. On the same image you can see the tip mounted with a small rotation in a holder in YZ plane. We need it for some of the further experiment described in the section 3.5.1.

3.2.1 Parabolic mirror

The most delicate part of the experimental setup is a parabolic mirror. To align the experimental setup the following conditions must be fulfilled:

- The structure's top facet should be placed in a focal point of parabolic mirror. For this, sample can be moved using precise XYZ stage. For fine tuning parabolic mirror can also be moved in XYZ space.

- Parallel laser beam should come to the parabolic mirror along its axis. It give us 4 degrees of freedom for the laser beam: two coordinates and two angles. All of them can be adjusted using two last mirrors before the beamsplitter.

Nevertheless, initial rough alignment of the setup is difficult, because changing the position of the parabolic mirror with a view to improve collection of light from the light emitter, breaks also the alignment of laser beam and decrease excitation quality. Additionally, the situation is

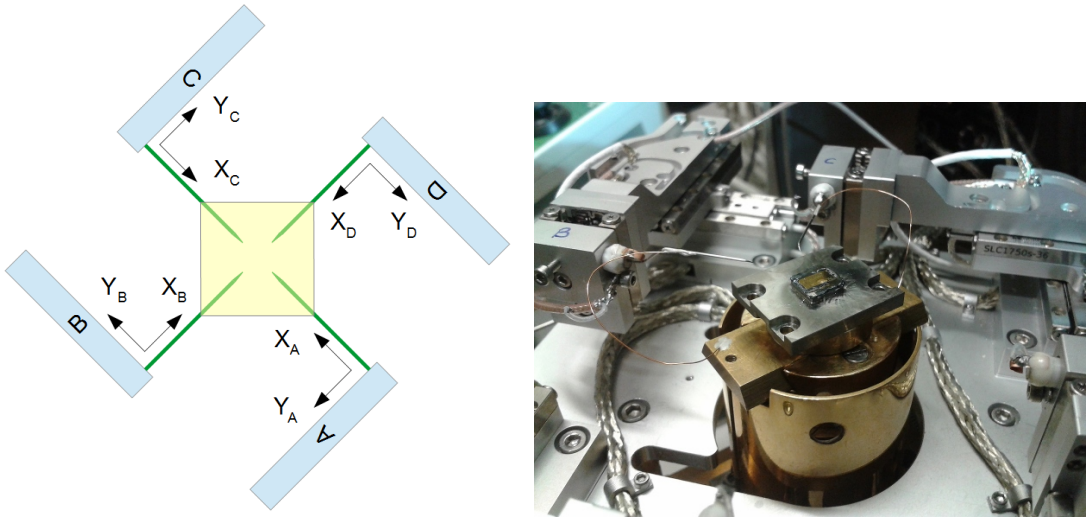

(a) (b)

Figure 3.3: (a) Schematic top view of 4 piezostages with mounted tips and their coordinate systems. Experimental sample is shown as a yellow square. (b) A photo of 2 piezostages B and C and a sample. Tips are connected to a cold finger with a wire to avoid the heating of the structure while pushing.

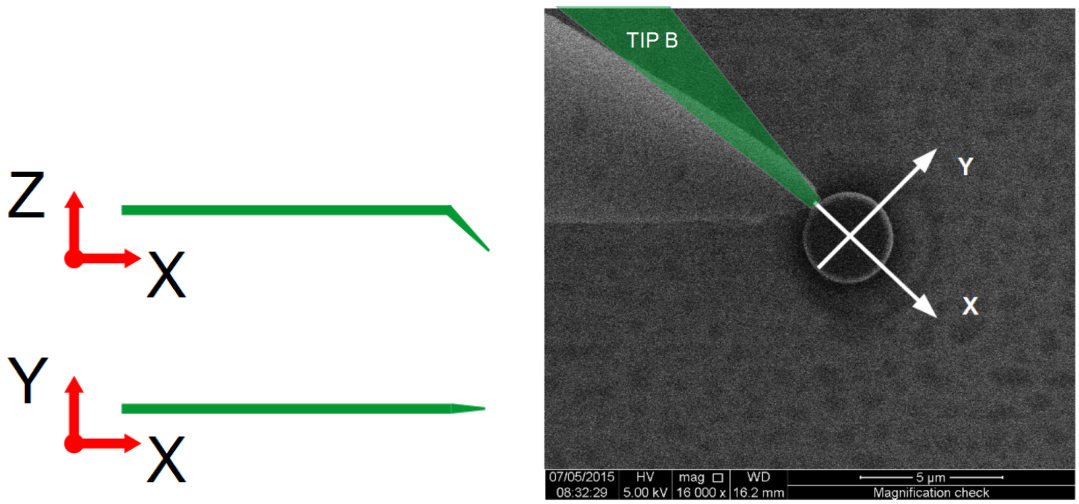

(a) (b)

Figure 3.4: (a) Schematic view of the tip in different planes. (b) Real top view of the tip touching the photonic wire taken with SEM. Tip is rotated a bit along X axis for some specific experiments. Green profile shows tip's position if tip is mounted without rotation.

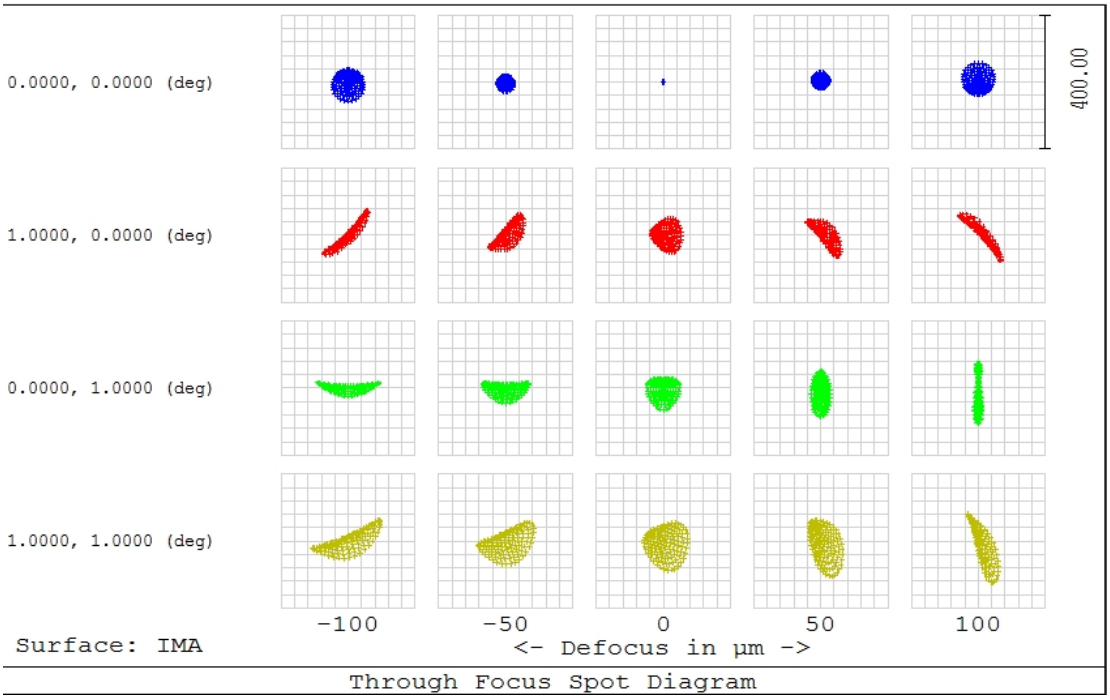

Figure 3.5: Simulation of beam profile around focal position of parabolic mirror made in terms of geometrical optics for parallel incident laser beam propagating along the mirror axis: (blue) without any tilt, (red) with 1 degree tilt with respect to X axis, (green) with 1 degree tilt with respect to Y axis, (yellow) with 1 degree tilt with respect to both axis. Parabolic mirror axes are shown further on the Figure 3.8a.

made difficult by the fact that we are not able to see the beam profile on the sample surface. And we have previously observed that quality of the laser spot (its diameter and roundness) at focal point of parabolic mirror degrades quickly if incident laser beam is slightly tilted or off-centered with respect to mirror's axis. On the Figure 3.5 the results of simulation of beam profile at different tilt angle of the incident laser beam at several position around the focal point of parabolic mirror are shown.

We have also done the same calculation in case if the laser beam is a bit (1 degree) convergent or divergent and we found out that it not only changes the distance to the focal point, but dramatically increases the size of the focused spot. The results of calculation are shown on the Figure 3.6.

To understand the dependence of laser spot on the incident beam alignment we performed additional study. Experimental setup is shown on the Figure 3.7. We used the same laser beam source prepared in the same condition by an anamorphic prism (is not shown on the figure) and a pinhole-based spatial filter. We repeated the same laser path that is used in an original experimental setup, which includes 3 dielectric mirrors and one beamsplitter. The last mirror before the beamsplitter was mounted on a one-dimensional translation stage, that allows us to move the incident beam along one of the axis of the parabolic mirror. We visualized laser spot formed by parabolic mirror on a TV screen using a microscope objective and a CCD camera.

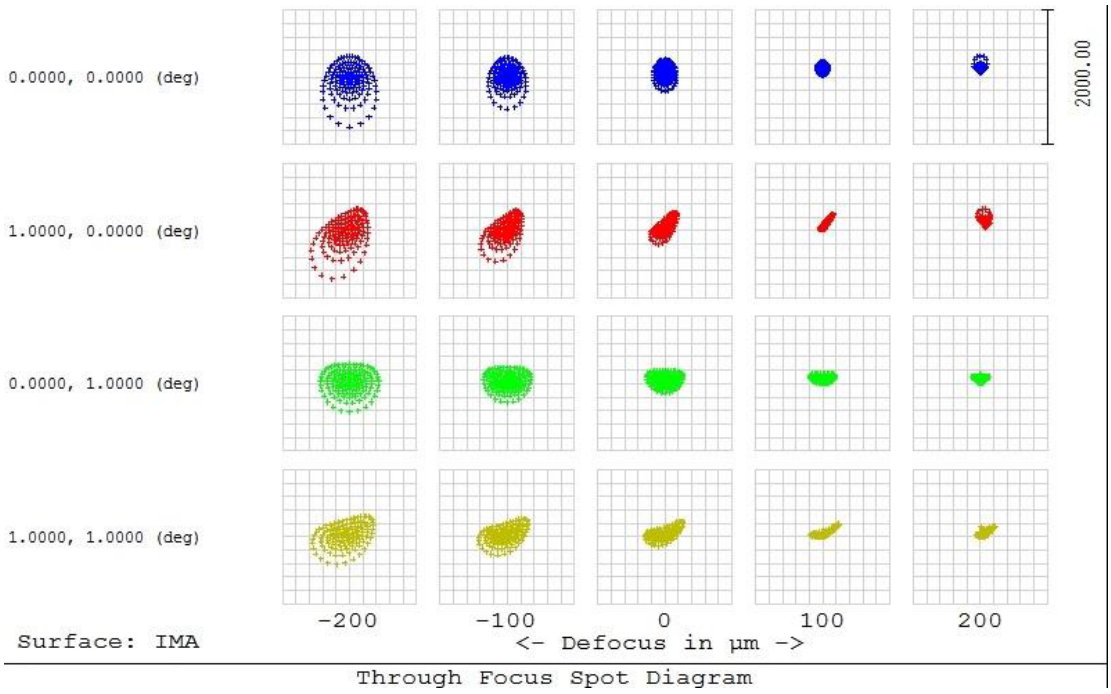

(a)

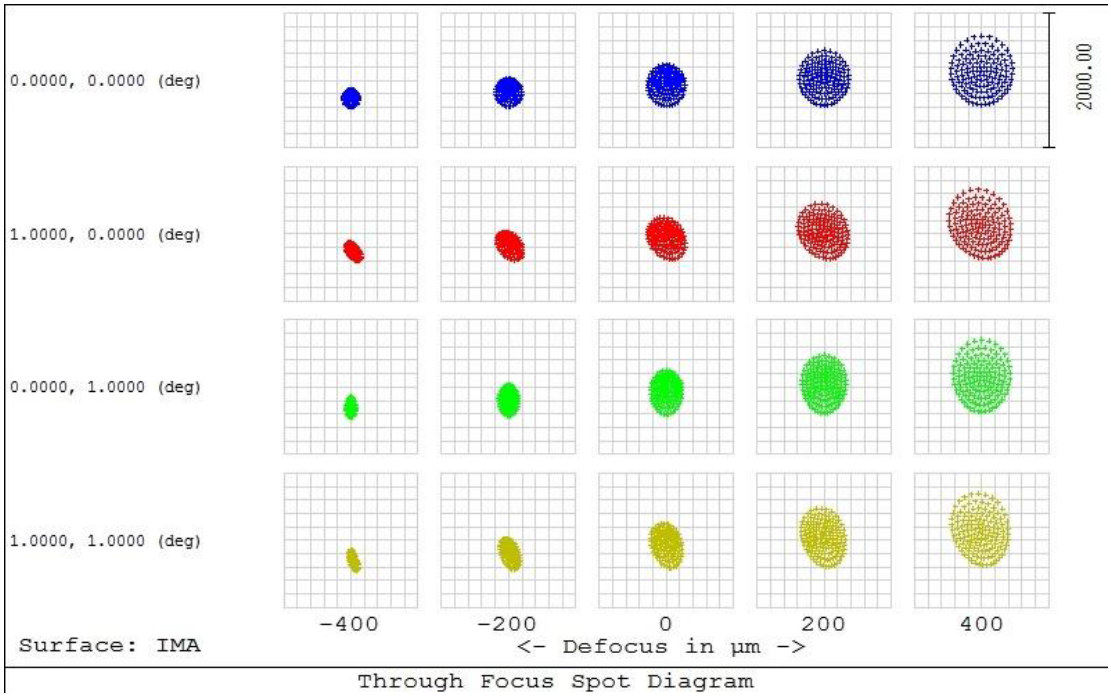

(b)

Figure 3.6: Simulation of beam profile around focal position of parabolic mirror made in terms of geometrical optics for (a) converging (b) diverging incident laser beam propagating along the mirror axis: (blue) without any tilt, (red) with 1 degree tilt with respect to X axis, (green) with 1 degree tilt with respect to Y axis, (yellow) with 1 degree tilt with respect to both axis. Parabolic mirror axes are shown further on the Figure 3.8a.

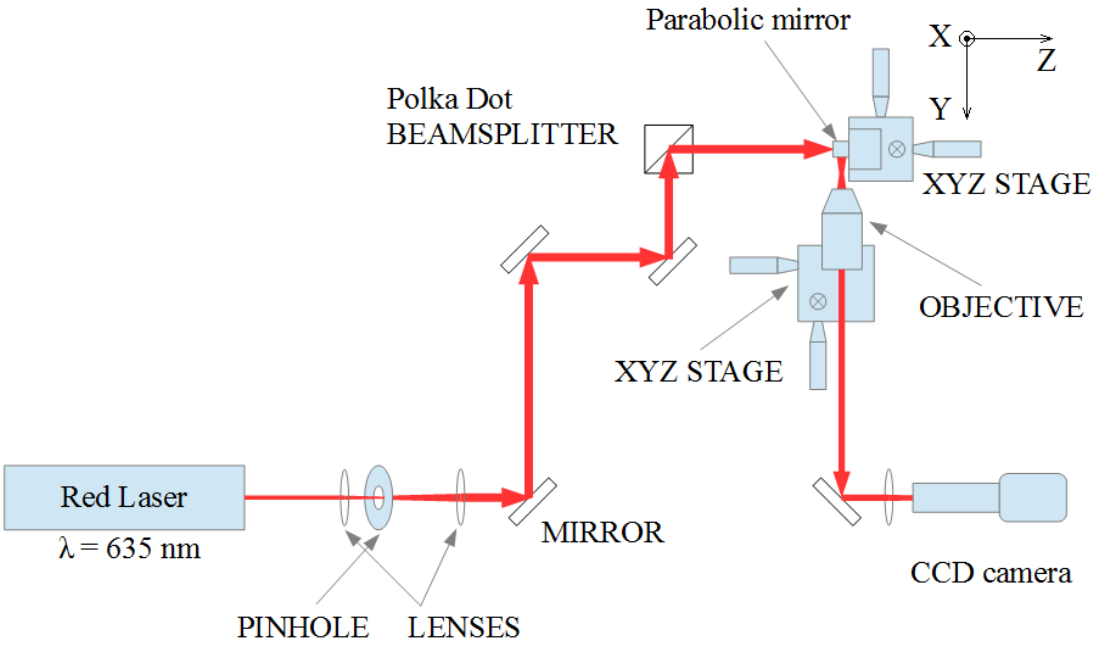

Figure 3.7: Experimental setup for study laser spot quality formed by parabolic mirror in different condition of incident laser beam.

Parabolic mirror and objective were mounted on XYZ stages.

To perform the initial alignment we used the flat surface of the parabolic mirror from the incident beam side. The mirror and its coordinate basis are represented on the Figure 3.8a. We adjusted incident laser beam tilt controlling the reflected beam to reach the normal incidence situation when both beams are superimposed.

After the proper alignment of the experimental setup, we wanted to study the dependence of spot quality on the four different factors: relative positions and tilts in orthogonal coordinate basis of the incident laser beam with respect to the axis of parabolic mirror.

To move the incident beam with respect to the parabolic mirror along X axis (Figure 3.8a) we simply moved parabolic mirror with XYZ stage and followed to it with the objective. For the Y axis we could use either the same way or translate the last mirror before the beamsplitter using its stage. To observe the dependence on a beam's tilt we had to do two actions: firstly we tilted a beamsplitter by certain degree and secondly we compensate the beam displacement after tilt by moving the parabolic mirror with XYZ stage by distance properly calculated from a tilt angle.

The best spot size that was reached is about 6 μm (Figure 3.8b). This value is acceptable for us, despite that the photonic wire's top diameter never exceeds 3 μm and some of the laser light will not reach the QD. The distance between two neighbor structures is 15 μm and it means that we can excite only one chosen structure.

We modify a bit the experimental setup as it shown on the Figure 3.9 to study how the laser beam passed twice through the parabolic mirror depends on the relative position of incident

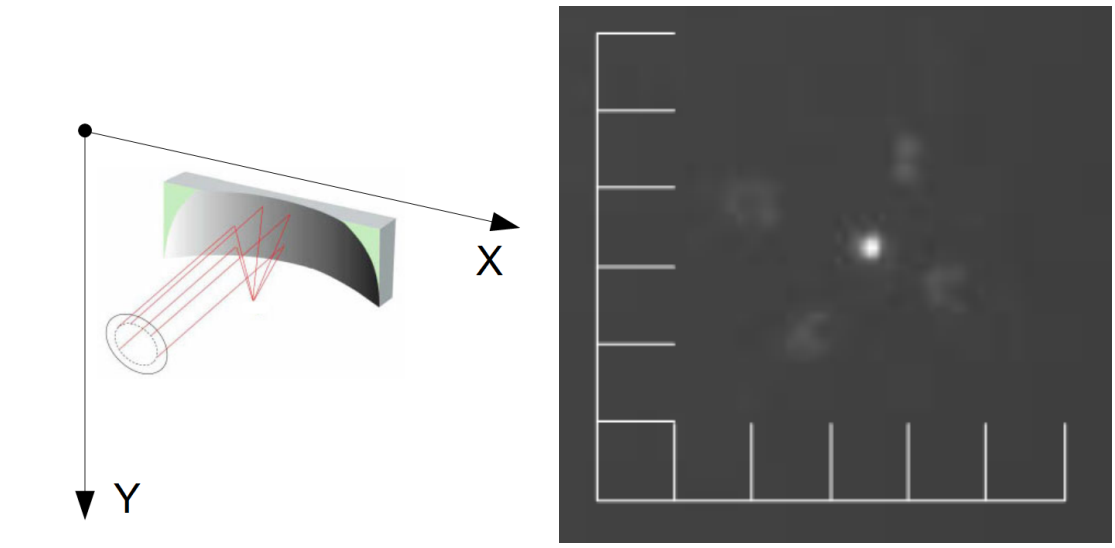

(a) (b)

Figure 3.8: (a) Schematic 3D view of the parabolic mirror. (b) The best spot size that was reached in the experiment is about 6 um. Grid on the image has a step of 100 um.

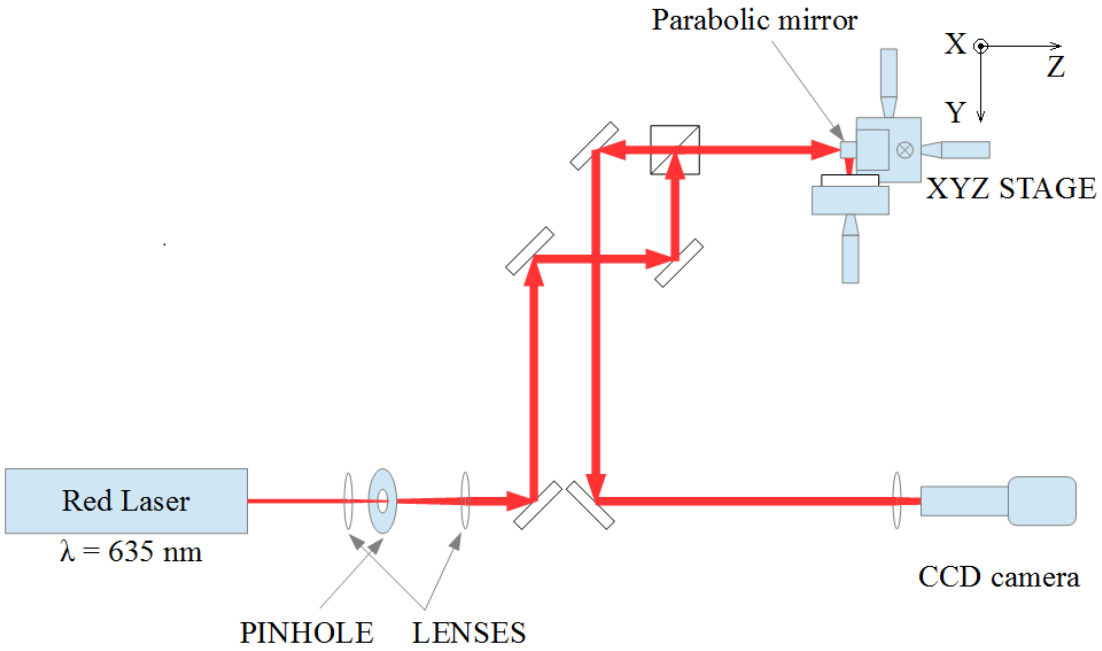

Figure 3.9: Experimental setup for study laser beam passed twice through the parabolic mirror.

laser beam and parabolic mirror's axis. This configuration corresponds to the experimental situation, in which imaging via the parabolic mirror is the only way to visualize the laser spot. In real experiment we used the knowledge acquired from this additional experiment to perform the initial alignment of the laser beam. For that in real setup we put the grating of the spectrometer in 'mirror' mode, a CCD camera in 2D image mode and align the laser beam using its reflection from the sample's substrate. Under that condition we have exactly the same situation for the laser beam as it is on the Figure 3.9.

Nevertheless, after such initial alignment, we don't know where exactly on the sample the laser spot is. To find this position we go to a region of the sample, where there are small, high and isolated pieces of GaAs on the substrate. Using CL signal from one of such piece we maximize it by moving the sample in XY plane. Unfortunately, precision of such repositioning is very low, so finally we have to adjust also the position of parabolic mirror to reach maximum of CL signal. At the last stage, we have to correct the laser beam position (because we lose a good laser alignment after we moved a parabolic mirror) to have the maximum PL signal from the same piece of GaAs.

3.3 Theoretical issues

In linear elasticity, the relation between stress σ and strain ϵ depend on the type of material under consideration. In general case it can be written in tensor form as $\epsilon_{ij} = S_{ijkl} \cdot \sigma_{kl}$, where S_{ijkl} is an elastic compliance tensor. Since the stress and strain tensors are symmetric, and since the stress-strain relation in linear elasticity can be derived from a strain energy density function, the following symmetries hold for linear elastic materials: $S_{ijkl} = S_{jikl}$, $S_{ijkl} = S_{ijlk}$ and $S_{ijkl} = S_{klij}$. Thus, in Voigt notation we can simply write it as:

$$\begin{pmatrix} \epsilon_1 \\ \epsilon_2 \\ \epsilon_3 \\ \epsilon_4 \\ \epsilon_5 \\ \epsilon_6 \end{pmatrix} = \begin{pmatrix} S_{11} & S_{12} & S_{13} & S_{14} & S_{15} & S_{16} \\ S_{12} & S_{22} & S_{23} & S_{24} & S_{25} & S_{26} \\ S_{13} & S_{23} & S_{33} & S_{34} & S_{35} & S_{36} \\ S_{14} & S_{24} & S_{34} & S_{44} & S_{45} & S_{46} \\ S_{15} & S_{25} & S_{35} & S_{45} & S_{55} & S_{56} \\ S_{16} & S_{26} & S_{36} & S_{46} & S_{56} & S_{66} \end{pmatrix} \begin{pmatrix} \sigma_1 \\ \sigma_2 \\ \sigma_3 \\ \sigma_4 \\ \sigma_5 \\ \sigma_6 \end{pmatrix}$$

, where 1 - xx, 2 - yy, 3 - zz, 4 - xy, 5 - xz, 6 - yz.

It can be more simplified if the investigated material has a symmetry. In the case of uniqueness and independence of material's properties along three mutually perpendicular directions (which are named X, Y and Z), such material is named orthotropic and its compliance tensor has only 9 independent components. Moreover, sphalerite GaAs has $F\bar{4}3m$ space group, for which there are only 3 independent components S_{11}, S_{12} and S_{44}:

$$\begin{pmatrix} \epsilon_1 \\ \epsilon_2 \\ \epsilon_3 \\ \epsilon_4 \\ \epsilon_5 \\ \epsilon_6 \end{pmatrix} = \begin{pmatrix} S_{11} & S_{12} & S_{12} & 0 & 0 & 0 \\ S_{12} & S_{11} & S_{12} & 0 & 0 & 0 \\ S_{12} & S_{12} & S_{11} & 0 & 0 & 0 \\ 0 & 0 & 0 & S_{44} & 0 & 0 \\ 0 & 0 & 0 & 0 & S_{44} & 0 \\ 0 & 0 & 0 & 0 & 0 & S_{44} \end{pmatrix} \begin{pmatrix} \sigma_1 \\ \sigma_2 \\ \sigma_3 \\ \sigma_4 \\ \sigma_5 \\ \sigma_6 \end{pmatrix}$$

To calculate the stress field that arises at the QD level due to displacement of the photonic wire's top we used commercial finite element calculation software COMSOL. Such calculations

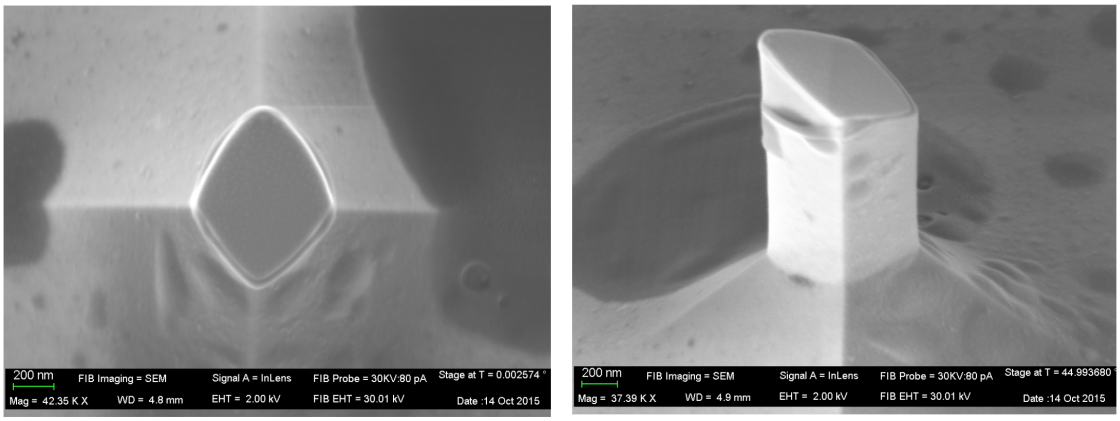

(a) (b)

Figure 3.10: (a) Scanning electron microscopy images of a typical photonic wire, cut by focused ion beam (FIB). In a it is possible to see the lozenge cross-section, with a major and a minor axis, responsible for the broken degeneracy of flexural modes. The seeming asymmetry between the top and bottom part of the lozenge is due to the cut being slanted, as evidenced by the side view in (b).

were done by Pierre-Louis de Assis from UFMG (Universidade Federal de Minas Gerais) in Brazil. The shape of structure's cross-section at the level of QDs in these calculations is a lozenge, that correspond better to a real structure's cross-section defined by the fabrication technique. Scanning electron microscopy images of a typical photonic wire cut by focused ion beam (FIB) are shown on the Figure 3.10.

The Z axis in this calculations is co-directed with the direction of growth of the structure, thus cross-section is placed in XY plane. Orthogonal mechanical modes correspond to X and Y axes. The model structure has a height of 17.2 μm, a top facet diameter of 1.9 μm and a half-angle of 2.3 degree. A QD layer is located 0.8 μm above the structure's base. Results of calculations presented on the Figure 3.11 for flexural mode X and Figure 3.12 - for Y.

We obtained that stress σ_{xx} and σ_{yy} is two order of magnitude smaller than σ_{zz}.

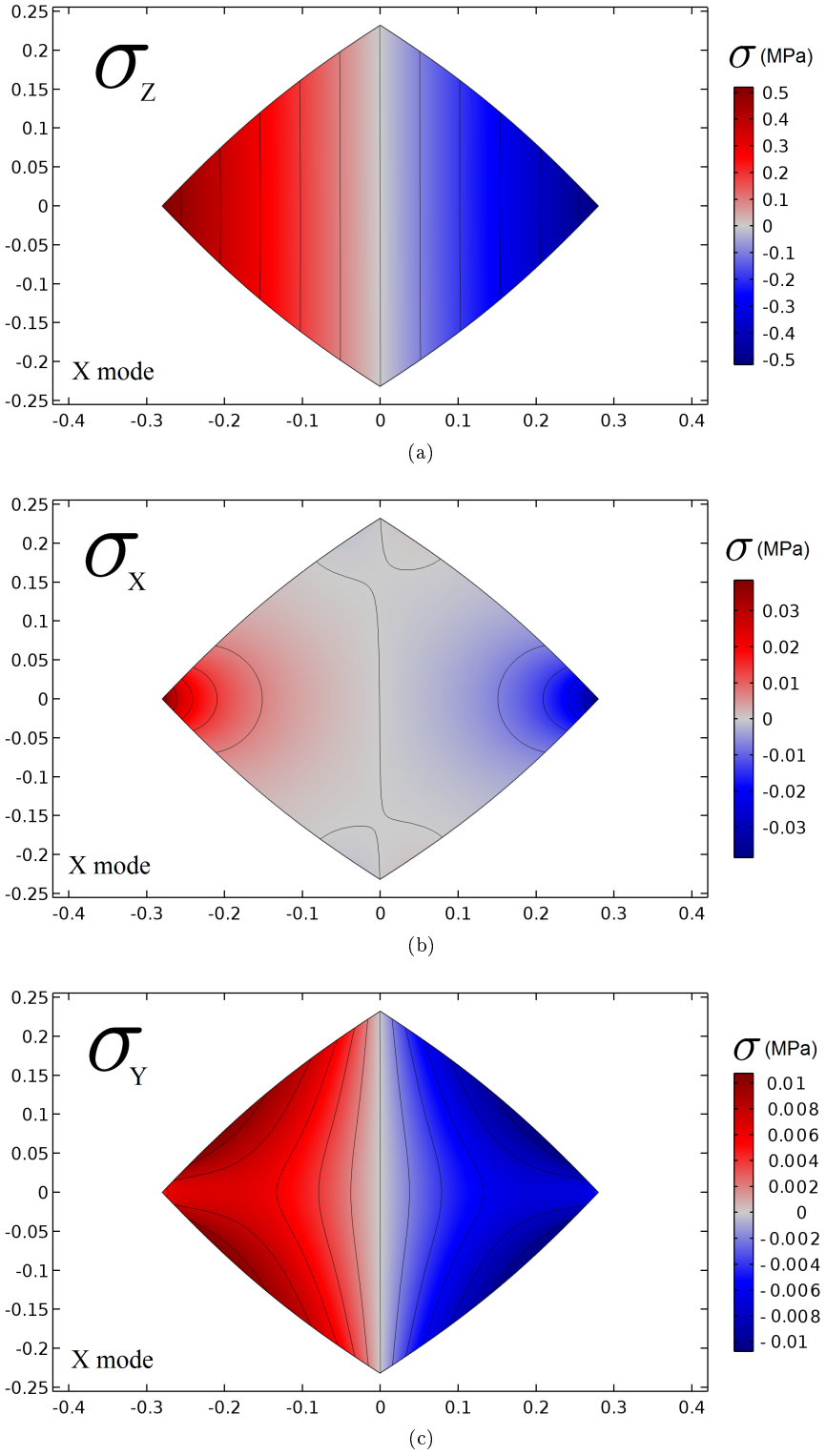

Figure 3.11: Stress component (a) σ_z (b) σ_x (c) σ_y for an oscillation amplitude of 1 nm for fundamental flexural mode X at the QD level, which is located 0.8 µm above the structure's base. Model structure has a height of 17.2 µm and top facet diameter of 1.9 µm. Values on the axes of the images in µm. Colorbar gives values of stress in MPa.

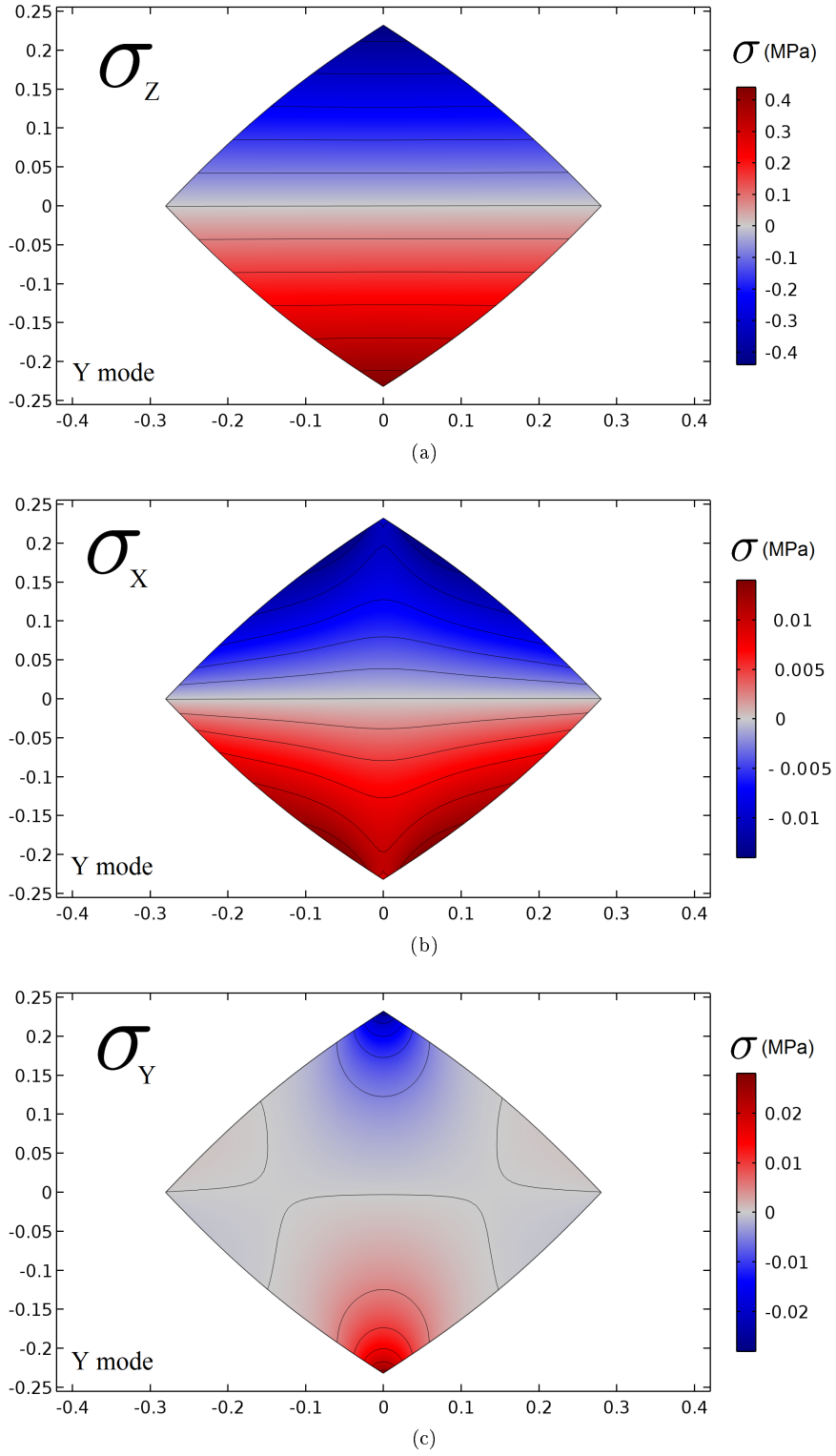

Figure 3.12: Stress component (a) σ_z (b) σ_x (c) σ_y for an oscillation amplitude of 1 nm for fundamental flexural mode Y at the QD level, which is located 0.8 μm above the structure's base. Model structure has a height of 17.2 μm and top facet diameter of 1.9 μm. Values on the axes of the images in μm. Colorbar gives values of stress in MPa.

3.3.1 A general case

In a general case we have the strain field on the QD plane:

$$\begin{aligned}\epsilon_x &= S_{11}\sigma_x + S_{12}\left(\sigma_y + \sigma_z\right)\\ \epsilon_y &= S_{11}\sigma_y + S_{12}\left(\sigma_x + \sigma_z\right)\\ \epsilon_z &= S_{11}\sigma_z + S_{12}\left(\sigma_x + \sigma_y\right)\end{aligned}$$

The energy shift for heavy holes relative to the conduction band in zinc-blende semiconductor is given by [42]:

$$\delta E = a\cdot(\epsilon_x+\epsilon_y+\epsilon_z)+b\cdot(\epsilon_z-\frac{\epsilon_x+\epsilon_y}{2}) = a\cdot(S_{11}+2S_{12})\cdot(\sigma_x+\sigma_y+\sigma_z)+b\cdot[S_{11}\cdot(\sigma_z-(\sigma_x+\sigma_y))-S_{12}\cdot\sigma_z] \tag{3.1}$$

where a,b are the deformation potentials of the material presented in a table 3.1.

	GaAs	InAs
a	-9	-6
b	-2	-1.8
d	-5.4	-3.6

Table 3.1: Deformation potentials of GaAs and InAs in eV. [43, 44]

We see that stresses on the X and Y directions introduce strain terms along other crystallographic directions and also merely introduce a difference between ϵ_x and ϵ_y compare to the uniaxial stress model presented in the next section. On the Figures 3.13 and 3.14 calculated components of strain tensor are presented for X and Y modes correspondingly. We can see that ϵ_z is about 3 times larger than ϵ_x and ϵ_y. At the same time from equation (3.1) we see that, in case when σ_x and σ_y are small comparing to σ_z, they have a small effect on the band gap energy shift.

3.3.2 The uniaxial stress model

Since σ_x and σ_y are small comparing to σ_z, we can represent our situation as a uniaxial stress model. Thus, the strain field on the QD plane is $\epsilon_x = \epsilon_y = S_{12}\sigma_z$ and $\epsilon_z = S_{11}\sigma_z$. The equation for the energy shift is then simplified as:

$$\delta E = \sigma_z\left[a\cdot(S_{11}+2S_{12})+b\cdot(S_{11}-S_{12})\right] \tag{3.2}$$

In our case, σ_z is not constant, but varies with position within the plane containing the QDs. We can see, that for a given flexural mode the strain varies only along the coordinate associated with that mode. This means that when the structure oscillates along the X axis, δE becomes $\delta E(x) \sim \sigma_z(x) = \frac{d\sigma_z}{dx}\cdot x$, with a linear dependence for the small displacement of 1 nm (see Figure 3.15).

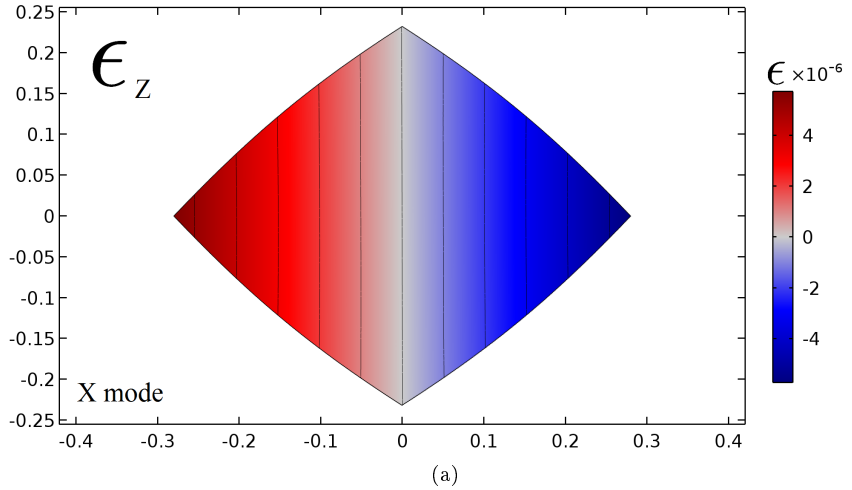

(a)

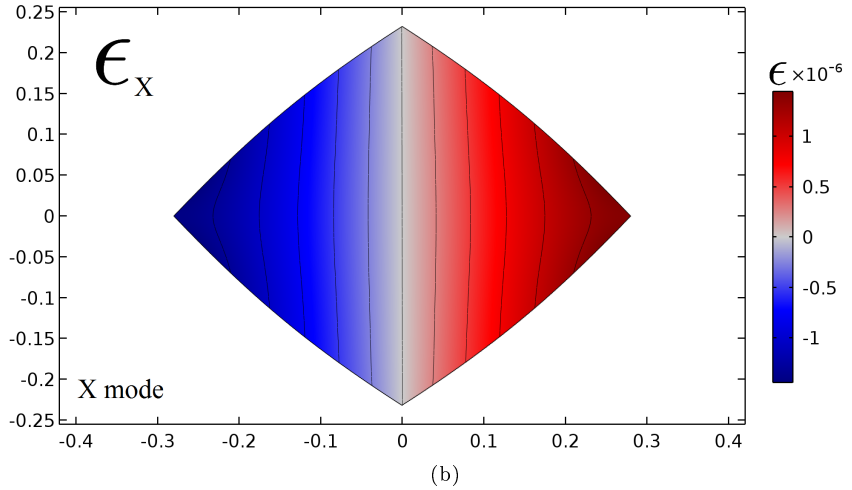

(b)

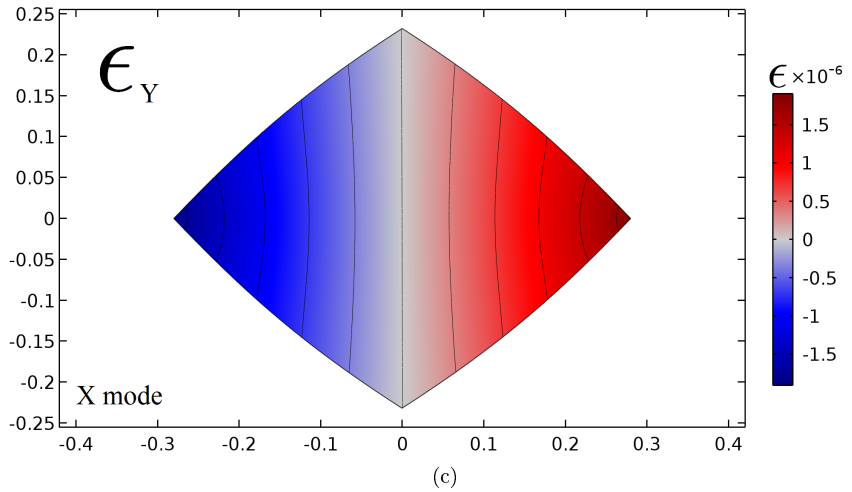

(c)

Figure 3.13: Strain component (a) ϵ_z (b) ϵ_x (c) ϵ_y for an oscillation amplitude of 1 nm for fundamental flexural mode X at the QD level, which is located 0.8 µm above the structure's base. Model structure has a height of 17.2 µm and top facet diameter of 1.9 µm. Values on the axes of the images in µm.

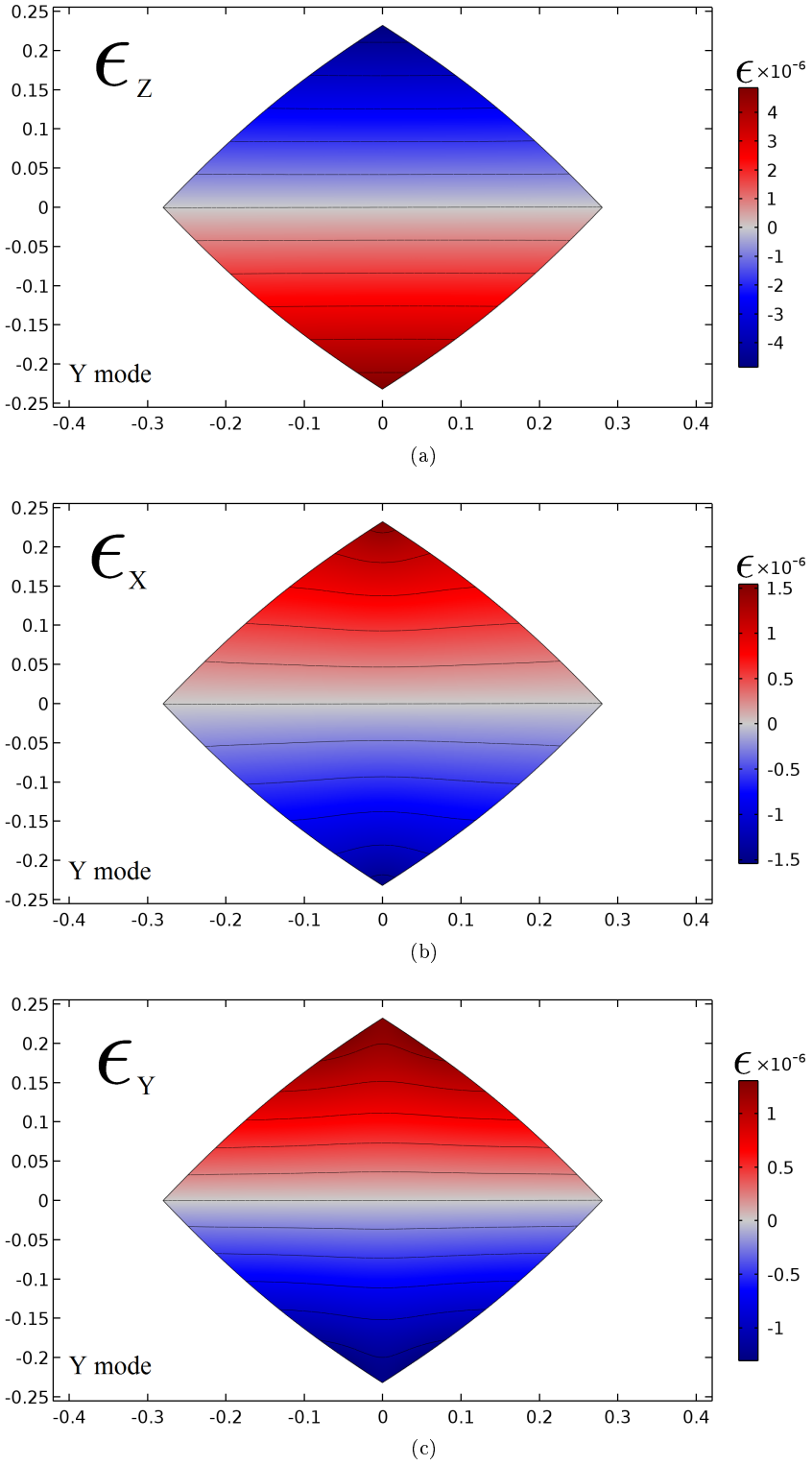

Figure 3.14: Strain component (a) ϵ_z (b) ϵ_x (c) ϵ_y for an oscillation amplitude of 1 nm for fundamental flexural mode Y at the QD level, which is located 0.8 µm above the structure's base. Model structure has a height of 17.2 µm and top facet diameter of 1.9 µm. Values on the axes of the images in µm.

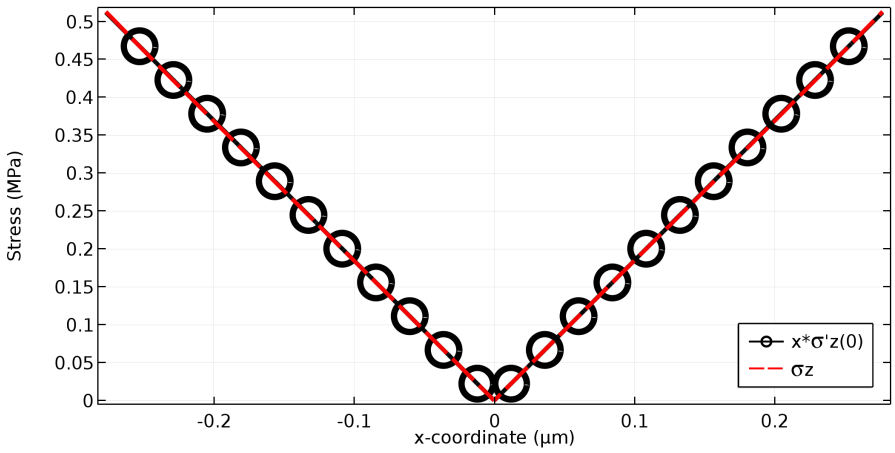

(a)

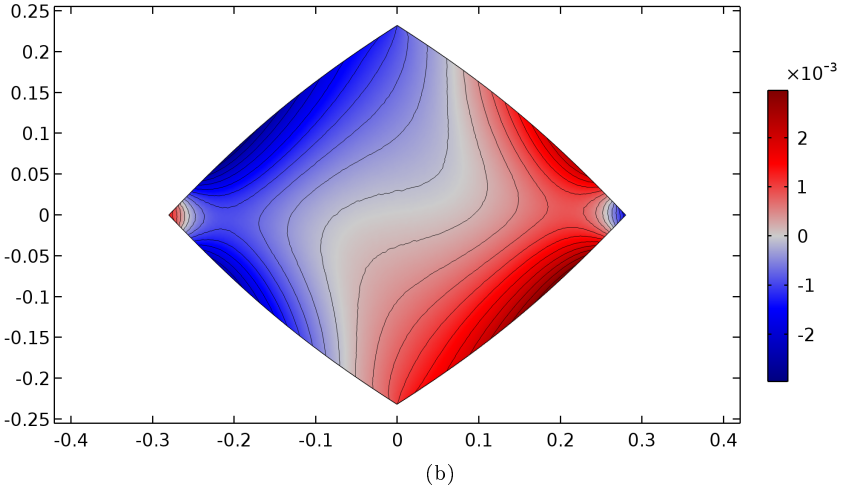

(b)

Figure 3.15: (a) Red curve demonstrates calculated stress component σ_z along X axis for y = 0, black circles - only its linear part. (b) A 2D map of the relative residual of the linear approximation of the stress component σ_z for oscillations along the X axis. It is never exceed 0.3%. Values on the axes of the images in μm. Provided data are obtained for an oscillation amplitude of 1 nm for fundamental flexural mode X at the QD level, which is located 0.8 μm above the structure's base. Model structure has a height of 17.2 μm and top facet diameter of 1.9 μm.

3.3.3 Comparison of the models

From [42] it is known that $S_{11} = 1.14\,10^{-5}\text{MPa}^{-1}$, $S_{12} = -0.35\,10^{-5}\text{MPa}^{-1}$ for GaAs and we can also use the same values for embedded InAs QD, because strain imposed on the QD caused by strain of GaAs. According to the formula (3.2) calculations give us energy shift expectation about -70 μeV/MPa. Simulation of z component of stress field was done by finite element method and give us a value of 0.5 MPa at the side of the QD's level per 1 nm of the displacement of the photonic wire's top, that corresponds to -35 μeV/nm.

Despite that in the uniaxial stress model we ignore the contribution from σ_x and σ_y, obtained value of energy shift is reliable. Comparison between δE calculated by formula (3.2) and formula (3.1) (which is presented on the Figure 3.16) demonstrate that the absolute difference between both approaches is below 1% for the largest part of the active area containing QDs. The largest deviation is observed at the edges of the structure in the direction of the flexural mode. Thus, the uniaxial stress model is acceptable approximation, while talking about bandgap shift.

From the calculation we have also obtained that shear stress σ_{xy} is one order of magnitude smaller than compressive/tensile stresses. It appears associated to an uniaxial compression along [111] given by [42]:

$$\delta E \sim \frac{d}{\sqrt{3}} S_{44},$$

where d is the deformation potential of the material presented also in a table 3.1. Thus, it does not result in a shift more than 0.6 μeV.

3.3.4 Conclusions

Results of simulations show that it is valid to approximate the energy shift in terms of uniaxial stress along the z direction. Both approaches allow us to obtain a $\delta E(x)$ as a linear function of x with values coincide to within a 1 %. The relative residual of the linear approximation of the stress field is never larger than 0.3%. Shear contributions can be neglected, as they amount to no more than a 1% correction.

For the structure with 17.2 μm height, 1.9 μm top facet diameter (D_{TOP}), 2.3 degree half-angle and a QD layer located 0.8 μm above the structure's base maximum expected value of relative energy shift is about 35 μeV per 1 nm of the structure's displacement. For the structures with other top diameter but the same other parameters this value changes proportionally to the change of structure's diameter at the QDs level ($D_{QD\,layer}$), which is equal to

$$D_{QD\,layer}\,[\mu\text{m}] = D_{TOP} - (17.2\,\mu\text{m} - 0.8\,\mu\text{m}) \cdot 2\tan(2.3) = D_{TOP}\,[\mu\text{m}] - 1.32\,\mu\text{m}$$

Thus, for the structure with 1.9 μm top diameter: $D_{QD\,layer} = 0.58$ μm. Finally, a maximum expected relative energy shift in μeV/nm can be estimated using the formula

$$\delta E_{MAX}\,[\mu\text{eV/nm}] \approx 35 \cdot \left(1 + \frac{D_{TOP} - 1.9}{0.58}\right) \approx 60 \cdot D_{TOP}\,[\mu\text{m}] - 79.$$

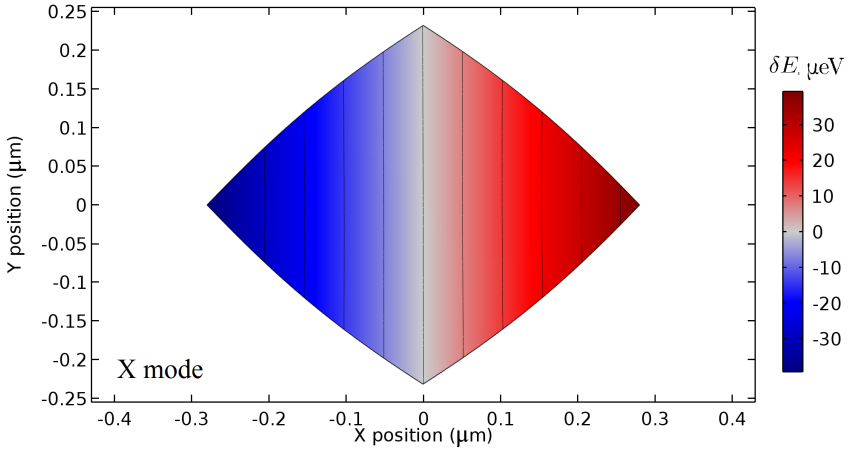

(a)

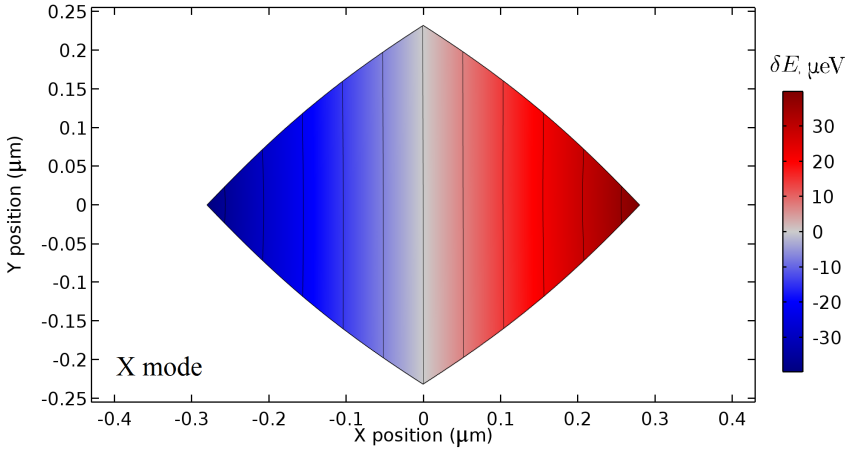

(b)

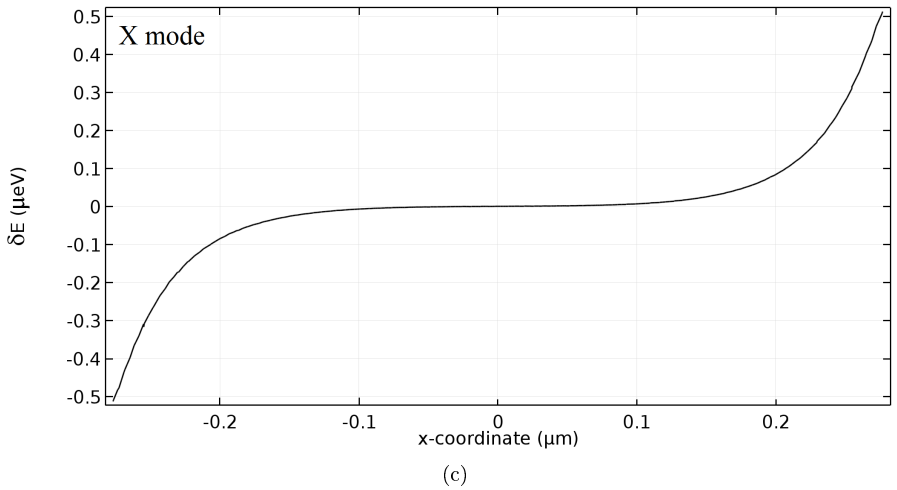

(c)

Figure 3.16: Band gap energy shift calculated using formula (a) (3.2) (b) (3.1) for an oscillation amplitude of 1 nm for fundamental flexural mode X at the QD level, which is located 0.8 μm above the structure's base. Model structure has a height of 17.2 μm and top facet diameter of 1.9 μm. Values on the axes of the images in μm. Colorbar indicates values in μeV. (c) Absolute difference between the two results for a cross-section at Y = 0.

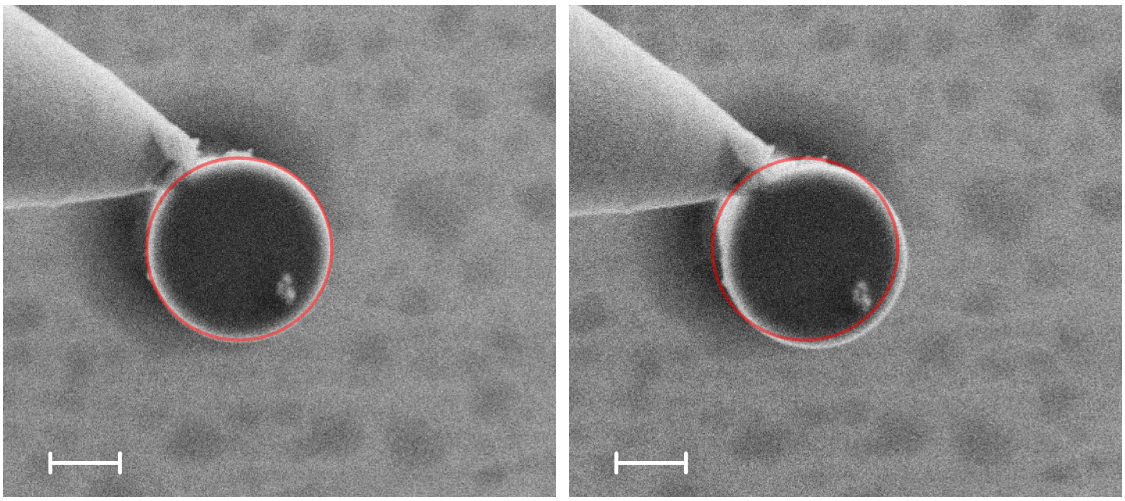

(a) (b)

Figure 3.17: SEM image (top view) of the photonic wire with 2.6 μm top diameter pushed with a nanomanipulator by (a) 460 nm (b) 600 nm. Red circle demonstrates position of the structure's top facet at the (a) image. White line gives a reference for a scale and is equal to 1 μm.

3.4 Experimental results with one tip

3.4.1 SEM imaging and positioning

Despite that we place the sample in the chamber of SEM microscope, we can not visually control the position of the tip with respect to the photonic wire during the photo-luminescence measurement, because a presence of e-beam affects on the measured photo-luminescence spectrum. The structure itself and the surface of the sample around start to store charges that affects the photo-luminescence spectrum. That's why we used a 'Live View' mode of the SEM only to set up the initial position. As soon as we bring a tip in contact with the structure, we blocked electron-beam. For precise displacement of the tip we use a piezocontroller output that returns a value of applied voltage that can be converted to the displacement in nm.

Nevertheless, we obtained several SEM images while pushing to demonstrate the displacement of the photonic wire. They are shown on the Figure 3.17.

3.4.2 Typical photo-luminescence spectra

Number of the lines on a photo-luminescence spectrum depends on a number of QDs embedded in a certain structure. In simple model it means that it is proportional to the area of the structure's cross-section at the level of QD layer, which can be modeled as a circle. Thus, it grows up quadratic with structure's diameter. Typical spectrum for the photonic wire with 1.71 μm of top diameter is shown on the Figure 3.18a. We can see that peaks are located very close to each other and are difficult to separate due to, firstly, high density of the QD inside the photonic wires for this experimental sample and, secondly, low spectral resolution of experimental setup.

Nevertheless, for some structures, we were able to find several standing away peaks when

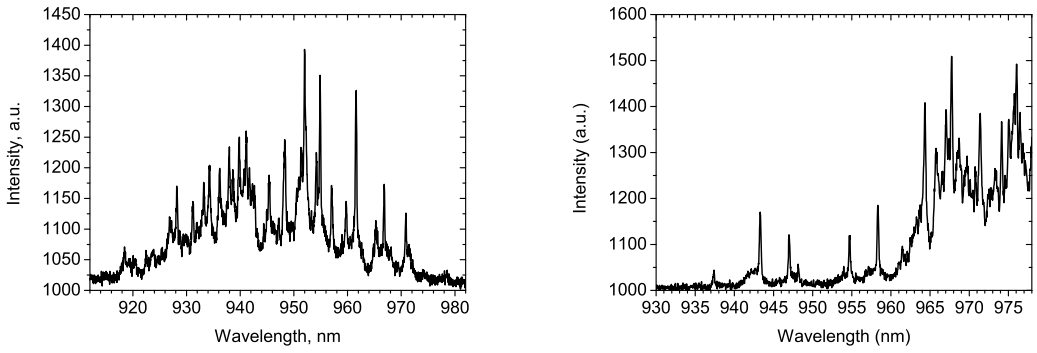

(a) (b)

Figure 3.18: (a) Typical photo-luminescence spectrum for the structure with 1.71 μm of top diameter. (b) Side of the photo-luminescence spectrum for 2.68 μm top diameter structure. There are several well separated peaks that are easy to follow.

looking in the edges of the QD spectral distribution (Figure 3.18b). Such peaks are good for our experimental study.

3.4.3 Impact of the tip on the photo-luminescence spectra

We have also observed that bringing the tip in contact with the structure affects on the photo-luminescence spectrum. Two spectra for the case when tip is far away from the structure and the case when tip touches it are shown on the Figure 3.19.

One of the possible explanation is the electrostatic effect of the tip that changes a QD transition energy. The other one is that heat transmitted from the tip to the QD that changes the bandgap and consequently a transition energy. Despite the tip is connected with to the cold finger with a wire, its temperature is probably still higher than temperature of the sample.

3.4.4 Photo-luminescence spectra and data analysis

On the Figure 3.20a observed blue-shift of the peak is shown. Presented data correspond to the structure with top diameter equals to 2.05 μm. Extracting a transition energy for each spectrum and plotting it as a function of structure's top's displacement, we see that it behaves linearly as predicted. Peak's position was found as a central value for Lorentzian fit of experimental data.

We can now compare obtained value of energy shift with what is expected from the theoretical calculations. As it was discussed in Section 3.3.2: simulated z component of stress field reaches the value of 0.5 MPa per 1 nm of the displacement for the structure with top facet diameter of 1.9 μm. We have also confirmed that this model is reliable for the calculations of energy shift, that is equal in this case to -35 μeV/nm. It means that for the QDs embedded in a structure with a top diameter of 1.9 μm we expect to observe energy shift in a range from 0 to 3.5 meV (depending on the position of certain QD) per 100 nm of the structure's displacement. Thus, for the structure with top diameter of 2.05 μm possible energy shift range is from 0 to approximately

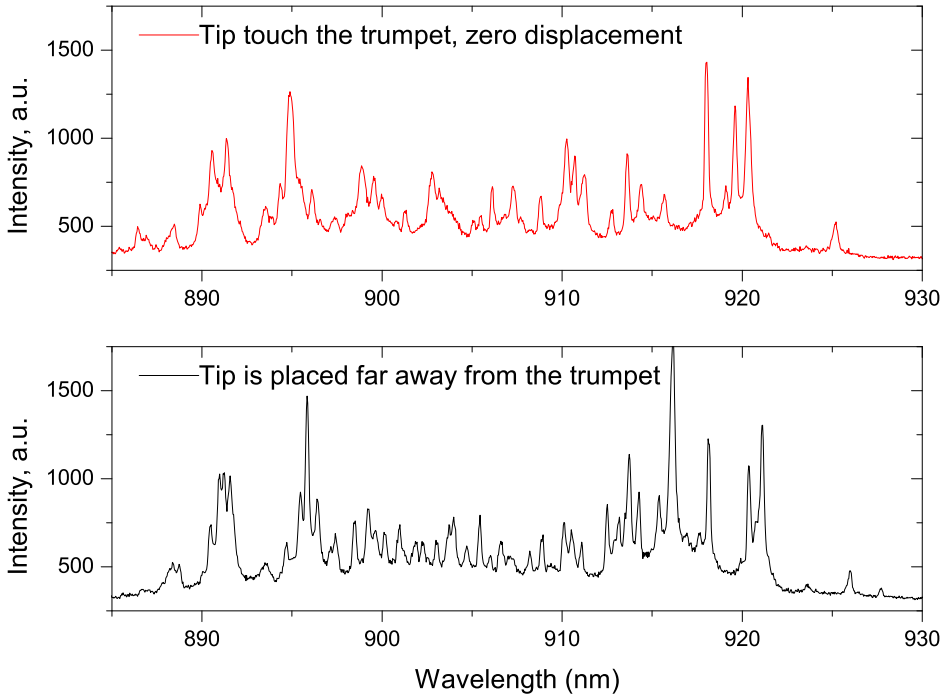

Figure 3.19: Impact of the nanomanipulator's tip on the photo-luminescence spectrum. Two cases are shown: tip is far away from the structure (black, lower spectrum) and tip touches the structure without pushing (red, upper spectrum).

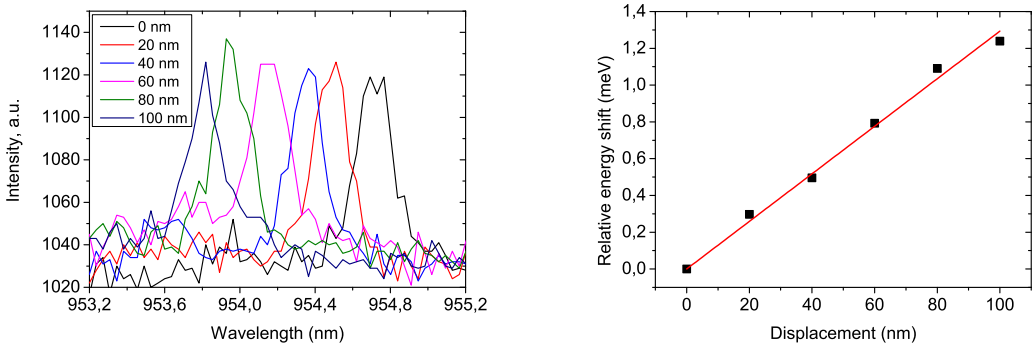

(a) (b)

Figure 3.20: (a) Photo-luminescence spectra demonstrating shift of the peak while increasing tip displacement from 0 to 100 nm with 20 nm step. (b) Peak's position (center for Lorentzian fit of the corresponding peak) versus tip's displacement. Presented data correspond to the structure with top diameter of 2.05 μm.

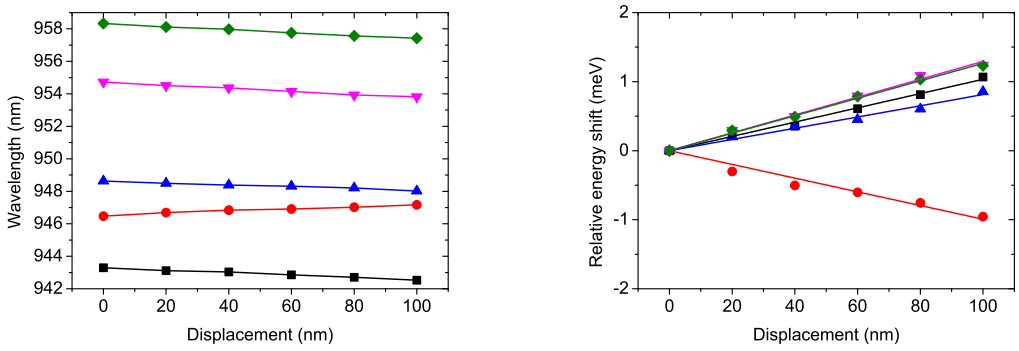

(a) (b)

Figure 3.21: (a) Absolute peak's position and (b) relative energy shift versus tip's displacement for several QD inside the photonic wire with top diameter of 3.11 μm.

4.4 meV per 100 nm of the structure's displacement. For the observed QD we found it equals to 1.2 meV that perfectly matches to the range, where we were expecting it to be.

Analysis of several peak from one set of photo-luminescence spectra confirms that they shift with a different slope. On the Figure 3.21a evolution of position for several peaks with pushing is shown. Peak's position means a central value for Lorentzian fit of experimental data. On the Figure 3.21b relative energy shift for these peaks is presented. Such behavior was predicted [21, 19] and caused by the fact that different QDs feels different strain (with the same amount of displacement of the photonic wire's top) depending on their position in the QD layer (accordingly to the strain map at the QD layer in section 3.3). These data were obtained for the structure with top diameter of 3.11 μm. Thus expected maximum energy shift is about 10.8 meV per 100 nm of the structure's displacement. Experimentally observed shifts do not exceed 2 meV. It is also matches an expected range of values.

3.4.5 Maximal reachable displacement

We were able to successfully push the photonic wire by almost 1 μm without breaking it. This is a limitation of our experimental setup in analog mode of tip's displacement (see in details in section 3.2). On the Figure 3.22 ways back and forth for two chosen peaks with opposite slopes for 1.64 μm top diameter structure are shown.

Relative energy shift is linear with the pushing amplitude on a whole way forward. On a way back (when we decrease pushing amplitude) peaks come back initially the same way. It means that bending of the structure in this range is elastic. However, a mismatch appears after passing through a position "400 nm" on the way back. After it happened the slope of peak's energy shift presented on the Figure 3.22b doesn't change, but position of the peak changes. We connect observed phenomenon with a slip of the tip on the structure's surface.

A sketches on the Figure 3.23 demonstrate a slip effect of the tip happening on a way back, i.e. while decreasing pushing amplitude. In the first case, slip of the tip leads to structure's displacement bigger than tip's displacement. In the second case, it leads to structure's displacement smaller than tip's displacement. On both experimental plots on the Figure 3.22b for the

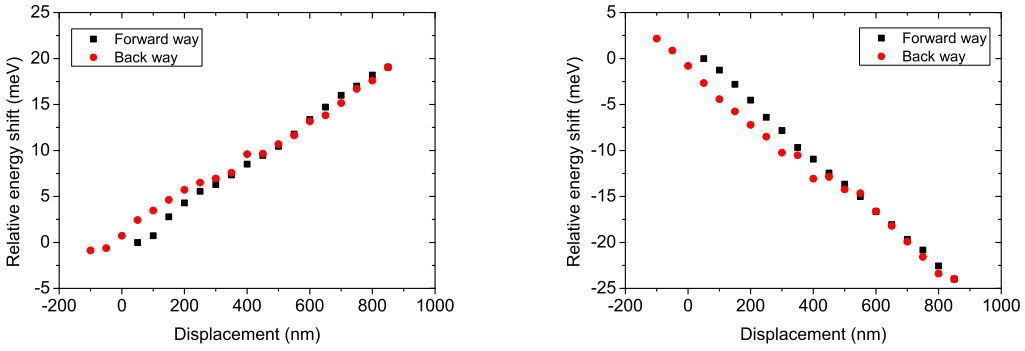

(a) (b)

Figure 3.22: Relative (a) blue- (b) red-shift of the peaks observed from the structure with top diameter of 1.64 μm while pushing back and forth by approximately 1 μm with 50 nm step. Black experimental points demonstrate a way forward, red - way back.

displacements from 0 to 400 nm we observe on a way back bigger (by absolute value) relative energy shift than it was on a way forward for the same value of displacement. It means that at some point (around position "400 nm") structure moved back by smaller distance than a tip that correspond to a situation presented on the sketch 3.23b.

We were also able to pull the photonic wire and observe that peak shifts the other way comparing with the pushing. This is represented on the same Figure 3.22 with coordinates less than 0. Pulling is possible because investigated structure becomes stuck to the tip electrostatically. They lose the connection after tip pulling more than 100 nm. At that point structure jumps back to '0' positions and peak on the photo-luminescence spectrum also moves back to the rest position.

For several other structures that we pushed back and forth just for 100-200 nm we didn't observe this 'relaxation' effect, whereas we were always able to pull the structure by approximately 100 nm.

We observed maximal energy shift for that structure of about 30 μeV per 1 nm of structure's displacement. According to the theoretical calculations presented in Section 3.3.2 we estimate a maximum energy shift for this structure as 20 μeV/nm. The fact that we observed higher energy shift than we predicted can be probably explained by a deviation in structure's geometry from a cone at very small base diameter. Diameter at the bottom of the ideal truncated conical shape structure with 1.64 μm top diameter is equal about 260 nm, which is quite small. Thus, we expect that it can be about 1.5 times higher due to non-perfectness of the fabrication technique.

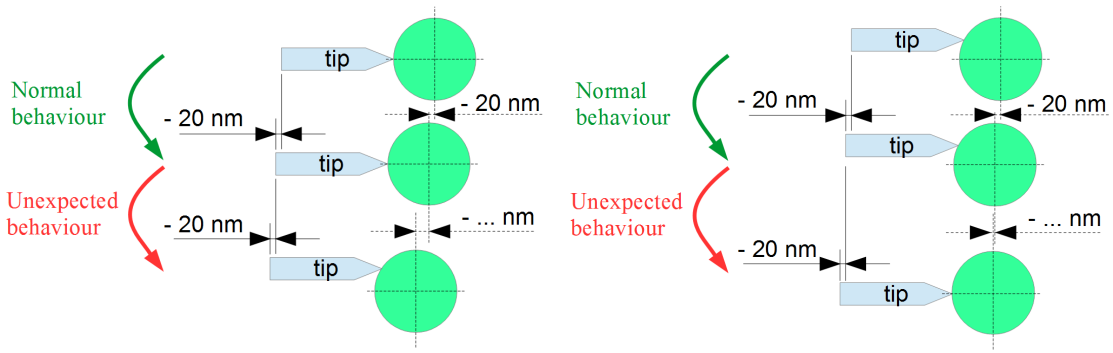

Figure 3.23: A sketch demonstrating a slip of the tip while moving back in case of (a) peak shifts more than expected (b) peak shifts less than expected. It is a possible explanations for the observed 'jump' of QDs' emission lines on a photo-luminescence spectra.

3.4.6 Merging 2 peaks

As it was already mentioned, depending of the QD's position within the QD layer inside the photonic wire a given bending exerts different strain (see Figure 3.16). It means that several QDs placed in the same photonic wire will react differently on its bending and therefore their energy shifts will be different. It gives us an opportunity to observe peaks' merging if two peaks are located close to each other on the photo-luminescence spectra, but are related to the 2 different QDs, which are placed far enough inside the structure. Merging is possible if either both peaks move the same way but with different speed or two peaks move the opposite ways as it shown on the Figure 3.24.

A possibility to bring transition energies of several QDs in resonance and hold them in this positions opens a door to studying collective effects in light-matter interaction, such as a superradiance.

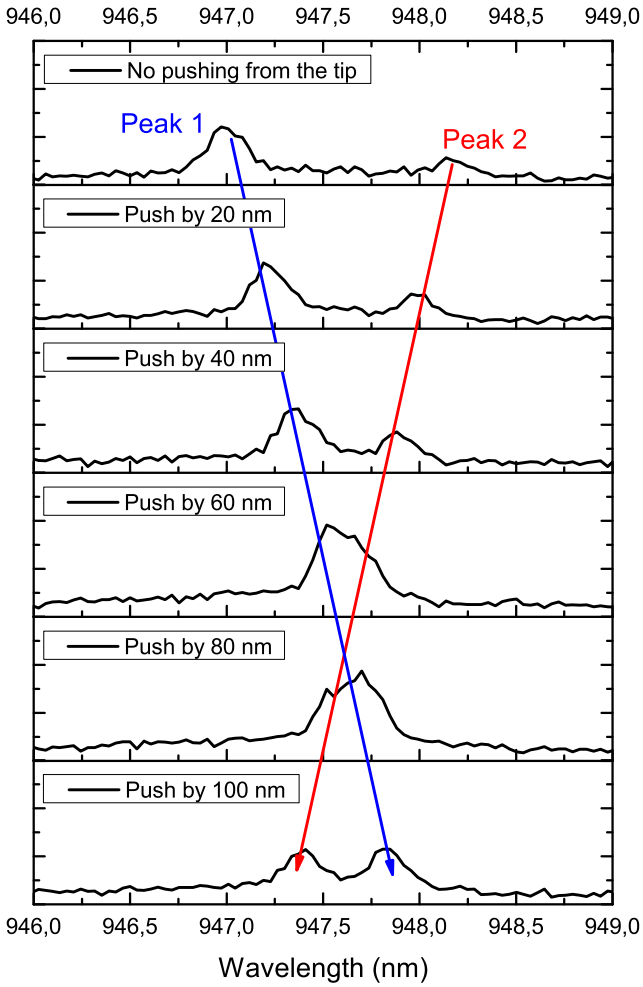

Figure 3.24: Experimental photo-luminescence spectra for the structure with top diameter of 3.11 μm while pushing for 100 nm with 20 nm step. Merging of 2 peaks is demonstrated. Peaks move towards each other that means they are related with 2 QDs feeling the strain with opposite signs.

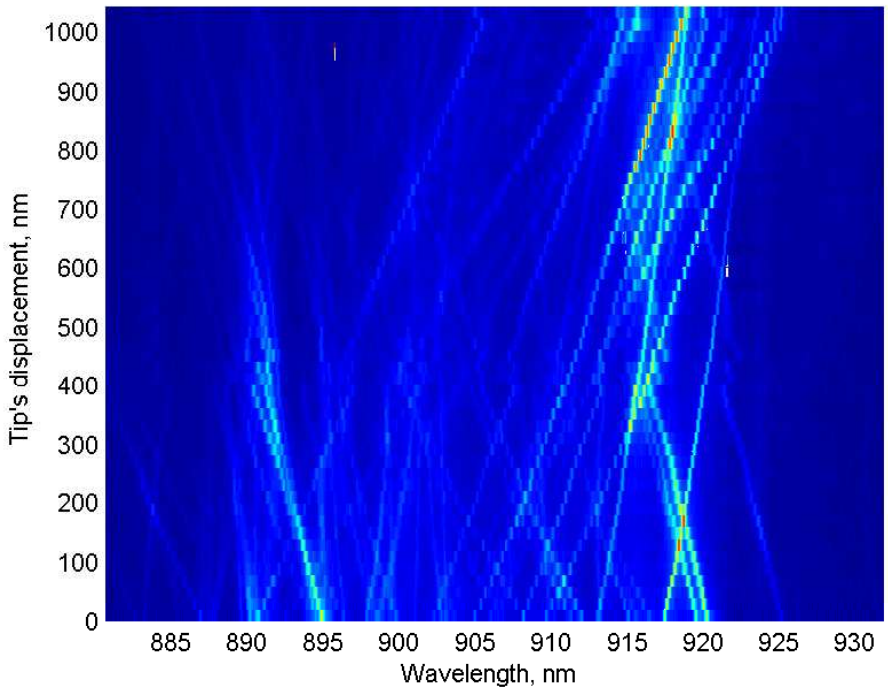

Figure 3.25: Color map showing peaks' displacement on a photo-luminescence spectra with different amount of pushing with nanomanipulator. X axis corresponds to the wavelength, Y - tip's displacement. Colors are distributed from blue (background) to red (peak). Measured structure has 2.05 μm top diameter.

3.4.7 Statistics of peaks' shift

3.4.7.1 Analysis of all peaks from one photonic wire

To analyze as many peaks as possible we repeat the experiment with a small step of nanomanipulator's displacement (20 nm) and in a big range (up to 1.04 μm). Resulting spectra were plotted as a 2D color map in axes wavelength and tip's displacement. Color for each point depends on the intensity and changes from blue (low intensity) to red (high intensity). This map for the 2.05 μm top diameter structure is represented on the Figure 3.25.

Thus, we were able to track 52 peaks and define theirs relative wavelength shifts. We can observe a strain relaxation that took place twice during the experiment in a range from 400 nm to 500 nm of tip's displacement. The emission wavelength of all QDs jumps back (simultaneously comes back to the value that was already registered at less tip's displacement). Since we registered this effect while we push on the structure, we can also connect it to the slip of the tip as it is shown on the Figure 3.26. It is also interesting to mention that after that point (at bigger tip's displacement) all emission lines with positive slope became brighter whereas lines with negative slope were brighter before that point and some of them even became non-registrable after passing through this point.

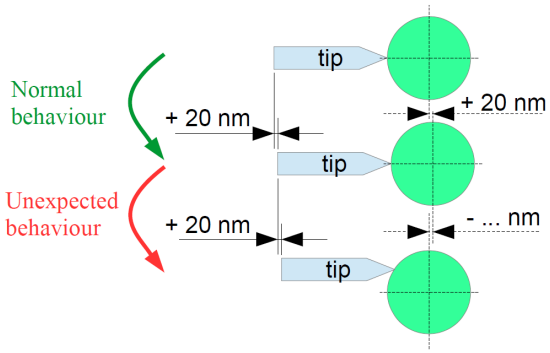

Figure 3.26: A sketch demonstrating a slip of the tip occurring on a way forward (i. e. while pushing on the structure), which is one of the possible explanations for the observed 'jump back' of QDs' emission lines on a photo-luminescence spectra.

Since QDs are distributed randomly within the layer we assume that probability to find a peak with certain energy shift is proportional to the length of the chord (Figure 3.27a), because all QD located on it experiences the same strain. Thus, it defines by the formula:

$$L(x) = R \int_{-\sqrt{1-x^2}}^{\sqrt{1-x^2}} dx = 2R\sqrt{1-x^2} \tag{3.3}$$

where L is the length on the chord, R the radius of the circle, x the distance from the 'zero-strain diameter' to the chord, where x = 0 means 'zero-strain diameter' and x = $\mp$1 means the side of the structure.

Normalized probability density then equals to:

$$\frac{L(x)}{\int_{-1}^{1} L(x)dx} = \frac{2}{\pi}\sqrt{1-x^2} \tag{3.4}$$

and shown on the Figure 3.27b.

The slope's distribution of all peaks is shown as a histogram on the Figure 3.28. Blue lines shows the exact value of the relative wavelength shift for all analyzed peaks. Red shaded area shows amount of peaks within a bin of 10 μeV/nm. Dark curve is a fit with respect to the distribution represented by the formula (3.4). The observed distribution has a maximum number of QD with relative energy shift close to 0 as it is predicted. Incomplete agreement between experimental data and theoretical expectation is due to the lack of more comprehensive statistics. Maximum relative energy shift from a fit is equal to 41 μeV/nm, which is in good agreement with theoretically predicted value of 44 μeV/nm.

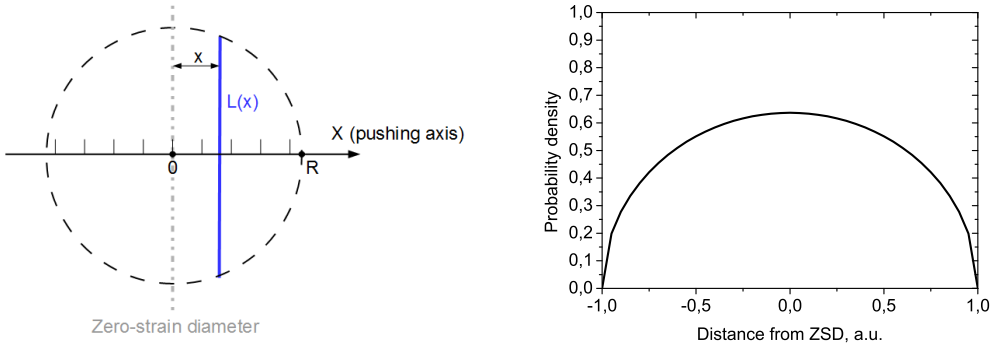

(a) (b)

Figure 3.27: (a) Sketch of the chord's length depending on the distance from the 'zero-strain diameter' (ZSD). (b) Normalized probability density to have a QD at certain distance from the 'zero-strain diameter'.

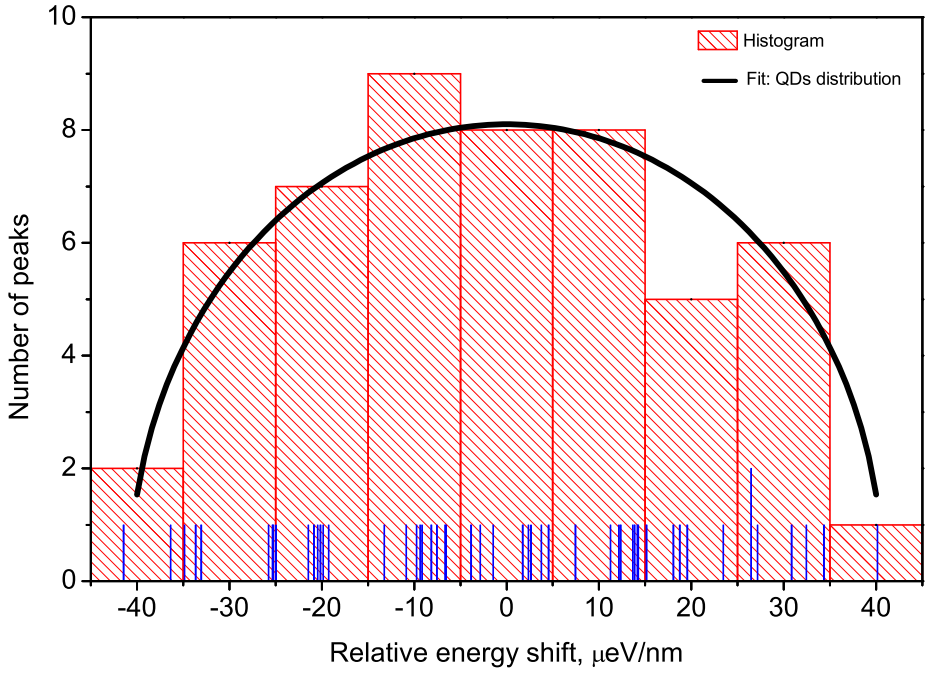

Figure 3.28: The shaded red histogram demonstrates the distribution of peaks' relative energy shifts in μeV per nm of tip's displacement within 10 μeV/nm bin. Blue lines shows the exact value of the relative energy shifts. Dark curve is a fit with respect to the distribution formula (3.4). Presented data correspond to 52 peaks observed for the structure with 2.05 μm top diameter. From a fit maximum relative energy shift is equal to 41 μeV/nm, which is in good agreement with theoretically predicted value of 44 μeV/nm.

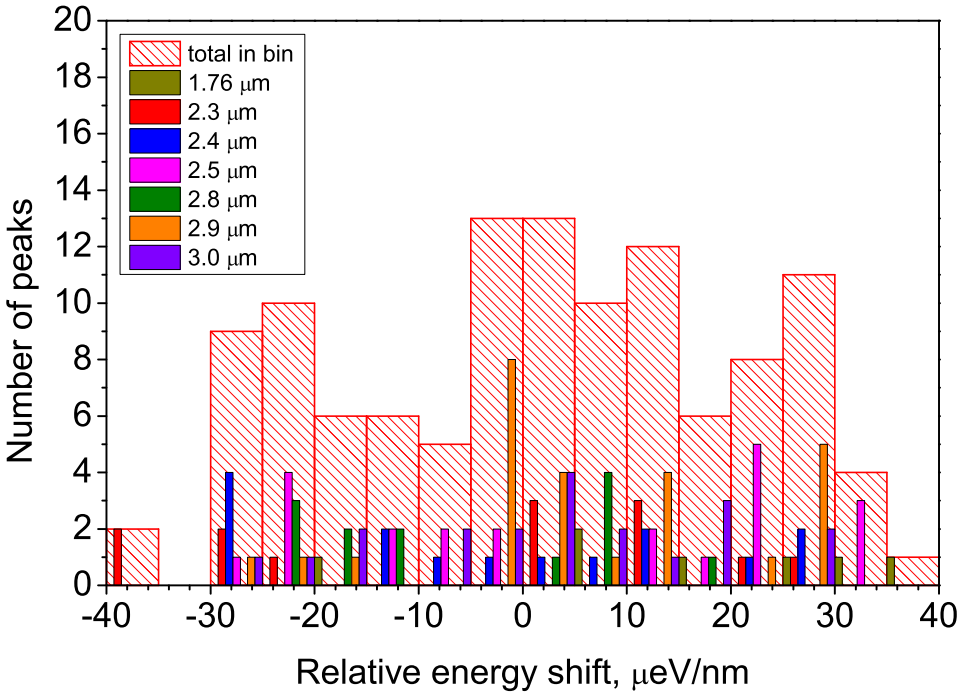

Figure 3.29: The shaded red histogram demonstrates the distribution of peaks' relative energy shifts in μeV per nm of tip's displacement for 7 photonic wires with diameters of 1.76 μm (dark yellow), 2.3 μm (red), 2.4μm (blue), 2.5μm (magenta), 2.8μm (dark green), 2.9μm (orange), 3.0μm (violet) with the size of the bin equals to 5 μeV/nm. Independent columns shows the amount of peaks for each structure in certain bin.

3.4.7.2 Different photonic wires

By default we assumed that all QD are distributed randomly within a QD layer and radiation wavelength doesn't connected with QD's positions. We have collected statistics for peaks' energy shifts for several structures with top diameter from 1.76 μm to 3 μm (about 10-20 peaks for each structure were analyzed) in order to check it and to find any growing features, which could make this assumption wrong. The histogram of peaks' wavelength shifts is shown on the Figure 3.29.

However, we didn't find any dependence between peak's shift and initial wavelength neither from the analyzed peaks from the long wavelength side for the photonic wires with diameter from 1.76 μm to 3 μm nor for the analysis of a whole spectrum for 2.05 μm top diameter photonic wire (section 3.4.7.1). Resulting distributions are represented on the Figure 3.30a and 3.30b for both experiment respectively.

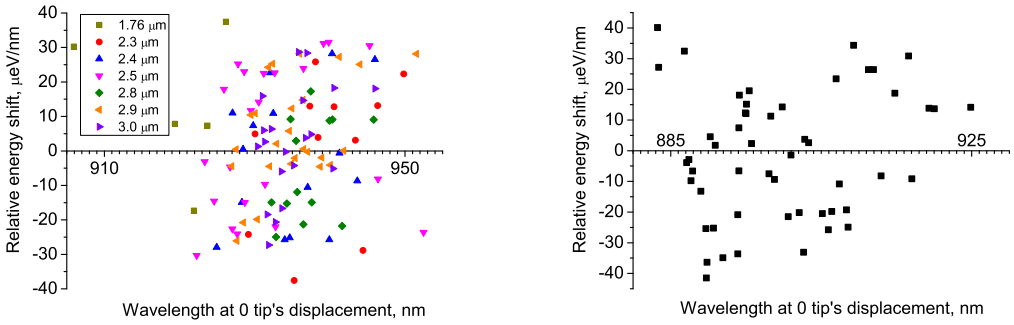

(a) (b)

Figure 3.30: (a) Distribution of peaks' relative energy shifts by initial wavelength for 7 structures with top diameters of 1.76 μm (dark yellow), 2.3 μm (red), 2.4μm (blue), 2.5μm (magenta), 2.8μm (dark green), 2.9μm (orange), 3.0μm (violet) . (b) Distribution of peaks' relative energy shifts by initial wavelength for a whole spectrum for a structure with 2.05 μm top diameter.

3.5 Mapping of QDs

Knowing the direction of peak's shift we can extract where the corresponding QD is located. If peak doesn't shift while pushing on the top of the structure it means that corresponding QD doesn't feel any stress and (accordingly to the strain map at the QD layer in section 3.3) it is located on a structure's diameter which is perpendicular to the direction of tip's displacement. This line will be named further as a 'zero-strain diameter' (ZSD). If radiation energy increases (wavelength decreases) it means that QD feels a compressive strain, otherwise – tensile strain. Moreover, if one peak shifts in the same way as the other but quicker (radiation wavelength changes more with the same amount of structure's top displacement) it means that related QD experiences more strain and that this QD is located further from 'zero-strain diameter' and vice versa.

From the calculations we see that strain is proportional to the distance from the 'zero-strain diameter' and that radiation energy changes linearly with strain: we can order the QD by the distance from 'zero-strain diameter'. It gives us the information about one coordinate of QD's position as it is shown on the Figure 3.31.

Repeating the same experiment along the other direction we can also get the information about the second coordinate and finally plot a map of relative QD's distribution inside the photonic wire. On the Figure 3.32 spectra for one peak while pushing in different direction are shown. Position of the related QD with respect to the 2 pushing axes is depicted on the Figure 3.33a.

Repeating this experiment from the third direction allows us to confirm the result obtained from two previous experiment. In this case every pair of experiments allows to calculate its own QD position. Comparing how close they are located to each other we can make a conclusion about quality of the experiment. In this case QD's position will be shown as a triangle which has 3 calculated positions at its corners (Figure 3.33b).

From all this we also can conclude that for every QD exists a direction, pushing along which

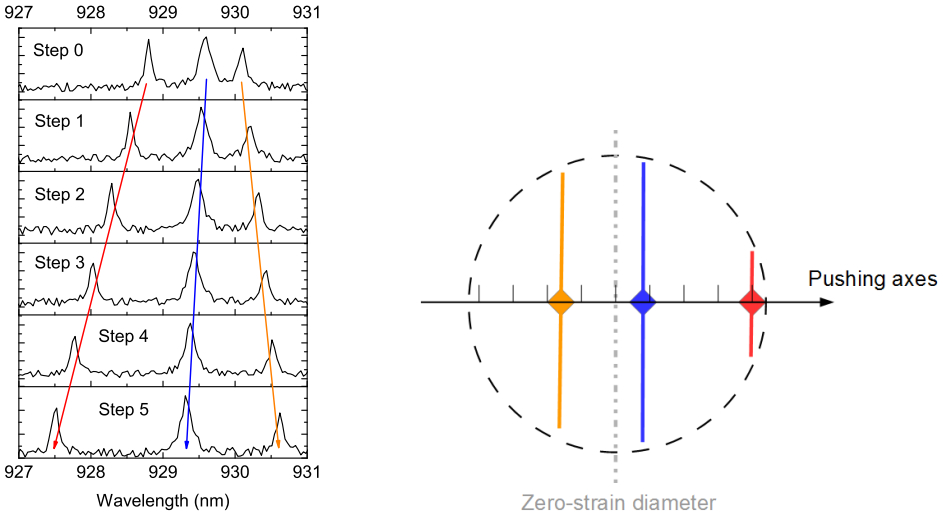

(a) (b)

Figure 3.31: Example of 1D mapping. (a) Photo-luminescence spectra showing positions of 3 peaks for different amount of mechanical pushing from top to bottom. (b) Positions of QDs related to these 3 peaks with respect to 'Zero-strain diameter'.

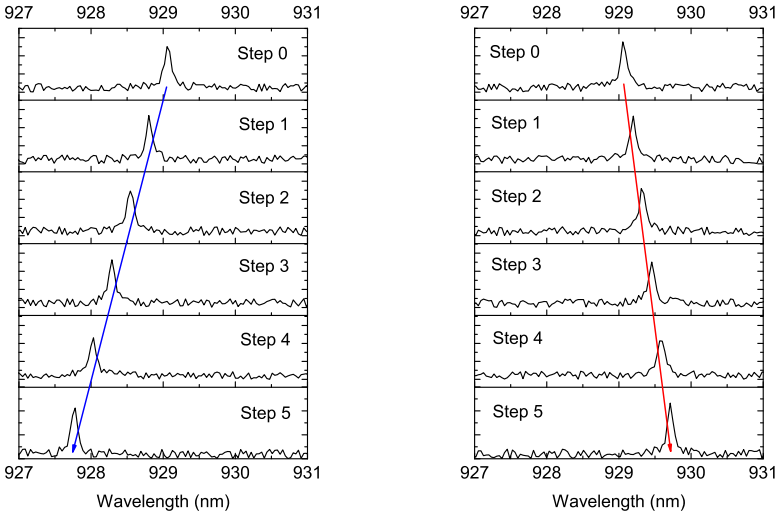

(a) (b)

Figure 3.32: Photo-luminescence spectra showing positions of the one chosen peak for different amount of mechanical pushing along (a) X axis and (b) Y axis from top to bottom. We see that one peak can shift differently (by speed and direction) depending on the direction of pushing.

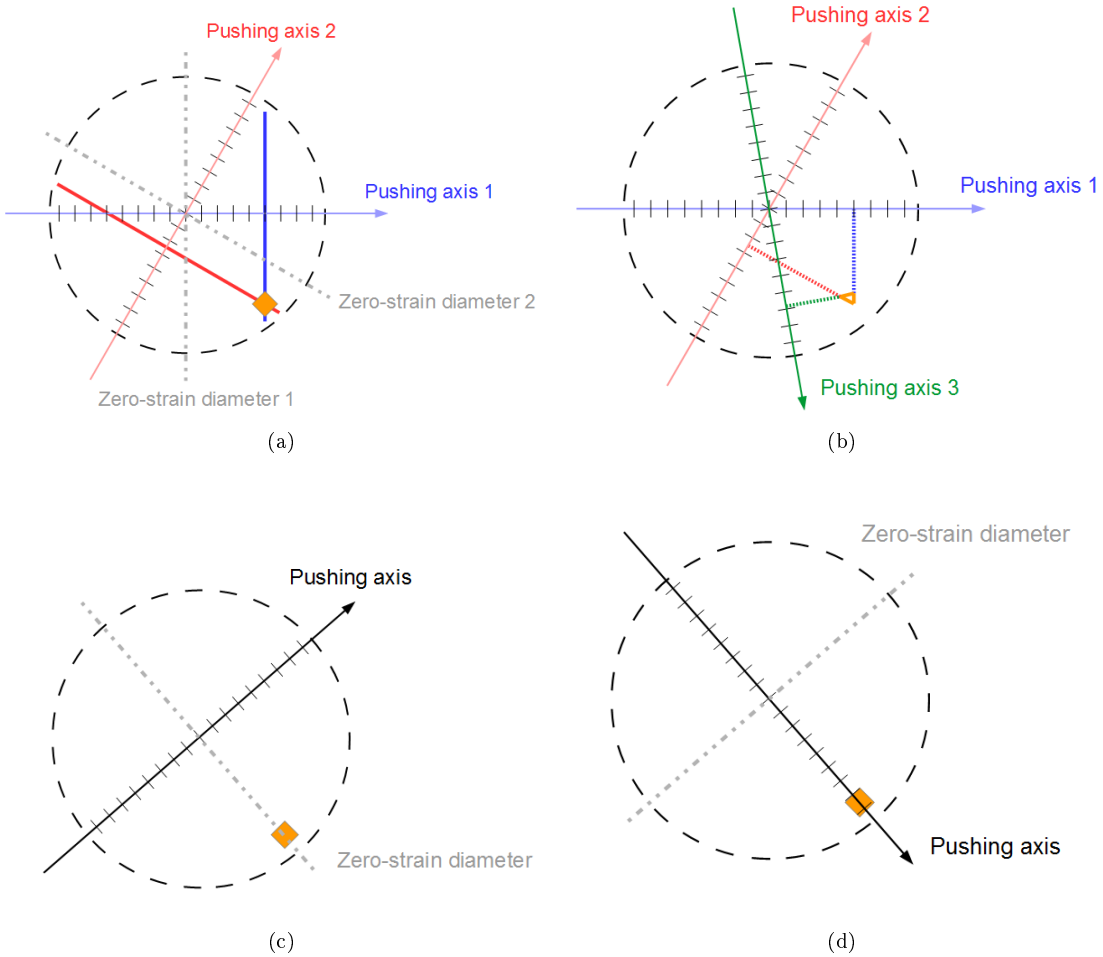

Figure 3.33: 2D mapping. (a) Position of the QD with respect to the 2 pushing axes. (b) Position of the QD with respect to the 3 pushing axes. (c) Orientation of pushing axis providing zero strain for certain QD. (d) Orientation of pushing axis providing maximum strain for certain QD.

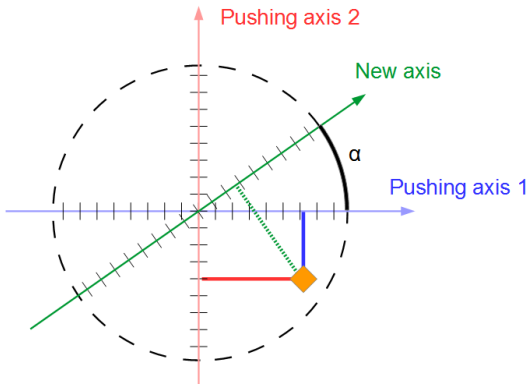

Figure 3.34: The sketch demonstrating how to find the energy shift along any chosen axis.

will not affect the energy of QD emission because QD is placed on 'zero-strain diameter' (Figure 3.33c), as well as perpendicular to this direction, pushing along which will lead to the maximal possible energy adjustment (Figure 3.33d).

If we know position of QD from previous measurements we can also assume the energy shift along any axis as a projection of the QD's position on this axis (Figure 3.34). If this axis has an angle α with orthogonal basis expected energy shift can be found as:

$$S_{new} = S_1 \cos(\alpha) + S_2 \sin(\alpha) \tag{3.5}$$

where S_i- energy shift along i-axis.

It should be mentioned that if we track only several spectral lines while pushing, we will be able to find only relative positions of corresponding QDs. It means that we will know only the distribution of the QDs with respect to each other and pushing axes, but we won't know how close any QD is to the side of the structure. In this case, the only way to know the absolute distribution is to calculate theoretically an absolute value for the relative energy shift at least for the one point of the QD layer (except the center, where this value is equal to 0). Nevertheless, if we track all spectral lines there is the other possibility to draw the absolute map of QDs distribution. It is only required to analyze the statistic of relative energy shifts as it was done in Section 3.30b. In that case we extract the absolute value of the maximum relative energy shift from the analysis of experimental data.

We have also presented a QD all-optical mapping technique based on a strain-tuning of QD's transition energy for the same types of structures in other our work [21].

3.5.1 One tip experiment from different directions

As it was said before, for every tip we defined X axis along the tip, Y – perpendicular to the tip. Displacement along these directions is a basic movement that can be done with the experimental setup. Besides that displacing the tip at the same time along both axes we are able to move it along any intermediate axis depending of the ratio between moving speeds along X and Y. We define an X' axis as a direction that has a 45 degree with respect X and Y, Y' – perpendicular to X'. To provide more or less the same contact area the tip was mounted with a small rotation (see Figure 3.4b). The sketch showing necessity of tip's rotation is depicted on the Figure 3.35.

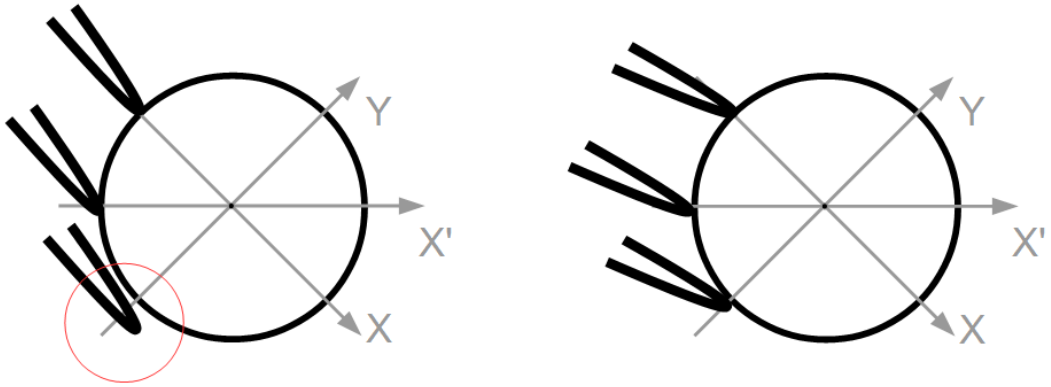

Figure 3.35: Sketch demonstrating the necessity of tip's rotation to carry out the experiment with pushing from different direction.

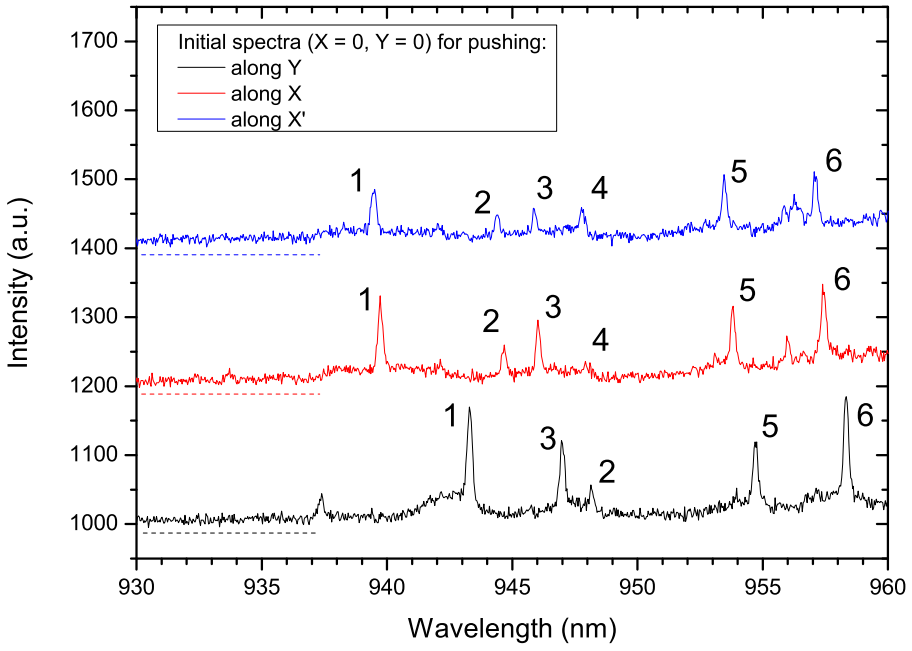

Figure 3.36: Photo-luminescence spectra of the structure with 3.11 μm top diameter when tip get in touch with the structure at different point. Spectra are shifted up for illustrative purposes, the common reference line is drawn with a dash line. Numbers make the connection between the same peak on a different spectra.

Since point of contact is different for pushing along 3 different direction, we observed that photo-luminescence spectra also looks different due to the different impact of the tip, which was described in the section 3.4.3. For some of the investigated structures it leads to the fact that it is hard to follow one peak through 3 experiments. This applies more to structures with bigger top diameter, because they contains more QDs and PL peaks are more densely distributed on the spectrum. On the Figure 3.36 comparison between 3 initial (i.e. tip is in touch with the structure, but do not yet push on it) spectra for the structure with 3.11 μm top diameter is shown. Spectra are shifted up for illustrative purposes, the common reference line is drawn with a dash line. Enumeration of the peaks was done after a careful analysis, taking into account not only peaks' behavior with pushing but also their power dependencies.

We carried out the experiment along Y, X and X' directions pushing by 100 nm with 20 nm step. Then, from each data set the relative energy shift in μeV per nm of tip's displacement was extracted for each of the peak along each of the direction. The resulting values are shown in the table 3.2. From (3.5) we expect:

$$S_X + S_Y = \sqrt{2} S_{X'} \tag{3.6}$$

	S_Y	S_X	$S_{X'}$	$\lvert S_X + S_Y - \sqrt{2} S_{X'} \rvert$
Peak 1	10	63	99	67
Peak 2	8	63	97	66
Peak 3	-10	15	3	1
Peak 5	13	11	31	20
Peak 6	13	11	31	20

Table 3.2: First three columns show relative energy shift in μeV per nm of tip's displacement for the structure with 3.11 μm top diameter, while pushing from 3 different directions Y, X and X' (see Figure 3.35) for different peaks. The value in the last column should be equal to 0 if the values of relative energy shift obtained from different measurements are in good agreement (see equality 3.6). The bigger the value the bigger is a mismatch.

But equality (3.6) is not fulfilled (see the last column of the table 3.2) for all peaks, however for the peak 3 it is almost the case. It means that QDs positions related to the peaks should be presented as triangles (see Figure 3.33b for a clear demonstration). Nevertheless, we can also represent them as circles inscribed in these triangles, because center of such circle corresponds to the smallest total mismatch of QD's position. Resulting QDs' distribution map is shown on the Figure 3.37. Big black circle corresponds to the side of the stricture with the value of energy shift of 108 μeV/nm, which follows from a theory (see Section 3.3.4). We connect an observed low matching of experimental results to the fact that we need to change a position of the tip from the one measurement to another.

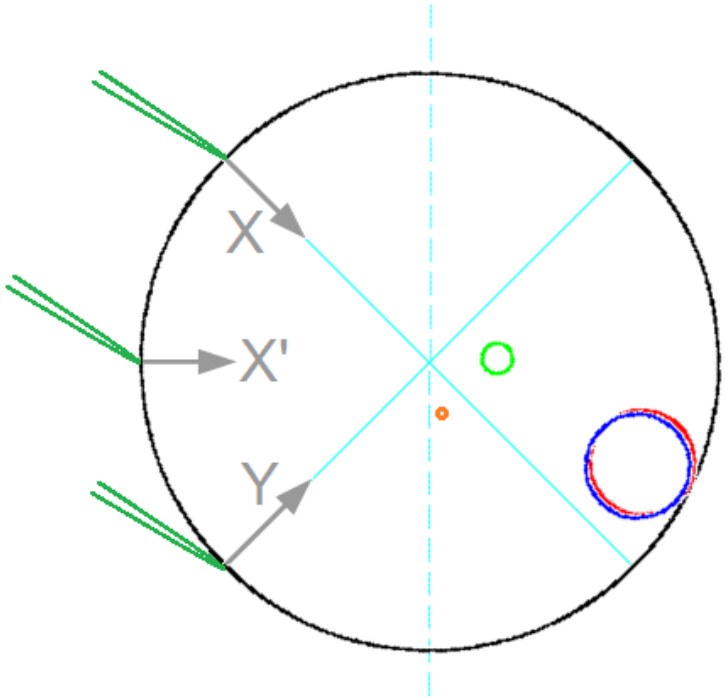

Figure 3.37: Map of the QDs' distribution for the structure with 3.11 μm top diameter. Positions of the QDs obtained during the experiment, when one tip is used to push along 3 axes. Position of each QD is presented as a circle of the corresponding color: red - peak 1, blue - peak 2, orange - peak 3, magenta - peak 4, green - peak 5. Data for the peak 3 demonstrate a good matching, so a corresponding circle is enlarged for a better visibility. Values for peaks 5 and 6 are almost the same, so the magenta and the green circles are overlapping. Big black circle is a side of the structure. Value of the energy shift that corresponds to it is equal to 108 μeV/nm. Light-blue lines show 'zero-strain diameters' for each pushing direction.

Nevertheless, we can note several interesting features:

- Peaks 1 and 2 demonstrate almost the same behavior during the experiment and most likely relates to the same QD. The same is true for the other pair of peaks: 5 and 6.
- We see on the Figure 3.36 that presence of the tip in initial position for pushing along Y direction affects a lot on the peaks 1 and 2 (comparing to the initial positions for pushing along X and X'), whereas there is almost no influence on the peaks 3,5,6. At the same time, QDs related to the peaks 1 and 2 located closer to the edge of the structure, than QDs related to the peaks 3,5,6 (see Figure 3.37). From this we can conclude that presence of the tip influences more on the QDs located closer to the edge of the structure.
- All observed emission lines on the spectra correspond to the QDs located on the opposite side from the tip. One can make an assumption that tip affects electrostatically on the emission intensity of the QDs located close to it.

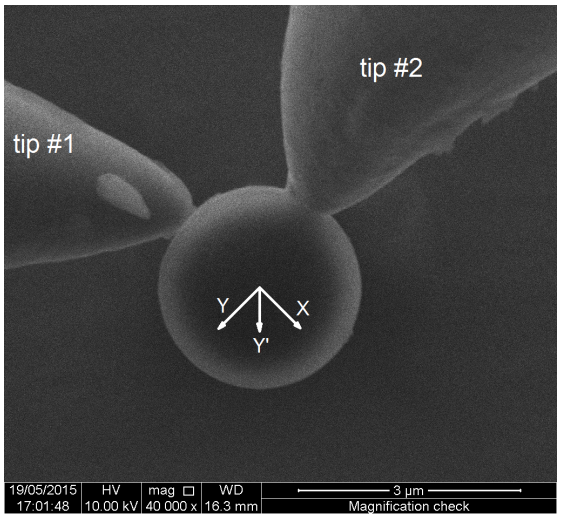

Figure 3.38: Top view image obtained with SEM. Two tips in contact with the 2.68 µm top diameter structure. Tip 1 is associated with the X direction, tip 2 - Y direction. Resulting iterative pushing along X and Y axes gives an overall shift along Y' axis.

3.5.2 Two tips experiment

To get rid of the problem with spectra matching we decided to get 2 tips in touch with the photonic wire in the same time. The initial position is shown on the Figure 3.38. The structure under investigation has a top diameter of 2.68 µm.

Thus, we are able to sequentially push on the structure from 2 orthogonal directions and see how it affects the photo-luminescence spectrum. We associate X axis as a direction along tip #1 and Y – along tip #2. We moved tips by 40 nm at each step. As an overall result photonic wire shifts along Y' direction. We have done 5 iterations of this experiment. Peaks' positions for 4 peaks on the photo-luminescence spectra are shown on the Figure 3.39a From the data that we have obtained for each peak independently it is possible to extract the value of the relative peak's spectral shift along X, Y and Y' axes. The sketch on the Figure 3.39b demonstrates the way how it can be done.

For the slope along X : we need to take a peak's position at initial (first) spectrum and measure its relative displacement using the second spectra. Then we need to measure a relative displacement from third to fourth spectra and add this value to overall displacement due to X pushing. For Y it is the same, but we started from the second measured spectrum. For Y' we have two non-overlapping sets of data. One starts from the initial spectrum (set number 1) and contains all odd spectra, the other one – even spectra (set number 2). These sets should be analyzed independently. For both sets we need to know a relative peak's displacement from one spectrum to the next one. Extracted data are shown for the peak #1 on the Figure 3.39c.

Resulting energy shift for each peak along each axes is represented in a table 3.3 as a slope of linear fit as discussed above. Values for the first and second data sets along Y' are averaged in the fifth column. In case of this experiment from (3.5) follows:

$$S_X + S_Y = \sqrt{2} S_{Y'}, \tag{3.7}$$

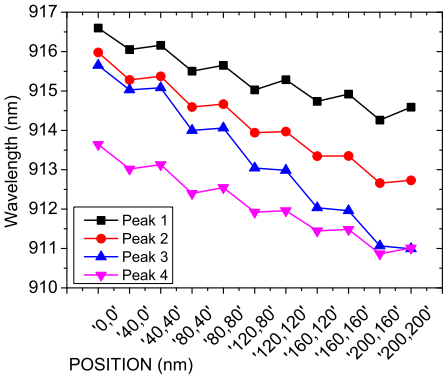

(a)

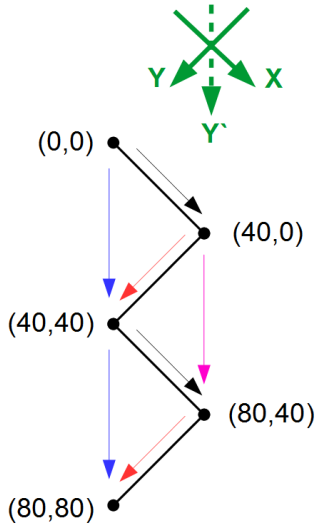

(b)

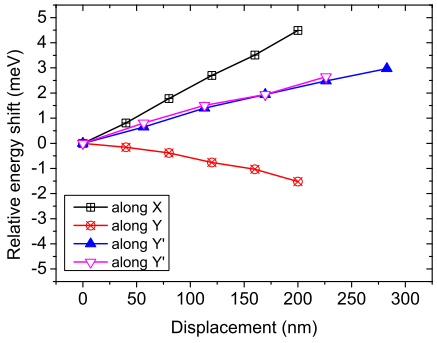

(c)

Figure 3.39: (a) Spectral positions for 4 peaks during the experiment with sequential pushing with 2 orthogonal tips. The structure under investigation has a top diameter of 2.68 μm. X-coordinate of the plot contains information about applied pushing from both tips in nm written in (first tip,second tip) notation. (b) Black spots demonstrate relative structure's displacement during the experiment. Color arrow between two positions shows that analysis of the peak's shift between these positions belongs to the group: blue - shift while pushing along Y' (first), magenta - Y' (second), black - X, red - Y. (c) Relative energy shift for the peak #1 from Figure (a) along 3 axes (X, Y and Y') with the same color coding as on the Figure (b) for axes identification.

	S_X	S_Y	$S_{Y'1}$	$S_{Y'2}$	$S_{Y'}$	$\lvert S_X + S_Y - \sqrt{2}S_{Y'} \rvert$
Peak 1	22	-7	11	12	11.5	1
Peak 2	26	-2	17	17	17	0
Peak 3	34	0	24	26	25	1
Peak 4	23	-3	14	14	14	0

Table 3.3: Relative energy shift for 4 peaks in μeV per nm of tip's displacement for the structure with 2.68 μm top diameter, while pushing iterative along X and Y directions using 2 tips. The value in the last column should be equal to 0 if the values of relative energy shift obtained from different measurements are in good agreement (see equality (3.6)). The bigger the value the bigger is a mismatch.

It holds approximately for every peak. The deviation from equality (3.7) is given in the last table's column. The mismatch observed for several peaks is in a range of accuracy of the measurements. Based on this data QDs distribution map is plotted on the Figure 3.40. Again as in the Section 3.5.1 we can note that QD are distributed closer to one side of the structure, which is far from the tips. We assume that electrostatic effect of the tips influences on the QD located close to it and suppresses radiative recombination.

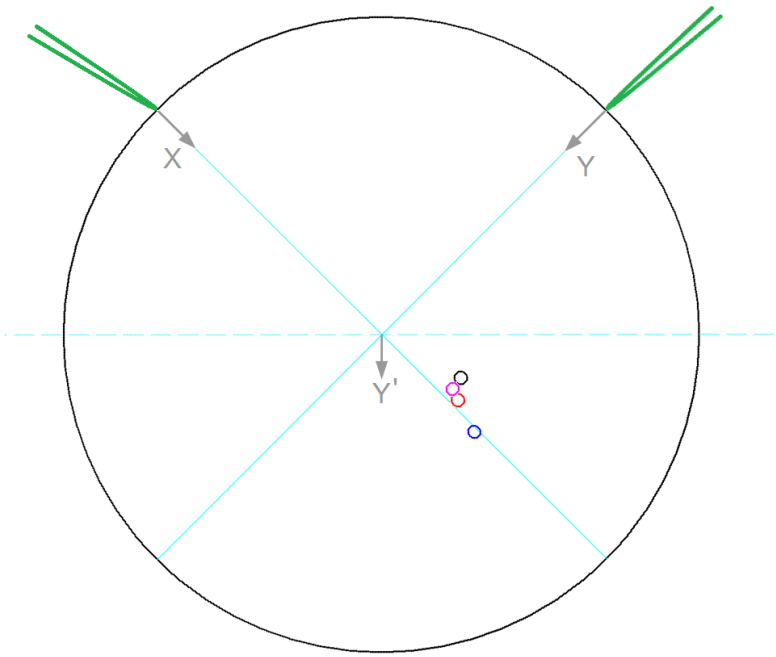

Figure 3.40: Map of QDs' distribution. It's shown using not triangles as it was described above, but circumscribed circles due to good matching of the results. Map of the QDs' distribution for the structure with 2.68 μm top diameter. Positions of the QDs obtained during the experiment, when two tips is used to push iterative along X and Y directions. Position of each QD is presented as a circle of the corresponding color from the Figure 3.39a: black - peak 1, red - peak 2, blue - peak 3, magenta - peak 4. Data are in good matching, so a corresponding circle is enlarged for a better visibility. Big black circle is a side of the structure. Value of the energy shift that corresponds to it is equal to 82 μeV/nm. Light-blue lines show 'zero-strain diameters' for each pushing direction.

3.6 Conclusions

In this chapter we observed the possibility of the strain tuning of semiconductor QDs in a range of several meV and control of emission wavelength over the time. To provide such tuning we statically pushed from the side on the structure containing QDs on purpose to bend it and hence to arise the stress at the QDs' layer.

We have found experimentally that QD's emission energy can be tuned by several meV while pushing photonic wire's top facet by 100 nm. We have also calculated theoretically amount of the stress arised at the QDs level and demonstrated that uniaxial stress model is reliable for the calculations of energy shift. We found theoretical and experimental results to be in good agreement.

We demonstrated that it is possible using such tuning to bring two QDs in resonance. Such condition opens up the possibility to study collective effects such as superradiance [37, 41] using this type of structures.

We also found this method very useful to determine the position of QDs. It is applicable not only for the photonic wires but for any types of structures with embedded stress-sensitive quantum emitters. It can be used along with existing all-optical imaging methods [45, 46, 47], which are in its turn limited if the quantum dots deeply embedded in photonic nanostructures, which is often the case for all types of modern semiconductor devices like a micropillar or a photonic wire used to optimize their coupling with light. The other all-optical method allowing to determine QDs' positions is also developed in our team and is presented in [21].

Chapter 4

Optical actuation of photonic wire's motion

Contents

4.1 Introduction

It has been previously observed [19, 20] that photonic wires are good Quantum Mechanical Oscillators with resonant frequency about 500 kHz and quality factor (Q) about 2000. Nevertheless, these results were obtained when the photonic wire was mechanically excited with a piezoelectric transducer (PZT). This method has several limitation. First of all, upper frequency of a piezoelectric transducer is limited to 1 MHz that excludes the possibility to excite any higher order modes. Frequencies of the higher order modes are situated in a several MHz range. Secondly, piezo excitation affects all structures on the sample. Thirdly, PZT's response is not flat in frequency, which leads to the appearance of several small peaks aside from the main resonant peak.

The method described in this chapter uses an optical actuation of photonic wire's motion. It allows to excite higher order modes and work directly only with one chosen structure. In our experiment, a modulated intensity laser beam interacts with a photonic wire. Such dynamic excitation leads to a resonant increase in the amplitude of the oscillations, when modulation frequency coincides with an eigenfrequency of the photonic wire. Several physical effects appear in light-matter interaction and affect the amplitude of the oscillations. One of these effects is photons' momentum: a radiation pressure [48], when photons reflect from the structure, and gradient (dipole) force, when photons are deviated. Such interaction can be described as interaction of the light wave's electric field with field-induced dipole moment [49]. Other effects influencing on the structure's oscillations are thermal expansion caused by non-symmetric heat of the structure by off-centered (relative to the axis of symmetry of photonic wire) laser beam [50] and electrostrictions caused by internal structure of GaAs. One of the goals of this chapter will be to discuss the contribution of those three effects.

4.2 Experimental setup for optical motion detection

The experimental setup was built using the software and methods developed in [51, 52, 53], allowing an exploration of nano-optical phenomena. On the Figure 4.1 the experimental configuration demonstrating the general idea of motion detection is shown.

The general idea of optical motion detection of μm-scale structures is based on detection of intensity's deviations of the laser beam reflected from the structure using a split photo-diode (SPD) technology. The SPD is a device consisting from 2 identical photo-diodes located very close to each other (see Figure 4.2b). The main feature of SPD is a possibility to measure the difference between signals of these two photo-diodes with a large gain. This technique is used in Atomic-Force Microscopy (AFM) to detect the motion of the cantilever (see Figure 4.2a). The SPD is discussed in details in Section 4.2.1.

In our case, a Probe laser is focused on the top of photonic wire using a microscope objective. Using a two lens system (one of which is the objective and the other mounted before the SPD) we image the plane of the top of the photonic wire on the SPD surface. Laser spot is placed in the middle of the SPD that means that both parts (which are named A and B) have equal laser intensity on it and the output difference signal is equal to 0. When structure shifts along X direction of the SPD, it changes the distribution of light intensities on the parts of SPD and leads to non-zero signal at the differential output of SPD, which is proportional to the displacement amplitude.

Oscillations of the photonic wire are then detected by measuring the amplitude of the signal from SPD at different frequencies. This allows us to determine, firstly, the eigenfrequency of

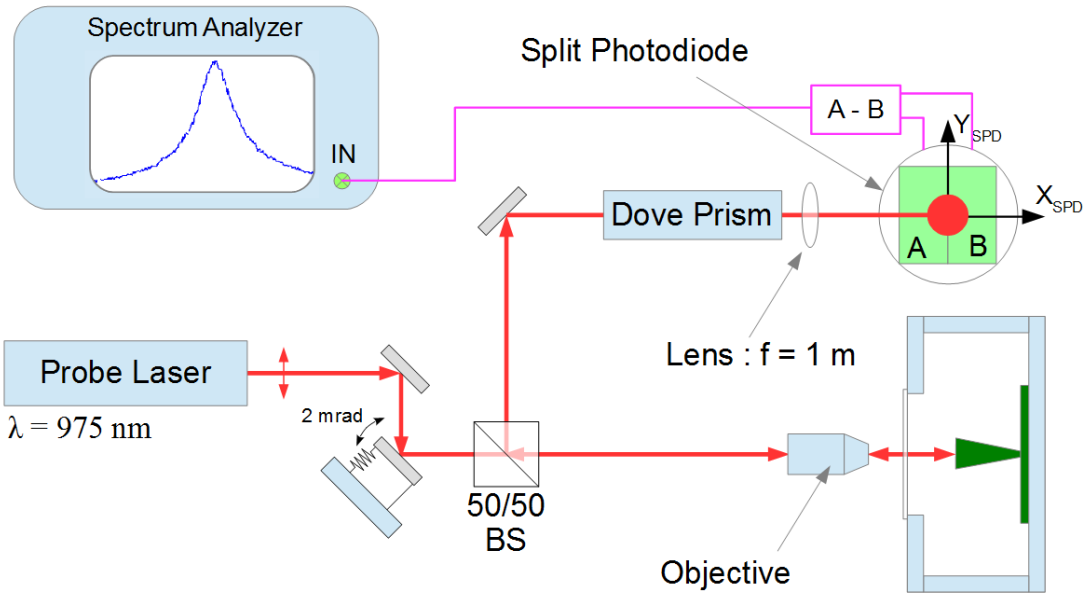

Figure 4.1: Schematic view of the experimental setup for motion detection of μm-scale structures.

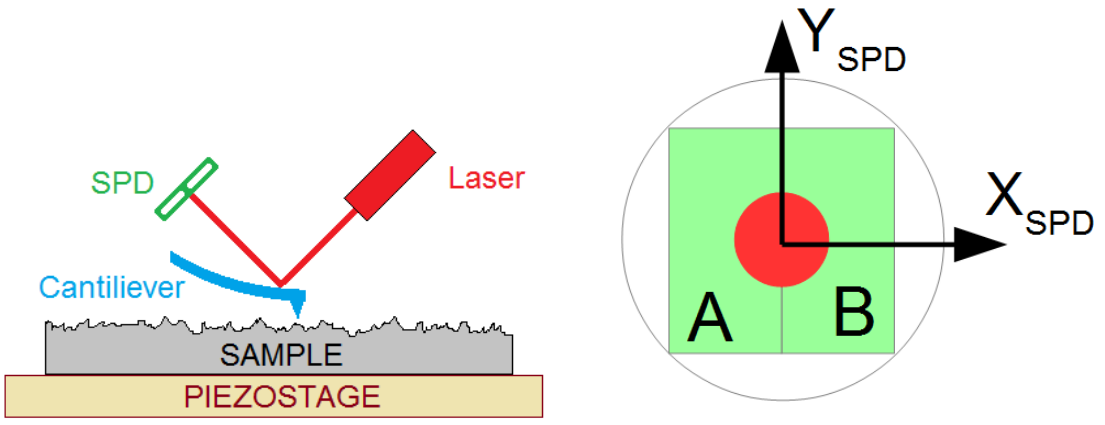

(a) (b)

Figure 4.2: (a) Block diagram demonstrating an operational principle of atomic-force microscopy using laser beam deflection detection technique. Position of the cantilever changes during its displacement with respect to the sample's surface due to their interaction. The reflection of the laser beam then displaces on the surface of the split photodiode (SPD). (b) Sketch demonstrating a face view of SPD together with laser beam position and its coordinate system.

the investigated structure, and secondly, the amplitude and phase of these oscillations.

This method of motion detection is very sensitive and allows us to detect even Brownian motion of the photonic wire, whose amplitude at T = 5K is about ten of picometers. Detection sensitivity depends on the geometrical laser parameters (its position with respect to the top of the photonic wire, as well as beam size), laser intensity, SPD parameters (gain of amplifier and noise level) and direction of the structure's oscillations with respect to the SPD. Detection sensitivity of SPD is discussed in details in Section 4.2.2.1.

4.2.1 Split photo-diode

As it was said before, SPD consists from 2 identical photo-diodes (PD) located very close to each other (see Figure 4.2b). In this section its operational principle will be presented.

4.2.1.1 Electrical structure of split photo-diode

Simplified scheme of device's internal structure is shown on the Figure 4.3.

SPD chip A photo-diode chip used in our home-made SPD is a Si PIN photo-diode Hamamatsu S4204. It has an active surface of 1 x 2 $mm^2$with 20 μm of dead zone in between of 2 parts. Its spectral response range is in the interval from 320 nm to 1100 nm with peak photo-sensitivity equal to 0.65 A/W at 960 nm; dark current is less than 1 nA per 1 element; cut-off frequency is equal to 30 MHz. Such outstanding parameters make it perfect for our measurements.

Power circuit SPD uses symmetric power input of 15 V from external power supply. Positive voltage then reduces twice: firstly to +12 V (which is applied to photo-diodes), secondly to +5 V. A voltage of +12 V is applied to cathode of each photo-diode (indicated as $+V_c$ at the Figure 4.3a). In this way, the amount of carriers, which contribute to the emergence of current, generated under the laser light is proportional to its intensity [54]. In its turn, negative voltage reduces directly to -5 V. Resulting symmetric 5 V source is required for all operational amplifiers.

One photo-diode path Each photo-diode has two independent amplifiers for low frequency (LF) and high frequency (HF) signals (see Figure 4.3b). The HF signal requires highest possible gain to be able to measure the laser's intensity fluctuations caused by oscillations of the experimental structure, whereas LF signal is much higher and requires smaller gain to avoid saturation of the amplifier.

A feedback loop of every operational amplifier here and further consists not only of resistivity, which defines the gain of the circuit, but also a capacity in parallel, which prevents the high frequency fluctuations on the output of an operational amplifier from coming back to its input.

It is important for the LF (HF) gain to be equal for both photo-diodes to avoid the predominance of signal coming from the one part of SPD over another. To minimize the temperature deviation of amplifiers' parameters one chip with two embedded amplifiers was used, where each photo-diode uses its own amplifier. The same is true for some resistances and capacities, which value has to be equal to provide a good balance in the electrical scheme.

LF path of the signal The photo-diode is a current source, which is converted to the voltage using a resistance R_c. An electrical symmetric low-pass filter is used to cut off all signal components with frequencies higher than 10 kHz. This allows us to isolate only the low-frequency

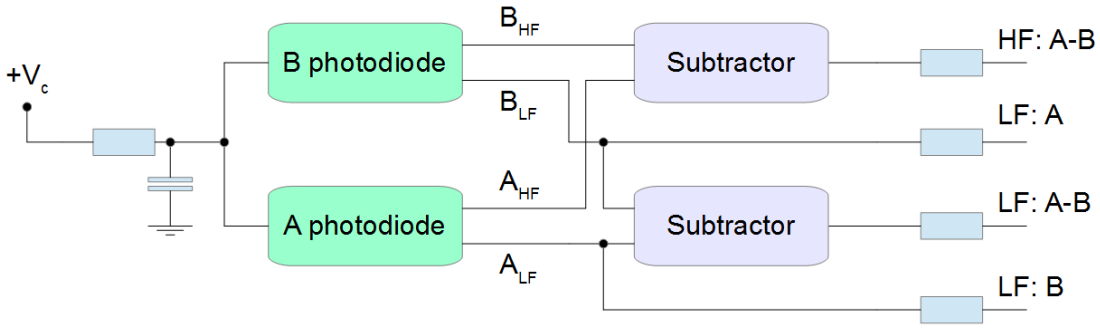

(a)

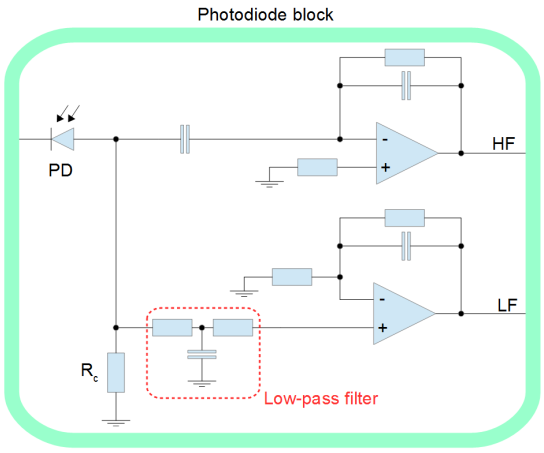

(b)

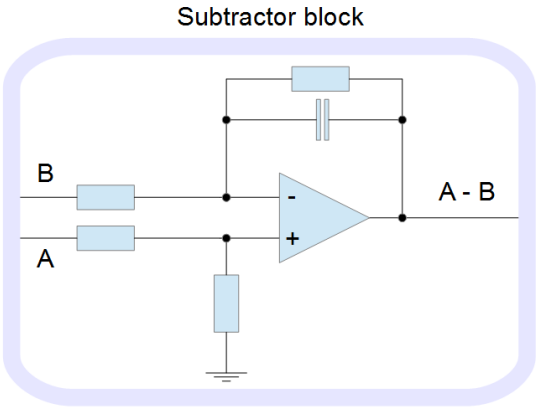

(c)

Figure 4.3: Simplified scheme of SPD's internal structure. (a) A flowchart of the device. Block related to A and B photodiodes (highlighted by green) is presented in detail on the plot (b). Block related to subtractor (highlighted by violet) is presented in detail on the plot (c). Blue rectangle is a schematic representation of a resistance, triangle - operational amplifier, two parallel lines - capacitor. (b) Photodiode block. (c) Subtractor block.

component of the signal. A voltage amplification circuit based on a operational amplifier is used further. The LF gain is almost constant within the whole frequency range of this channel and can be simply found experimentally as a ratio between the voltage at the LF SPD's output and incoming laser power.

HF path of the signal A capacity is used to transmit only high frequency photo-current fluctuations to HF path. A circuit based on an operational amplifier is used to convert it in voltage. Frequency range for that path is from about 100 kHz to 20 MHz with frequency dependent gain on it, which will be discussed additionally in (4.2.1.2).

Subtractor A subtractor scheme (see Figure 4.3c) is then used to obtain a difference signal (named 'A minus B' or just 'A-B'). A subtractor is also based on an operational amplifier. Two independent subtractor are used for LF and HF signals.

Outputs The device has 4 BNC outputs: two for LF signal of each photo-diode, two for LF and HF difference signal. A 50 Ω resistance is mounted before each output.

4.2.1.2 High frequency and low frequency gain of split photo-diode

As it was discussed in Section 4.2.1.1, each photo-diode in SPD has two independent amplifiers for LF and HF signals. The LF (HF) gain is equal for both photo-diodes, however, LF and HF amplifiers have different gains. Both gains are defined by internal electrical structure of amplifiers. We found both gains experimentally.

LF gain To define LF gain we placed a laser beam on the one part of SPD and measured a ratio between the voltage at the LF SPD's output and incoming laser power. We also repeated the experiment with the other part to be sure that gains for two photo-diodes are equal. Measured LF gain is about 622 μV/μW for laser wavelength equal to 970 nm. For the other wavelength it can be recalculated using the photo-sensitivity curve of the SPD's chip. Nevertheless, for us only the ratio between LF and HF gains is important, and it will be constant for any laser's wavelength.

HF gain We used a HF 'A-B' channel to measure HF gain, because our SPD doesn't have a HF outputs for each photo-diode independently. But using LF outputs for each photo-diode we controlled that laser is focused only on the one of them, so measured in such way value is equal to the HF gain of one photo-diode. We found that HF gain depends a lot on the frequency. To measure it we used a combination of analog acousto-optic modulator (AOM) and Vector Network Analyzer (VNA) Rohde&Schwarz ZNB4. The experimental setup is shown on the Figure 4.4.

The VNA is used to determine the amplitude of the signal at chosen frequency. In the experiment, the VNA sends a Sin signal of given amplitude on given frequency to the AOM, which modulates the laser intensity, and measures the response on the same frequency using the signal from the HF output of the SPD. It should be mentioned that the VNA measures a ratio of Sin amplitudes of incoming (from SPD) signal to outcoming signal. Thus, to recover the SPD signal in μV it is required to multiply measured value on the initially chosen amplitude of outcoming Sin signal produced by the VNA. Using the VNA it is possible to span a frequency from 100 kHz to 4.5 GHz, whereas cut-off frequency of SPD's HF output is about 20 MHz.

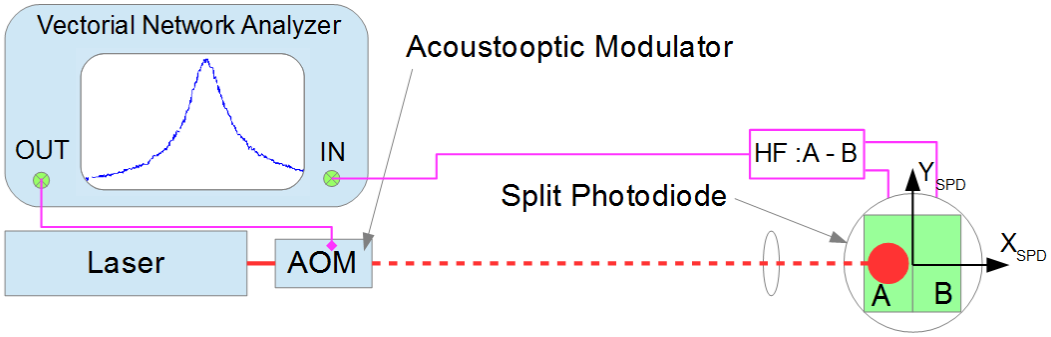

Figure 4.4: Schematic view of the experimental setup to measure the gain of HF path of SPD.

The AOM transmit amount of laser light depending on the applied voltage. In our experiment it is initially biased to transmit about a half of an incoming laser light. This working point provides maximum range in which modulation of laser transmission linearly depends on the applied to AOM voltage's modulation (see Figure 4.5a). Thus, knowing the Sin amplitude of applied voltage modulation and incoming laser power, it is possible to calculate the Sin amplitude of laser modulation on the SPD.

The HF gain is then calculated as a ratio of measured signal in μV to the amplitude of laser's modulation in μW. Above we have found a LF gain to be equal 622 μV/μW. Gain ratio (ratio of HF gain to LF gain) is shown on the Figure 4.5b. It demonstrates maximum value at about 2 MHz.

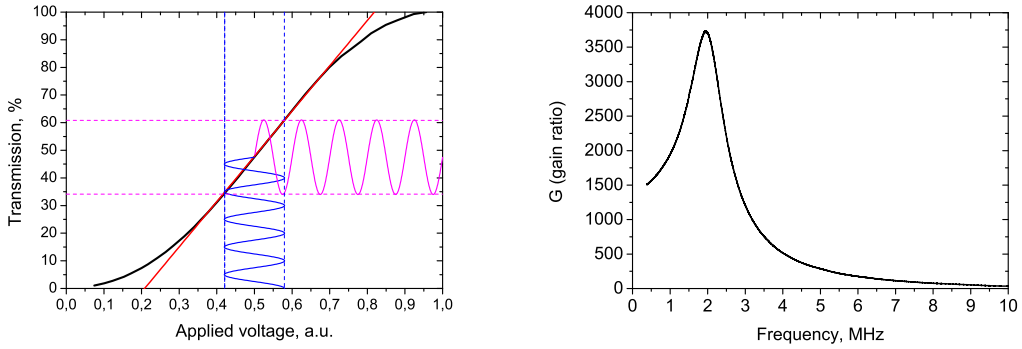

(a) (b)

Figure 4.5: (a) Demonstration of laser modulation using AOM. Black trace shows dependence of AOM transmission on the applied voltage in arbitrary units. Red trace is its linear fit around a half of maximum possible voltage, which is the bias used in the experiment. Blue Sin trace demonstrates the modulation of applied to AOM voltage produced by VNA. Magenta Sin trace shows correspondent modulation of laser transmission caused by applied voltage modulation. (b) Frequency dependence of ratio between HF and LF gain of SPD.

4.2.1.3 Limitations of the detection

Detection of structures' motion is limited by the noises in the system. Sensitivity of SPD, as an electronic device, is limited by thermal noise generated by the random thermal motion of charge carriers (Johnson–Nyquist noise), shot noise caused by the discreteness of carriers of electric charge. Such noises are unavoidable for all electronic device. Thus, noise measured in the absence of the laser light coming to the SPD is named electronic noise. Its spectrum was measured from 'A-B' channel of SPD using a Spectrum Analyzer (SA) as is presented on the Figure 4.6a. We can see that it demonstrates the same behavior as a gain ratio of SPD (Figure 4.5b) with a maximum at about 2 MHz. It is caused by the fact that amplifiers enhance both the useful signal and the parasitic noise equally.

When laser is shone on a single photo-diode (A or B part of SPD), it creates charge carriers proportionally to the laser's intensity. But laser's intensity fluctuates in time, what is known as laser total intensity noise. It results partly from optical shot noise and partly from technical noise such as vibrations of resonator mirrors, etc. Thus, laser's noise at the surface of photo-diode leads to signal's noise at the output of the device. The higher the intensity, the higher signal's noise.

Influence of the laser intensity noise on the signal can be minimized, when the laser is equally balanced between two parts of SPD. In this case, one part of the laser noise is measured by A part of SPD, the other - by B part. As a result, they compensate each other. Thus, a signal from 'A-B' channel is only limited by the optical shot noise, the power of which depends linearly on the laser power. On the Figure 4.6b dependence of the noise spectral density at the frequency of 500 kHz on the Pump laser (lasers used in the experiments will be presented in the Section 4.2.6.4) power is shown for the cases, when laser is focused only on the one part of the SPD and balanced between two parts. At zero laser power both traces start from the value of the electronic noise at this frequency ($\sim$0.8 pW/Hz). Noise density for the single photo-diode demonstrates the superlinear rise with increasing laser power, whereas for the balanced case noise density increases linearly. It means that Pump laser is shot noise limited.

On the Figure 4.6c power dependencies of the noise of both Pump and Probe lasers are shown for the balanced case in log-log scale after subtraction of the electronic noise contribution. The Pump laser balanced noise (black squares) rises linearly as expected from the shot noise of a well behaved laser. This laser is not too noisy so that its small technical noise is well rejected by the balanced detection. In contrast, we can see that dependence for the Probe laser (blue triangles) rises superlinearly, which means that noise of this laser is not fully rejected by SPD. Since this laser is delivered through the optical fiber such noise can also be a positioning noise caused by fiber's oscillations. The origin of this noise is so far not completely understood.

A quantitative comparison of the noise component in the measured signal will be carried out in Section 4.2.4.

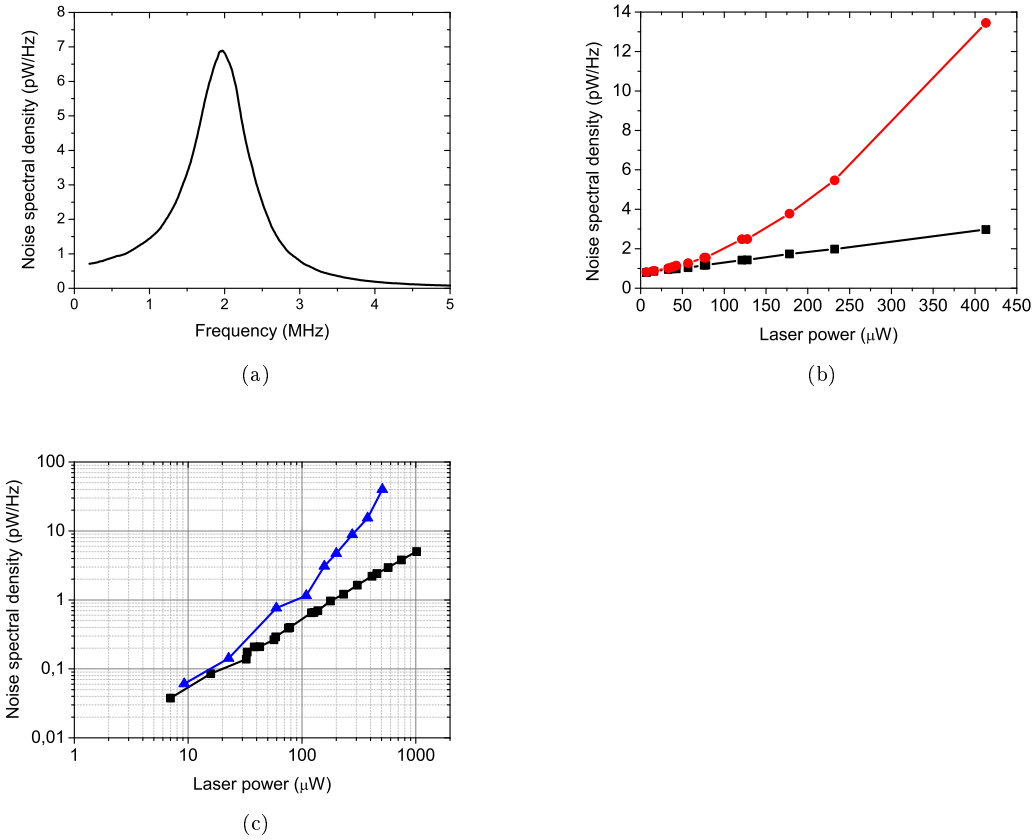

Figure 4.6: (a) Spectrum of the electronic noise (at the absence of the laser light) of the SPD. (b) Dependence of the noise spectral density on the laser power at the frequency of 500 kHz. Experimental data presented by red circles correspond to the case, when laser is focused only on the A part of the SPD. Black squares correspond to the case, when laser is balanced between two parts (black trace). Presented data were obtained with the Pump laser. (c) Dependence of the noise spectral density on the laser power at the frequency of 500 kHz for Pump laser (black squares) and Probe laser (blue triangles). In each experiment laser is balanced between two parts of the SPD. A component of the noise spectral density in the absence of the laser light is subtracted for both traces.

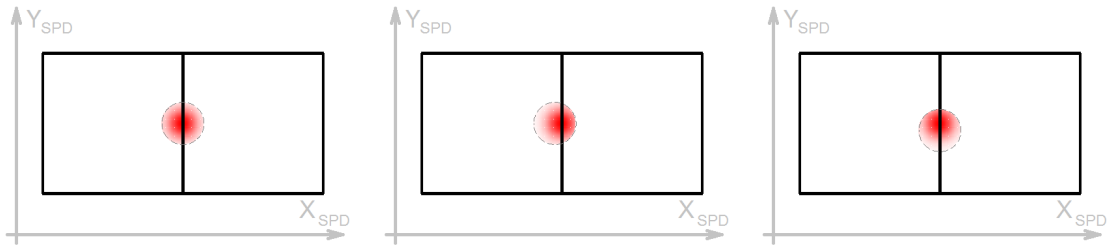

(a) (b) (c)

Figure 4.7: Laser intensity distribution on the SPD's surface for different relative positions of the photonic wire and the laser beam. (a) Laser is at the center of the photonic wire. (b) Laser is shifted horizontally from the center of the photonic wire. (c) Laser is shifted vertically from the center of the photonic wire. On all images dashed circle shows position of the photonic wire's top facet.

4.2.2 Detectivity

As it was shortly said, SPD has an differential output ('A-B'), voltage on which (V_d) is proportional to the difference of intensity between 2 parts (A and B) of the SPD. If photonic wire is fixed at one position (it means there no any externally excited motion), laser is focused somewhere on its top facet (for simplicity of explanation imagine it to be at the center) and is imaged equally (by intensity) on the SPD surface, then the 'A-B' signal is equal to 0. Distribution of the laser intensity on the surface of SPD is presented on the Figure 4.7a. If we shift the photonic wire along X direction of the SPD (Figure 4.7b) the 'A-B' signal changes, because the distribution of the laser intensity changes. The possibility to detect the displacement of the photonic wire is defined by possibility to distinguish values from 'A-B' signal between these two positions, that defines the detectivity as a derivative of 'A-B' signal with respect to coordinate. Besides, if we shift the photonic wire along Y direction of the SPD (Figure 4.7c) the 'A-B' signal doesn't change, because changed laser intensity is still symmetrically distributed between A and B parts of SPD. It turns the detection sensitivity to be a vector, which we named $\vec{\beta}$:

$$\vec{\beta} = \begin{pmatrix} \frac{\partial V_d}{\partial x} \\ \\ \frac{\partial V_d}{\partial y} \end{pmatrix} \equiv \begin{pmatrix} \beta_x \\ \\ \beta_y \end{pmatrix}$$

Thus, the amplitude of the signal for photonic wire's displacement depends on the angle between $\vec{\beta}$ and direction of this displacement. In the described case the detectivity vector is coincident with X direction of the SPD ($\beta_y = 0$). In further simulations (Section 4.2.2.1) it will be shown that amplitude and direction of $\vec{\beta}$ depend on the relative position of the photonic wire and a laser beam.

More formal, a difference signal V_d is a two-dimensional (2D) function in SPD's coordinates, which depends on the relative position of the laser spot on the top facet of the photonic wire. And the detectivity is a gradient of this function, i.e. a vector field demonstrating for each point the direction of the greatest rate of increase of the function, and the magnitude of the vector is the slope of the function in vector's direction. The way to measure it quantitatively will be

presented later in a Section 4.2.4.

4.2.2.1 Simulation of the detectivity

This section is devoted to the numerical simulation of the arbitrary detectivity of motion using SPD technique described above. The goal of simulation is to calculate the detectivity vector for 2D grid of all relative positions of the laser and the photonic wire for different ratios between laser beam diameter and the top diameter of the photonic wire. Arbitrary detectivity means that only such factors like laser's beam size and its position with respect to the top facet of the photonic wire will vary to see, how they influence on the result. Calibration of the detectivity taking into account gains of SPD's amplifiers is obtained experimentally and is discussed in Section 4.2.4.

Laser intensity profile Laser has a profile of two-dimensional Gaussian, which is in more general way defined as

$$G(x,y) = h \cdot e^{-\left[a(x-x_0)^2+2b(x-x_0)(y-y_0)+c(y-y_0)^2\right]} \tag{4.1}$$

where parameters a, b, c are defined as

$$\begin{cases} a &= \frac{\cos^2(\theta)}{2\sigma_X^2} + \frac{\sin^2(\theta)}{2\sigma_Y^2} \\ b &= -\frac{\sin(2\theta)}{4\sigma_X^2} + \frac{\sin(2\theta)}{4\sigma_Y^2} \\ c &= \frac{\sin^2(\theta)}{2\sigma_X^2} + \frac{\cos^2(\theta)}{2\sigma_Y^2} \end{cases} \tag{4.2}$$

where $\sigma_{X,Y}$ are the standard deviations (sometimes called also the Gaussian RMS widths) along its axes, x_0 and y_0 are the coordinates of the Gaussian's center, θ is an angle of the rotation of the Gaussian's axes with respect to the axes of the coordinate system in clockwise direction, h is a height of the Gaussian, i.e. the value that it takes at the center.

Due to the spatial filter, which is mounted on the laser path (see Section 4.2.6.4 for the details), laser profile is expected to be centrally symmetric (which means that $\sigma_X = \sigma_Y \equiv \sigma$). The shape of the laser was checked visually. Attenuated laser beam was sent directly to the Watek WAT-920N camera, whose chip is sensitive to the infra-red light. It allowed us to visualize a laser beam profile on a TV screen and verify that it is symmetric within the measurement error. Thus, in this simulation laser beam profile is taken as centrally symmetric 2D Gaussian:

$$G(x,y) = h \cdot e^{-\left[(x-x_0)^2+(y-y_0)^2\right]/\left[2\sigma^2\right]} \tag{4.3}$$

Laser beam diameter is defined as a distance between 2 points at which laser intensity decreases at $1/e^2$ level from its maximum. Thus, for Gaussian beam it is equal to 4σ.

In these calculations integrated laser intensity is chosen to be equal 1 arbitrary unit of intensity. This fact defines height of the Gaussian via the expression

$$\int_{-\infty}^{\infty}\int_{-\infty}^{\infty} G(x,y)dxdy = 1 \tag{4.4}$$

Substituting (4.3) in (4.4) we obtain

$$h = \frac{1}{2\pi\sigma^2} \tag{4.5}$$

It also means that in these calculations all variables that have a dimension of intensity are expressed in the same arbitrary units of intensity.

Photonic wire's top contour Profile of the top of photonic wire is defined by the mask used during the structure's growth, which is expected to be circular. Nevertheless, for some real structures top facet is slightly elliptical. In the most general view an ellipse is described by

$$a\,(x-x_0)^2 + 2b\,(x-x_0)\,(y-y_0) + c\,(y-y_0)^2 = 1 \tag{4.6}$$

where parameters a, b, c are given in (4.2), x_0 and y_0 are the coordinates of the ellipse's center. Semi-minor and semi-major axes of ellipse are then equal to $\sqrt{2}\sigma_X$ and $\sqrt{2}\sigma_Y$.

Nevertheless, for these calculations we assumed a circular photonic wire's top contour, that simplifies (4.6) as

$$\frac{(x-x_0)^2 + (y-y_0)^2}{R^2} = 1 \tag{4.7}$$

where R is the top radius of the photonic wire.

In these calculations top radius of the photonic wire is set to be equal 1 arbitrary unit of length, so all variables that have a dimension of length are expressed in these arbitrary units. Thus, introducing r as a ratio between laser beam diameter and the top diameter of the photonic wire, we obtain $r = (4\sigma)/(2R)$. Since R is equal to 1 arbitrary unit of length for one fixed ratio between diameters of the laser beam and photonic wire we get a laser width $\sigma = r/2$ in arbitrary units of length.

Laser at the SPD For one fixed ratio between diameters of the laser beam and photonic wire we can calculate for each given relative position of the laser with respect to the center of photonic wire: how much light reflects to the SPD and how it is balanced between two parts of SPD. Sketches on the Figure (4.8) demonstrate both a top view image of the sample and a top view image of the SPD surface for one given relative position of the laser with respect to the center of photonic wire's top facet. It is clearly shown that only a part of the laser light, which shines the top facet of the photonic wire, reflects to the SPD. Thus, we can introduce a photonic wire's top profile function in the coordinate system associated with its center as

$$T(x,y) = \begin{cases} 1 & if\ x^2 + y^2 \le 1 \\ 0 & otherwise \end{cases} \tag{4.8}$$

Introducing the sizes of the SPD L_X and L_Y as it is shown on the Figure 4.8b we get an expression for the symmetric 2D Gaussian laser beam's profile, whose center is coincident with the center of SPD:

$$G(x,y,r) = \frac{2}{\pi r^2} \cdot e^{-2\left[x^2 + (y - L_Y/2)^2\right]/r^2} \tag{4.9}$$

There are several notations used further in the simulation:

- I_A (I_B) - the integrated intensity of the laser light on the part A (B) of the SPD;
- $I_{tot} = I_A + I_B$ - the integrated intensity of the laser light on the SPD (total intensity);

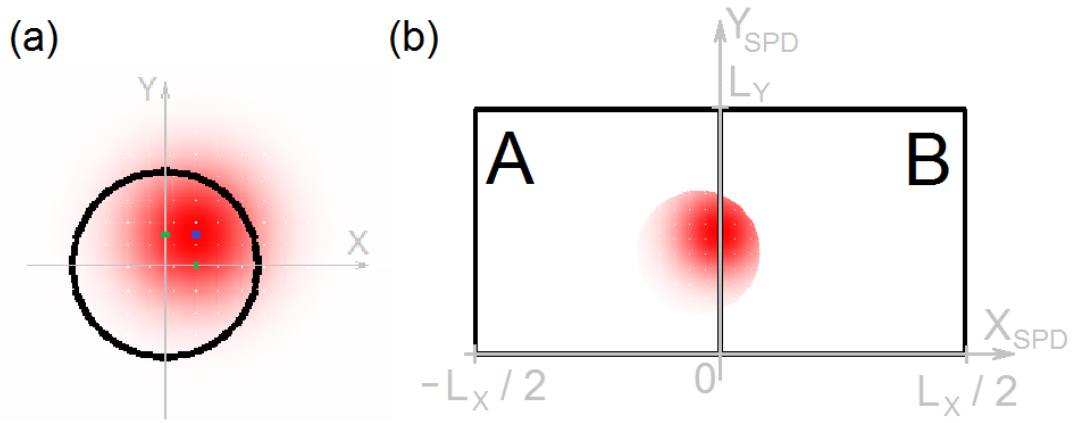

Figure 4.8: (a) Sketch demonstrating a top view image of the sample. Black circle shows photonic wire's top facet's contour. 2D Gaussian laser beam is shown by red color. Color brightness is proportional to the intensity of the laser. Violet dot demonstrates central position of the laser beam. Green ticks at the axes shows the relative displacement of the laser with respect to the center of photonic wire. (b) Sketch demonstrating a top view image of the SPD. Two parts of the SPD are marked as A and B. Laser is initially aligned with the center of SPD, but only a part of the laser light reflects to the SPD by the photonic wire. This amount depend on the relative displacement of the laser with respect to the center of photonic wire.

- $I_d = I_A - I_B$ - difference in integrated intensity of the laser light between parts A and B of the SPD;
- $\vec{\beta}$ - detectivity vector, whose components β_x and β_y are defined as directional derivatives of difference signal I_d along X and Y directions of SPD.

It is finally possible to give explicit expressions for the integrated intensities

$$\begin{cases} I_A(x,y,r) & = \int_0^{L_Y} \int_{-L_X/2}^{0} G(x,y,r) \cdot T(x-x', y-y') dx' dy' \\ I_B(x,y,r) & = \int_0^{L_Y} \int_{0}^{L_X/2} G(x,y,r) \cdot T(x-x', y-y') dx' dy' \\ I_{tot}(x,y,r) & = I_A(x,y,r) + I_B(x,y,r) = \int_0^{L_Y} \int_{-L_X/2}^{L_X/2} G(x,y,r) \cdot T(x-x', y-y') dx' dy' \\ I_d(x,y,r) & = I_A(x,y,r) - I_B(x,y,r) \end{cases} \tag{4.10}$$

where x and y are the coordinates of the relative position of centers of the laser beam and photonic wire's top facet, $G(x,y,r)$ is a laser intensity profile defined by (4.9), $T(x,y)$ is a profile of the photonic wire's top defined by (4.8), L_X and L_Y are the sizes of the SPD along its X and Y axes respectively, r is a ratio between laser beam diameter and the top diameter of the photonic wire.

It should be mentioned that in the simulation a dead zone of SPD is not taken into account. It is seen from the fact that integration by x includes 0 as a bound for both $I_A(x,y)$ and $I_B(x,y)$. Nevertheless, it does not affect a lot on the quality of the result, because a dead zone of the SPD is only 20 μm size, whereas a laser beam size (at the SPD surface) used in experiments is about 500 μm.

Dependence on the position of laser beam with respect to the top facet of photonic wire We fix the Probe laser beam diameter to be equal the top diameter of the photonic wire (r = 1 = 100%) and calculate 2D matrices $I_{A,B}(x, y)$ (where x and y are relative distances between center of the photonic wire's top facet and center of Gaussian laser beam on it) as well as $I_{tot}(x, y)$ and $I_d(x, y)$ using formulas from (4.10). The results are represented as pseudo-color maps on the Figure 4.9.

The 2D map of detectivity is then calculated using finite difference method for the expressions $\beta_{x[y]}(x, y) = \frac{\partial I_d(x,y)}{\partial x[y]}$ and $\vec{\beta}(x, y) = (\beta_x\ \beta_y)^T$. On the Figure 4.10 components of detectivity vector are represented as pseudo-color maps, and detectivity itself is shown as a vector field.

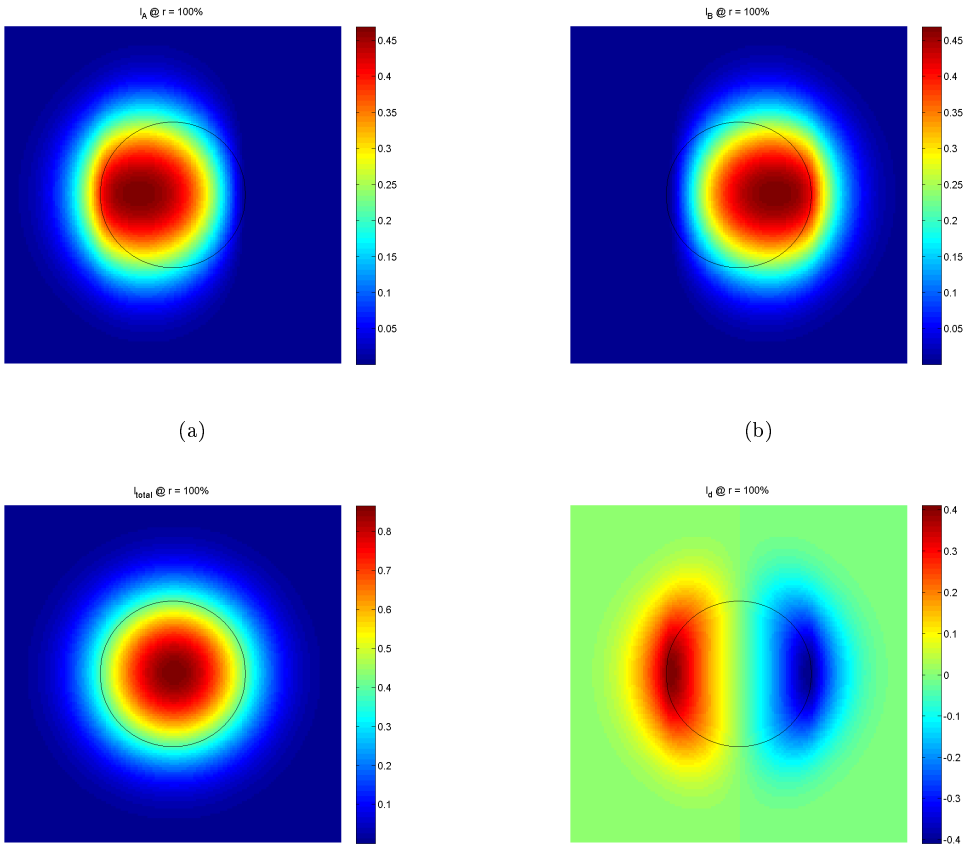

Figure 4.9: Simulation of (a,b) integrated laser intensity on the A (B) part of SPD (c) total laser intensity on the SPD (d) difference in intensity between A and B part of SPD in case when the Probe laser beam diameter is equal the top diameter of the photonic wire. Black contour on each plot demonstrates the edge of the photonic wire's top facet.

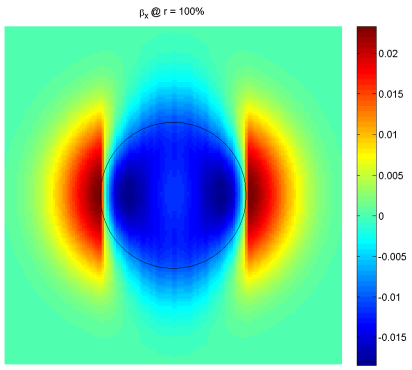

(a)

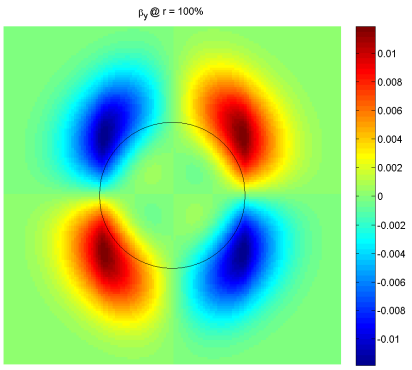

(b)

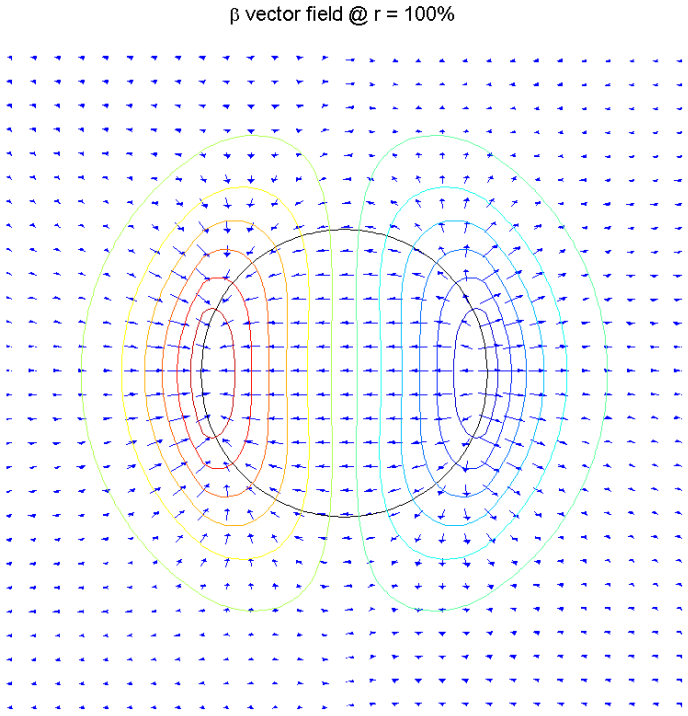

(c)

Figure 4.10: Calculation from the results of simulation of (a) β_x (b) β_y (c) $\vec{\beta}$. On (c) color contour demonstrates $I_d(x, y)$ map. Black contour on each plot demonstrates the edge of the photonic wire's top facet. Probe laser beam diameter is equal the top diameter of the photonic wire.

Dependence on the ratio between laser beam size and top diameter of photonic wire It is also interesting to compare the detectivity for different ratio between laser beam size and top diameter of photonic wire. Detectivity at $y = 0$ (central horizontal cross-section) is always coincident with X axis of SPD due to the symmetry of the photonic wire and the laser with respect to the Y axis of SPD. It means that magnitude of the sensitivity is equal to absolute value of the sensitivity along the X axis of SPD ($\left|\vec{\beta}(x,0)\right| = |\beta_x(x,0)|$). That's why it is very convenient to demonstrate on $\beta_x(x,0)$: how the detectivity changes along one chosen direction for different r. Such dependencies are shown on the Figure 4.11. We can see that when the laser size is small compare to the photonic wire's top facet our motion detection technique is only sensitive when the laser is placed close to the edge of photonic wire. This is understandable, because at such points, when structure oscillates, it either goes out of the laser beam spot (reflected integral intensity drops dramatically) or goes under the laser beam spot (reflected integral intensity dramatically increases); whereas when laser is placed at the center of the photonic wire, structure's oscillations change the intensity distribution very little.

The central point (0,0), i.e. when laser is placed at the center of the photonic wire, is a very specific point for the experiment. In the Section (4.2.1.3) it was shown that the Probe laser is very noisy. Thus, to minimize the structure's oscillations induced by the Probe laser noise, it should be placed at the center of the photonic wire. Dependence of the detectivity on the ratio between diameters of laser and structure's top facet for the central point is demonstrated on the Figure 4.11b. We can see that, when the laser diameter is smaller then top diameter of the structure, increase of the beam size also increases the detectivity at the central point, but decreases the maximal reachable detectivity. When laser size is about 1.4 times bigger than structure's diameter (r = 1.4), central point becomes a point of maximum detectivity. Further increase of the beam size decreases the detectivity, because it decreases difference in laser light intensity between two adjacent points. In limit case, when laser beam diameter tends to infinity, the detectivity tends to zero for any laser position.

4.2.3 Identification of laser beam diameter

As a consequence of the detectivity simulations from the previous section, we can mention that $I_{tot}(x,y,r)$ from (4.10) depends on r, which is a ratio of diameters of the laser and photonic wire. Thus, measuring experimentally Total Intensity (TI) map ($I_{A+B}(x,y)$), we can identify a real laser beam diameter.

Used SPD has no 'A+B' output, but it has independent 'A' and 'B' outputs. So whenever we need a Total Intensity map, we measure 2D maps for A and B channels and then sum them.

On the Figure 4.12 experimental map is shown together with its fit. Data are obtained for the structure with 5.5 μm top diameter. Value of r from a fit is 0.75, which means that laser has a diameter of 4.13 μm.

Besides, from TI map it is possible to define the position of the photonic wire's center with respect to the scanning range. This possibility will be widely used in further experiments to demonstrate the position of the structure's top facet.

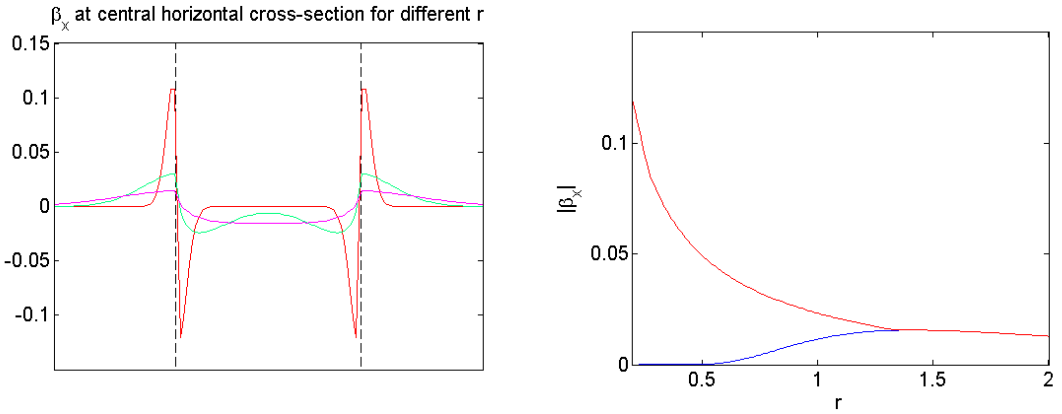

(a) (b)

Figure 4.11: (a) Detectivity magnitude along central horizontal cross-section, when ratio between laser beam diameter and the top diameter of the photonic wire is equal to 0.2 (red), 0.8 (green) and 1.4 (magenta). Dashed lines demonstrate the edges of the photonic wire. (b) Blue trace demonstrates the dependence of the detectivity at the central point on the ratio between laser beam size and top diameter of photonic wire (r); red - maximum value of $\beta_x(x, 0)$.

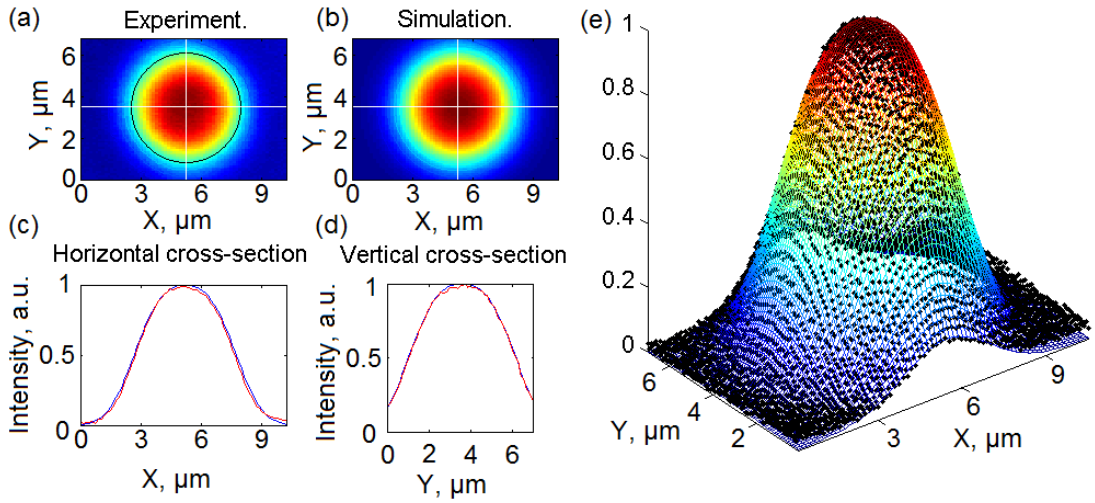

Figure 4.12: (a) Experimental 2D map of the sum of signals from 'A' and 'B' channels of SPD obtained for the structure with top diameter of 5.5 μm. Black circle demonstrates the contour of the structure's top facet. Its center was defined using fit of the data. (b) Fit of the experimental data with a model for $I_{tot}(x, y, r)$ from (4.10). Horizontal and vertical central cross-sections are shown on the plots (c) and (d) respectively. Red trace corresponds to experimental data, blue - model fit. (e) Visualization of experimental data (black points) and its fit (colored mesh) in 3D.

4.2.4 Calibration of oscillations amplitude

To make the calibration of the amplitude of the signal from SPD (in Volts) on the amplitude of the displacement of photonic wire's top (in the units of length, e. g. nm) we could translate the whole sample with the experimental structure by relatively small known (or easily measurable) distance and measure the amplitude of the signal to have a value of β. Nevertheless, our sample is mounted in a heavy cryostat (see Section 4.2.6.3) that makes a realization of its small displacement to be a complicated task. Besides, there is no much space inside the cryostat, so it's also not possible to put an adjustable stage for a sample inside. However, displacement of the experimental sample is analogous to displacing a microscope objective before it. From the SPD's point of view displacement of the objective in any direction at a certain distance is equivalent to the displacement of observed object of the same distance in the opposite direction.

Thereby, we mounted the microscope objective on a 3-axes translation stage Nanomax-312D/M (not shown on the scheme of the experimental setup), which has 3 level of precision of position tuning along each axis: the coarse manual adjustment in a range of 4 mm with 10 μm precision, the fine manual adjustment in a range of 300 μm with 1 μm precision, and finally open-loop piezo-adjustment in a 20 μm range with accuracy of 20 nm. Nevertheless, utilization of open-loop technology limits the position repeatability at about 500 nm. This piezostage is used for precise control of lasers' focus (Z axis), and to displace laser beam with respect to the photonic wire (XY plane).

Using a home-made software we run an XY point-by-point scan. For every point of 2D scan we measure a LF 'A-B' signal (see Figure 4.13). Once its done, we compute the gradient vector field of detectivity. For the simple demonstration on the top right image the difference signal along central horizontal cross-section is shown. Its derivative is shown on the right down image. These values show directly the detectivity, because (as it was shown before) Y-projection of detectivity for all points on central horizontal cross-section is equal to 0.

Obtained in that way (using LF difference output of SPD) values for the detectivity must be scaled by ratio between HF and LF gains of SPD (see details in Section 4.2.1.2) to determine the detectivity of the structure's oscillations via HF difference output of SPD. Thus, the detectivity depends on the frequency of oscillations.

Now we can roughly estimate, structure's motion of which order of magnitude it is possible to detect using this experimental technique. Value of detectivity obtained via LF channel is about 10 mV/μm. Gain ratio at f $\sim$ 500 kHz is about 1500, which means that oscillations of 15 pm amplitude will produce a signal of 225 μV. Assuming a Probe laser noise at the same frequency to be equal 100 pW/Hz (see Figure 4.6c), we get a parasitic signal of about 224 μV, if measured with 10 Hz bandwidth. To reduce the parasitic signal and improve the detection at small amplitudes, it is required to use better Probe laser. There is a possibility to reduce laser's noise by a factor of 30, if the laser will be shot noise limited (see Figure 4.6c).

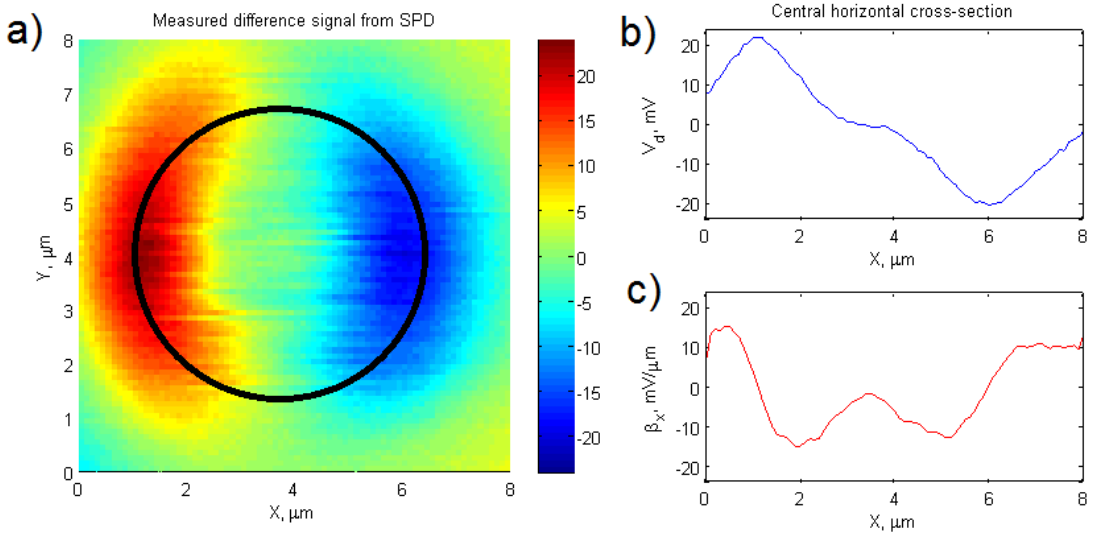

Figure 4.13: (a) Experimental 2D map of voltage at low frequency difference output of SPD for the photonic wire with top diameter of 5.31 μm. Black circle demonstrates the edge of the structure's top facet. (b) Central horizontal cross-section (white line on the previous plot) of the difference signal. (c) Calculated low-frequency detectivity.

4.2.5 Optimization of oscillations' detection

As it was mentioned before, the photonic wire has two linear orthogonal eigenmodes. It means that maximum detectivity for one mode can be reached only when the second mode can not be detected at all.

To manipulate the direction of the photonic wire's oscillations with respect to the orientation of the SPD a truncated right-angle prism (Dove prism) is used in our setup and mounted in between of the objective and an imaging lens (the one before SPD). A laser beam coming into the prism has one total internal reflection from the bottom face before going out. Therefore, image passing through the prism goes out inverted (Figure 4.14a). Rotation of the dove prism along its longitudinal axis by some angle rotates the image by twice this angle (Figure 4.14b). Thus, from the photonic wire's point of view we rotate the SPD in order to obtain desirable mutual position of detectivity vector and directions of its mechanical modes. There are two main cases:

1. Realization of the best possible detection of one mode. In this case its direction should be coincident with the direction of detectivity vector. Consequently, the second mode will be not detectable at all.

2. Realization of the possibility to detect both modes. In this case direction of detectivity vector is placed in between of two modes, which are orthogonal.

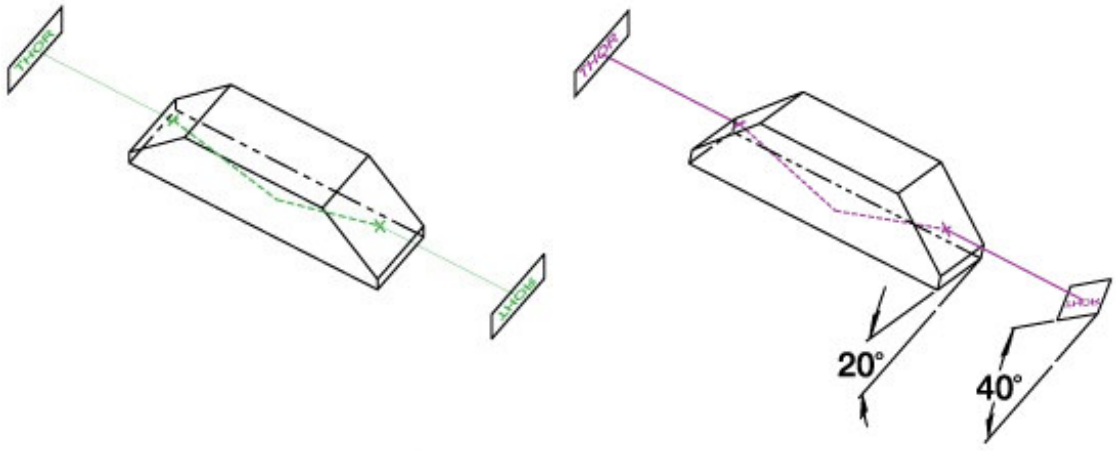

(a) (b)

Figure 4.14: Sketch demonstrating the operation principle of Dove prism. (a) non-rotated Dove prism. (b) rotated Dove prism. [55]

4.2.6 Elements of experimental setup

4.2.6.1 Telescopic system

To adjust the position of probe laser on the top of the photonic wire we use a tiltable mirror. This mirror has two closed-loop piezo-elements allowing to tilt mirror from 0 to 2 mrad vertically and horizontally applying external voltage from 0 to 10 V via a piezo-controller. Tilt of the mirror by some angle tilts the laser beam by twice this angle. Changing the propagation angle of the parallel laser beam incident to the objective, we change the position of the laser spot on the sample. The angle of mirror's tilt is proportional to the laser's spot displacement in case if the angle is small. Nevertheless, this method require to be complemented by a telescopic system (Fig. 4.15b) to change the angle of the incoming laser beam at the entrance pupil of the microscope objective without changing its position. It allows us to provide larger tilt angle and to avoid hitting the side of the objective by some part of the laser beam (or even quit out of the objective's entrance as it is shown on the Fig. 4.15a). We used symmetric telescopic system (also known as 2f-2f setting, that means that the focal distances of both lens are equal) with f = 400 mm.

4.2.6.2 Objectives

Depending on the photonic wire's top diameter different Probe laser beam size is required to perform the optimal motion detection (See Section 4.2.2.1). To change a laser beam size we used two different objective:. first is a Olympus LMPLan IR objective with a numerical aperture (NA) of 0.4, focal distance (FD) of 9 mm and working distance (WD) of 8.1 mm, the second is a ZEISS LD Plan NEOFLUAR objective with NA = 0.75, FD = 2.2 mm, WD = 1.7 mm.

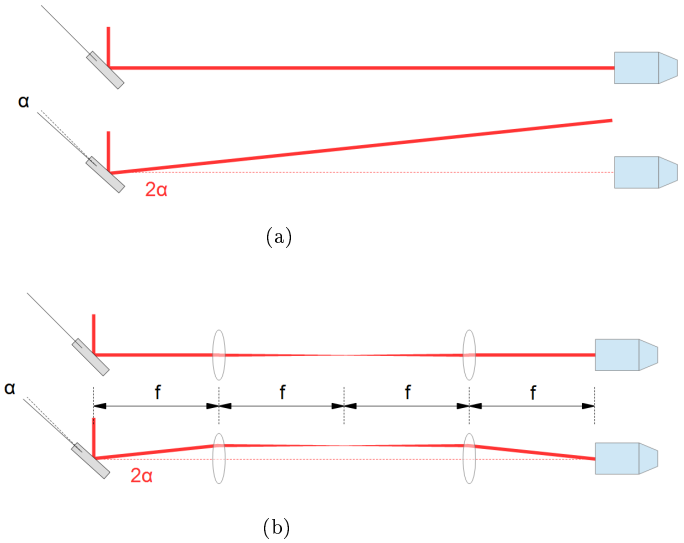

Figure 4.15: Sketch demonstrating manipulations with a laser beam by (a) tiltable mirror only and (b) with a telescopic system.

4.2.6.3 Sample holder

Motion amplitude depends also on the quality of the vacuum around the investigated structure. For that reason and also to be able to perform the measurements at low temperatures the experimental sample was placed into the continuous helium flow optical cryostat from Oxford Instruments Company. Liquid helium storage tank connects with a cryostat via a transfer tube, which allows to collect a gas and send it back to the recovery system.

Circular entrance window of the cryostat has a diameter of 10 mm and thickness of 0.5 mm. The cryostat is mounted on a 2-axes translation stage (not shown on the scheme of the experimental setup) that provides a coarse adjustment of sample's position with respect to the microscope objective in a range of several mm with precision of 10 μm .

4.2.6.4 Optical sources

Two different lasers are used in this experiment.

As a Probe laser (laser used for the motion detection) we used a continuous-wave (CW) diode laser delivering the laser light through the optical fiber produced by THORLABS. The laser is BL976-PAG700 controlled via CLD1015 driver. Maximal laser output power is about 700 mW that allows us to have as much light on the SPD as it is required to obtain the maximal sensitivity without saturation of the device. The wavelength of the laser is about 976 nm that corresponds to an energy below the bandgap of GaAs.

For the optical actuation of the photonic wire's motion a Toptica DL100 Pro laser is used (so-called Pump laser). It is a CW laser with tunable wavelength from 910 to 985 nm. In our case the wavelength of 920 nm was chosen, firstly, so that the energy of the laser is below the bandgap of GaAs, secondly, to provide a possibility to reject this laser but not the other from the SPD using a long-pass wavelength filter. Maximum laser power at the output is about 40

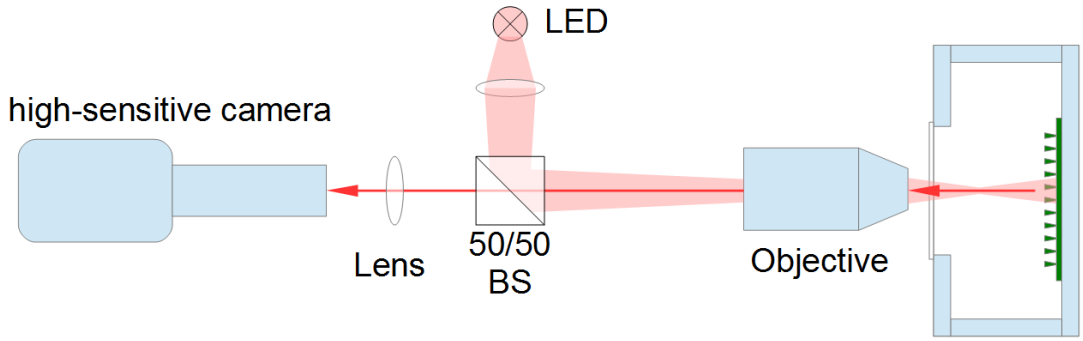

Figure 4.16: Sketch representing operation of the visualization system.

mW.

For each laser source an optical isolator is set up after the laser light output (not shown on the scheme of the experimental setup) to shield the source from the adverse back reflection of laser light, which may lead to instabilities (intensity noise) in a laser beam or even damage the light source. Optical isolator is a magneto-optic device consisting from two polarizers with angle of 45 degree between their axes and a Faraday rotator, which rotates the polarization of incoming beam by 45 degree. Thus, light can be transmitted in one way but not in the other.

Besides, each laser passes through a pinhole-based spatial filter, which allows to correct an elliptical cross-section of the laser beams. Such filter consist of 2 lenses and a pinhole mounted between them. Distance from each lens to the pinhole is equal to their focal distances. Parallel laser beam is focused on the pinhole by the first lens. Focal distance and a size of a pinhole are chosen to cut off all non-perfectness of the beam. Second lens recovers a parallel laser beam. Choosing a focal distance of the second lens we can define the diameter of the laser beam. We used a system of 10 cm lens, 20 μm pinhole and again 10 cm lens for the Pump laser; and a system of 5 cm lens, 20 μm pinhole and 3 cm lens for the Probe laser.

4.2.6.5 Visualization system

To be able to observe in a real time the experimental sample with the investigated structure and a relative laser spot position on its top facet we used a visualization system consisting from infrared (IR) LED with wavelength at peak emission of 935 nm and a Watek WAT-920N camera (sketch of the Figure 4.16), whose chip is sensitive to IR light.

The LED is used to lit as uniformly as possible the sample. It emits a quickly diverging light beam, which is delivered to the sample through 2 lens system (the second of which is the objective). The LED is mounted not in a focus of the first lens and in such ways turns to be unfocused at the focal plane of the objective, where the sample is located.

The same way as with SPD we image the sample plane on the camera's chip using a two lens system (one of which is the objective and the other mounted before the camera). The image from the camera is transmitted on a TV screen.

4.2.6.6 Software and computer control

To perform measurements we used a software that allows us to control the positions of the objective piezostage and tiltable mirrors for both lasers via National Instruments NI 6363 USB card. This card has 16 bit DAC and ADC converters, 4 analog output and 16 analog input.

Our software allows us to define a 2D matrix of all Pump laser positions with respect to the top of the photonic wire with specified number of experimental points in X-Y plane, and then make an independent point-by-point measurements of the system's response on external influence.

4.2.6.7 Temperature controller

The ITC 601 proportional–integral–derivative (PID) temperature controller is used to measure current temperature and to control the internal heater of the cryostat, which allows to adjust the temperature in a range from 5 K to about 350 K. Accuracy of temperature measurement is 0.1 K.

4.3 Motion excitation

A method of motion excitation by a piezo electrical transducer glued at the back of the sample holder was described in the work [19]. In the present work the motion of the investigated structure is excited optically with a second laser added to the experimental setup (Fig. 4.17).

To excite the motion of the photonic wire laser intensity is modulated by analog acousto-optic modulator (AOM) at the mechanical resonance frequency. The amplitude of excited motion on each chosen frequency is determined by Vector Network Analyzer (VNA), as it was already presented in the Section 4.2.1.2. In the case when the driving frequency coincides with the mechanical frequency of the wire VNA detects the resonance, which is at about 500 kHz for typical photonic wire.

If the light from Pump laser reaches the SPD it brings a strong parasitic signal, because the amplitude of modulation of its intensity is much higher then the modulation of Probe laser intensity caused by oscillation of the photonic wire. To cut off this light linear polarization of the Pump laser set up to be perpendicular to linear polarization of the Probe laser. It allows us to use a polarizing beamsplitter (PBS) to reject the Pump laser light. Nevertheless, the rejection ratio of PBS is about 200, which is not enough to filter out all light from Pump laser, so in addition to it Pump and Probe lasers are separated by wavelength that allows us to use a long-pass wavelength filter ($\lambda_{cut-off}$ = 950 nm), which transmit the light from the Probe laser (λ = 976 nm) but not from the Pump laser (λ = 920 nm), before the SPD (not shown on the experimental setup scheme). Its rejection ratio is about 1000 that makes a Pump laser not detectable by SPD.

To investigate how the interaction of the Pump laser light and photonic wire depends on laser's position with respect to the top of the structure, we used a mirror that can be tilted vertically and horizontally in a range of 500 μrad by applying an external voltage from 0 to 150 V to each of two embedded piezo-elements. Using an external voltage source that gives a voltage from 0 to 150 V on its output proportionally to the voltage from 0 to 10 V on its input, we were able to manipulate this mirror via computer by the way explained before for the Probe laser.

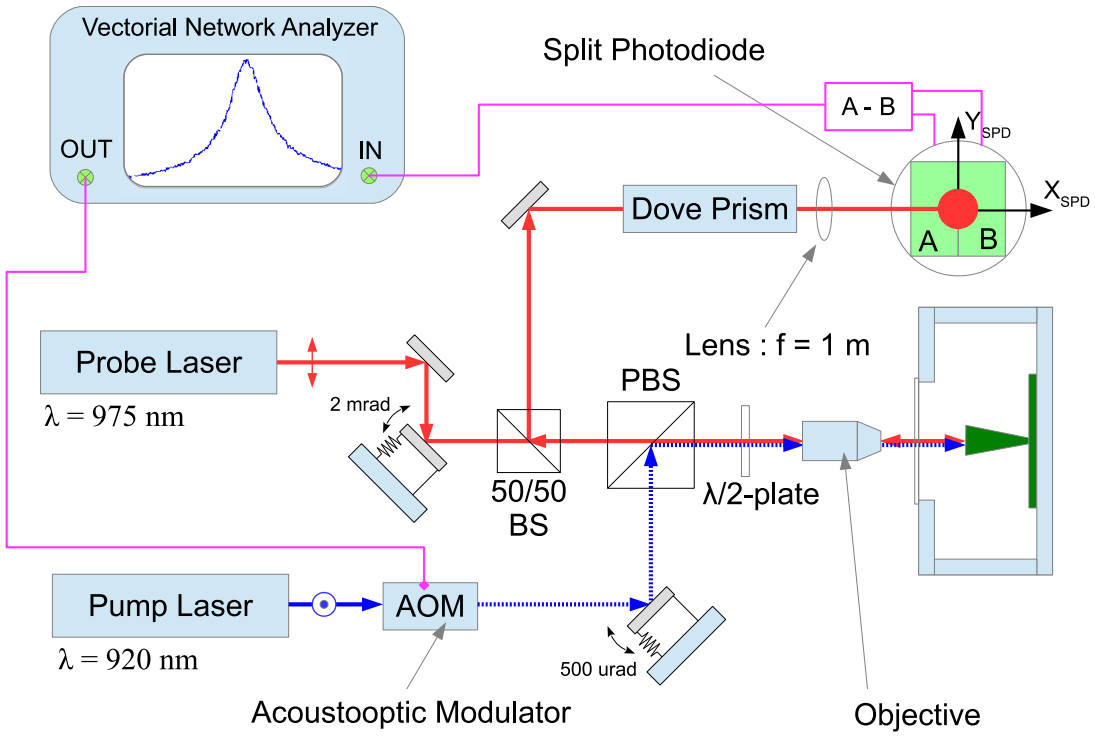

Figure 4.17: Schematic view of the experimental setup for detection of optically induced oscillations of μm-scale structures.

To investigate the dependence of the Pump laser polarization on the excitation of the mechanical motion of the photonic wire we mounted a half-wave plate (λ/2-plate) in between the PBS and the objective. Rotation of the λ/2-plate by some angle rotates the polarization of both lasers by twice this angle. Thereby, we can choose the Pump laser polarization interacting with a photonic wire. Reflected lasers' beams pass through λ/2-plate again and recover their initial polarizations. Thus, Probe laser pass through PBS, while Pump laser is rejected.

4.3.1 Physics of induced motion

Several physical effects appear in light-matter interaction and affect the amplitude of the oscillations. These are effects caused by photons' momentum: radiation pressure, when photons are reflected from the structure, and gradient (dipole) force, when photons are deviated. As you can see from the Figure 4.18, both are trying to bend the wire in the same way. So, in simple words, laser attracts the wire.

Since the photonic wire is fixed at one end and free at the other, we consider its displacement as a rotation under the influence of torque appearing in the interaction with the laser beam. We can describe its behavior as a one-dimensional harmonic oscillator using Newton's second law.

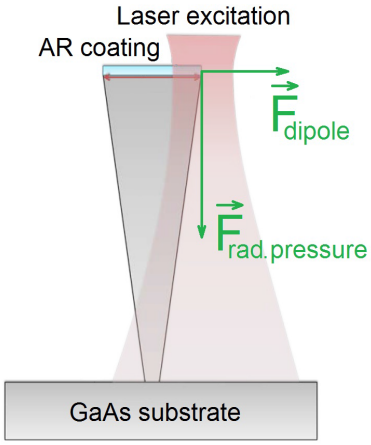

Figure 4.18: Sketch, demonstrating the forces appearing in light-matter interaction as a result of photons' momentum transfer.

The viscous friction force is directed against the speed of movement and is directly proportional to this speed via friction coefficient α.

$$M = I \cdot \frac{d^2\theta(t)}{dt^2} = -\left[C \cdot \theta(t) + \alpha \cdot \frac{d\theta(t)}{dt}\right] + M_0 \cdot \cos(\omega t + \delta) \tag{4.11}$$

where M_0 - is a torque appearing in the interaction with the laser beam, I - is a moment of inertia, C - is a coefficient of restitution, ω- is a frequency of laser's modulation.

We introduce new variables to simplify the equation $\omega_0 = \sqrt{C/I}$, $N_0 = M_0/I$ and $\gamma = \alpha/(2I)$. Without loss of generality, we can set the phase of external impact (δ) at 0. Thus equation has a view:

$$\theta''(t) + 2\gamma\theta'(t) + \omega_0^2\theta(t) = N_0 \cdot \cos(\omega t) \tag{4.12}$$

General solution (solution for $N_0 = 0$) of the differential equation has a structure:

$$\theta_G(t) = D_1 \cdot e^{\lambda_1 t} + D_2 \cdot t^{\delta(\lambda_1 - \lambda_2)} \cdot e^{\lambda_2 t} \tag{4.13}$$

where $\lambda_{1,2}$- are roots of the characteristic equation $\lambda + 2\gamma\lambda + \omega_0^2\lambda = 0$ and $\delta(x)$ is the following function:

$$\delta(x) = \begin{cases} 1 & if\, x = 0 \\ 0 & otherwise \end{cases} \tag{4.14}$$

Thus we have several possible solutions depending of the values of γ and ω_0:

$$\theta_G(t) = e^{-\gamma t} \cdot \begin{cases} D_1 \cdot e^{\sqrt{\gamma^2 - \omega_0^2}t} + D_2 \cdot e^{-\sqrt{\gamma^2 - \omega_0^2}t} & if\, \gamma > \omega_0 \\ D_1 + D_2 \cdot t & if\, \gamma = \omega_0 \\ D_1 \cdot \cos\left(\sqrt{\omega_0^2 - \gamma^2}t\right) + D_2 \cdot \sin\left(\sqrt{\omega_0^2 - \gamma^2}t\right) & if\, \gamma < \omega_0 \end{cases} \tag{4.15}$$

We can see that any solution tends to 0 when $t \to \infty$ because of the term $e^{-\gamma t}$. It means that general solution doesn't contribute in the solution of forced oscillations.

A particular solution of the differential equation with a $\cos(\omega t)$ at the right side has a structure:

$$\theta(\omega, t) = D_1 \cdot \cos(\omega t) + D_2 \cdot \sin(\omega t) \tag{4.16}$$

where $D_{1,2}$ - are the constants with a time.

Physically it means that forced oscillations occurs at the frequency of the excitatory force. Putting (4.16) in equation (4.12) we obtain that

$$\theta(\omega, t) = \frac{N_0}{\left(\omega_0^2 - \omega^2\right)^2 + (2\gamma\omega)^2} \left[\left(\omega_0^2 - \omega^2\right) \cdot \cos(\omega t) + 2\gamma\omega \cdot \sin(\omega t)\right] \equiv A(\omega) \cdot \cos(\omega t + P(\omega)) \tag{4.17}$$

where

$$\begin{cases} A(\omega) & = \frac{N_0}{\sqrt{\left(\omega_0^2 - \omega^2\right)^2 + (2\gamma\omega)^2}} \\ P(\omega) & = \operatorname{arctan2}\left(\{-2\gamma\omega\}, \left\{\omega_0^2 - \omega^2\right\}\right) \end{cases} \tag{4.18}$$

Function arctan2(x) is introduced in Appendix A on page 111.

A quality factor (Q) of such resonant excitation by definition is equal to $\omega_0/(2\gamma)$. From (4.18) we can conclude that amplitude at zero frequency is equal to $A(0) = N_0/\omega_0^2$, whereas amplitude at fundamental frequency of the oscillator is $A(\omega_0) = N_0/(2\gamma\omega_0) = A(0) \cdot Q$, i. e. Q times higher. Maximum of amplitude is attained at the frequency $\omega_{MAX} = \omega_0\sqrt{1 - 1/(2Q^2)}$ and is equal to $A_{MAX} = A(\omega_0)/\sqrt{1 - 1/(4Q^2)}$. However, for the structures with high Q these values are very close to ω_0 and $A(\omega_0)$ respectively. At the same time, phase changes from 0 to $-\pi$ passing though the resonance, and at ω_0 is always equal to $-\pi/2$. Quality factor only changes the steepness of the phase change: the higher Q, the sharper transition. On the Figure 4.19 spectra for the amplitude and phase are shown in arbitrary units for 3 different values of quality factor.

To summarize, measuring amplitude and phase spectra we can find amplitude of the structure's motion and the force causing this motion. Moreover, it is easier to study effects appearing in light-matter interaction in dynamic mode, than in static mode, because it leads to Q times bigger displacement amplitude, which is easier to measure.

4.3.2 VNA measurements

A VNA measures $A(\omega)$ and $P(\omega)$ spectra that allows us to find all parameters in initial equation. Nevertheless, in real experiment we have a background noise that has a component on the same frequency ω but it can have a different phase. Thus, measured signal is covered by:

$$S(\omega, t) = A(\omega) \cdot \cos(\omega t + P(\omega)) + b \cdot \cos(\omega t + \varphi) \equiv \widetilde{A}(\omega) \cdot \cos\left(\omega t + \widetilde{P}(\omega)\right) \tag{4.19}$$

where b - is the amplitude of the noise at that frequency and φ - is its phase.

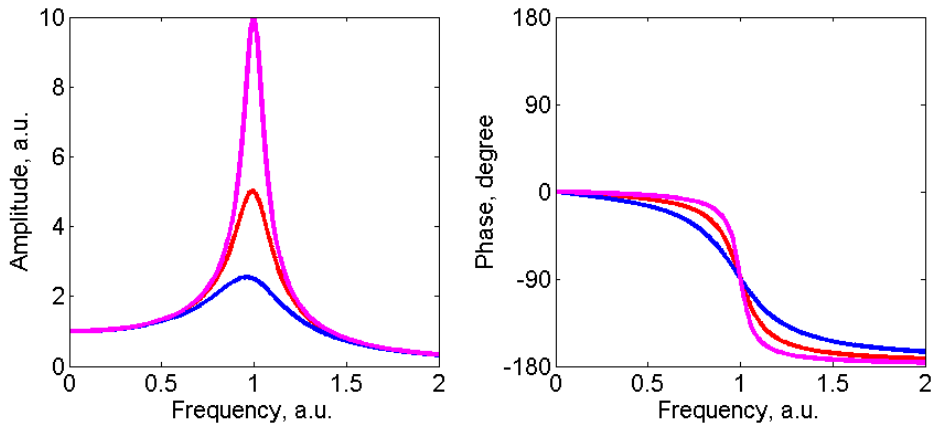

Figure 4.19: Spectra of the amplitude (left) and phase (right) of the mechanical resonance. Values of the amplitude are given in arbitrary units, where 1 a.u. corresponds to the static (frequency is equal to 0) displacement amplitude. Values of the frequency are given in arbitrary units, where 1 a.u. corresponds to the fundamental frequency of the oscillator. Three traces belong to different values of quality factor: Q = 2.5 (blue), 5 (red) and 10 (magenta).

$$\begin{cases} \widetilde{A}(\omega) & = \sqrt{b^2 + \frac{N_0^2 + 2bN_0\left[\left(\omega_0^2-\omega^2\right)\cdot\cos(\varphi) - 2\gamma\omega\cdot\sin(\varphi)\right]}{\left(\omega_0^2-\omega^2\right)^2+(2\gamma\omega)^2}} \\ \widetilde{P}(\omega) & = \arctan2\left(\left\{-2\gamma\omega N_0 + b\left[\left(\omega_0^2-\omega^2\right)^2+(2\gamma\omega)^2\right]\sin(\varphi)\right\},\right. \\ & \qquad \left.\left\{\left(\omega_0^2-\omega^2\right)N_0 + b\left[\left(\omega_0^2-\omega^2\right)^2+(2\gamma\omega)^2\right]\cos(\varphi)\right\}\right) \end{cases} \tag{4.20}$$

Origin of such background signal can be electrical interference or scattered laser light, reaching the detector. In case if we have several such parasitic signals, they can be still described by one term added in equation (4.19). Consider two background noises and show that they can be represented as one united noise:

$$S_{BG}(\omega,t) = b_1\cdot\cos(\omega t+\varphi_1) + b_2\cdot\cos(\omega t+\varphi_2) \equiv b(\omega)\cdot\cos(\omega t+\varphi(\omega)) \tag{4.21}$$

where

$$\begin{cases} b(\omega) & = \sqrt{b_1^2+b_2^2+2b_1b_2\cdot\cos(\varphi_1-\varphi_2)} \\ \varphi(\omega) & = \arctan 2\left(\{b_1\cdot\sin(\varphi_1)+b_2\cdot\sin(\varphi_2)\},\{b_1\cdot\cos(\varphi_1)+b_2\cdot\cos(\varphi_2)\}\right) \end{cases} \tag{4.22}$$

It can be also generalized in case of any number of background signals.

Besides, a VNA does not receive the signal back instantaneously. There are delays connected mostly with response time of electronics. It means that there is an overall phase shift of the signal (ψ), thus:

$$S(\omega,t) = A(\omega)\cdot\cos(\omega t+P(\omega)+\psi) + b\cdot\cos(\omega t+\varphi+\psi) \equiv \widetilde{\widetilde{A}}(\omega)\cdot\cos\left(\omega t+\widetilde{\widetilde{P}}(\omega)\right) \tag{4.23}$$

A phase delay does not affect on the amplitude of the signal but on its phase. Resulting phase is:

$$\begin{aligned}\widetilde{\widetilde{P}}(\omega) &= \arctan 2\left(\left\{N_0\left[\left(\omega_0^2-\omega^2\right)\cdot\sin(\psi)-2\gamma\omega\cdot\cos(\psi)\right]+b\left[\left(\omega_0^2-\omega^2\right)^2+(2\gamma\omega)^2\right]\sin(\varphi+\psi)\right\},\right.\\ &\left.\left\{N_0\left[\left(\omega_0^2-\omega^2\right)\cdot\cos(\psi)+2\gamma\omega\cdot\sin(\psi)\right]+b\left[\left(\omega_0^2-\omega^2\right)^2+(2\gamma\omega)^2\right]\cos(\varphi+\psi)\right\}\right) \qquad (4.24)\end{aligned}$$

It is not very convenient for us to use $\widetilde{\widetilde{P}}(\omega)$ spectrum for a fit, because values such as $\varphi_1=-\pi+\delta$ and $\varphi_2=\pi-\delta$ (where δ- is some very small angle) physically realize almost similar configuration because phase is 2π-periodic, whereas a least-squares fitting procedure considers these values as distant and calculates a wrong deviation. To get rid of the problem we can use $\cos\left(\widetilde{\widetilde{P}}(\omega)\right)$ or $\sin\left(\widetilde{\widetilde{P}}(\omega)\right)$ for a fit. But there is a better approach using real and imaginary components of the signal allowing to simplify model functions. Consider the following:

$$\begin{aligned}S(\omega,t) &= \widetilde{\widetilde{A}}(\omega)\cdot\cos\left(\omega t+\widetilde{\widetilde{P}}(\omega)\right)=\Re\left\{\widetilde{\widetilde{A}}(\omega)\cdot e^{i\left[\omega t+\widetilde{\widetilde{P}}(\omega)\right]}\right\}=\\ &= \Re\left\{\widetilde{\widetilde{A}}(\omega)\cdot e^{i\widetilde{\widetilde{P}}(\omega)}\right\}\cdot\Re\left\{e^{i\omega t}\right\}-\Im\left\{\widetilde{\widetilde{A}}(\omega)\cdot e^{i\widetilde{\widetilde{P}}(\omega)}\right\}\cdot\Im\left\{e^{i\omega t}\right\}= \qquad (4.25)\\ &= \Re\left\{\widetilde{\widetilde{A}}(\omega)\cdot e^{i\widetilde{\widetilde{P}}(\omega)}\right\}\cdot\cos(\omega t)-\Im\left\{\widetilde{\widetilde{A}}(\omega)\cdot e^{i\widetilde{\widetilde{P}}(\omega)}\right\}\cdot\sin(\omega t)\equiv R(\omega)\cdot\cos(\omega t)-I(\omega)\cdot\sin(\omega t)\end{aligned}$$

A VNA can measure any pair of signal parameters: amplitude and phase or its real and imaginary parts. Model equations are:

$$\begin{cases}R(\omega) &= N_0\frac{\left(\omega_0^2-\omega^2\right)\cdot\cos(\psi)+2\gamma\omega\cdot\sin(\psi)}{\left(\omega_0^2-\omega^2\right)^2+(2\gamma\omega)^2}+b\cdot\cos(\varphi+\psi)\\ I(\omega) &= N_0\frac{\left(\omega_0^2-\omega^2\right)\cdot\sin(\psi)-2\gamma\omega\cdot\cos(\psi)}{\left(\omega_0^2-\omega^2\right)^2+(2\gamma\omega)^2}+b\cdot\sin(\varphi+\psi)\end{cases} \qquad (4.26)$$

4.3.2.1 VNA spectra analysis

One more technical detail remains. To make the fitting procedure converging with higher speed it is better to keep approximately the same order of magnitude for all variables. That's why we introduced new dimensionless variable, whose value is always about 1 for all our measurements $x=\omega/\omega_0$, and a new parameter $h=N_0/2\gamma\omega_0$. We also used a quality factor (Q) as a parameter. Fitting model then can be represented as:

$$\begin{cases}R(x,h,Q,\psi,b,\varphi) &= h\cdot\frac{Q\cdot\left(1-x^2\right)\cdot\cos(\psi)+x\cdot\sin(\psi)}{[c/w\cdot(1-x^2)]^2+x^2}+b\cdot\cos(\varphi+\psi)\\ I(x,h,Q,\psi,b,\varphi) &= h\cdot\frac{Q\cdot\left(1-x^2\right)\cdot\sin(\psi)-x\cdot\cos(\psi)}{[Q\cdot(1-x^2)]^2+x^2}+b\cdot\sin(\varphi+\psi)\\ A(x,h,Q,\psi,b,\varphi) &= \sqrt{b^2+\frac{h^2+2bh[Q\cdot(1-x^2)\cdot\cos(\varphi)-x\cdot\sin(\varphi)]}{[Q\cdot(1-x^2)]^2+x^2}}\\ P(x,h,Q,\psi,b,\varphi) &= \arctan 2\left(\left\{h\cdot\left[Q\cdot\left(1-x^2\right)\cdot\sin(\psi)-x\cdot\cos(\psi)\right]+b\left[\left[Q\cdot\left(1-x^2\right)\right]^2+x^2\right]\sin(\varphi+\psi)\right\},\right.\\ &\left.\left\{h\cdot\left[Q\cdot\left(1-x^2\right)\cdot\cos(\psi)+x\cdot\sin(\psi)\right]+b\left[\left[Q\cdot\left(1-x^2\right)\right]^2+x^2\right]\cos(\varphi+\psi)\right\}\right)\end{cases} \qquad (4.27)$$

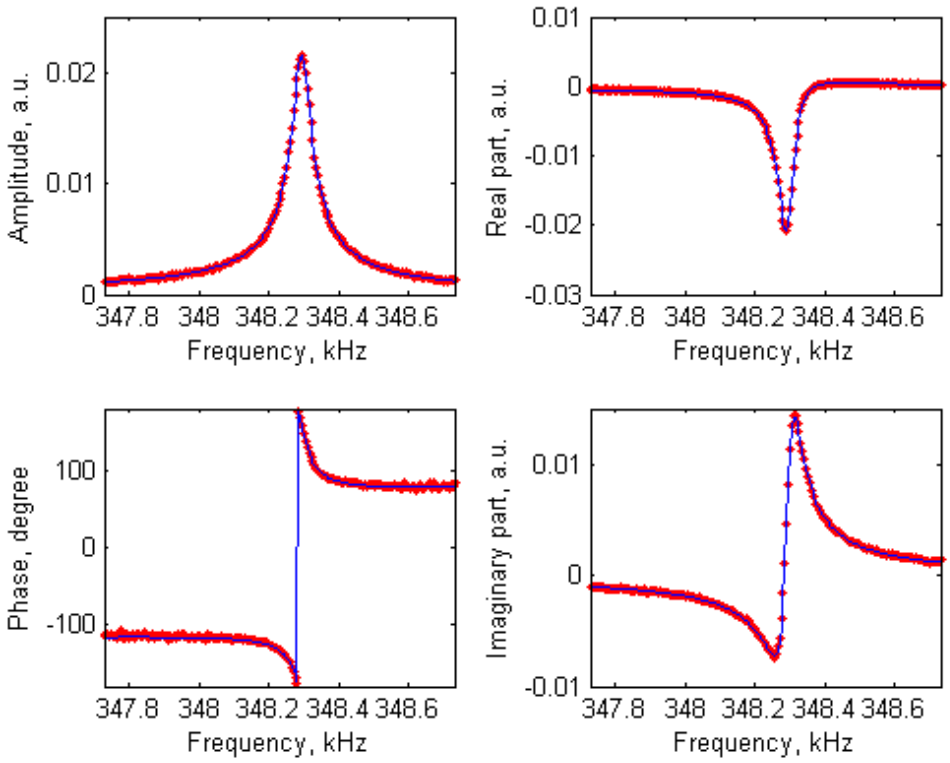

Figure 4.20: Typical spectra for amplitude, phase, imaginary and real parts. Red points shows experimental points, blue curves - fit using model (4.27).

We can mention that $A(x = 1, b = 0) = h$. It means that parameter h has a meaning of amplitude at resonance, when parasitic signal is missing. Typical spectra measured by VNA are presented on the Figure 4.20.

4.4 Experimental results

4.4.1 Static heating

Although GaAs is almost transparent for wavelengths of both lasers, we observed a shift of mechanical resonance while increasing laser's power. Such effect is caused by the absorption of laser light leading to heating of the structure. To measure how much do we heat the structure in average we fixed lasers' powers at very low level and measured thermal dependence of resonant frequency. For that we heated the structure using an internal heater of the cryostat. It allows us precisely set the temperature and control it. A temperature dependence of mechanical frequency is shown on the Figure 4.21a. This experiment were done for the photonic wire with a top diameter of 5.5 μm. Experimental setup were adjusted for maximum detectivity of

the mechanical mode with higher frequency (f $\sim$ 415 kHz). Probe laser position is set to the center of the photonic wire's top facet. Pump laser's position were shifted from the center by approximately 1 μm in direction of the mechanical mode's oscillations in order to be able, firstly, induce structure's motion, secondly, keep whole laser spot within the top facet of the structure. We found central frequency of mechanical resonance using fit of VNA's data while heating the structure from room temperature (293 K) to 308 K and then on a way back, while the structure cooled down. For every measured point we waited until the frequency becomes stable in time, that means that our system is at stationary equilibrium condition. It took about 10 minutes for a heat on 2 K and about 20 minutes to cool on the same amount. From a linear fit of measured data it follows that heating of the structure by 1 degree causes the decrease of the mechanical frequency by approximately 26.4 Hz.

Besides that, we measured how mechanical resonance changes with increasing of probe and pump laser's power. For the probe laser (λ = 976 nm) resonant frequency decreases linearly by 113.6 Hz while increasing laser power by 1 mW. This dependence is shown on the Figure 4.21b. Knowing results of both experiments we can convert them into dependence of photonic wire's average temperature on probe laser power (Figure 4.21c). Since both experimental dependencies are linear, such dependence also will demonstrate linear behavior. We found that heating of photonic wire by 1 degree is caused by increasing of probe laser power by 234 μW.

Same experiment for the pump laser (λ = 920 nm) were carried out and its results were also converted into dependence of photonic wire's average temperature on laser power (Figure 4.21d). In this case heating of photonic wire by 1 degree is caused by increasing of pump laser power by 154 μW. In means that smaller amount of pump laser light is required to heat the structure by 1 degree.

Firstly, such behavior is in agreement with theoretical model of GaAs absorption spectrum. On the Figure 4.22 experimental data and theoretical calculations of the optical dielectric function of GaAs at 300 K are shown. A bandgap of GaAs at 300 K is about 1.42 eV ($\lambda \sim$ 873 nm). Below this value theoretical model predicts the absorption, which is decreasing while decreasing the energy.

Secondly, photonic wires contain a layer of QDs, which can also take part in the absorption of light. Spectral analysis shows a presence of QDs, whose transition energies are about 1.35 eV ($\lambda \sim$ 920 nm), whereas there are no QDs with energy about 1.27 eV (λ = 976 nm). This fact can also be the explanation of higher light absorption of pump laser compare to the probe laser.

4.4.2 Orientation of mechanical modes

As it was presented in Section 4.2.5, a Dove prism can be used to adjust the detectivity of the photonic wire's mechanical mode. Thus, we can use it to define the direction of both modes with respect to the crystallographic axes. As a global reference for the experimental setup we took a surface of the table. It should be mentioned that both sample and SPD are mounted perpendicularly to it. From SEM images we know that crystallographic axes are aligned along the columns and rows of the structures' array. Thus, we can understand its orientations with respect to the any reference using visualization system of the experimental setup described in section 4.2.6.5. Looking at the sample using camera we identified that sample is turned by 5 degree in plane, which is perpendicular to the table (see Figure 4.23).

We will observe maximum detectivity for the mechanical mode, when Dove prism brings its direction to be coincident with detectivity vector for that mutual position of the probe laser and structure's top facet. While rotating further the Dove prism we rotate by twice the angle

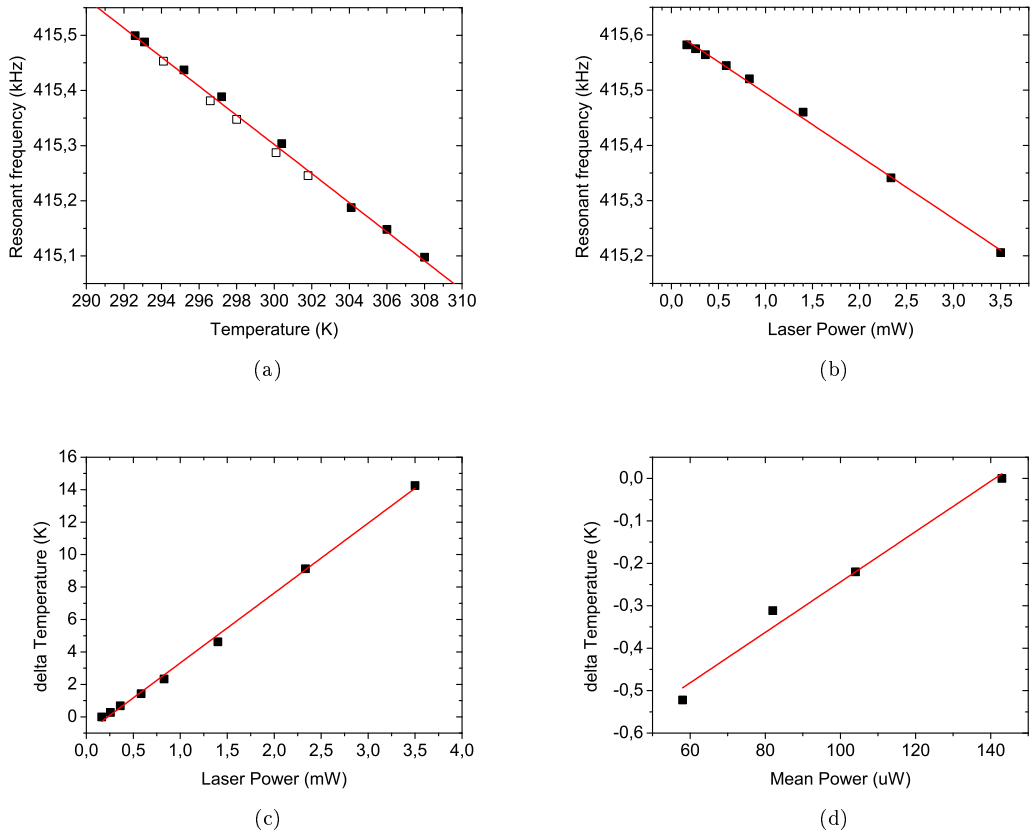

Figure 4.21: (a) Dependence of mechanical resonant frequency on photonic wire's average temperature. Data obtained during heating are shown by filled squares, whereas data obtained during cooling - by hollow squares. It demonstrates decreasing of resonant frequency by 26.4 Hz per 1 degree of heating. (b) Dependence of mechanical resonant frequency on probe laser power. It demonstrates decreasing of resonant frequency by 113.6 Hz while increasing probe laser power by 1 mW. (c) Dependence of photonic wire's average temperature on probe laser (λ = 976 nm) power calculated from two previous data sets. It demonstrates heating of photonic wire by 1 degree while increasing probe laser power by 234 μW. (d) Dependence of photonic wire's average temperature on pump laser (λ = 920 nm) power. It demonstrates cooling of photonic wire by 1 degree while decreasing pump laser power by 154 μW. In all cases: (1) resonant frequency is found as a central frequency parameter from a formula for a fit of experimental data obtained using VNA; (2) red line is obtained as a line fit of experimental points; (3) presented data are related to the photonic wire with top diameter of 5.5 μm.

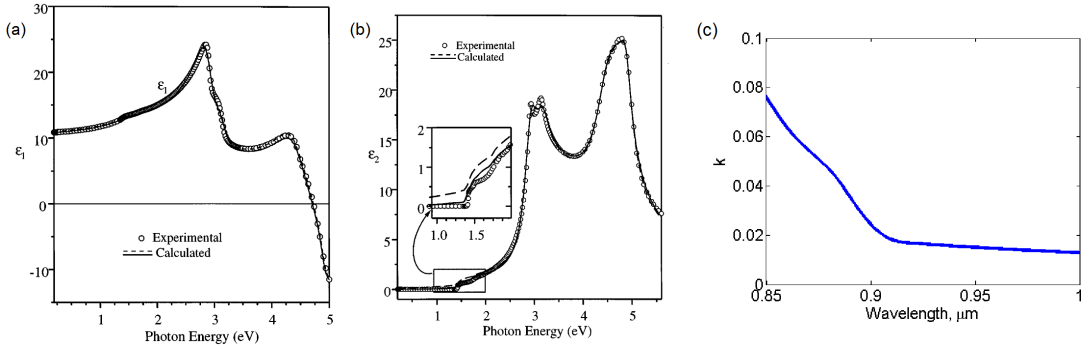

Figure 4.22: Spectral dependence of (a) real and (b) imaginary parts of the optical dielectric function of GaAs at 300 K. Solid and dashed traces is the result of theoretical calculations using models described in [56] and [57] respectively. Hollow circles is the experimental data obtained using spectroscopic ellipsometry and published in [58]. (c) Spectral dependence of the extinction coefficient, which is responsible for the light absorption, obtained with a model from [56]. It is equal to 0.017 for $\lambda = 920$ nm and 0.014 for $\lambda = 976$ nm. It means that it requires more laser's power on the higher wavelength to heat the structure by the same 1 degree, which is in agreement with the obtained results.

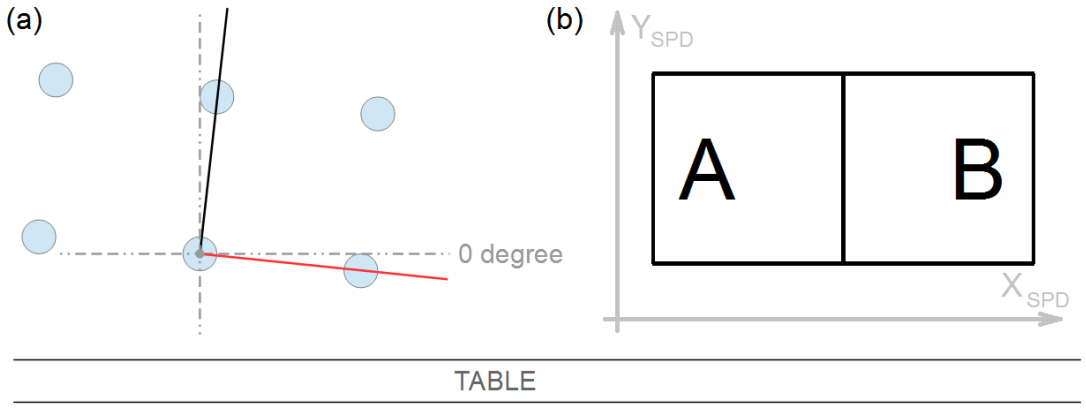

Figure 4.23: (a) Demonstration of 5 degree tilt of the Big Trumpet sample with respect to the table, whose orientation is taken as a global reference. Black and red lines show the directions of crystallographic axes of the sample. (b) SPD is mounted with no rotation with respect to the table.

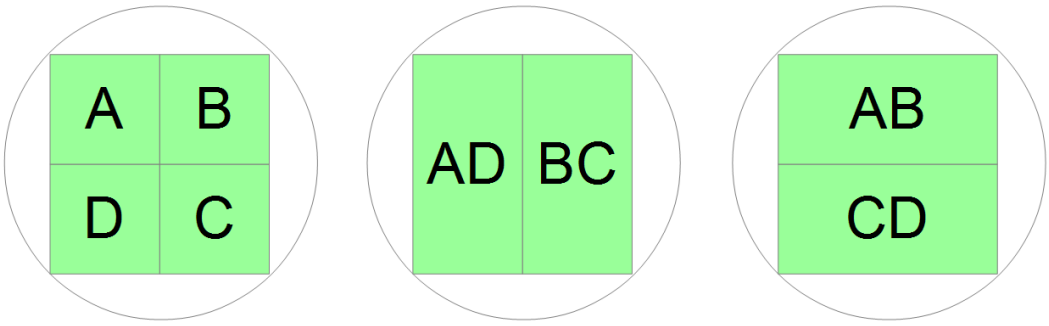

Figure 4.24: Sketch demonstrating that one QPD (on the left) with photodiodes A, B, C and D placed in 2x2 matrix can be considered as 2 SPDs with, first (at the center), two parts: A+D and B+C, second (on the right), two parts: A+B and C+D.

a mutual orientation of detectivity vector and direction of the mode's oscillations. So mode's detectivity in rotated case is defined by projection of mode's direction to the detectivity vector. We have already previously defined $\vec{\beta}(x, y)$ as a detectivity vector in coordinate system of SPD, so we define angle $\theta(x, y)$ as an angle between detectivity vector and X-direction of SPD, where x and y - are relative positions of the probe laser and photonic wire's top facet. Moreover, we introduce angle α - is a current angle of Dove prism orientation and α_{ref} - is an angle of Dove prism orientation, at which an image exerts only inversion ($\alpha_{ref} = 170$ degree, this angle is relative and only have meaning as a reference angle). Thus, a mechanical mode that has an angle γ with respect to the table has the detectivity dependence on Dove prism angle as:

$$D(\alpha) = |\cos(\gamma + 2 \cdot (\alpha - \alpha_{ref}) - \theta(x, y))| \tag{4.28}$$

For simplicity we set the probe laser at the center of photonic wire, so detectivity vector is coincident with X-direction of SPD ($\theta = 0$). We also introduce $\alpha'_{ref} = 2\alpha_{ref}$. This angle is equal to 340 degree for our experimental setup. Thus we obtain:

$$D(\alpha) = \left|\cos\left(\gamma + 2 \cdot \alpha - \alpha'_{ref}\right)\right| \tag{4.29}$$

Therefore, measuring this dependence we can extract γ and find orientation of the mode.

For this experiment we used a quadrant photo-diode (QPD), which has the same operating principle as SPD, but it has 4 parts instead of 2. These parts are located in a 2x2 matrix. A QPD has outputs corresponding to the difference signal in between, first, left part and right parts, second, up and down parts, so one QPD can be considered as 2 SPD in the same time. It is demonstrated on the Figure 4.24. There a QPD has 4 photo-diodes A, B, C and D, whereas virtual SPDs have, first, one part representing the sum of signals A and D. the other - sum of signals B and C, second, one part - A+B, the other - C+D. This is done for a better identification of mode orientation, because fitting of experimental data by model (4.29) is not very accurate, when values are relatively small. It can be compensated by the experimental points from the second channel, because, when the mode is almost not detectable from the first channel, it has maximum detection from the second channel.

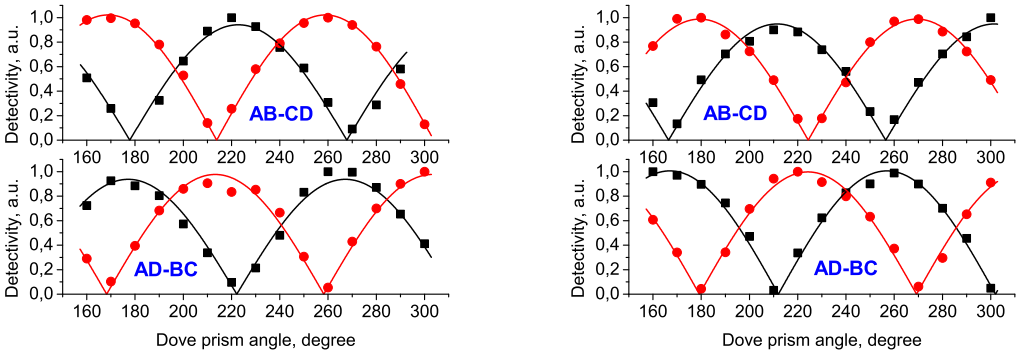

Figure 4.25: (a) Dependence of photonic wire's mechanical mode detectivity on the Dove prism angle measured with QPD from 2 orthogonal difference channels: upper image correspond to (A+B)-(C+D) configuration, lower - to (A+D)-(B+C). Filled squares are the experimental points, solid lines - fit with a model (4.29). Black color corresponds to lower frequency mode, red - higher frequency mode. Data were obtained for the optically excited photonic wire with top diameter of 5.76 μm. (b) The same experiment carried out several days after with the same structure at the same experimental condition.

Typical experimental results are presented on the Figure 4.25a. Upper plot corresponds to the data obtained via (A+B)-(C+D) differential channel, lower - to (A+D)-(B+C). Filled squares are the experimental points, solid lines demonstrate fit with a model (4.29). Black color corresponds to lower frequency mode, red - higher frequency mode. Detectivity for each point was extracted from experimental mechanical spectra as h parameter in model (4.27), and were normalized by maximum. Data were obtained for the structure with top diameter of 5.76 μm. As we can see, it demonstrates expected behavior for each mode individually, but, firstly, the angular difference between two modes is not equal to 90 degree, while they should be orthogonal, secondly, for unknown reasons this difference changes from one experimental day to another (compare it with the data presented on the Figure 4.25b, which relate to the same photonic wire measured at the same experimental conditions).

On the Figure 4.26a orientations for both mechanical modes, which are aligned with crystallographic axes of the sample, are shown by black and red lines for lower and higher frequencies correspondingly. Modes' orientations measured in first and second experiment are shown respectively by green and blue colors. We can see that they deviate from expected positions in a range of ±10 degree. We have also investigated that modes orientations during the one experimental day do not depend on a probe or pump laser powers, type of motion's excitation (piezo or laser-induced) and position of the pump laser on structure's top facet in case of laser-induced motion.

The same experiment was also provided with the other sample. Modes' orientations of photonic wires with top diameter of 2 μm and 1.9 μm were investigated using optical excitation and single SPD at two different days. Results are shown on the Figure 4.26b. Experimental data for two structures give almost equal results in a range of 1 degree, which is about a standard error

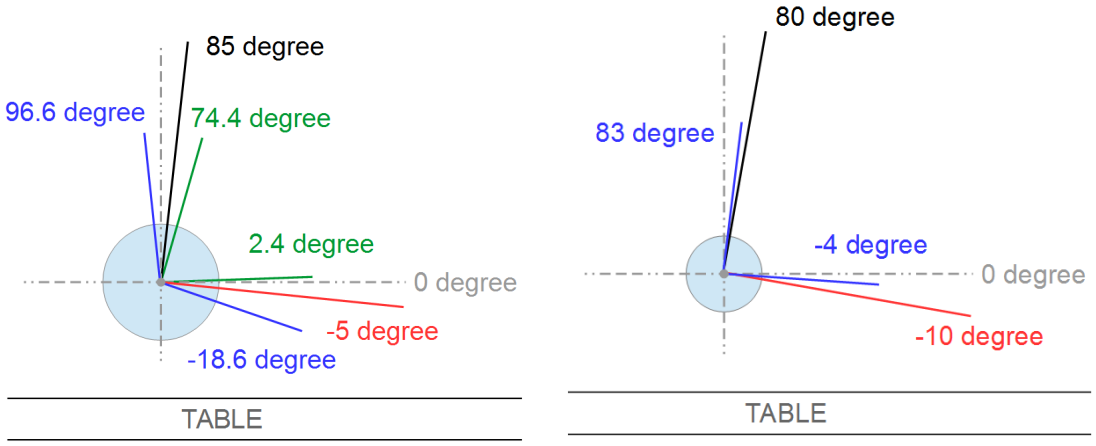

(a) (b)

Figure 4.26: (a) Sketch demonstrating orientations of the mechanical modes of photonic wire with top diameter of 5.76 μm. All angles are given with respect to the table, whose orientation is taken as a reference with a value of 0 degree. Lower frequency mode (shown by black line) is expected to be almost perpendicular to the table, whereas higher frequency mode (shown by red line) - almost parallel. Measured modes' orientations deviate from the expected positions in a range of ±10 degree from one experiment (green orientations) to another (blue orientations). (b) Modes' orientations for the photonic wires with top diameter of 2 μm and 1.9 μm. Computational error does not exceed 1 degree. Modes' orientations are shown by blue color, whereas red and black directions show the sample's orientation, which is rotated by 10 degree.

of fitting procedure. Two modes are almost orthogonal and their directions almost correspond to the sample's orientation, whereas for that sample orientation of crystallographic axes was not checked using SEM.

4.4.3 Laser-induced motion

4.4.3.1 2D map of laser-induced motion at room temperature

We have already presented a typical mechanical spectra for one mutual position of pump laser and photonic wire (see Figure 4.20). Using our software it is possible to move the pump laser across some area measuring for every point mechanical response of the system. Position of the probe laser is fixed during the scan. It means that detectivity of the mode's oscillation amplitude is the same for all experimental points and equal to

$$\beta_{1,2} = \left|\vec{\beta}_{LF}(x_0, y_0)\right| \cdot G_{LF\to HF} \cdot \left|\cos\left(\gamma_{1,2} - \theta(x_0, y_0) + 2 \cdot \alpha - \alpha'_{ref}\right)\right| \tag{4.30}$$

where $\gamma_{1,2}$ is the angle of the direction of the mode's oscillation, α is the angle of the Dove prism's orientation during the experiment and $\alpha'_{ref} = 340$ degree is its reference (see Section 4.4.2 for the details), θ is the angle between detectivity vector and X-direction of SPD, x_0, y_0 are the relative coordinates of the center of the structure's top facet and position of the pump

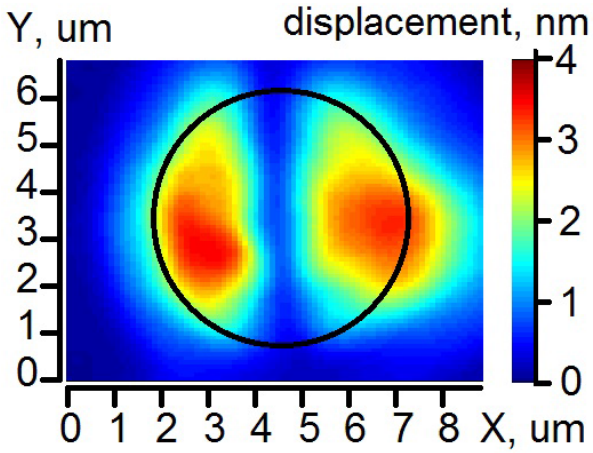

Figure 4.27: A 2D map of laser-induced motion at room temperature. Observed for the structure with top diameter of 5.3 μm and length of 26 μm. Laser diameter is about 4.2 μm and peak-to-peak intensity modulation at the mechanical frequency is equal to 180 μW. Black circle shows position of the top facet of the structure.

laser, $G_{LF\to HF}$ is a frequency dependent coefficient, which reveals the fact that detectivity was measured via low-frequency difference output of SPD, whereas structure's motion is detected via high-frequency output (see Section 4.2.1.2 and Figure 4.5b).

To find the amplitude of the oscillation in nm we divide a measured signal's amplitude at resonance (h) to the detectivity ($\beta_{1,2}$) for that mode. On the Figure 4.27 a typical 2D displacement map is shown for the one of mechanical modes. This data set is obtained at room temperature, when probe laser is fixed at the center of the photonic wire and Dove prism is set up at the maximum detectivity for that mode. Observed structure has a top diameter of 5.3 μm and length of 26 μm. Laser diameter is about 4.1 μm and peak-to-peak intensity modulation at the mechanical frequency is equal to 180 μW.

We can also define a position of the photonic wire at the scanning area, measuring a 2D map of 'A+B' signal from SPD while scanning by the pump laser across the area (see details in Section 4.2.3). It allows us to draw a black circle showing the contour of the photonic wire's top facet on the Figure 4.27.

From the fit we also find a quality factor (Q) of the oscillator. This value is almost the same for all experimental points and approximately equal to 2500 for this structure. In means that structure's dynamic displacement of 4 nm corresponds to 1.6 pm of static displacement (Q times less as it was described in Section 4.3.1) or static angle of $6.15\cdot10^{-8}$ rad. Angular stiffness (C) of that structure was calculated using commercial finite-element software COMSOL and is equal to $1.63\cdot10^{-9}$ N*m, that gives us estimation of resultant torque as 10^{-16} N*m. We will further compare this value with the theoretical calculations (see Section 4.4.3.2). For a moment we can simply estimate the maximum possible contribution of static radiation pressure force to the torque. We measured that reflection from the structure's top is equal to 30%. If we assume that all laser power is concentrated at the side of the structure, it gives us a value of radiation pressure force of 0.6 pN and correspondent torque of $1.6\cdot10^{-18}$N*m, which is about 60 times less that measured value.

4.4.3.2 Theoretical calculations of optical forces

Calculation were carried out by our colleague Taha Benyattou from INL (Institut des Nanotechnologies de Lyon). It was done by FDTD (finite-difference time-domain) method. It is a grid-based differential numerical modeling method, in which the time-dependent Maxwell's equations (in partial differential form) are discretized using central-difference approximations to the space and time partial derivatives. The resulting finite-difference equations are solved in a leapfrog manner: the electric field vector components in a volume of space are solved at a given instant in time; then the magnetic field vector components in the same spatial volume are solved at the next instant in time; and the process is repeated over and over again until the desired transient or steady-state electromagnetic field behavior is fully evolved. It is a very powerful method, requiring nevertheless a lot of time and memory due to the grid spatial discretization, which must be sufficiently fine to resolve both the smallest electromagnetic wavelength and the smallest geometrical feature.

In these calculations medium size photonic wire with length of 18 µm and top diameter of 2 µm was observed. Laser with diameter of 2 µm is focused at the top facet of the structure and propagates along its axis as it was demonstrated at the Figure 4.18. We also assumed that laser power is constant and equal to 1 W. Model structure also included an anti-reflecting coating at its top facet for wavelength of 920 nm. To have a good simulation, it is necessary to take into account multiple reflections of the light propagating along the axis of the photonic wire from its base. To study this point, simulations of different time durations were done. The simulation time is measured in length by multiplying the time t by the speed of the light. It was done for the cases: $c \cdot t = 100$, 300 and 1000 µm, that takes 40 minutes, 2 hours and 7 hours of calculation time at our machine respectively. The spectrum which corresponds to the value of the electric field to the proximity of the surface of the photonic wire in case, when laser is focused at the side of its top facet is shown on the Figure 4.28 for all 3 cases. There is a hollow for a wavelength close to 0.9 µm, linked to the fact that an anti-reflection layer is present on the surface. The three curves are approximately superimposed. However, we see that for $c \cdot t =$ 100µm, the simulation time is not enough to provide the sufficient precision of calculations. On the other hand, the spectra are very similar for the two cases $c \cdot t = 300$ µm and $c \cdot t = 1000$ µm, that helps us to define the required calculation time. Results of calculations of electro-magnetic field are shown on the Figure 4.29 for the wavelength of 900 nm for all 3 cases.

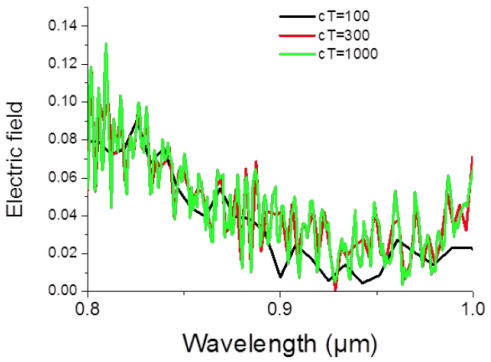

Figure 4.28: The spectrum of electric field to the proximity of the surface of the photonic wire in case, when laser is focused at the side of its top facet for different computation time.

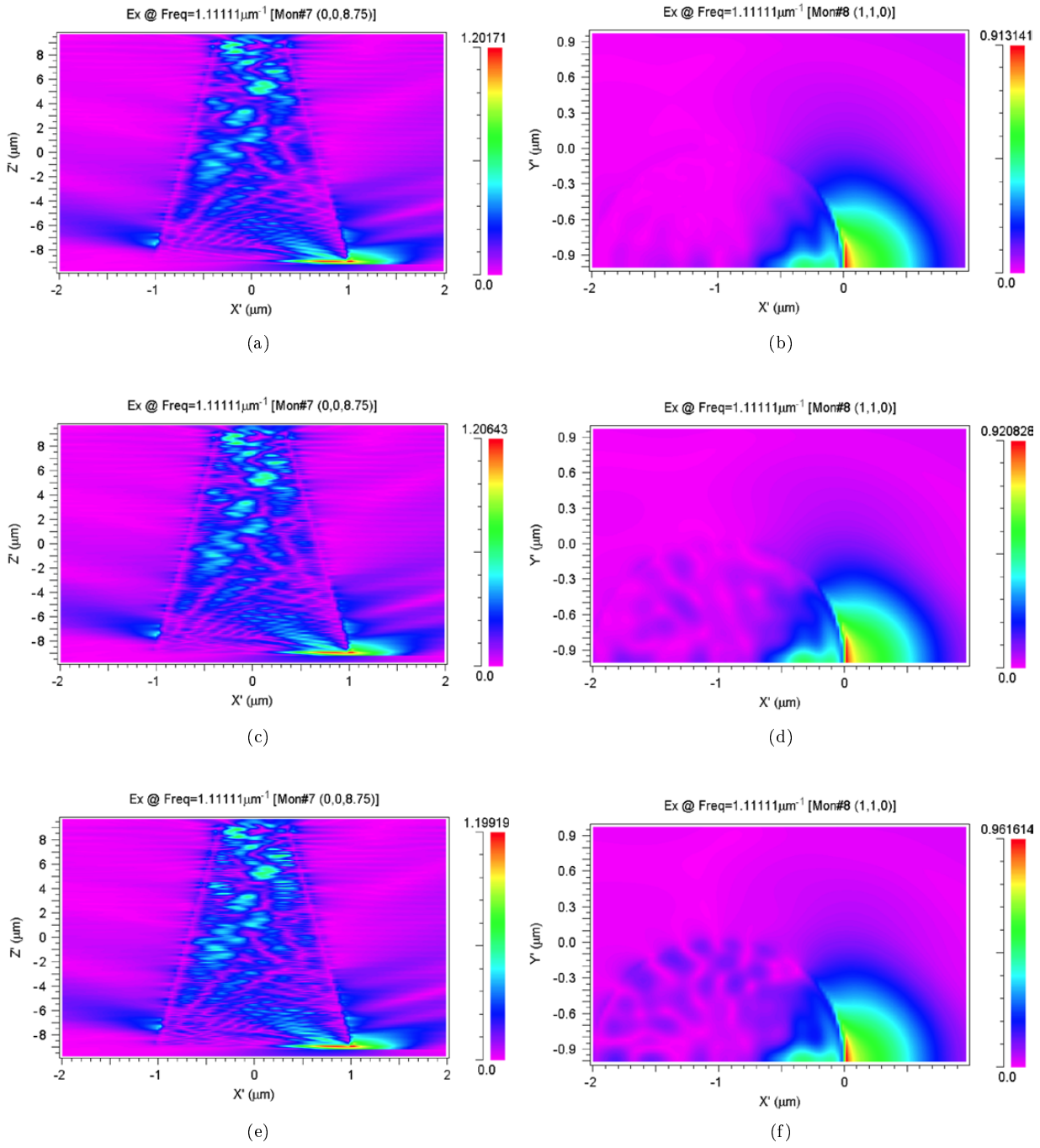

Figure 4.29: Calculation of electro-magnetic field for the wavelength of 900 nm in case, when laser is focused at the side of the structure. Three model cases: $c \cdot t = 100$, 300 and 1000 μm correspond to 3 lines of the figure. Left column shows longitudinal central cross-section, right column - perpendicular cross-section at the level of top facet of the structure.

Nevertheless, the same calculations for the big structure with length of 26 µm and top diameter of about 5.5 µm are complicated, because of a huge amount of required memory. That's why such calculation was done for 2D structure's model for the following conditions: laser diameter - 2 µm, laser power - 100 µW and laser wavelength - 900 nm.

Dependencies of appearing forces on the laser position along the structure's top facet are shown on the Figure 4.30a, whereas corresponding torques are shown on the Figure 4.30b. Resulting torque is shown on the Figure 4.30c.

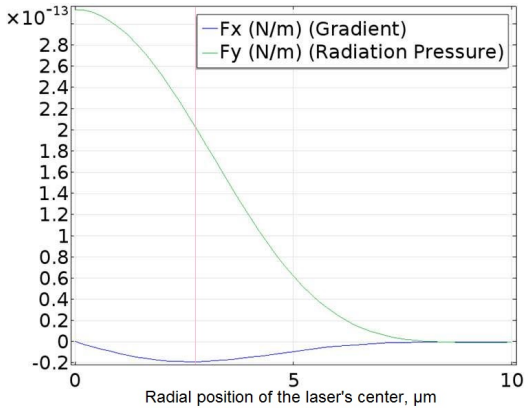

(a)

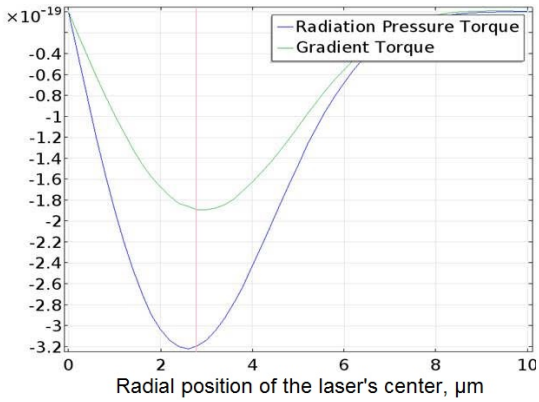

(b)

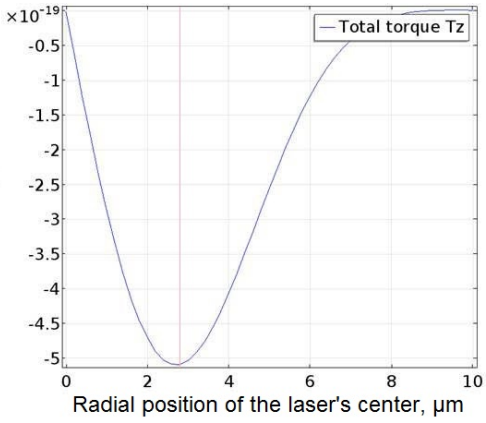

(c)

Figure 4.30: (a) Forces appearing in light-matter interaction: radiation pressure (green) and gradient (blue) forces appear along and perpendicular to structure's symmetry axis correspondingly. Negative sign of gradient force just means that its direction is opposite with direction of X axis in used coordinate system. (b) Torques appearing in light-matter interaction due to radiation pressure (blue) and gradient (green) forces. (c) Resulting torque. On all plots rose vertical line shows the edge of the structure, which has a diameter of 5.5 µm. Calculations were done for the laser diameter of 2 µm, power of 100 µW and wavelength of 900 nm.

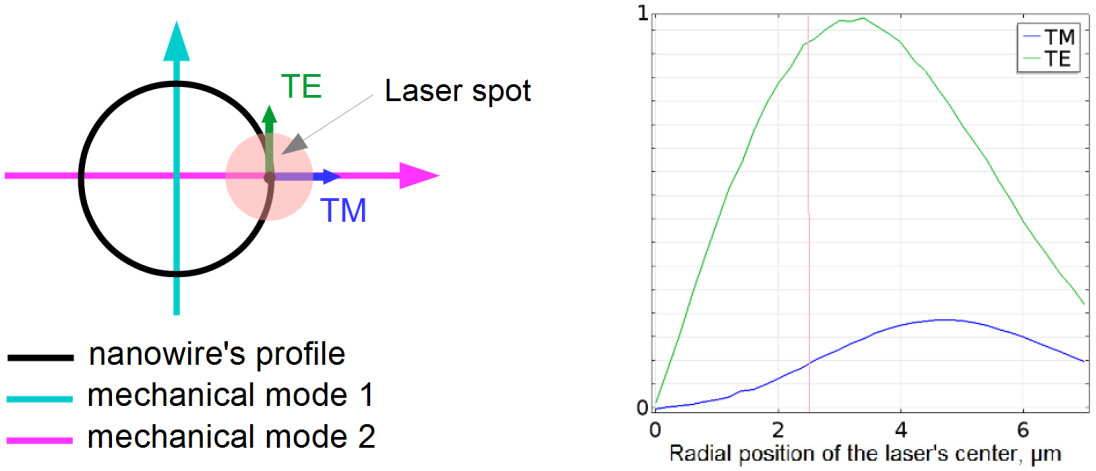

(a) (b)

Figure 4.31: (a) Sketch demonstrating notation of TE and TM modes of laser polarization. Top view on the structure. (b) Comparison of torques appearing, when laser is TE-polarized (green), TM-polarized (blue) in arbitary units, calculated for the the following conditions: structure's top diameter is equal to 5 μm, length - 18 μm, laser diameter - 1 μm, laser power - 1 W and laser wavelength - 1 μm. Rose vertical line shows the edge of the structure.

We can see that radiation pressure force has a maximum at the center of the structure and decreases while laser moves to its side. However, large radiation pressure force at the center of the structure arises zero torque, because it is placed on the axis of the structure and collinear with it. Contrary, gradient force equals to zero at the center of the structure, which is expected due to its symmetry. We also can see, that despite gradient force is smaller than radiation pressure force, it arises comparable torque.

Maximum resulting torque is observed, when the laser is about at the side of the structure, and is equal to about $5 \cdot 10^{-19}$ N*m at laser power of 100 μW. We see that this value is about 2 order of magnitude smaller than what we expected from the experimental results (10^{-16} N*m, see Section 4.4.3.1). It makes us think that other effects could take a place during the experiment.

In all above calculations we assumed that laser is TE-polarized, i.e. tangentially to the structure (when laser is placed at its side), as it is demonstrated with the sketch on the Figure 4.31a. Comparison of torques appearing, when laser is TE- or TM-polarized was calculated for the structure with top diameter of 5 μm and length of 18 μm, when laser has a diameter of 5 μm, power of 1 W and wavelength of 1 μm. Results are presented at the Figure 4.31b. We can see that torque for TM-polarized light is several times smaller than for TE-polarized laser. Moreover, it has a maximum, when laser is placed out of the structure's top by approximately laser's radius, whereas maximum for TE-polarization is observed, when the center of the laser spot is about at the side of the structure.

Thus, changing the orientation of linear pump laser polarization we can experimentally check the origin of the observed effect.

4.4.3.3 Dependence on laser polarization

Theoretical calculations demonstrate a strong dependence of displacement's amplitude on the laser polarization. To check such dependence experimentally we used a λ/2-plate in between the PBS and the objective (see the scheme of the experimental setup on the Figure 4.17). Rotating the λ/2-plate we rotate the polarization of Pump laser by twice this angle and, thus, change the mutual orientation of mechanical mode polarization and laser polarization. Rotation of half-wave plate, however, leads to the beam deviation of about hundred nm and requires a small correction of the position of the Pump laser on the structure's top facet. We have done this experiment twice with the same photonic wire. First time, we made this correction manually looking after each rotation for the maximum of peak's amplitude at the VNA. In the second case, we initially found the relative coordinates of this laser position with respect to the center of the structure, and then we came back to this position after each rotation automatically. For that after each rotation we did the following procedure:

- measure the Total Intensity 2D Map of the Probe laser (using 'A+B' channel of SPD);
- identify center of the structure from it;
- compare current central position with the initial one;
- move the Probe laser to the center of the structure;
- measure the detectivity;
- calculate the required displacement for the Pump laser to come back to the same experimental point;
- move the Pump laser to the experimental point;
- measure the spectra of mechanical response using VNA.

Nevertheless, detection of the structure's center has a precision of about 20-50 nm. That's why after each rotation of half-wave plate we repeated measuring procedure 50 times and averaged the result. On the Figure 4.32 data from the first approach are shown by the orange hollow diamonds, and from the second approach - by filled black circles. We can see that both approaches give approximately the same result.

Changing the angle of laser's polarization we assumed to observe a change in amplitude of the motion caused by a change of the torque (which is linearly connected to it). Only a part of the torque caused by a gradient force will change, whereas a radiation pressure force will be the same. Gradient force is proportional to the laser's intensity, which is a square of the electro-magnetic field. Any laser's polarization's orientation can be decomposed in a basis of TM- and TE-polarization, and then resulting torque is a sum of torques appearing in TM- and TE-cases independently. Formally we conclude with:

$$M(\delta) = M_G(\delta) + M_{RP} = cos^2(\delta) \cdot M_{TE} + sin^2(\delta) \cdot M_{TM} + M_{RP} \tag{4.31}$$

where δ is an angle between current configuration of laser's polarization and TE-configuration, M_G and M_{RP} are parts of the torque caused by gradient and radiation pressure forces respectively.

Red solid curve on the Figure 4.32 shows a fit of the experimental data with (4.31). In the experiment it was assumed that mechanical mode is oriented along the crystallographic

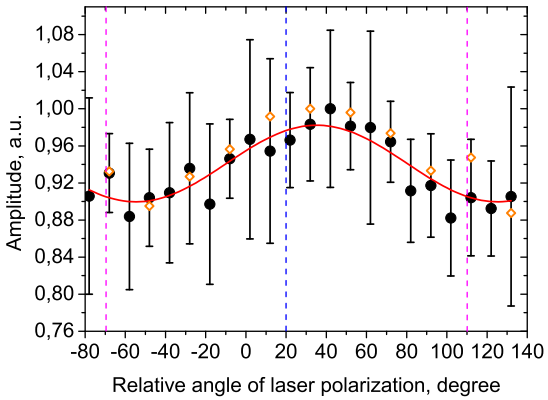

Figure 4.32: Amplitude of exited motion in arbitrary units depending on the laser polarization. Orange hollow diamonds - manual position correction, black filled circles - automatic position correction. Red curve is a fit for the data presented by black filled circles. Vertical dashed lines shows orientation of the laser polarization for TM- (magenta) and TE-configuration (blue). Data were obtained at room temperature for the structure with length of 26 μm and top diameter of 5.5 μm. Center of the Pump laser was shifted by 2.5 μm in the direction of the mechanical mode of the structure.

axis of the sample, however in Section 4.4.2 unstable orientation of mechanical modes was demonstrated. It can be the explanation of the observed mismatch between the maximum and minimum of the fit with laser's angles for TM- and TE-configurations (which are shown by vertical dashed lines).

From the calculation in previous section we can roughly take $M_{TE}/M_{TM} \sim 9$ (see Figure 4.31b), and assume $M_{RP} \sim 1.7 \cdot M_{TE}$ (see Figure 4.30b), so we expect to observe a ratio between maximum and minimum of amplitude about $M(90)/M(0) \sim 0.67$. Whereas from the experimental data we obtain 0.92. It means that the other effect, which does not depend on laser orientation has a presence, so we can write a total torque as

$$M_{TOTAL}(\delta) = M(\delta) + M_?$$

Thus, observed ratio corresponds to $M_{TOTAL}(90)/M_{TOTAL}(0)$, from which we can obtain $M_? \sim 8.4 \cdot M_{TE}$. From that we can conclude that there is the other effect (or effects) that influence on the results and its contribution is significant. However, to explain the mismatch in comparison of observed and calculated forces made above, we have to obtain $M_? \sim 100 \cdot M_{TE}$.

4.4.3.4 2D map of laser-induced motion at low temperature

To understand the origin of additional forces appearing in the experiment we repeated the experiment and obtained a 2D map of laser-induced motion at low temperature (T $\sim$ 6 K), which is presented on the Figure 4.33 for the photonic wire of 5.5 μm top diameter and length of 26 μm. Laser diameter is about 4.1 μm and intensity modulation at the mechanical frequency is equal to 180 μW.

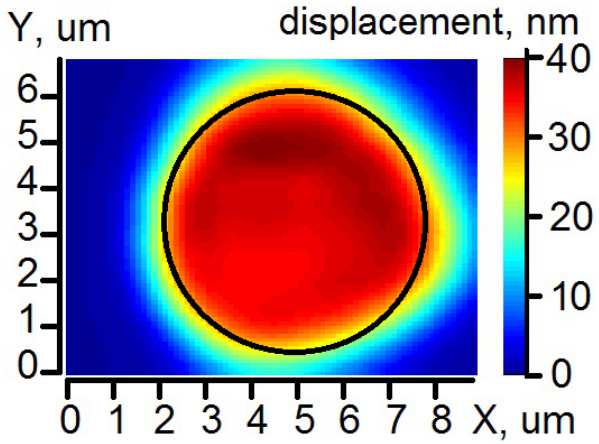

Figure 4.33: A 2D map of laser-induced motion at low temperature. Observed for the structure with top diameter of 5.5 μm and length of 26 μm. Laser diameter is about 4.2 μm and intensity modulation at the mechanical frequency is equal to 180 μW. Black circle shows position of the top facet of the structure.

We can see that amplitude of the motion is increased approximately by a factor of 10 with respect to the room temperature and behavior of such motion is also changed. As soon as laser hit the structure it starts oscillate and amplitude of such oscillations does not depend on the position of the laser on the top facet of the structure. It is true that decreasing of the temperature also improves the vacuum inside the cryostat and thus decreases damping of the motions or, in other words, increases Q-factor. But it increases only in about 3 times and does not explain fully the rise of the oscillations amplitude.

It makes us think that a temperature effects such a heating of the structure under the laser radiation takes place. Indeed, the speed of heat propagation changes with temperature. It is defined by heat diffusion coefficient, which varies from $D = 3.1 \cdot 10^{-5}$ m^2/s at room temperature to $D = 1$ m^2/s at 4 K for GaAs. It means that heat will be redistributed over the structure after about L^2/D second, where L is the length of the photonic wire. If speed of a heat propagation is big enough it means that temperature field of the structure is changing instantaneously with change of laser power. Thus, if $\Omega_{heat} = D/L^2 > f_{mechanical}$ thermal effect is instantaneous. Otherwise, it is not.

Both mechanical frequencies also depend on the temperature, but change in mechanical frequency is just about 10 %, whereas frequency of heat distribution changes more than 4 order of magnitude when temperature is decreasing. For example for the photonic wire with top diameter of 5.5 um and length of 26 um we experimentally found two modes at about 350 and 415 kHz at 300K, which are shifting to 370 and 430 kHz respectively at 4 K. In its turn, frequency cut-off of heat distribution at T = 300 K is equal to 46 kHz, which is lower than mechanical frequency, whereas at T = 4 K it is equal to 1.4 GHz, which is much higher. Thus, we can consider thermal distribution at low temperature as an instantaneous effect, whereas at room temperature it is not.

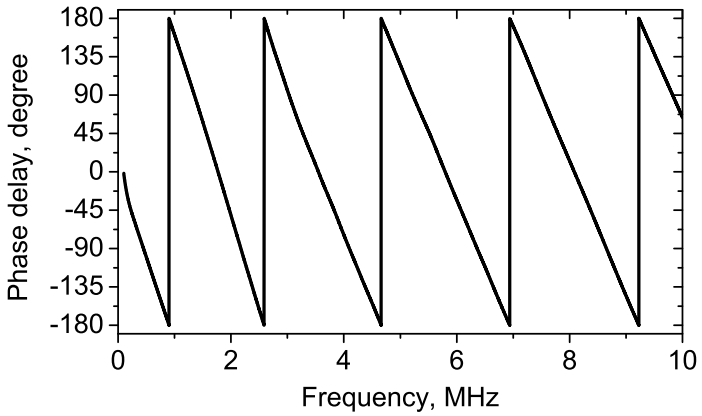

Figure 4.34: Phase delay due to signal propagation through the electric circuits of the experimental setup.

4.4.3.5 Analysis of delays in motion excitation

To understand whenever the effect exciting the motion of the photonic wire is instantaneous or not, we need to analyze a phase behavior of mechanical spectra. First of all, we take into account a phase delay related to delay of electronic circuits. To measure this value we focused modulated Pump laser on the substrate and measured a phase delay using VNA in configuration that we used to measure gain of the SPD (see Figure 4.4). Such phase delay almost linearly depends on frequency (see Figure 4.34). It means that we have a constant delay in time (which is about 100 μs) that leads to different phase delay depending on the frequency.

If the effect is instantaneous the phase should evolve from 0 to -180 degree across the resonance and should be equal to -90 degree at resonance. On the Figure 4.35a the phase behavior for the instantaneous effect is shown together with phase delay caused by electronic, which is equal to 70 degree around 348 kHz. However, it is also possible for the phase to evolve from 180 degree to 0 degree passing through 90 degree at resonance, because we measure the structure's oscillations via 'A-B' channel of SPD. Such 180 degree difference means that after beginning of motion excitation structure's projection on the SPD goes first to the B part, whereas in case described above it goes first to A part. Corresponding phase evolution is shown on the Figure 4.35b.

On the 2D map of laser-induced motion at room temperature we observed two regions with high amplitude of oscillations, which are separated by a line where motion is equal to zero (see Figure 4.27). This line is perpendicular to the mechanical mode and symmetrically divides the structure on left a right parts. From theory we expect that when laser is at some certain on the left part structure moves to the left, because laser attracts the photonic wire. When laser on the symmetric point at the right side it leads to the same effect but to the right. Summing up, we should observe a phase evolution like on the Figure 4.35a for the one side, and like on the Figure 4.35b for the other side. In other words, shift of the laser from the one side to another changes phase at resonance by 180 degree.

Real phase evolution for 2 points from left and right sides for laser-induced motion at room temperature is shown on the Figure 4.36. Values of the phases at resonance after subtraction

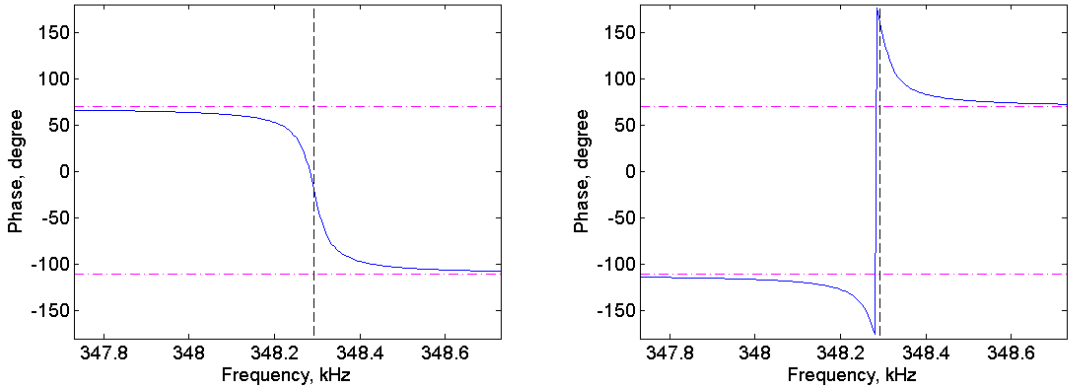

(a) (b)

Figure 4.35: Phase evolution over the resonance for the instantaneous effect including a phase delay caused by electronic. Blue trace shows the phase behavior, vertical dashed black line is a position of a resonance frequency, horizontal dashed-dotted magenta lines demonstrate limits in which phase evolves due to the shift caused by electronic. Realisation of the situation on the figure (a) or (b) depend on the initial direction of structure's displacement.

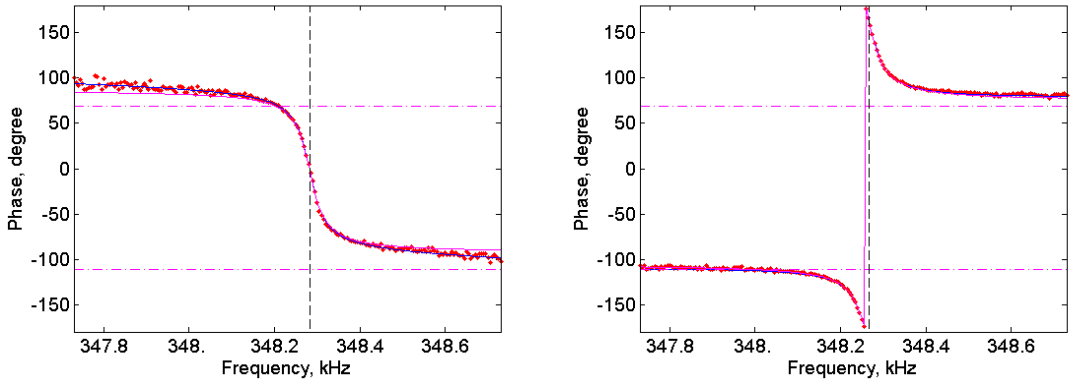

(a) (b)

Figure 4.36: Phase evolution over the resonance observed at room temperature including a phase delay caused by electronic. Red points are the experimental data obtained for the structure with top diameter of 5.5 μm and length of 26 μm. Blue traces show the fit of the experimental points using equations 4.11. Magenta traces shows phase evolution after subtraction the influence from background signal. Vertical dashed black line is a position of a resonance frequency, horizontal dashed-dotted magenta lines demonstrate limits in which phase should evolve due to the shift caused by electronic. (a) Phase evolution for the experimental point from the right side of the map, (b) left side of the map.

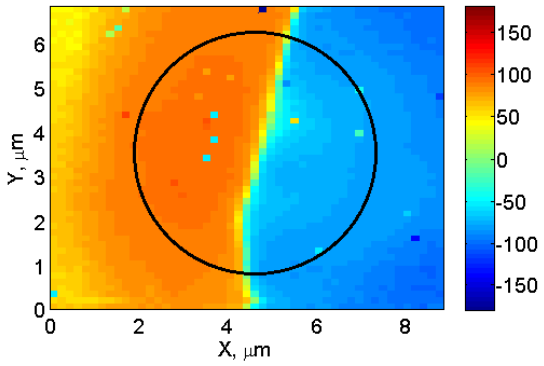

Figure 4.37: 2D map of phase delay at resonance for the structure with top diameter of 5.5 μm and length of 26 μm. Values are given after subtraction of electronic phase delay. Black circle shows edged of the structure.

of electronic phase delay are 95 degree and -73 degree for the left and right sides respectively. We can see that change of the side leads to phase change by 168 degree, which is about the predicted value of 180 degree. However, values are different from expected 90 and -90 degrees by 5 and 17 degrees respectively. It means that observed effect is not absolutely instantaneous, however it is not so far from it.

To see properly the phase change while moving the laser from left to the right part the phase map is plotted on the Figure 4.37. It shows values of phase at resonance for every experimental point. We see that value of the phase is almost constant for the all points from left or right parts, whereas it changes by ∼180 degree when crossing the central line.

Now, we can do the same analysis for the data obtained at low temperature (see Figure 4.33). On the Figure 4.38a a phase evolution through the resonance is presented for the one point at the center of the photonic wire. A 2D map of phase delay at resonance is presented on a Figure 4.38b. From these data we can conclude, firstly, that physical effect (or at least one of effects appearing and playing a significant role in light-matter interaction) taking a place at low temperature is also not instantaneous (phase at resonance is 27 degree). Moreover, deviation of the phase from expected value is 63 degree that makes it "less instantaneous" than in situation at room temperature. The other important conclusion is that phase map is not separated by left and right sides, which means that structure always bends to the same side not depending on the laser's position on its top facet.

The last result means that for any position of the laser the photonic wire reacts identically. It breaks the symmetry that predicts the structure behaves in inverted manner, when laser shifts from its left to right part along the direction of the mechanical mode. We connect such behavior to intrinsic non-symmetry of the structure basis after the growth. On the Figure 4.39a the basis of the same structure is shown from the side. On the Figure 4.39b the top view of the basis of the other broken structure is shown. It is easily to see on both SEM images that conical fixed end of the structure is shifted from the apex of the pyramid.

Knowing that, we can assume that laser heat the structure, this heat reaches structure's

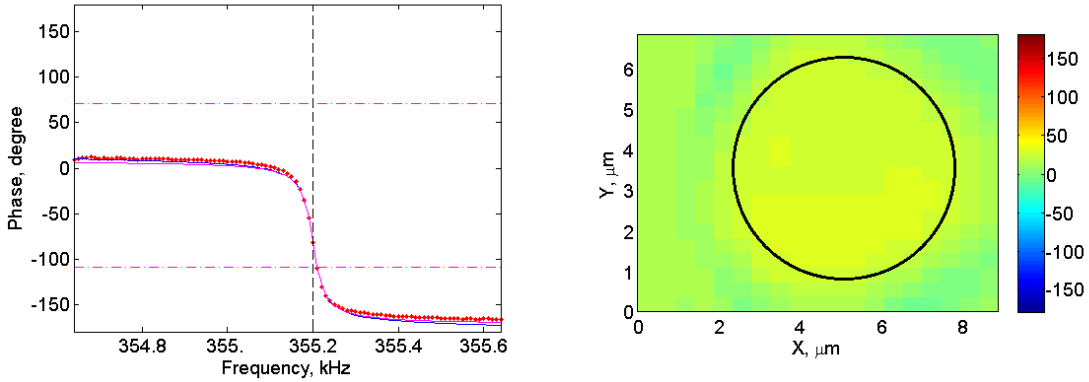

(a) (b)

Figure 4.38: (a) Phase evolution over the resonance observed at low (T $\sim$ 6 K) temperature for the point at the center of the photonic wire including a phase delay caused by electronic. Red points are the experimental data obtained for the structure with top diameter of 5.5 µm and length of 26 µm. Blue traces show the fit of the experimental points using equations 4.11. Magenta traces shows phase evolution after subtraction the influence from background signal. Vertical dashed black line is a position of a resonance frequency, horizontal dashed-dotted magenta lines demonstrate limits in which phase should evolve due to the shift caused by electronic. (b) 2D map of phase delay at resonance for the same structure. Values are given after subtraction of electronic phase delay. Black circle shows contour of the strucutre's top facet.

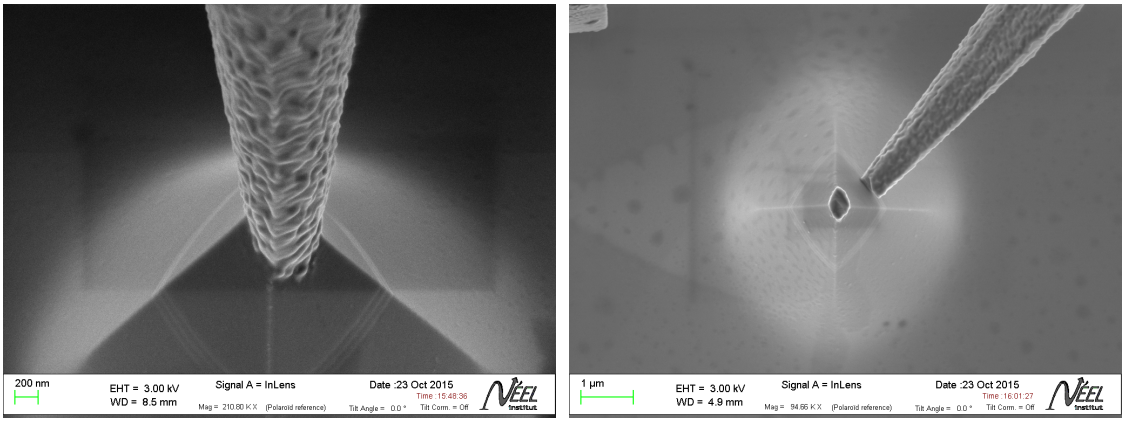

(a) (b)

Figure 4.39: (a) SEM image of the basis of the structure with top diameter of 5.5 µm and length of 26 µm. Side view. (b) SEM image of the basis of the broken structure. Top view.

basis due to a quick heat diffusion. It is then distributed around the basis in a same way not depending on a laser's position and it leads to structure's oscillations always in the same direction defined by the structure's non-perfectness.

Preliminary experiments provided with Short Trumpet sample demonstrate that phase map is uniform not only for the low temperature (T$\sim$ 6 K), but also for the room temperature (T $\sim$ 300 K). Such behavior requires the most thorough research. Provisionally, we can connect it to the fact that eigenfrequencies of the short structure ($\sim$ 9 MHz) is only 3 times bigger than the frequency cut-off of heat distribution at T = 300 K ($\sim$ 3.4 MHz), whereas for the big structure this ratio was about 7.

4.4.4 Excitation of higher order mode

One of the advantages of optical excitation is a possibility to excite not only the first mechanical mode, which has a frequency lower than 1 MHz and also available through piezo-excitation, but also higher modes, which are in a range of several MHz and not available for the piezo-excitation. On the Figure 4.40 spectra corresponding to the first and second order flexion modes of the structure with top diameter of 5.5 μm and length of 26 μm are shown. The Dove prism was adjusted for the maximum detectivity of this mode. Analogously, it was also possible to detect first and second flexion modes in orthogonal direction. For that the Dove prism was appropriately reoriented.

We can see that detected amplitude of the second flexion mode is about 260 times smaller than for the first order mode, whereas detectivity lower by approximately 15 times, because of lower gain of SPD's amplifier (see Figure 4.5). It means that real amplitude of oscillations is about 17 times lower. In the Section 4.3.1 it was shown that amplitude of the motion at resonance is inversely proportional to the resonant frequency. It means, that ratio of amplitudes of the first and second flexion modes should correspond to the inverted ratio of their frequencies. From the experiment we found a frequency ratio approximately to be equal 23.

Above it was shown that amplitude of the motion at the first order mode is about 4 nm. It means that amplitude of the second order flexion mode is about 150 pm. Such small motion is still well detectable with our experimental setup. Detection of the next flexion mode requires better SPD, because bandwidth of the current one is limited by 20 MHz, whereas third flexion mode is assumed to be at about 30 MHz.

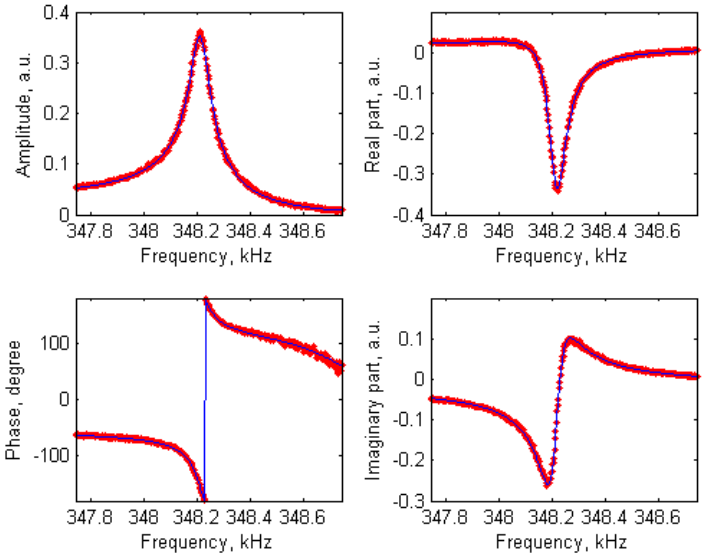

(a)

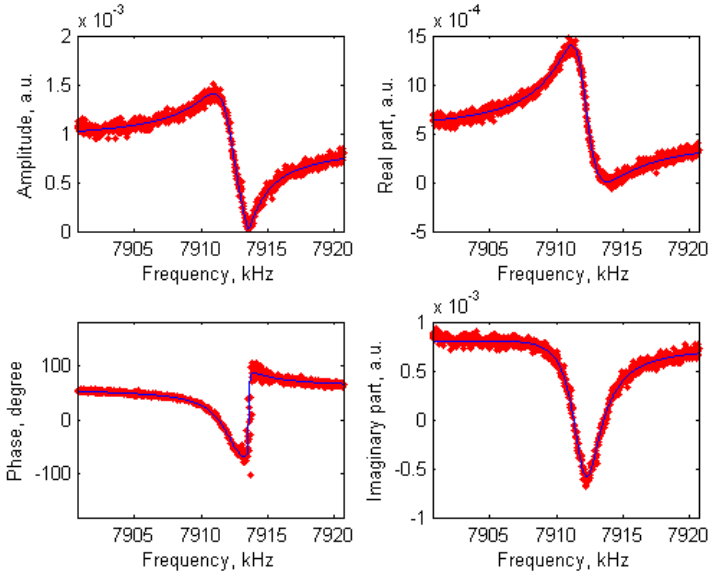

(b)

Figure 4.40: Mechanical spectra for the (a) first and (b) second flexion modes at room temperature for the structure with top diameter of 5.5 μm and length of 26 μm. A Dove prism is adjusted for the maximum detectivity. Red points demonstrate the experimental data. Its fit with the model (4.27) is shown by blue traces.

4.5 Conclusions and perspectives

In this chapter we demonstrated a possibility of an optical actuation of photonic wire's motion. Comparing to existing technique of piezo-excitation it allows to excite higher order modes. Moreover, it allows to work directly with one chosen structure. Optical approach also allows an extremely precise static positioning tuning of the photonic wire. Despite that origin of laser interaction with a photonic wire was not completely understood, presented results are very promising for further investigations.

To confirm impact of the thermal effect on structure's oscillations it is required to repeat the experiment with the laser on the other wavelength, at which there is an absorption of the light by GaAs. Currently, we connect a huge influence of thermal effect on the experimental results with the absorption by wetting layer of the InAs QDs embedded into the photonic wires.

All expected effects can also be simulated by FDTD method. Thus, taking into account thermal effect as well as electrostrictions should make the theoretical calculations more reliable.

It should be also possible to detect the vertical breathing mode of photonic wire's oscillations. For that the interferometric method can be used (see for example [59, 60]). It means that photonic wire's top facet plays a role of one of the mirrors in Michelson interferometer.

Existence of a coupling between a presence of a laser and an amplitude of the structure's motion suggests the possibility not only of a motion's actuation but also motion's damping, i.e. reduction of the structure's motion amplitude. For that a feedback cooling technique should be used (see for example [61]). In general that means that motion of the mechanical resonator is controlled using real-time information about its state via a time-dependent external force. In our case it is required the development of the system, which tracks the position of the photonic wire's top facet with high precision ($\sim$ several pm) and at high speed (several times bigger than structure's eigenfrequency). Thus, knowing at each moment the direction of structure's displacement, we will be able to prevent it, sending a laser pulse, which induces the motion in opposite direction. Such motion cooling will allow to reduce a jitter of a QD emission caused by its coupling to a strain.

Apart from the applications, in which laser is used in dynamic mode, it is also possible to benefit from its static use. Moving the laser over the photonic wire's top facet allows us to carry out a precise tuning of the structure's position and, therefore, a QDs' emission. From the previous Chapter we know that QD can be tuned by approximately 35 μeV per 1 nm of structure's top displacement. In this Chapter it was presented that structure's static displacement under the laser of 180 μW power is about 1.6 pm. Despite that these values were obtained for the different structures, we can roughly estimate that 1 W laser can tune QDs in a range of 350 neV.

Appendix A. Definition of arctan2

Every equation of the form $y(x) = A \cdot \cos(x) + B \cdot \sin(x)$ can be represented as $y(x) = C \cdot \cos(x - D)$,where C and D - parameters calculated from A and B. To demonstrate it we are considering following transformations:

$$\begin{aligned} y(x) &= A \cdot \cos(x) + B \cdot \sin(x) = \sqrt{A^2 + B^2} \cdot \left(\frac{A}{\sqrt{A^2 + B^2}} \cdot \cos(x) + \frac{B}{\sqrt{A^2 + B^2}} \cdot \sin(x) \right) = \\ &= \sqrt{A^2 + B^2} \cdot \left(\widetilde{A} \cdot \cos(x) + \widetilde{B} \cdot \sin(x) \right) \end{aligned}$$

We see that just introduced coefficients $\widetilde{A}$ and $\widetilde{B}$ satisfy the expression $\sqrt{\widetilde{A}^2 + \widetilde{B}^2} = 1$. It means that it exist the angle D for which $\cos(D) = \widetilde{A}$ and $\sin(D) = \widetilde{B}$. We have got:

$$y(x) = \sqrt{A^2 + B^2} \cdot (\cos(D) \cdot \cos(x) + \sin(D) \cdot \sin(x)) = C \cdot \cos(x - D)$$

where $C = \sqrt{A^2 + B^2}$.

To find D we can note that $D = \arctan\left(\widetilde{B}/\widetilde{A}\right)$, but thus we will not be able to recover D correctly, because $\arctan(x)$ is only defined in $\left[-\frac{\pi}{2}; \frac{\pi}{2}\right]$region, whereas $D \in (-\pi; \pi]$ and can be found properly considering the sign of known $\cos(D)$ and $\sin(D)$. That's why here we will use a notation of $D = \text{arctan2}\left(\widetilde{B}, \widetilde{A}\right)$ meaning that D can be found as $D = \arctan\left(\widetilde{B}/\widetilde{A}\right)$ with respect to signs of $\cos(D)$ and $\sin(D)$. Moreover, we can note that $D = \text{arctan2}\left(\widetilde{B}, \widetilde{A}\right) = \text{arctan2}(B, A)$, because $\sqrt{A^2 + B^2} \geq 0$ and such that we can multiply $\widetilde{A}$ and $\widetilde{B}$ on it without changing their signs.

Chapter 5

Observation of nanostructures motion using SEM

Contents

5.1 Introduction

In this chapter we discuss the possibility to detect and manipulate the oscillations of nano-scale structures using a scanning electron microscope (SEM), which is based on ideas presented in [62]. This work has been carried out in collaboration with Pierre Verlot (Institut Lumière Matière, Université Claude Bernand Lyon 1).

Outstanding achievements of modern physics in fabrication of micro- and nanostructures led to development of nanomechanics as a field of science. The difficulty of direct measurement of the position of a small mechanical oscillator has led to the development of different techniques. Nowadays, all detection methods are based on the fact that such resonators actively interact with electromagnetic environment. There are several commonly used optical methods of motion detection of micro-structures, such as Split Photo-diode technique [53] or interferometry, which are based on a detection of changes in position on phase of the laser light interacting with a nanostructure. The other popular method is applicable to membranes and double-clamped wires and beams. In this method resonator is introduced into electrical circuit, for example, is used as a one of two halves of a capacitor. In this case, position's oscillations lead to capacity's oscillations.

Such micro- and nano-electromechanical systems (MEMS and NEMS) found a large application in modern sensing technologies due to their huge sensitivity, which is a result of their small sizes and masses. For example, mechanical resonators are used to detect small quantities of adsorbed mass through shifts in oscillation frequency, which was initially observed using quartz plate [63]. Different types of NEMS structures demonstrates huge sensitivity [64, 65, 66, 67, 68], reaching nowadays the sensitivity of $1.3 \times 10^{-25} kg/\sqrt{Hz}$ for carbon nanotube based structures [69], which is already quite close to ultimate limit [70].

Besides that, the light field used for measurements always affects on a resonator. Such effect is called a back-action. And in case of its small size it becomes notable. Firstly, the possibility to affect a mechanical resonator via light field was observed in Fabry-Perot interferometer and was caused by radiation pressure [71]. Further, the possibility to cool a mechanical resonators using laser radiation pressure was demonstrated for a Fabry-Perot resonator [72, 73, 74], and some other equivalent systems [75, 76].

The possibility to act on the mechanical properties of resonator and, in particular, the possibility to cool it into its ground state is interesting for fundamental studies related with quantum effects. The theory of ground state cooling of a mechanical oscillator using dynamical back-action was presented in [77]. It has been reported that it is possible to actively cool the motion of a mechanical resonator to its ground state [15, 16, 14].

Further developments tends to successive decreasing of resonator's size in order to obtain lower mass and therefore higher sensitivity, lower power consumption, etc. For example, currently existing carbon nanotube resonators demonstrates fantastic mechanical properties: very high resonant frequencies [78, 79], high quality factors [80], and remarkable mass and force sensitivity [81, 82]. Nevertheless, application of all optical detection methods is limited by the diffraction limit of light. This makes it difficult to detect the motion of the structures, those size is less than 100 nm. In this order, we present a new method, which illuminates the oscillator with an electronic beam and uses secondary electrons to detect the motion of the nano-structures.

5.2 Experimental setup

5.2.1 A general principle

A SEM, as it follows from its name, uses a beam of accelerated electrons (e-beam) as a source of illumination. The e-beam is focused on the sample using an electromagnetic lens. Interaction with the sample leads to energy loses via many mechanisms, such as heat, light emission (cathodoluminescence), X-ray emission, emission of low-energy secondary electrons, etc. Besides, high-energy back-scattered electrons can be observed. All interaction's products carry information about the sample's properties. The SEM produces the two-dimensional (2D) map of the investigated structure by scanning with e-beam across a chosen area and detecting some of those signals. Usually, the image is formed by detecting secondary electrons (SEs), because they represent not only the relief of the structure, but also its composition, because they are produced in inelastic collisions.

A schematic representation of the experimental method is shown on the Figure 5.1,a. In our technique we use oscillations of SEs' signal to detect the motion of the nano-objects. A secondary electrons flux is modulated by the oscillations of the nanostructure shined by the focused e-beam. Spectral analysis of the signal of the secondary electron detector (SED) of the SEM reveals the oscillation modes of the investigated structure (see Figure 5.1,c).

A SEM has several modes of e-beam's position control. In spot mode e-beam is permanently fixed at one position. In line mode (1D mode) e-beam scans along one coordinate, but not the other In image mode (2D mode) e-beam scans across a rectangular area line-by-line.

During the experiment we acquire in imaging mode a 2D map (see Figure 5.1,b) of the sample by scanning the e-beam, when the object is fixed, i.e. changing in a signal is defined by relative position of e-beam and the object. Consequently, we obtain the same result, if we move the object with respect to the fixed e-beam. Thus, for one chosen and fixed position for both e-beam and object the signal will be modulated by oscillations of the object. The amplitude of this modulation is proportional to derivative of the signal with respect to the coordinate in the direction of object's oscillations at that relative position of e-beam and the object. It means that the best detection can be reached at the edge of the object (see inset on the Figure 5.1,b). For one-dimensional case the idea is governed by the formula:

$$\delta I_{SE}(t) \backsimeq \left(\frac{\partial I_{SE}}{\partial x}\right)_{x_0} \delta x(t), \tag{5.1}$$

where x_0 is a rest position and $I_{SE}(x)$ is an averaged in time signal from SED as a function of a relative position of the e-beam and the object.

Image contrast is a subject of adjustment, because it directly defines the detection sensitivity. All this is true while the amplitude of the motion is relatively small. It means that signal's gradient stays about the same for all relative positions of e-beam and the object during the oscillation period.

5.2.2 Description of the experimental configurations

To analyze a spectral composition of the signal from the SED we used an Agilent MXA N9020A spectrum analyzer (SA). Spectrum analyzer allows us to determine the amplitude of the signal for a given frequency within very wide range from 10 Hz to 26.5 GHz. Thus, the highest detection frequency is limited only by bandwidth of the SED, which is about 50 MHz.

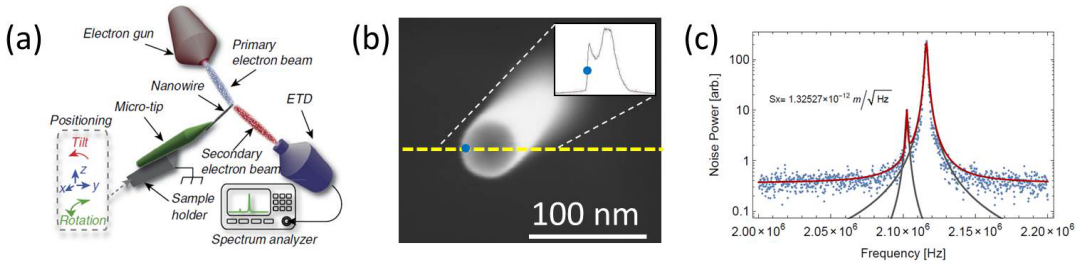

Figure 5.1: (a) A schematic representation of the experimental technique. Focused e-beam (blue) is shone on the singly-clamped oscillating structure. A secondary electrons flux (red) is modulated over the oscillations of the structure. A spectrum analyzer demonstrates oscillation modes of the investigated structures obtained from the video output of secondary electron detector of SEM (b) A SEM image of the nanowire in top-view configuration. The data on the inset shows intensity along the yellow dashed line. The blue dot shows a good position of the e-beam for the motion detection of the structure. (c) Obtained spectrum. It demonstrates two peaks corresponding to two mechanical modes of the nanowire and a thermal background (T = 300K). [62]

Typical experimental sample contains a lot of nanostructures. It is mounted on a universal positioning stage (allowing adjustment of sample's position in three-coordinate and three-angle coordinate systems) inside the chamber of SEM to provide initial coarse tuning of the sample's position with respect to the e-beam.

Inside the microscope's chamber the sample is stored in a secondary vacuum. Better vacuum provides less pollution of the sample due to deposition and reduces the damping factor of mechanical resonator. To provide less level of sample's pollution a plasma cleaner is recommended. It is a source of low-energy plasma allowing to remove the impurities and contaminations formed on the investigated structure under the influence of e-beam. All removed contaminants are then pumped out of the chamber by the vacuum system.

We used 2 different microscopes. First is the Zeiss Ultra55+ SEM, which provides better vacuum in a sample's chamber ($\sim 2-3\cdot10^{-6}$ mbar) and a better stability. It has wide operating voltage range from 0.02 to 30 kV and reaches sub-nanometer resolutions.

Second - FEI Quanta SEM, which allows us to perform the experiments at T ~6 K.

5.3 Experimental structures

For this experiment we have got several different types of samples. Some of them have top-view (planar) configuration, that means that we observe the structure from the top. Some structures have side-view configuration (we observe them from the side), that allows to investigate spectra over the length of the structures.

5.3.1 Vapor-liquid-solid growth mechanism

Most amount of the structures that we investigated were grown using the vapor-liquid-solid (VLS) growth mechanism initiated with a gold catalyst [83]. The VLS mechanism is a bottom-up technique that is often used for the growth of one-dimensional (1D) structures, such as

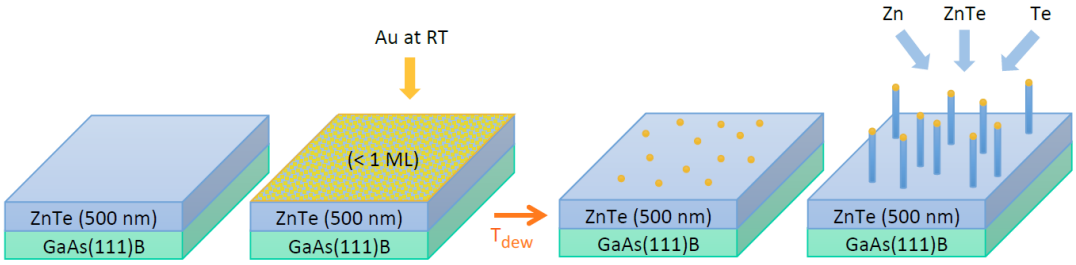

Figure 5.2: Schematic illustration of $ZnTe$ nanowires growth from the vapor phases. This reaction is catalyzed by gold-silicon droplet deposited on the wafer surface.

nanowires, from chemical vapour deposition or molecular beam epitaxy. A presence of liquid alloy phase increases significantly the growth speed (with respect to the direct adsorption of a gas phase on to a solid surface) due to quick adsorption of a vapour to supersaturation levels, from which crystal occurs. Localization of liquid droplets allows to grow 1D structures. The physical characteristics of such structures are controllable and depend on the size and physical properties of the liquid alloy.

A schematic illustration of $ZnTe$ nanowires growth from the vapor phases is shown on the Figure 5.2. [84]

Generally, the VLS process can be described as follows:

1. Preparation of a liquid alloy droplet upon the substrate.

   (a) A thin film of catalyst (typically gold is used) is deposited onto a wafer substrate by sputter deposition or thermal evaporation.

   (b) The wafer is annealed at temperatures higher than the eutectic point of this two materials, creating alloy droplets on the wafer surface. The thicker the film, the larger the droplets.

2. Axial crystal growth due to supersaturation and nucleation at the liquid/solid interface in chemical or physical vapour deposition process, which takes place in a vacuum deposition system.

As a prior step this method requires an appropriate preparation of substrate.

5.3.2 Samples with planar configuration

The most interesting results we obtained with InAs nanowires grown by Moira HOCEVAR using VLS mechanism described in the previous subsection. Each structure is a nanowire of several μm length and several tens of nm in diameter. All investigated structures have a wurtzite crystal structure and grow in the [0001] growth direction. It means that structures have hexagonal cross-sections.

We have got several samples with different structure's density and diameters (20 and 50 nm).

On the example of one of the sample (NW218) we briefly consider the growing process and parameters: the substrate was prepared by dispersion of colloids with diameter 50nm, and

further desoxydation at 500°C under As flux. The growth were done at 420°C with a In/As ratio of 50 by opening In shutter during 75 min.

A typical SEM image obtained with conventional in-lens SE detector are shown later in the Subsection 5.3.2.2.

5.3.2.1 Measurement of the height of the nanowire

To measure the height of the nanowire in planar configuration, we focused SEM image, firstly, on the top of the structure, then on its basis. Thus, relative changing of the working distance (WD) of the objective is equal to the structure's height. This approach is demonstrated on the Figure5.3. We can see hexagonal shape of the structure, when we are focused on its basis, and a round shape given by the gold droplet, when focus is on the top. Precision of read-out of the working distance is about 1 nm, but accuracy of height's detection is not as good and limited by accuracy of personal perception of focused image of the SEM's operator. With our samples we assume this value to be less than 100 nm.

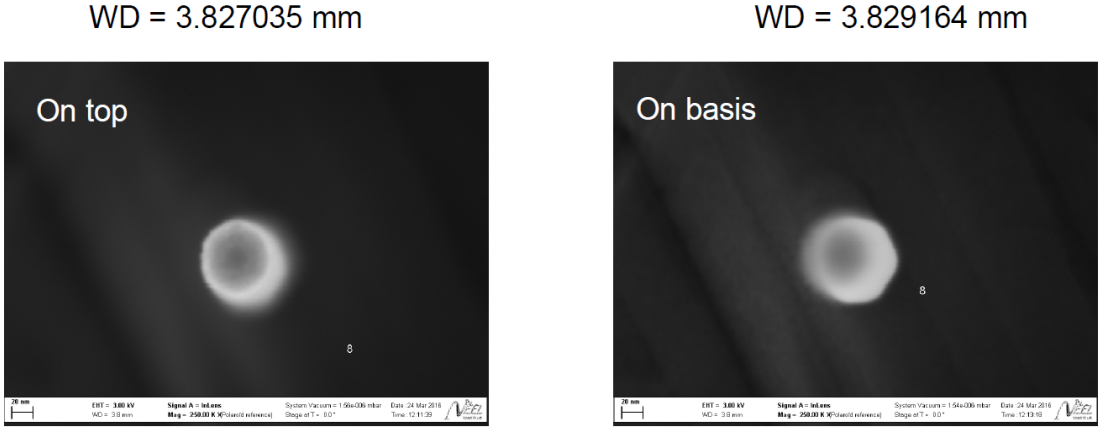

Figure 5.3: Demonstration of measurement of the structure's height. E-beam is focused (a) at the top (b) at the bottom of the investigated structure. Difference in working distances for this cases gives approximate height of the structure. Precision of the method is less than 100 nm.

5.3.2.2 Identification of unbroken structures

We can make a preliminary conclusion about unbroken structures using the information about the shape of the top surface of the investigated structure. If the structure is broken the shape will be hexagonal as at the basis. Whereas for unbroken structures the shape is round, because of the gold droplet at the top of the nanowires, which remains from the growing technique.

Nevertheless, in Zeiss SEM we also have a possibility for simple distinction of broken and unbroken structures over some relatively big sample's surface by using an Energy Selective Backscattered (ESB) in-lens detector. This method is more practical, because it does not required investigations of the structures one by one. The ESB detector registers only secondary electrons, which energy is higher than some certain value. By adjusting this limit we can separate SEs coming from different materials, because they have different energies. Thus, image obtained

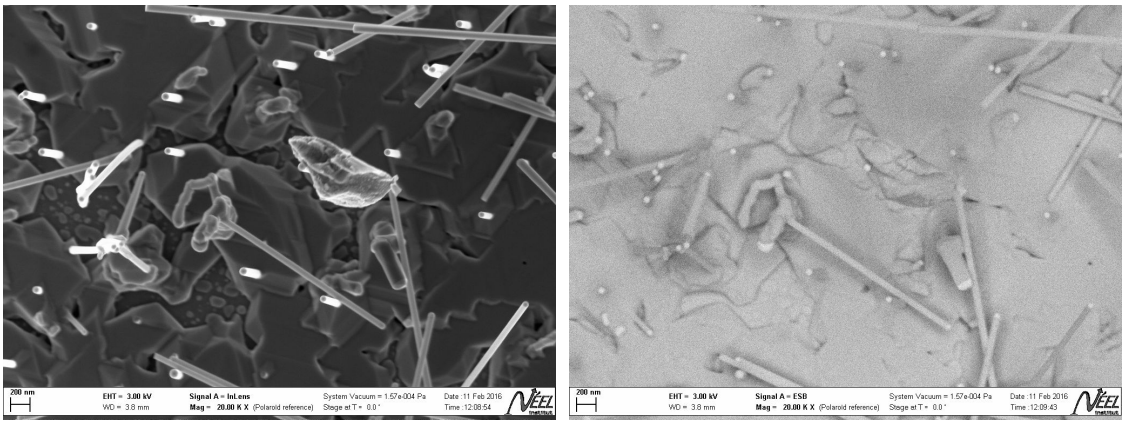

(a) (b)

Figure 5.4: SEM images of InAs nanowires obtained with (a) conventional SE in-lens detector, (b) Energy Selective Back-scattered (ESB) detector. The ESB detector allows to emphasize the chemical composition with an image's contrast. It helps us to identify gold droplets (appearing as white spots) on the top of the nanowires and identify unbroken structures.

with ESB detector emphasizes the chemical composition of the investigated structure. In our case we can easily identify gold droplets on the top of the nanowires (see Figure 5.4b).

5.3.2.3 Calculations of eigenfrequencies

To evaluate spectral range, in which we expect to observe eigenfrequencies of experimental structures, we carried out theoretical calculations using COMSOL. In our model the structure was represented as a right hexagonal prism with a height (h) and a radius of circumcircle for its basis (a). Real structures are not ideal and their cross-section is not a regular hexagon, which leads to difference in frequencies of two orthogonal modes of the same order. On the Figure 5.5 a regular hexagon is shown (black contour) compare with a real cross-section (blue contour). We introduce a quantitative parameter of such non-symmetry (k) as a ratio between a shortest distance from the center to the edge for real and ideal structures.

In our model for the real structure we assume the same value of side's length as for a regular hexagon. Due to this fact, the mass for the real and ideal structures is not the same. And the bigger non-symmetry (smaller parameter 'k') the bigger mass difference, which is a disadvantage of this model. Nevertheless, experimentally we mostly observed a mechanical modes splitting of about 1% that tells us about high symmetry of the our structures. For example, experimental spectrum on the Figure 5.11 has a splitting of about 0.6% that corresponds to $k > 0.99$. So model's mass loss is negligible in the range of k, for which we performed the calculations, that makes the results obtained with this model reliable.

A general view of the first three vibration modes is presented on the Figure 5.6a. Values of the different order eigenfrequencies of symmetric (ideal) structure with typical for our sample parameters is shown on the Figure 5.6b. We see that the first mode is in MHz range. Vibration modes of different orders demonstrate the same behavior with the change of model's parameters, so the data only for the first order mode are presented on the Figures 5.6c and 5.6d.

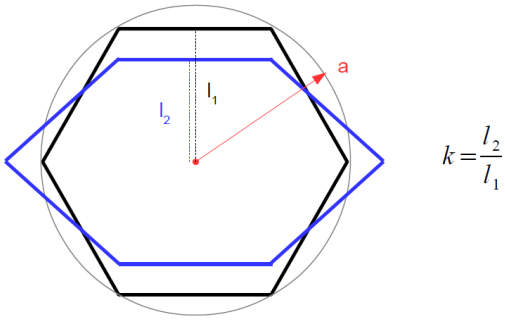

Figure 5.5: Schematic illustration of structure's cross-section for ideal (black) and real (blue) model. Parameter 'a' is a radius of circumcircle for regular hexagon, l_1- shortest distance from the center to the edge of regular hexagon, which depends only on 'a'; l_2 - the same value for real hexagon; parameter 'k' is a ratio between l_2 and l_1.

We can see that frequency grows linearly with increase of a radius and drops quadratically with increase of structure's height, as it is expected for the mechanics of a singly clamped narrow beam [25].

$$f \sim \frac{R}{L^2}$$

Decreasing of parameter 'k' breaks the symmetry of the structure and therefore splits frequencies of orthogonal modes of the same order.

5.3.3 Samples with side-view configuration

We had also at our disposal several samples in side-view configuration.

Several samples containing ZnTe nanowires were grown by Marta ORRU (see Figure 5.7,a) using the VLS technology, which is presented above. All samples were grown at GaAs (111) substrate with ZnTe (111) buffer layer with an Au as a catalyst. To prepare the samples for side-view observations a small piece (~ 1 mm^2) was cut from the relatively big sample. Such piece always has a triangular shape, because of the growth direction. This piece then was glued on a special holder with a cantilever with a flat side oriented perpendicularly to the holder's substrate. These structures have small diameters of about 15 nm, which opens up some limitation of our system (see Subsection 5.6.3).

Some samples were provided by Pierre VERLOT (silicon carbide nanowires) and Alexandros TAVERNARAKIS (carbon nanotubes) presented also in Figure 5.7. The structures were grown from a catalyst directly on a cantilever by a CVD method at a temperature which is progressively ramped up to $830\,C$, into an atmosphere of Ar and CH_4 as flux.

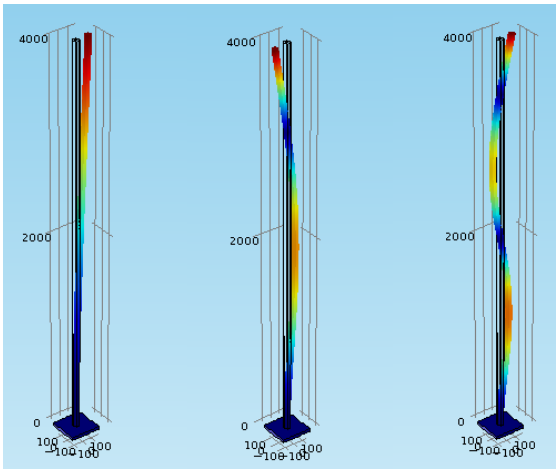

(a)

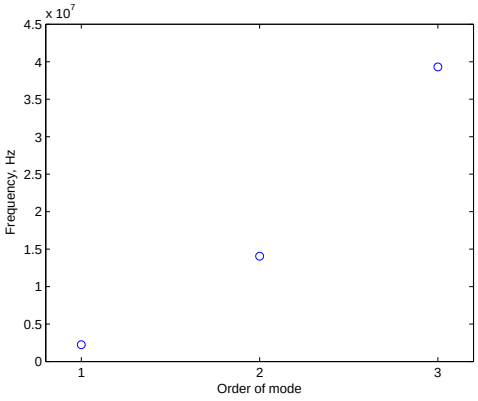

(b)

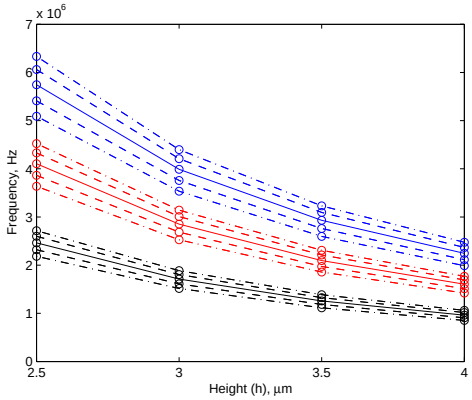

(c)

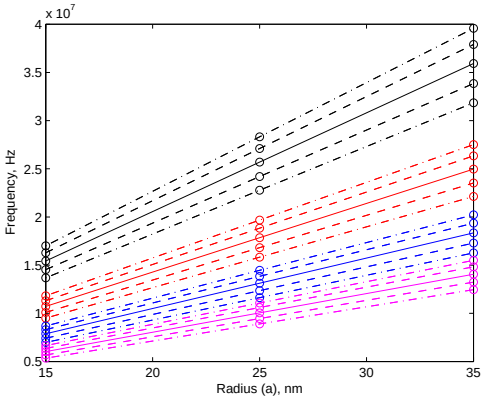

(d)

Figure 5.6: (a) First three vibrations modes are shown from left to right. (b) Values for the different order of eigenmodes for the structure with h = 4.0 μm, a = 35 nm, k = 1. (c) Dependence of first order eigenfrequency on the height 'h' of the structure for 3 different radius 'a': black - 15 nm, red - 25 nm, blue - 35 nm. (d) Dependence of first order eigenfrequency on the radius 'a' of the structure for 4 different height 'h': black - 2.5 μm, red - 3 μm, blue - 3.5 μm, magenta - 4.0 μm. Different line styles on the plots (c) and (d) correspond to the different parameter 'k': solid line - 1, dashed line - 0.95, dash-doted line - 0.9.

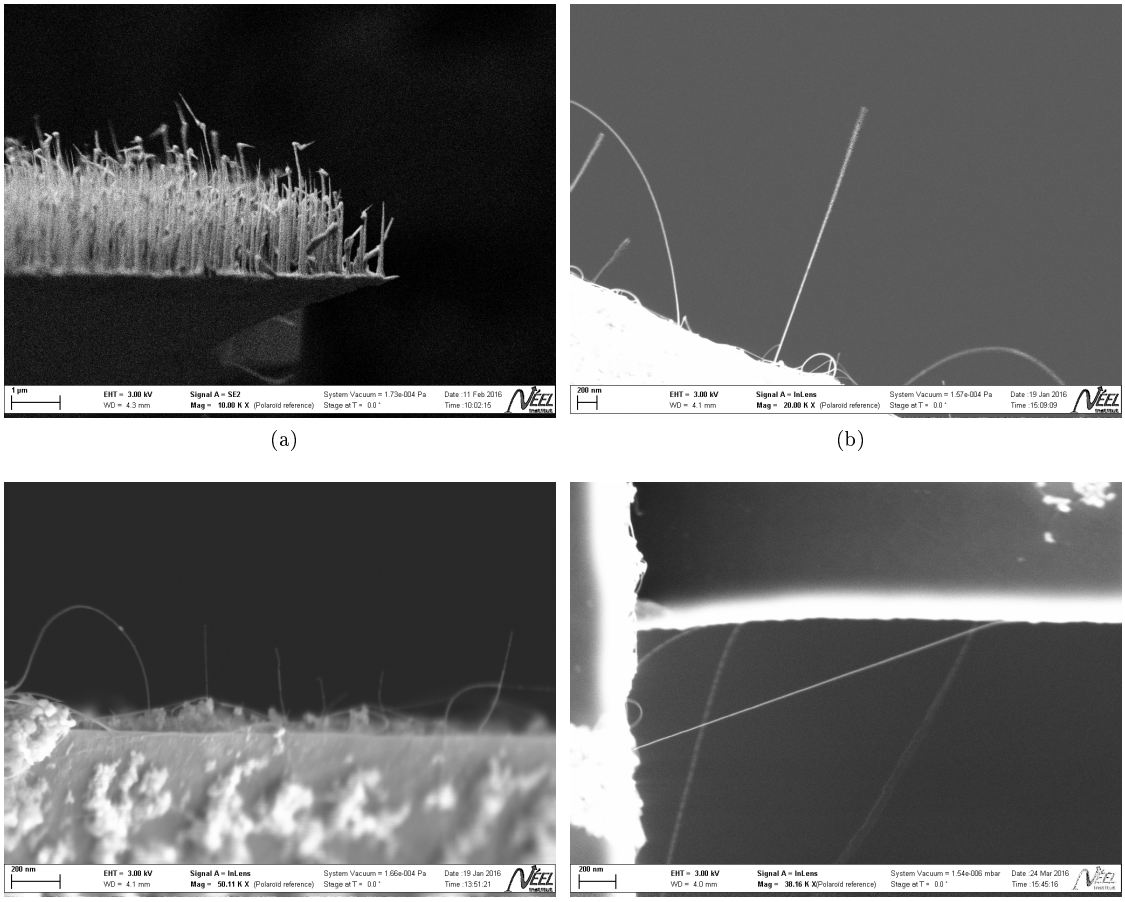

(a) (b)

(c) (d)

Figure 5.7: Nanowires grown for observations in side-view configuration. (a) ZnTe nanowires from Marta ORRU. (b) Silicon Carbide nanowires from Pierre VERLOT (c) single-clamped and (d) double-clamped carbon nanotubes from Alexandros TAVERNARAKIS.

5.4 Back-action effect

The back-action effect is that any measurements of the resonator's dynamics affect on its property. Such contribution becomes important for the small devices.

Dynamics of one-dimensional mechanical resonator is governed by the general equation:

$$M\,\frac{\partial^2 x(t)}{\partial t^2} = -k\,x(t) - M\,\Gamma_0\,\frac{\partial x(t)}{\partial t} + F_{th}(t), \tag{5.2}$$

where M is an effective mass, k is a spring constant, Γ_0 is intrinsic damping rate, $F_{th}(t)$ is the thermal Langevin force, which is responsible for the Brownian motion [85], with the spectral density $S_F^{th}[\Omega] = 2\,M\,\Gamma_0\,k_B\,T$, where k_B is a Boltzmann constant.

Solving such equation in Fourier space we obtain that mechanical susceptibility $\chi[\Omega]$ at given frequency Ω is defined as:

$$\chi[\Omega] = \frac{1}{M\,(\Omega_0^2 - \Omega^2 - i\Gamma_0\Omega)}, \tag{5.3}$$

where Ω_0 is a resonance frequency. Quality factor of the system is then defined as $Q = \Omega_0/\Gamma_0$.

When we try to measure the mechanical system we influence on it. Such influence can be described as a external force field, which depends on the coordinate. In the simple one-dimensional case at first approximation we can write [62]:

$$F_{ext}(x) = F_0 + x \cdot \frac{\partial F}{\partial x}. \tag{5.4}$$

Here $\frac{\partial F}{\partial x}$ is a force gradient. The system in such field then can be described by the same equations, but with introduction some effective parameters:

$$k_{eff} = k + \frac{\partial F}{\partial x}, \tag{5.5}$$

where k is a spring constant. As a result, it affects on system dynamics through:

$$\omega = \sqrt{\frac{k}{M}} \rightarrow \omega_{eff} = \sqrt{\frac{k_{eff}}{M}} \tag{5.6}$$

In more general case, to describe the effect of external force field F_{ext} we need to add it to the right part of equation (5.2). Taking into account that, firstly, the point of the application of external force vary in a time, secondly, the effect can be retarded, we finally obtain the equation:

$$M\,\frac{\partial^2 x(t)}{\partial t^2} = -k\,x(t) - M\,\Gamma_0\,\frac{\partial x(t)}{\partial t} + F_{th}(t) + (R * F_{ext}(x_p))(t) \tag{5.7}$$

where x_p is the time-dependent point of application of the force, $R(t)$ is a time response function introduced to take into account some possible retardation effects.

In general, this equation can be represented in the same style as in absence of external force with introducing an effective mechanical susceptibility $\chi_{eff}[\Omega]$, resonance frequency Ω_{eff} and damping Γ_{eff} (depending on the retardation effect). And the effective temperature can be defined $T_{eff} \approx T\,\frac{\Gamma_0}{\Gamma_{eff}}$.

In the work [62] it was presented that dynamical back-action cooling can be mediated not only by electromagnetic resonance but also by an electro-thermal mechanism.

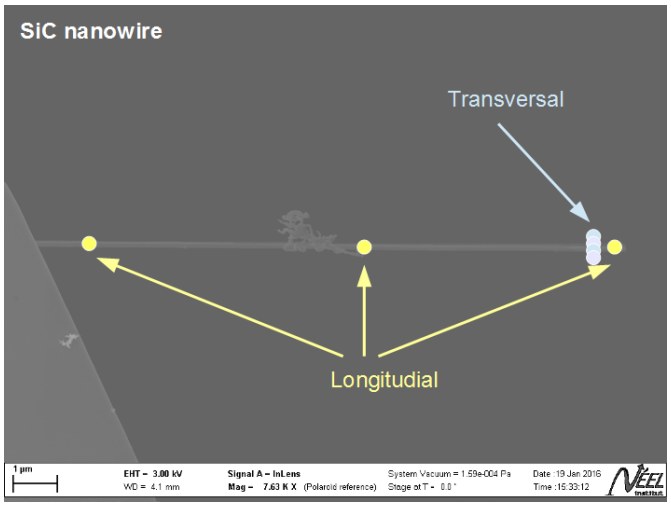

Figure 5.8: Demonstration of longitudinal (yellow) and transversal (light-blue) types of experiments for the structures in side-view configuration.

5.5 Experimental results

5.5.1 Dependence of the back-action on longitudinal and transversal position of e-beam

For samples in side-view configuration we can measure the longitudinal (for different e-beam position along the structure) and transversal (for different e-beam position perpendicularly to the structure) dependencies of spectrum's behavior (see demonstration on the Figure 5.8).

For the SiC nanowire presented on a Figure 5.8 we measured 13 longitudinal spectra at 5 K with about 1 μm step along each of the left and the right sides of the structure. They are shown on the Figure 5.9 at the left and right side from the structure's image respectively. Experimental spectra are shifted to be presented oppositely to the point on the structure where it was measured. The experiment was configured in a quick mode that means that each spectra were obtained in a wide range, quickly and with relatively big bandwidth, not allowing to define the width of the mechanical peak. But in this experiment only information about presence of the peak was required.

We found that on the right side we can detect the motion of the structure starting almost from its basis. However, we were not able to detect it closer to the free-end, that probably means that detection sensitivity becomes too small. Oppositely, for the left side, we were not able to detect any motion (except one point) despite that the sensitivity of the motion detection is almost equal for both sides of the structure (see Figure 5.10,c). Such effect was observed in [62] and is related to the dynamical back-action (See Section 5.4). It happens when the force exerted by the e-beam has the same direction on both sides of the structure, for example if it comes from a thermally induced bending [50, 86]. Thus, the e-beam damps the motion of the structure, when it is focused on the one side (see data for the left side) and oppositely for the other side it cancels the intrinsic damping. More precise measurements are required to demonstrate such effect to the full. A transverse evolution of the e-beam back-action was measured in [62].

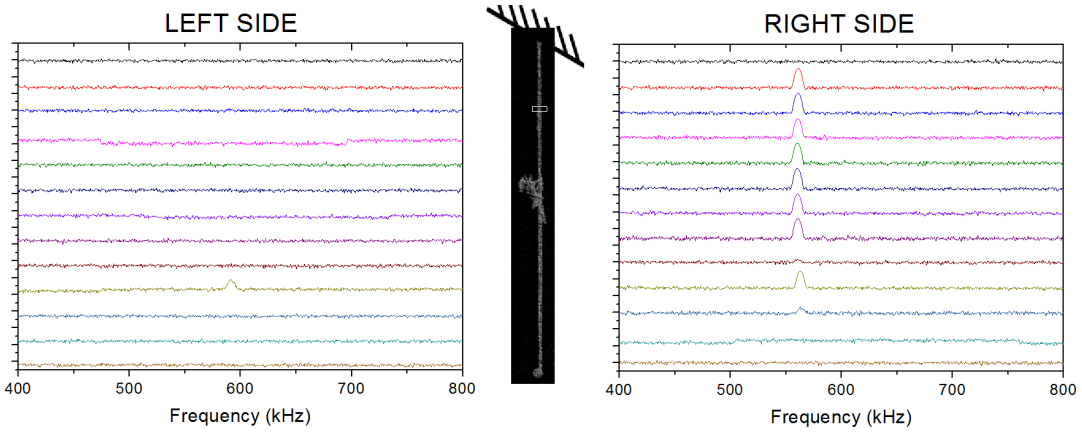

Figure 5.9: Longitudinal spectra for the cases when e-beam is placed (left) on the left edge of the structure (right) on the right edge of the structure. The structure is a SiC nanowire presented on the Figure 5.8. White rectangle at the level of the third spectra counting from the structure basis is zoomed at the Figure 5.10,a.

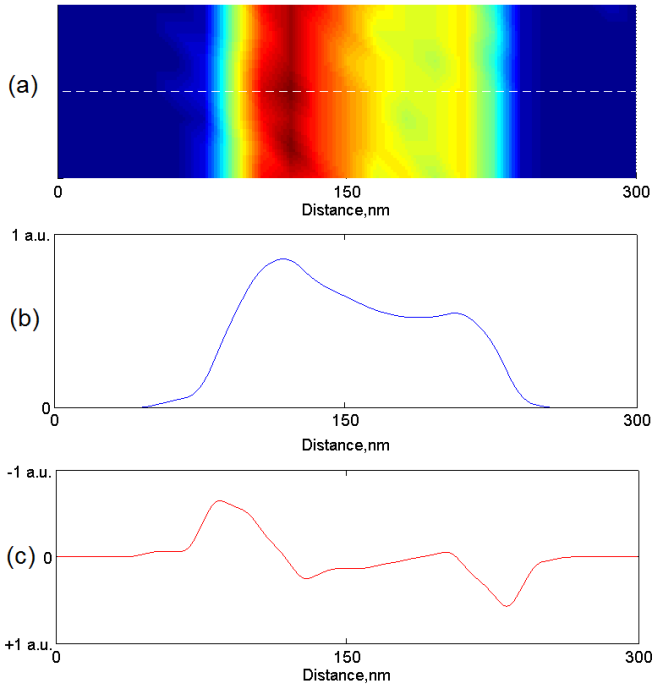

Figure 5.10: (a) Zoom of the SEM image at the level of the third spectra counting from the structure basis (see Figure 5.9). White dashed line shows a position for which a line cut on the plot (b) is presented. (b) DC detector voltage at the level of the third spectra counting from the structure basis. (b) Sensitivity of the motion detection, which is defined as a derivative of the DC detector voltage.

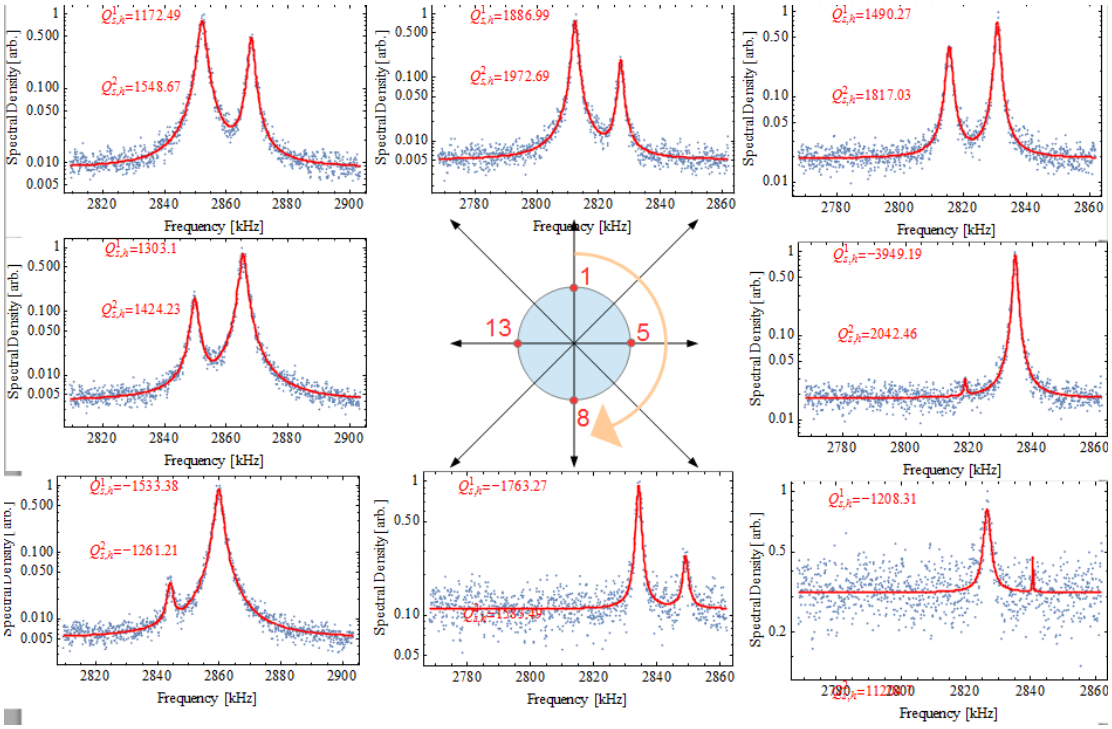

Figure 5.11: Experimental spectra for 9 from 16 experimental points obtained during the angular dependence measurement of an InAs nanowire (see Figure 5.13,a). Red dot demonstrates position of the e-beam for each spectrum and the arrow shows the corresponding spectrum. For each spectra raw data are shown by blue color and a fit with a double Lorentzian model by red color.

5.5.2 Dependence of the back-action on angular position of e-beam

For the InAs nanowire (a structure with a planar orientation, see Figure 5.13,a for the SEM image of the investigated structure) we measured spectra for different angular position of the e-beam with respect to the top facet of the structure (see Figure 5.11). For each angular position e-beam was placed at the most sensitive point on a radius, which often corresponds to the edge of the structure. A typical experimental spectra demonstrates 2 peaks which are related to two orthogonal mechanical vibration modes of the structure. We acquired data for 16 points on the upper surface circumference of the nanowire of interest, which means 22.5 degree step in between of 2 points. For each angular position we collected 3 spectra. Obtained spectra were subsequently fitted using a double Lorentzian model and the obtained fitting parameters (frequency, amplitude and damping rate) were averaged in order to reduce the impact of the position drifts. On the Figure 5.11 experimental data for 9 from 16 measured points are shown. Red dot demonstrates position of the e-beam for each spectrum and the arrow shows the corresponding spectrum. For simplicity of demonstration, a spectrum corresponding to certain e-beam position is represented from the same side of the structure's schematic image, which is placed in the center.

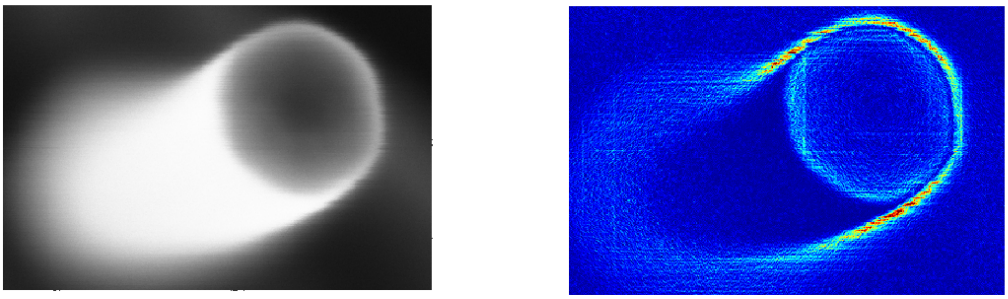

(a) (b)

Figure 5.12: (a) SEM image of a real InAs nanowire. (b) Sensitivity map: color represents the amplitude of the sensitivity. Red color correspond to high sensitivity, whereas blue color means low sensitivity.

5.5.2.1 Analysis of peaks' heights

In 2D case detection sensitivity is a vector, which direction is defined by the direction of quickest raise of image intensity. Besides, possibility to detect the structures motion in some given direction is defined by the projection of this vector on the oscillation direction. For most experimental points e-beam is located on the edge of the structure where sensitivity vector is coincident with a radius of the structure. It means that from point to point we should observe how one peak on a spectra is increasing, whereas the other - decreasing. And then vice versa. Experimental data presented on a Figure 5.11 confirms such behavior. Nevertheless, we found that independent studies of the measurement sensitivity for each oscillation direction are not possible due to small drift of the experimental system and, as a result, poor control of the electro-mechanical gradient.

Moreover, a real structure view does not correspond the top view, because structures are not exactly perpendicular to the substrate. It also affects the motion sensitivity on a different sides of the structure. A real InAs nanowire and its sensitivity map are presented on the Figure 5.12.

However, the measurement sensitivities are given by the projection of the gradient of Secondary Electrons 2D map at the certain experimental point over each vibrational direction. And as long as it remains radial, we can expect the ratio between peaks' heights behaves as a tangent of angular e-beam position. It allows us to get rid of the knowledge of the exact value of the sensitivity at each point. More formally it is represented by these equations:

$$g_i \sim \vec{\nabla} I_{SE} \cdot \vec{e_i}$$

$$\vec{e_1} \perp \vec{e_2}$$

$$r = \frac{g_1}{g_2} = \frac{sin(\theta - \theta_0)}{cos(\theta - \theta_0)} = tan(\theta - \theta_0)$$

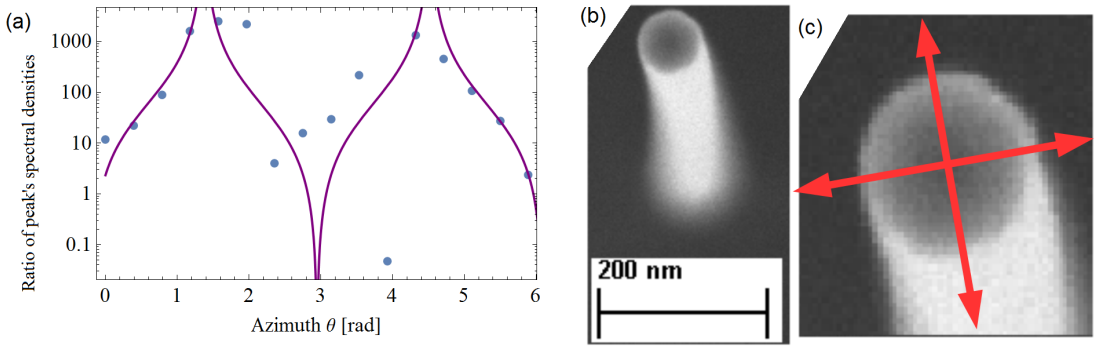

Figure 5.13: (a) Dependence of the ratio between peaks' spectral densities on the angular position of e-beam. Points - experimental data, line - fit with tangent-square model. (b) SEM image of the investigated InAs nanowire. (c) Directions of two orthogonal mechanical modes of the structure extracted from the angular dependence of ratio of peaks' spectral densities.

where g_i defines motion detectivity for each mode, and θ_0 defines the direction of the second mode ($\vec{e_2}$), r is a ratio between them.

For each experimental point from the data set for each peak we calculated the spectral density, which is proportional to the square of the displacements. Thus, we fit this data with a tangent-square model

$$Model(a, \theta_0) = a \cdot tan^2(\theta - \theta_0)$$

as shown on the Figure 5.13a.

From the value of θ_0 we can determine the orientation of two vibrational modes with respect to the image of the investigated structure. The result is shown on the Figure 5.13c.

5.5.2.2 Analysis of peaks' central positions

We found out that central frequencies for both modes have overall drift and a periodic Sine behavior with the angle of e-beam position. Results are presented on the Figure 5.14.

A systematic linear frequency increase taking place for both mechanical resonance modes was observed and does not depend on the clockwise or counterclockwise direction of going around of the experimental points. Thus, we relate it to some static mechanism occurring during the experiment (deposition, charge doping, etc). Remaining after subtraction of this linear increase frequencies dependencies demonstrate a 2π-periodic behavior. This periodicity leads us to think that this effect is caused by heating of the structure with the e-beam. And indeed, due to non-perpendicularity of the structure (with respect to the substrate) each experimental point experiences different interaction of a e-beam and a structure.

Besides, obtained data show that the evolution of the frequencies splitting between the two orthogonal modes is π-periodic (see Figure 5.15). We expect that such behavior is a signature of radial force gradients, that is the direct manifestation of the measurement back-action force (see Section 5.4 and Ref. [62]).

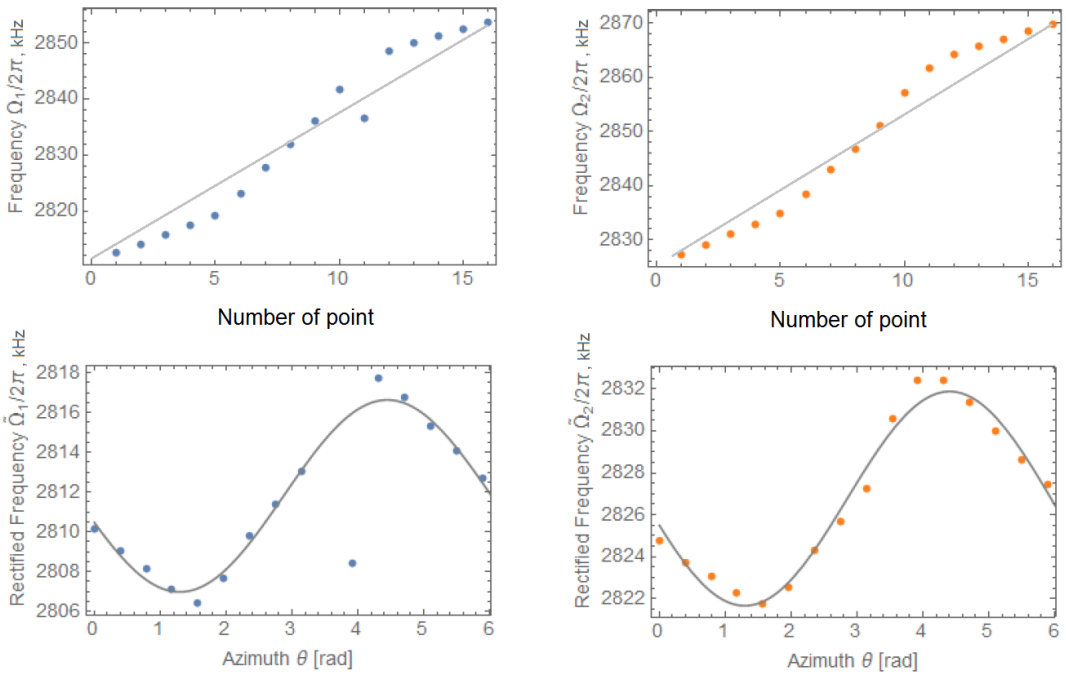

Figure 5.14: Analysis of angular dependence of the central frequency of (left column, blue) first peak (right column, yellow) second peak. Absolute values of central frequencies are presented on the upper line, constant shift (obtained from a line fit that is shown by the gray lines) is subtracted on the down line. Solid curves on the down images - fit of the points with a Sin model.

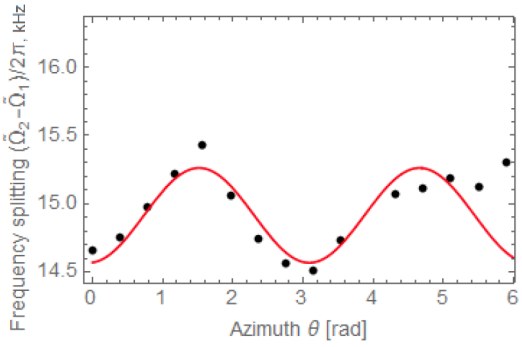

Figure 5.15: Frequency splitting between the two orthogonal modes. Point - experimental data, solid red curve - π-periodic sinusoidal fit.

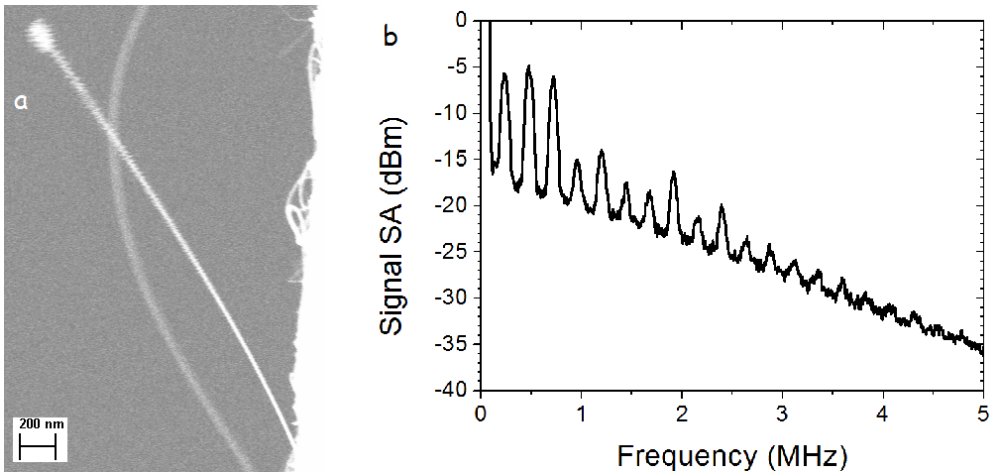

Figure 5.16: Observations of higher order modes (harmonics) for the SiC nanowire with big mass. (a) An SEM image of the structure. (b) Spectrum of many harmonics obtained with the e-beam placed at the top of the structure.

5.5.3 Higher order modes

For the structures, which oscillates at lower frequency, we observed higher order modes. For example, a SiC nanowire on the Figure 5.16 has a 'ball' on its free end, which increases its mass and decreases oscillation frequency. Related spectrum is shown on the same image. The e-beam was placed at the top of the structure.

5.6 Limitations of the technique

Despite all the advantages of this technique of motion detection, it also has some drawbacks.

5.6.1 Deposition

The most significant problem is that we deposit matter on the structure, that makes structure polluted and that changes its eigenfrequencies.

On the Figure 5.17 three spectra for different time are presented for the typical carbon nanotube. Spectra were obtained in the second experimental setup (FEI Quanta SEM) at T $\sim$ 6 K. Spectral line demonstrates quick shift with frequency about 240 Hz/s that limits the measurements as well as calculations of real Q-factor, because acquisition time for that spectra was equal to 4.6 s.

For the first experimental setup (Zeiss Ultra55+ SEM) at T $\sim$ 300 K we have also observed frequency shift for the carbon nanotubes. Assuming that the spring constant doesn't change over deposition process we can find a mass change in a time from the frequency shift using the formula:

$$r_m(t) = \frac{m(t)}{m(0)} = \left(\frac{f(0)}{f(t)}\right)^2$$

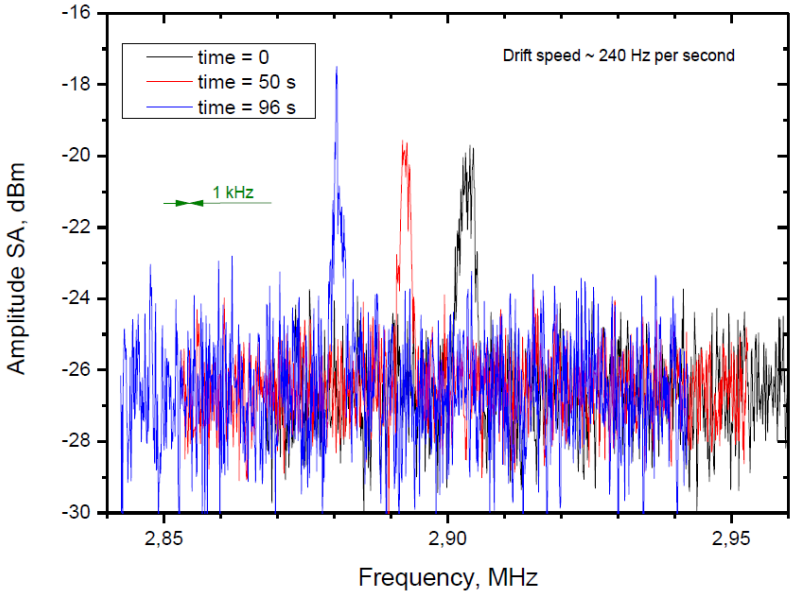

Figure 5.17: A typical frequency shift in time observed for the carbon nanotubes using FEI Quanta SEM at T = 6 K. It occurs due to the mass deposition over the time under the e-beam.

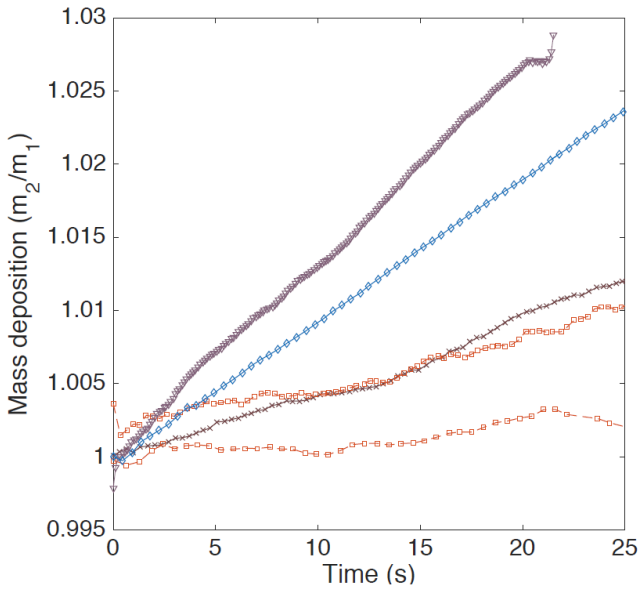

Figure 5.18: Mass deposition over time for the carbon nanotube at T = 300 K. Experimental data were acquired at different experimental conditions for acceleration current and position of the e-beam. Brown cross - low current, e-beam is in the middle; red empty square and blue empty diamond - low current, e-beam is on the edge, dark purple reversed triangle - double the current, e-beam is on the edge.

A LabView script written by Alexandros TAVERNARAKIS was used to collect the data for mass deposition over the time (Figure 5.18). This script reads the spectrum from SA right after it was acquired, finds the peak on the spectrum and returns position of the maximum measured value as a central frequency of the peak. Experimental data were acquired for one carbon nanotube at different experimental conditions for acceleration current and position of the e-beam. We observed almost linear mass deposition over time, but the speed of the deposition changes from one measurement to another. First of all, the deposition of mass is realized precisely where the electrons penetrate and interact with the matter (the nanotube). Since the nanotube is thermally driven it presents a thermal variance. The bigger the variance the slower the deposition. Unfortunately, we were not able to confirm it experimentally, because carbon nanotubes are very small and thus extremely sensitive to external perturbations so by just slightly moving the e-beam the deposition slope changes a lot. You can see it comparing 3 data sets (2 presented by red empty square and one - by blue empty diamond) obtained when the e-beam is placed on the edge of the structure. Nevertheless, we can conclude that we can manipulate the deposition speed by slightly moving the e-beam and can decrease it up to almost zero-deposition case (lowest curve on the Figure).

Besides, the acceleration current is the catalyst of the deposition, so by increasing the current the deposition also increases. Related data presented by dark purple reversed triangles.

5.6.2 Instability of the central positions

On the long-time acquired 2D image of the structure in side-view configuration (Figure 5.19) we can see how the structure vibrates with two different central positions. Quantitative measurements of such structures is complicated, because change in a central position of oscillation means change in a detection sensitivity. Such kind of instability is caused by a heating of the mechanical resonator due to a presence of e-beam at its center [75, 87]. When we shine a nanowire at its center (where the probability of the structure's presence is the maximum) by a strong e-beam we heat it and therefore excite the mechanical oscillations of the structure. But it decreases the probability of the structure's presence at the center and therefore brings it back to equilibrium condition. And then e-beam heats again the structure, and so on, and so forth... Finally, we observe an instability of the oscillations.

5.6.3 Structures' reaction on a presence of e-beam

We also observed that some closely spaced thin nanowires feel the electrostatic environment from the scanning e-beam. As a result structures are bending in the scan direction of the e-beam (Figure 5.20).

E-beam scanning area can be physically rotated respectively to the sample. However, on the screen scanning area is always represented in the same way. It makes an illusion that samples physically rotates respectively to the e-beam. We used that feature and confirmed that bending direction is always coincident with the scanning direction of e-beam.

In such conditions it is very difficult to place the e-beam on the certain place at the structure, because its position on the SEM image doesn't correspond to the position, when the e-beam is turned to the spot mode.

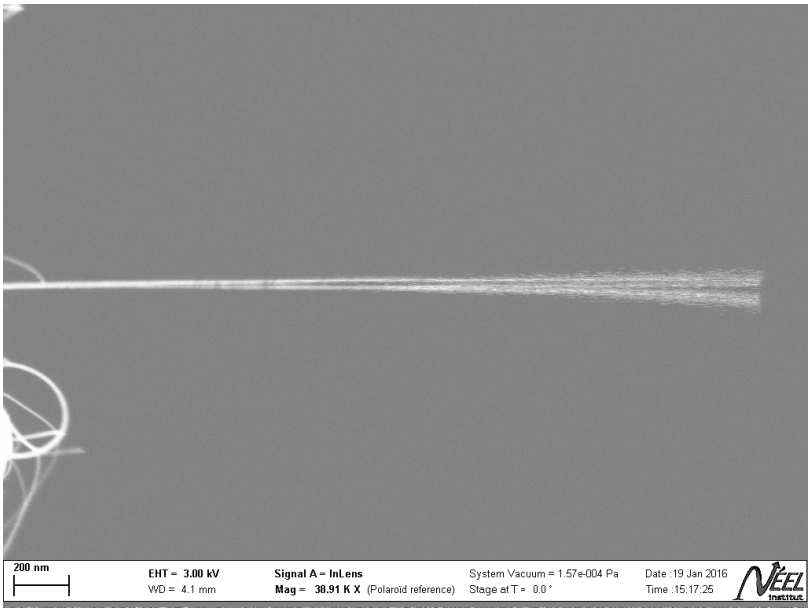

Figure 5.19: Demonstration of vibrations around two different central positions for the SiC nanowire.

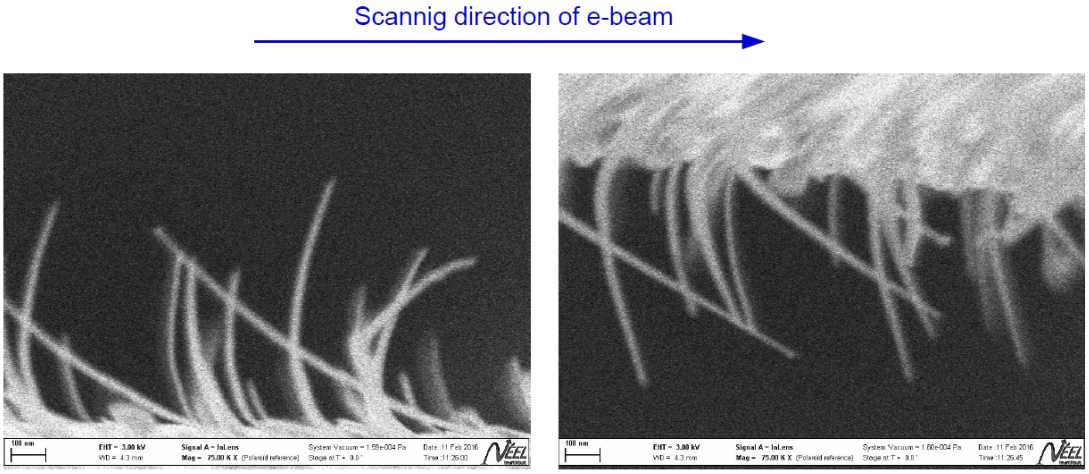

Figure 5.20: Reaction of the structures (ZnTe nanowires) on a presence of e-beam. On the right image scanning area of e-beam is rotated by 180 degree that changes the direction of e-beam scan and confirms that the direction of structures' bending is coincident with the direction of e-beam scanning.

5.7 Conclusions

In this chapter the original technique of nanostructures motion observation using SEM was presented. We obtained satisfactory results, which demonstrate the possibility to detect such motion at the level comparable with optical measurements. This method allows to get access to the motion's measurements for the structures as small as 20 nm, whereas all optical methods are limited by the light diffraction limit. The fact that experimental sample is placed straightforwardly in the SEM allows us to obtain a good quality images of the sample in a real time.

We have also demonstrated that we can suppress the motion of structure via back-action effect. However, further experiments are required to estimate the possibility to cool down the motion.

We also discussed main limitations of the technique. Mass deposition is definitely the most important of them. In order to make the SEM measurements as non-invasive as possible it it is required to have a plasma cleaner from the technical side, and to carry out additional experiments for deeper understanding of conditions for realization of zero-deposition case.

It is also interesting to note that it is possible to distinguish 2 mechanical modes, that is a benefit for an ultra-sensitive nano-mechanical detection, related to the corresponding ability to self-discriminate the external noise mode in phase-coherent measurements [88, 89].

Chapter 6

Summary and Perspectives

This thesis work is devoted to studying of the opto-mechanical interactions, which are becoming significant for the micro- and nano-structures due to their small sizes. A coupling between theirs optical and mechanical properties opens up a wide range of possible applications. Within the framework of the thesis the efforts were concentrated on demonstration of QDs strain-tuning and mapping for the QD-based micro-structures as well as on the detection and manipulation of the micro-structures motion.

Thesis begins with an overview about semiconductor QDs and photonic wires. Theirs general properties as well as the fabrication process of self-assembled InAs QDs embedded in a GaAs photonic wire were presented.

In Chapter 3 the experimental technique allowing static large range (several meV) strain tuning of semiconductor QDs embedded in a photonic wires were developed. Presented method also allows to determine the exact positions of QDs inside the structure. This technique is applicable to various types of micro-structures, in which emission of QD is coupled to a strain field. One of the key advantages of this method is a possibility to operate with deeply embedded QDs, which are therefore inaccessible with some optical methods.

In the next chapter a possibility of an optical actuation of photonic wire's motion was demonstrated. Comparing to existing technique of piezo-excitation it allows us to excite higher order modes, that was also shown. Despite that the origin of laser interaction with a photonic wire was not completely determined, presented results are very promising for further investigations. Besides, such light-matter interaction opens up the possibility for the realization of the feedback cooling, i.e. structure's motion damping, that will allow to reduce a jitter of an embedded QD's emission caused by its coupling to a strain. Moreover, precise tuning of the structure's position and, therefore, a QDs' emission can be implemented based on a static use of this effect.

In the last chapter an original technique of nanostructures motion detection and manipulation using Scanning Electron Microscope was presented. A common trend to structures' miniaturization in order to achieve better device's characteristics (higher sensitivity, lower power consumption, etc) arouse our interest in it. This method allows to get access to the motion's measurements for structures as small as 20 nm, whereas all optical methods are limited by the light diffraction limit. Despite a number of shortcomings, this method is very promising both for a simple control of the nano-oscillator's mechanical properties and for a motion suppression or amplification via back-action effect.

Bibliography

[1] D. Bouwmeester, A. Ekert, A. Zeilinger. Book. The Physics of Quantum Information. Springer Berlin Heidelberg (2000). 2

[2] Q. A. Turchette, C. J. Hood, W. Lange, H. Mabuchi, and H. J. Kimble. Measurement of conditional phase shifts for quantum logic. Phys. Rev. Lett. 75, 4710-4713 (1995). 2

[3] K. J. Vahala. Optical microcavities. Nature 424, 839-846 (2003). 2

[4] A. Dousse, L. Lanco, J. Suffczynski, E. Semenova, A. Miard, A. Lemaıtre, I. Sagnes, C. Roblin, J. Bloch, and P. Senellart. Controlled light-matter coupling for a single quantum dot embedded in a pillar microcavity using far-field optical lithography. Phys. Rev. Lett. 101, 267404 (2008). 2

[5] O. Gazzano, S. Michaelis de Vasconcellos, C. Arnold, A. Nowak, E. Galopin, I. Sagnes, L. Lanco, A. Lemaıtre, and P. Senellart. Bright solid-state sources of indistinguishable single photons. Nature Communications 4, 1425 (2013). 2

[6] P. Lodahl, A. Floris van Driel, I. S. Nikolaev, A. Irman, K. Overgaag, D. Vanmaekelbergh, and W. L. Vos. Controlling the dynamics of spontaneous emission from quantum dots by photonic crystals. Nature 430, 654-657 (2004). 2

[7] N. S. Malik. Thesis. Les fils photoniques: une géométrie innovante pour la réalisation de sources de lumière quantique brillantes. Université de Grenoble (2011). 2, 6, 10

[8] J. Claudon, J. Bleuse, N. S. Malik, M. Bazin, P. Jaffrennou, N. Gregersen, C. Sauvan, P. Lalanne, and J.-M. Gerard. A highly efficient single-photon source based on a quantum dot in a photonic nanowire. Nature Photonics 4, 174-177 (2010). 2

[9] M. E. Reimer, G. Bulgarini, N. Akopian, M. Hocevar, M. B. Bavinck, M. A. Verheijen, E. P. A. M. Bakkers, L. P. Kouwenhoven, and V. Zwiller. Bright single-photon sources in bottom-up tailored nanowires. Nature Communications 3, 737 (2012). 2

[10] Hoai Anh Nguyen. Thesis. Two-mode giant optical nonlinearity with a single quantum dot in a photonic waveguide. Université de Grenoble (2016). 2, 7

[11] M. S. Hanay, S. Kelber, A. K. Naik, D. Chi, S. Hentz, E. C. Bullard, E. Colinet, L. Duraffourg, and M. L. Roukes. Single-protein nanomechanical mass spectrometry in real time. Nature Nanotechnology 7, 602 (2012). 2

[12] H. Okamoto, N. Kitajima, K. Onomitsu, R. Kometani, S. I. Warisawa, S. Ishihara, and H. Yamaguchi. High-sensitivity charge detection using antisymmetric vibration in coupled micromechanical oscillators. Appl. Phys. Lett. 98, 13-16 (2011). 2

[13] D. Rugar, R. Budakian, H. J. Mamin, and B. W. Chui. Single spin detection by magnetic resonance force microscopy. Nature 430, 329-332 (2004). 2

[14] A. D. O'Connell, M. Hofheinz, M. Ansmann, R. C. Bialczak, M. Lenander, E. Lucero, M. Neeley, D. Sank, H. Wang, M. Weides, J. Wenner, J. M. Martinis, and A. N. Cleland. Quantum ground state and single-phonon control of a mechanical resonator. Nature 464, 697-703 (2010). 2, 114

[15] J. D. Teufel, T. Donner, D. Li, J. W. Harlow, M. S. Allman, K. Cicak, A. J. Sirois, J . D. Whittaker, K. W. Lehnert, and R. W. Simmonds. Sideband cooling of micromechanical motion to the quantum ground state. Nature 475, 359-363 (2011). 2, 114

[16] J. Chan, T. P. M. Alegre, A. H. Safavi-Naeini, J. T. Hill, A. Krause, S. Groeblacher, M. Aspelmeyer, and O. Painter. Laser cooling of a nanomechanical oscillator into its quantum ground state. Nature 478, 18 (2011). 2, 114

[17] T. P. Purdy, R. W. Peterson, and C. A. Regal. Observation of radiation pressure shot noise on a macroscopic object. Science New York 339, 801 (2013). 2

[18] T. A. Palomaki, J. D. Teufel, R. W. Simmonds, and K. W. Lehnert. Entangling mechanical motion with microwave fields. Science New York 342, 710 (2013). 2

[19] Inah Yeo. Thesis. Une boite quantique dans un fil photonique: spectroscopie et optomécanique. Université de Grenoble (2012). 2, 3, 18, 40, 62, 83

[20] I. Yeo, P-L. de Assis, A. Gloppe, E. Dupont-Ferrier, P. Verlot, N. S. Malik, E. Dupuy, J. Claudon, J-M. Gérard, A. Auffèves, G. Nogues, S. Seidelin, J-Ph. Poizat, O. Arcizet and M. Richard. Strain-mediated coupling in a quantum dot–mechanical oscillator hybrid system. Nature Nanotechnology 9, 106-110 (2014). 2, 3, 18, 62

[21] P.-L. de Assis, I. Yeo, A. Gloppe, H. A. Nguyen, D. Tumanov, E. Dupont-Ferrier, N. S. Malik, E. Dupuy, J. Claudon, J.-M. Gérard, A. Auffèves, O. Arcizet, M. Richard, and J.-Ph. Poizat. Strain-Gradient Position Mapping of Semiconductor Quantum Dots. Phys. Rev. Lett. 118, 117401 (2017). 2, 40, 51, 59

[22] I. Stranski, L. Krastanow. Zur Theorie der orientierten Ausscheidung von Ionenkristallen aufeinander. Abhandlungen der Mathematisch-Naturwissenschaftlichen Klasse IIb. Akademie der Wissenschaften Wien. 146, 797-810 (1938). 6

[23] I. Yeo, N. S. Malik, M. Munsch, E. Dupuy, J. Bleuse, Y.-M. Niquet, J.-M. Gérard, J. Claudon, E. Wagner, S. Seidelin, A. Auffeves, J.-P. Poizat, and G. Nogues. Surface effects in a semiconductor photonic nanowire and spectral stability of an embedded single quantum dot. Appl. Phys. Lett. 99, 233106 (2011). 8

[24] M. Munsch, N. S. Malik, E. Dupuy, A. Delga, J. Bleuse, J.-M. Gérard, J. Claudon, N. Gregersen, and J. Mork. Dielectric GaAs antenna ensuring an efficient broadband coupling between an InAs quantum dot and a gaussian optical beam. Phys. Rev. Lett. 110, 177402 (2013). 10, 11

[25] A.N. Cleland. Book. Foundations of nanomechanics: from solid-state theory to device applications. Springer (2003). 12, 120

[26] S. Kumar, R. Trotta, E. Zallo, J. D. Plumhof, P. Atkinson, A. Rastelli and O.G. Schmidt. Strain-induced tuning of the emission wavelength of high quality GaAs/AlGaAs quantum dots in the spectral range of the 87Rb D2 lines. Appl. Phys. Lett. 99, 161118 (2011). 18

[27] F. Ding, R. Singh, J. D. Plumhof, T. Zander, V. Krapek, Y. H. Chen, M. Benyoucef, V. Zwiller, K. Dorr, G. Bester, A. Rastelli, and O. G. Schmidt. Tuning the Exciton Binding Energies in Single Self-Assembled InGaAs/GaAs Quantum Dots by Piezoelectric-Induced Biaxial Stress. Phys. Rev. Lett. 104, 067405 (2010). 18

[28] J. E. Avron, G. Bisker, D. Gershoni, N. H. Lindner, and E. A. Meirom. Entanglement on Demand through Time Reordering. Phys. Rev. Lett. 100, 120501 (2008). 18

[29] S. Seidl, M. Kroner, A. Högele, K. Karrai, R. J. Warburton, A. Badolato, and P. M. Petroff. Effect of uniaxial stress on excitons in a self-assembled quantum dot. Appl. Phys. Lett. 88, 203113 (2006). 18

[30] R. Trotta, P. Atkinson, J. D. Plumhof, E. Zallo, R. O. Rezaev, S. Kumar, S. Baunack, J. R. Schröter, A. Rastelli, and O. G. Schmidt. Nanomembrane Quantum-Light-Emitting Diodes Integrated onto Piezoelectric Actuators. Adv. Mater. 24, 2668-2672 (2012). 18

[31] W. Langbein, P. Borri, U. Woggon, V. Stavarache, D. Reuter, and A. D. Wieck. Control of fine-structure splitting and biexciton binding in $In_xGa_{1-x}As$ quantum dots by annealing. Phys. Rev. B 69, 161301 (2004). 18

[32] A. I. Tartakovskii, M. N. Makhonin, I. R. Sellers, J. Cahill, A. D. Andreev, D. M. Whittaker, J-P. R. Wells, A. M. Fox, D. J. Mowbray, M. S. Skolnick, K. M. Groom, M. J. Steer, H. Y. Liu, and M. Hopkinson. Effect of thermal annealing and strain engineering on the fine structure of quantum dot excitons. Phys. Rev. B 70, 193303 (2004). 18

[33] R. J. Young, R. M. Stevenson, A. J. Shields, P. Atkinson, K. Cooper, D. A. Ritchie, K. M. Groom, A. I. Tartakovskii, and M. S. Skolnick. Inversion of exciton level splitting in quantum dots. Phys. Rev. B 72, 113305 (2005). 18

[34] X. Wu, X. Dou, K. Ding, P. Zhou, H. Ni, Z. Niu, D. Jiang, and B. Sun. In situ tuning the single photon emission from single quantum dots through hydrostatic pressure. Appl. Phys. Lett. 103, 252108 (2013). 18

[35] R. H. Dicke. Coherence in Spontaneous Radiation Processes. Phys. Rev. 93, 99 (1954). 18

[36] N. Skribanowitz, I. P. Herman, J. C. MacGillivray, and M. S. Feld. Observation of Dicke Superradiance in Optically Pumped HF Gas. Phys. Rev. Lett. 30, 309 (1973). 18

[37] V. V. Temnov and U. Woggon. Superradiance and Subradiance in an Inhomogeneously Broadened Ensemble of Two-Level Systems Coupled to a Low-Q Cavity. Phys. Rev. Lett. 95, 243602 (2005). 18, 59

[38] V. V. Temnov and U. Woggon. Photon statistics in the cooperative spontaneous emission. Optics Express 17, 5774-5782 (2009). 18

[39] D. Meiser and M. J. Holland. Intensity fluctuations in steady-state superradiance. Phys. Rev. A 81, 063827 (2010). 18

[40] D. Meiser and M. J. Holland. Steady-state superradiance with alkaline-earth-metal atoms. Phys. Rev. A 81, 033847 (2010). 18

[41] A. Auffèves, D. Gerace, S. Portolan, A. Drezet and M. França Santos. Few emitters in a cavity: from cooperative emission to individualization. New Journal of Physics 13, 093020 (2011). 18, 59

[42] Yu. Cardona. Book. Fundamentals of Semiconductors Physics and Materials Properties. Springer (2010). 31, 35

[43] Yu. A. Burenkov, Yu. M. Burdukov, S. Yu. Davidov, and S. P. Nikanorov. Sov. Phys. Solid State 15, 1175-1177 (1973). 31

[44] Yu. A. Burenkov, S. Yu. Davydov, and S. P. Nikanorov. Sov. Phys. Solid State 17, 1446-1447 (1975). 31

[45] E. Rittweger, K.Y. Han, S.E. Irvine, C. Eggeling and S. W. Hell. STED microscopy reveals crystal colour centres with nanometric resolution. Nature Photonics 3, 144-147 (2009). 59

[46] E. Betzig, and R. J. Chichester. Single Molecules Observed by Near-Field Scanning Optical Microscopy. Science 262, 1422-1425 (1993). 59

[47] K. Matsuda, T. Saiki, S. Nomura, M. Mihara, Y. Aoyagi, S. Nair, and T. Takagahara. Near-field optical mapping of exciton wave functions in a GaAs quantum dot. Phys. Rev. Lett. 91, 177401 (2003). 59

[48] P. Lebedew. Untersuchungen über die Druckkräfte des Lichtes. Annalen der Physik 311, 433-458 (1901). 62

[49] A. Ashkin. Acceleration and trapping of particles by radiation pressure. Phys. Rev. Lett. 24, 156-159 (1970). 62

[50] T. Ikuno, S. Honda, T. Yasuda, K. Oura, and M. Katayama. Thermally driven nanomechanical deflection of hybrid nanowires. Appl. Phys. Lett. 87, 213104 (2005). 62, 124

[51] Arnaud Gloppe. Thesis. Nano-optomécanique au coeur d'un faisceau laser focalisé: cartographie du champ de force optique et action en retour bidimensionnelle. Université de Grenoble (2014). 62

[52] A. Gloppe, P. Verlot, E. Dupont-Ferrier, A. Siria, P. Poncharal, G. Bachelier, P. Vincent, and O. Arcizet. Bidimensional nano-optomechanics and topological backaction in a non-conservative radiation force field. Nature Nanotechnology 9, 920-926 (2014). 62

[53] B. Sanii, and P.D. Ashby. High sensitivity deflection detection of nanowires. Phys. Rev. Lett., 104, 147203 (2010). 62, 114

[54] K. M. Booth, and S. L. Hill. Book. The essence of optoelectronics. Prentice Hall (1998). 64

[55] Thorlabs website: https://www.thorlabs.com/newgrouppage9.cfm?objectgroup_id=681080

[56] A. D. Rakić and M. L. Majewski. Modeling the optical dielectric function of GaAs and AlAs: Extension of Adachi's model. J. Appl. Phys. 80, 5909-5914 (1996). 92

[57] S. Ozaki and S. Adachi. Spectroscopic ellipsometry and thermoreflectance of GaAs. J. Appl. Phys. 78, 3380-3386 (1995). 92

[58] E. D. Palik. Handbook of Optical Constants of Solids I. Academic, Orlando, FL (1985). 92

[59] P.-A. Mante, C.-Y. Ho, L.-W. Tu, and C.-K. Sun. Interferometric detection of extensional modes of GaN nanorods array. Optics Express 20, 18717-18722 (2012). 110

[60] Y. Hadjar, P-F. Cohadon, C. G. Aminoff, M. Pinard, and A. Heidmann. High-sensitivity measurement of mechanical Brownian motion. Europhys. Lett. 47, 545-551 (1999). 110

[61] A. Hopkins, K. Jacobs, S. Habib, and K. Schwab. Feedback cooling of a nanomechanical resonator. Phys. Rev. B 68, 235328 (2003). 110

[62] A. Niguès, A. Siria, and P. Verlot. Dynamical backaction cooling with free electrons. Nature Communications 6, 8104 (2015). 114, 116, 123, 124, 128

[63] G. Z. Sauerbrey. Verwendung von Schwingquarzen zur Wägung dünner Schichten und zur Mikrowägung Physik 155, 206 (1959). 114

[64] B. Ilic, H. G. Craighead, S. Krylov, W. Senaratne, C. Ober and P. Neuzil. Attogram detection using nanoelectromechanical oscillators J. Appl. Phys. 95, 3694 (2004). 114

[65] Y. T. Yang , C. Callegari , X. L. Feng , K. L. Ekinci , and M. L. Roukes. Zeptogram-Scale Nanomechanical Mass Sensing. Nano Lett., 6, 583–586 (2006). 114

[66] H. B. Peng, C. W. Chang, S. Aloni, T. D. Yuzvinsky, and A. Zettl. Ultrahigh Frequency Nanotube Resonators. Phys. Rev. Lett. 97, 087203 (2006). 114

[67] X. L. Feng, Rongrui He, Peidong Yang, and M. L. Roukes. Very High Frequency Silicon Nanowire Electromechanical Resonators. Nano Lett. 7, 1953-1959 (2007). 114

[68] K. L. Ekinci, X. M. H. Huang, and M. L. Roukesb. Ultrasensitive nanoelectromechanical mass detection. Appl. Phys. Lett. 84, 4469 (2004). 114

[69] K. Jensen, K. Kim, and A. Zettl. An atomic-resolution nanomechanical mass sensor. Nature Nanotechnology 3, 533-537 (2008). 114

[70] K. L. Ekinci, Y. T. Yang, and M. L. Roukes. Ultimate limits to inertial mass sensing based upon nanoelectromechanical systems. J. Appl. Phys. 95, 2682 (2004). 114

[71] A. Dorsel, J. D. McCullen, P. Meystre, E. Vignes and H. Walther. Optical Bistability and Mirror Confinement Induced by Radiation Pressure. Phys. Rev. Lett. 51, 1550-1553 (1983). 114

[72] S. Gigan, H. R. Bohm, M. Paternostro, F. Blaser, G. Langer, J. B. Hertzberg, K. C. Schwab, D. Bauerle, M. Aspelmeyer, and A. Zeilinger. Self-cooling of a micromirror by radiation pressure. Nature 444, 67-70 (2006). 114

[73] O. Arcizet, P.-F. Cohadon, T. Briant, M. Pinard, and A. Heidmann. Radiation pressure cooling and optomechanical instability of a micromirror. Nature 444, 71-74 (2006). 114

[74] D. Kleckner and D. Bouwmeester. Sub-kelvin optical cooling of a micromechanical resonator. Nature 444, 75-78 (2006). 114

[75] T. J. Kippenberg, H. Rokhsari, T. Carmon, A. Scherer, and K. J. Vahala. Analysis of Radiation-Pressure Induced Mechanical Oscillation of an Optical Microcavity. Phys. Rev. Lett. 95, 033901 (2005). 114, 132

[76] A. Schliesser, P. Del'Haye, N. Nooshi, K. J. Vahala, and T. J. Kippenberg. Radiation Pressure Cooling of a Micromechanical Oscillator Using Dynamical Backaction. Phys. Rev. Lett. 97, 243905 (2006). 114

[77] I. Wilson-Rae, N. Nooshi, W. Zwerger, and T. Kippenberg. Theory of ground state cooling of a mechanical oscillator using dynamical backaction. Phys. Rev. Lett. 99, 093901 (2007). 114

[78] J. Chaste, M. Sledzinska, M. Zdrojek, J. Moser, and A. Bachtold. High-frequency nanotube mechanical resonators. Appl. Phys. Lett., 99, 2011-2014 (2011). 114

[79] E. A. Laird, F. Pei, W. Tang, G. A. Steele, and L. P. Kouwenhoven. A high quality factor carbon nanotube mechanical resonator at 39 GHz. Nano Lett. 12, 193-197 (2012). 114

[80] J. Moser, A. Eichler, J. Guttinger, M. I. Dykman, and A. Bachtold. Nanotube mechanical resonators with quality factors of up to 5 million. Nature Nanotechnology, 9, 1007-1011 (2014). 114

[81] J. Chaste, A. Eichler, J. Moser, G. Ceballos, R. Rurali, and A. Bachtold. A nanomechanical mass sensor with yoctogram resolution. Nature Nanotechnology, 7, 301-304 (2012). 114

[82] J. Moser, J. Guttinger, A. Eichler, M. J. Esplandiu, D. E. Liu, M. I. Dykman, and A. Bachtold. Ultrasensitive force detection with a nanotube mechanical resonator. Nature Nanotechnology, 8, 493-496 (2013). 114

[83] R. S. Wagner and W. C. Ellis. Vapor-liquid-solid mechanism of single crystal growth. Appl. Phys. Lett. 4 , 89 (1964). 116

[84] Pamela Rueda-Fonseca. Thesis. Magnetic quantum dots in II-VI semiconductor nanowires. Université de Grenoble (2015). 117

[85] R. Kubo. The fluctuation-dissipation theorem. Rep. Prog. Phys. 29, 255 (1966). 123

[86] A. Siria, M. S. Rodrigues, O. Dhez, W. Schwartz, G. Torricelli, S. LeDenmat, N. Rochat, G. Auvert, O. Bikondoa, T. H. Metzger, D. Wermeille, R. Felici, F. Comin and J. Chevrier. X-ray pushing of a mechanical microswing. Nanotechnology 19, 445501 (2008). 124

[87] I. Tsioutsios, A. Tavernarakis, J. Osmond, P. Verlot and A. Bachtold. Real-time Measurement of Nanotube Resonator Fluctuations in an Electron Microscope. Nano Lett. 17, 1748-1755 (2017). 132

[88] E. Gavartin, P. Verlot, and T. J. Kippenberg. Stabilization of a linear nanomechanical oscillator to its thermodynamic limit. Nature Communications 4, 2860 (2013). 134

[89] E. Gil-Santos, D. Ramos, J. Martınez, M. Fernandez-Regulez, R. Garcıa, A. San Paulo, M. Calleja, and J. Tamayo. Nanomechanical mass sensing and stiffness spectrometry based on two-dimensional vibrations of resonant nanowires. Nature Nanotechnology 5, 641-645 (2010).

134